Mechanical behaviour of cohesionless soils: Implications for offshore foundation design



Kathy Ziwei Wen

St Peter's College

University of Oxford

A thesis submitted for the degree of

Doctor of Philosophy

Trinity 2024

Abstract

Mechanical behaviour of cohesionless soils: Implications for offshore foundation design

Kathy Ziwei Wen

St Peter's College, University of Oxford

A thesis submitted for the degree of *Doctor of Philosophy*

Trinity 2024

The design of offshore wind turbine (OWT) foundations necessitates a thorough understanding of the mechanical behaviour of its founding soil. The soil's stiffness, G_0 and stiffness degradation, G/G_0 are key factors influencing the foundation's resistance to cyclic loading. This thesis undertakes a parametric study of G_0, and the G/G_0 complemented by an experimental study using the Resonant Column Apparatus (RCA). Many empirical models predicting G_0 and G/G_0 for cohesionless soils rely on the coefficient of uniformity, C_u. However, C_u can be altered by changing the average diameter, d_{50}, fines content $F.C$ and gravel content $G.C$ which have opposing impacts on G_0 and G/G_0 making sole reliance on C_u unreliable. Experimentally, it is shown that within the elastic region, G/G_0 varies minimally across all investigated parameters.

The cyclic behaviour and underlying physical mechanisms are explored through extensive tests in the Variable Dynamic Direct Simple Shear (VDDCSS) apparatus. Specifically key features such as densification, generation of porewater pressure, accumulated ratcheting and changes to stiffness, energy dissipation and post-cyclic strength are explored. Drainage condition notably influences these behaviours, with cyclic amplitude, loading symmetry, and relative density also playing significant roles.

The experimental findings offer theoretical insights that inform OWT foundation design. A numerical study on a reference turbine reveals that realistic variations in G_0 have minimal impact on the system's natural frequency, however, can significantly influence OWT fatigue performance depending on pile diameter. This underscores the complexity of fatigue analysis, where stiffness and fatigue are not directly linked, necessitating a careful design approach. Finally, comparing experimental, model, and field tests on piles highlights potential links between soil behaviour at the elemental and field scales, with similar mechanisms governing both.

Acknowledgements

I extend my sincere gratitude to my esteemed supervisors, Professor Byron Byrne, and Dr Róisín Buckley, for their invaluable guidance and unwavering support throughout my research journey. Their expertise and mentorship have been instrumental in shaping the trajectory of my academic pursuits and my personal and professional development.

Special thanks to Clive Baker for his contributions to laboratory and engineering support, and to Alison May for her role in procuring new laboratory and field equipment.

I am particularly thankful to the dedicated Fugro team at Wallingford, who not only provided comprehensive training on soil testing equipment but also went above and beyond in accommodating my research interests. My heartfelt thanks to Neil Cotrell, Symmone Fyffe, Molly Thompson, Aiden Greenough, and Emily Vizi for generously sharing their time, knowledge, and expertise. Your efforts have greatly enriched my research.

It has truly been a pleasure to be part of the Civil Engineering Group at Oxford, surrounded by so many bright and helpful individuals. I consider myself fortunate to have forged so many meaningful connections along the way. A sincere appreciation goes to Daniel Dehtyriov, Yixiong Jing, Ioannis Kamas, and Markella Zormpa, for the impromptu philosophical musings, controversial political discussions, shared laughter, and supportive camaraderie within the confines of Room 11.

To my dear friends from Australia and new friends I've met throughout this journey— Farheen Javed, Hoan-Vu Vu, Jahzeel Ani, Chantelle Cheung, Carmen Fung, Michele Lu, Lorraine Lung, Rebecca Thai, Jennifer Troung, Madhumita Varma and Sijia Yi —I am deeply grateful for our enduring friendship that has bridged the distance between Oxford, Sydney, Chengde and Geneva. Your thoughtful gestures, kind words, and continuous support have created a comforting sense of 'home' during my time abroad. Your friendship and encouragement, even from afar, has been a constant source of strength and pivotal in fuelling my perseverance.

Finally, to my family and especially my parents whom I am bound by an immeasurable debt of love. Without your unconditional support and inspiration, this could not have been possible.

Table of Contents

1 Chapter 1 5

1.1 Motivation and Background 5

1.2 Offshore wind turbine foundations 7

1.3 Loading conditions for offshore wind turbines 9

1.4 Considerations for serviceability limit state design 10

1.4.1 API/DVNGL method 10

1.4.2 PISA Design methods 11

1.4.3 PICASO project 12

1.5 Considerations for fatigue limit state design 13

1.6 Behaviour of cohesionless soils 14

1.6.1 Generalised behaviour of cohesionless soils 15

1.6.2 Strength of soils 16

1.6.3 Stiffness of soils 19

1.6.4 Drainage conditions 23

1.7 Cyclic loading 25

1.7.1 Drainage considerations 27

1.7.2 Accumulated ratcheting 29

1.7.3 Generation of excess porewater pressure 32

1.7.4 Evolution of stiffness 32

1.7.5 Evolution of energy dissipation 33

1.8 Research Objectives 33

2 Chapter 2 36

2.1 Introduction 36

2.2 *In-situ* testing methods 37

2.2.1 Cone penetration test 37

2.2.2 CPT-D_r correlations 38
2.2.3 *CPT-G_0* correlations 40
2.3 Test Material 42
2.3.1 Cuxhaven sand 42
2.3.2 North England sand 46
2.3.3 Leighton buzzard sand 48
2.3.4 Classification tests 48
2.4 Bender Element test (BE) 49
2.4.1 Characteristic points 50
2.4.2 Cross-correlation 51
2.5 Resonant Column Apparatus (RCA) 52
2.5.1 Wave Equation for Torsional Oscillations 52
2.5.2 Derivation of Shear Strain 55
2.5.3 Energy dissipation Calculation 56
2.5.4 Apparatus used in this study 57
2.5.5 Test procedure 59
2.5.6 Limitations of System 62
2.6 Commissioning of the RCA 63
2.6.1 Calibration of RCA device 63
2.6.2 Comparison of measured data with results obtained by others 64
2.6.3 Repeatability tests 65
2.6.4 Effects of specimen preparation 66
2.7 Variable Dynamic Direct Cyclic Simple Shear (VDDCSS) 67
2.7.1 Stress-strain response in the VDDCSS 68
2.7.2 Failure states in the VDDCSS 70
2.7.3 Cyclic definitions 70
2.7.4 Loading asymmetry 72

2.7.5 Multidirectional loading 73
2.7.6 Apparatus used in this study 76
2.7.7 Test procedure 77
2.7.8 Limitations of apparatus 78
2.8 Commissioning of the VDDCSS 80
2.8.1 Monotonic tests 80
2.8.2 Cyclic tests 81
3 Chapter 3 84
3.1 Introduction 84
3.2 Review of published trends 86
3.2.1 Database of stiffness tests 87
3.2.2 Parametric study on G_0 94
3.2.3 Parametric study on stiffness degradation 98
3.2.4 Key observations 102
3.3 Test schedule and results 104
3.4 G_0 results 109
3.4.1 General observations 109
3.4.2 Discussion of measurement techniques 110
3.4.3 G_0 measurements 112
3.4.4 Saturated vs dry response 114
3.4.5 Soil stiffness profile of NE and CX sand 115
3.5 Obtaining representative stiffness parameters via the RCA 116
3.5.1 Elastic degradation of soil 116
3.5.2 Discussion and implications for design 118
3.6 Stiffness degradation parameters of cohesionless soils 119
3.6.1 Stiffness degradation 119
3.6.2 Effect of p'_0 121

3.6.3 Effect of D_r 122
3.7 Conclusions 123
4 Chapter 4 126
4.1 Introduction 126
4.2 Monotonic behaviour of soil 129
4.2.1 Test schedule and results 129
4.2.2 Monotonic response of soils 130
4.2.3 Discussion 134
4.3 Drained cyclic VDDCSS tests 135
4.3.1 Test schedule and results 135
4.3.2 Densification with cycles 139
4.3.3 Accumulated ratcheting with cycles 142
4.3.4 Stiffness and energy dissipation with cycles 145
4.3.5 Post-cyclic behaviour 147
4.3.6 Multidirectional cyclic loading 151
4.4 Undrained VDDCSS tests 155
4.4.1 Test results schedule and results 156
4.4.2 Porewater pressure generation with cycles 160
4.4.3 Accumulated ratcheting with cycles 162
4.4.4 Stiffness and energy dissipation with cycles 164
4.4.5 Stress-path behaviour 167
4.4.6 Post-cyclic behaviour 169
4.4.7 Multidirectional loading 171
4.5 Reflections on cyclic behaviour 177
4.5.1 Drained and undrained cyclic behaviour 177
4.5.2 Influence of material type 183
4.5.3 Implication for design methods of OWT foundations 187

4.6 Conclusions 192
5 Chapter 5 194
5.1 Introduction 194
5.2 Elastic analysis of laterally loaded piles 195
5.2.1 Analytical solutions for foundation stiffness 196
5.2.2 Numerical solutions for foundation stiffness 197
5.3 Fatigue analysis of OWT monopiles 199
5.3.1 Analytical predictions of f_0 199
5.3.2 Eigenvalue analysis 200
5.3.3 Damage calculation 201
5.4 Case study of 10MW DTU 202
5.4.1 Load determination 203
5.4.1 Modelling the OWT structural components 204
5.4.2 Modelling the soil-foundation system 205
5.4.3 Validation of 1D numerical method 207
5.4.4 Natural frequency 209
5.4.5 Fatigue and damage 213
5.4.6 Discussion 217
5.5 Application to model and field tests 219
5.5.1 Linking G_0 to foundation stiffness 'k_{max}' 220
5.5.2 Relationships for elastic behaviour 224
5.5.3 Relationships for full monotonic behaviour 228
5.5.4 Relationships for cyclic behaviour 232
5.5.5 Comparison with high cycle accumulation models 241
5.5.6 Discussion 245
5.6 Conclusion 246
6 Chapter 6 249

6.1 Introduction 249
6.2 Key contributions 250
6.3 Future research 253
7 References..... 257

Nomenclature

Greek alphabet variables

α	CSL curve fitting exponent
α_s	Angle of impacted soil
δ_{dec}	Logarithmic decrement
γ	Shear strain
γ'	Suberged unit weight of soil
γ_{acc}	Accumulated ratcheting
γ_{ave}	Average shear stress
γ_{cyc}	Cyclic shear stress
γ_{max}	Maximum unit weight of sand
γ_{min}	Minimum unit weight of sand
γ_r	Reference shear strain taken at shear stiffness degradation $G/G_0 = 0.5$
γ_{tl}	Linear threshold shear strain
γ_{tv}	Volumetric threshold shear strain
$\gamma_{0.7}$	Shear strain at shear stiffness degradation $G/G_0 = 0.7$
ε	Axial strain
ζ_b	Cyclic amplitude ratio
ζ_c	Cyclic asymmetry ratio
η	Energy dissipation (analogous with damping ratio)
λ	CSL curve fitting constant
θ_{acc}	Accumulated pile rotation
θ_e	Elastic pile rotation
θ_G	Ground level pile rotation
ν	Poisson's ratio
σ	Normal stress
σ_{atm}	Atompspheric stress
σ'	Effective normal stress
σ'_v	Effective vertical stress
ρ	Density of sand
τ	Shear stress
τ_{ave}	Average shear stress

τ_{cyc} Cyclic shear stress

τ_{peak} Peak shear stress

τ_{res} Residual shear stress

φ' Soil friction angle

Ψ State parameter

ω_r Resonant angular frequency

Latin alphabet variables

A Initial shear stiffness curve fitting constant

A_{eq} Equivalent shear area

c' Apparent cohesion

C_u Coefficient of uniformity

C_z Coefficient of curvature

d_{50} Particle size at 50% passing

D Damage factor

D_p Pile diameter

D_r Relative density

e Void ratio

e_{max} Maximum void ratio

e_{min} Minimum void ratio

E Young's modulus

E_E Elastic energy (per cycle)

E_H Hysteresis energy loss (per cycle)

EI Pile bending stiffness

f Loading frequency

f_0 Natural frequency of wind turbine

f_n Resonant frequency of soil specimen

f_s Sleeve friction

f_{1P} First excitation frequency, the constant rotational speed of the rotor

f_{3P} Second excitation frequency, the rotor blades pass the tower

F_r Friction ratio

G Shear stiffness

G_0 Initial shear stiffness from shear velocity relationship

G_{max} Initial shear stiffness from stress-strain relationship

G_s	Specific gravity
G_{sec}	Secant shear stiffness
G/G_0	Shear stiffness degradation
h	Loading eccentricity
H	Horizontal load
I	Moment of inertia
I_c	Behaviour index
k_{max}	Initial pile stiffness
k_{sec}	Secant pile stiffness
K_0	Coefficient of lateral pressure
K_L	Lateral soil-structure stiffness
K_{LR}	Lateral rotational soil-structure stiffness
K_R	Rotational soil-structure stiffness
L_p	Pile length
L_{tt}	Length of tip to tip from bender elements
m	Initial shear stiffness curve fitting exponent
M	Moment load applied at mudline
N	Number of cycles
N_f	Cycles to failure
p	Distributed lateral soil reaction (p-y and PISA monotonic methods)
p'	Mean effective stress
p'_0	Mean effective confining stress
P_a	Atmospheric pressure tken as 101.6kPa
q	Deviatoric stress
q_c	Cone tip resistance
q_t	Corrected cone tip resistance
Q_{tn}	Normalised cone tip resistance
s_u	Undrained shear strength of soil
t_a	Time of first arrival
t_W	Pile wall thickness
u	Porewater pressure
v_G	Ground level pile displacement
V_s	Shear velocity

x	Length of impacted soil
y	Lateral pile displacement (p-y and PISA monotonic methods)
y_e	Elastic pile displacement
z	Vertical distance

Common abbreviations

AOD	Above ordnance datum
BE	Bender Element
CPT	Cone penetration test
CPTu	Cone penetration test with porewater pressure
CS	Critical state
CSL	Critical state line
CT	Characteristic threshold (analogous to phase transformation)
CX	Cuxhaven
DK	Dunkirk
F.C	Fines content
FE	Finite element
FLS	Fatigue limit state
G.C	Gravel content
LBS	Leighton buzzard sand
LVDT	Linear variable differential transformer
NE	North England
OWT	Offshore wind turbine
PT	Phase transformation
PT_{cyc}	Phase transformation during cyclic loading
PTL	Phase transformation line
RL	Relative level
RCA	Resonant column apparatus
SLS	Serviceability limit state
SS	Steady state
SSL	Steady state line
SCPT	Seismic cone penetration test
ULS	Ultimate limit state
VDDCSS	Variable direct dynamic cyclic simple shear

The realisation that life is absurd cannot be an end, but only a beginning – Albert Camus

CHAPTER 1

Introduction

1.1 Motivation and Background

Sustainable forms of energy production are anticipated to rapidly develop within the coming decades as countries move to reduce carbon emissions to mitigate the adverse effects of climate change (Gielan et al. 2019). Energy extraction from offshore wind turbines (OWTs) has become an increasingly popular method of energy production in Europe, with the EU setting goals to achieve 500 GW of installed wind capacity by 2030 (European Commission 2023). To ensure the economic viability of future OWTs, scientific and industrial advancements are a necessity to reduce costs and increase functionality. With OWT foundations contributing a significant cost component of the structure, producing optimised foundation design has become a significant focus in securing OWTs as a renewable energy resource.

The research presented in this thesis is focused on exploring mechanical behaviour of cohesionless soils under cyclic loading and how their behaviour impacts the design of OWT foundations founded in such soils. The performance of OWT foundations

is governed by several physical mechanisms that are unique to offshore environments. These mechanisms are primarily generated by continuous cyclic loading at various amplitudes and directions induced by wind, waves, rotor operation, and other environmental conditions. Extreme weather events such as storms can lead to the failure of the OWT system and are a major consideration for ultimate limit state (ULS) design. The operational cyclic loads cause accumulated deformation and rotation, potentially making the structure non-operational, a major consideration in serviceability limit state (SLS) design. Furthermore, continuous cyclic loading causes fatigue damage to the structure and in some cases can lead to resonance of the OWT, which is considered in fatigue limit state (FLS) design. The founding soil properties and soil-structure interaction largely govern the performance of OWTs. A detailed understanding of the underlying soil mechanics governing foundation behaviour is hence of considerable interest.

The soil's stiffness is a key component that indicates the resistance of the soil to loading and ultimately influences the overall stiffness of OWT foundations. Soil stiffness and its applicability to the design of OWT foundations forms a key component of this research. Foundation behaviour is predicted using methods of varying complexity. This work demonstrates that soil stiffness is a crucial design parameter at all levels of OWT foundation design. Therefore, a strong understanding of the physical factors that contribute to soil stiffness is of interest for geotechnical engineers, an activity undertaken by several previous researchers such as Hardin and Black (1966); Sagaseta (1991); Menq (2003) and Wichtmann and Triantafyllidis (2009). This research aims to expand on this theoretical work by experimentally investigating the small-strain stiffness of cohesionless soils. This research explores the elastic bounds of cohesionless soil behaviour, which is particularly pertinent for the development of constitutive models that require delineation

between elastic and plastic soil behaviour such as Papadimitriou and Bouckovalas (2002) and Benz (2007).

In the context of offshore environments, the cyclic behaviour of soil and physical mechanisms that contribute to such behaviours additionally form a pivotal aspect of foundation design. Several notable features that characterise the cyclic behaviours of soils and foundations in response to cyclic loading have been identified in literature such as, densification, development of excess porewater pressure, accumulated ratcheting, changes in stiffness and energy dissipation. This research aims to experimentally explore the factors that contribute to these behaviours and determine the mechanisms that govern this behaviour through element testing. This ultimately develops the theoretical understanding of cyclic soil behaviour which will subsequently influence the cyclic behaviour of OWTs founded in cohesionless soils.

The application of these experimental outcomes to OWT design forms the final element of this research. Soil stiffness is known to influence the natural frequency, f_0, of OWT systems which dictates the fatigue performance of OWTs. An evaluation of the role of stiffness variation on f_0 and subsequently fatigue performance is presented. Finally, the connection between cyclic behaviour measured by element tests and behaviour observed in model and field pile tests is also explored, with implications for design discussed. The incorporation of experimental findings into simple empirical models are seen to improve design methodologies of OWT foundations undergoing cyclic loading.

1.2 Offshore wind turbine foundations

Several foundation design concepts have emerged to facilitate the growing demand of OWTs. Some typical design concepts are illustrated in Figure 1-1. As the demand for offshore wind as an energy source becomes greater (growing from 2MW turbines to >10MW). The OWT structures themselves are required to be larger, in both the swept

diameter of the OWT as well as the length of structure. To accommodate this growth, different foundation concepts have been developed allowing for larger OWT to be supported and for the structures to be installed in deeper water.

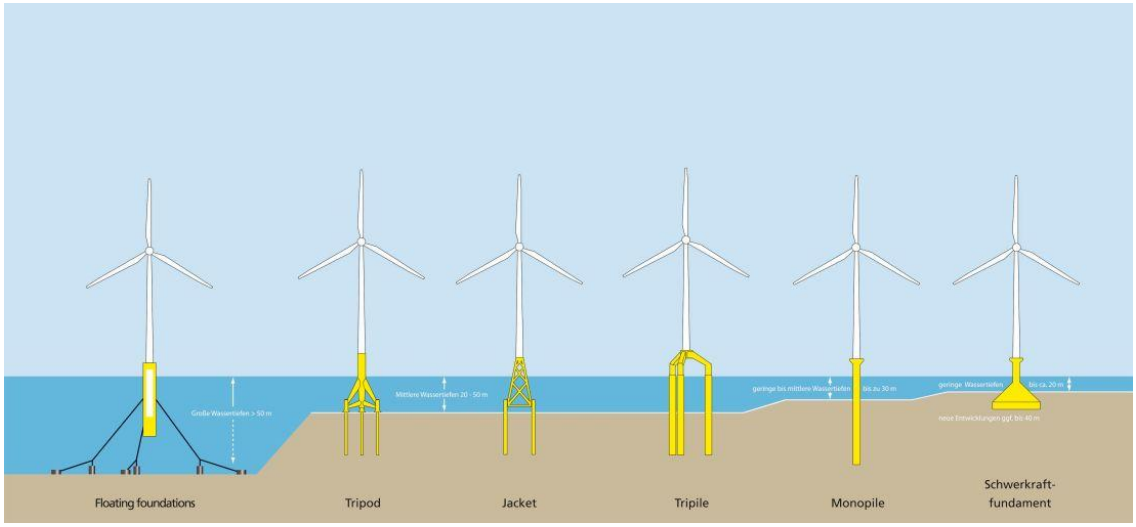


Figure 1-1 Typical OWT foundation types applied in industry (Source: German Offshore Wind Energy Foundation – Blickfang (Foundation Offshore Wind Energy, n.d)

Despite the various foundation types, monopiles have dominated the OWT industry. The structures are hollow, and tubular made from steel. Due to its simple and robust geometry, they are well suited for mass fabrication and can be more easily installed in a range of soil types compared to other foundation concepts (Kallehave et al. 2015). It appears that the monopile strikes an optimal balance between economic feasibility and constructability and implementation, therefore much of the design implications of this current research are related to monopiles.

It is worth mentioning here that as OWTs move towards deeper waters, there will be a limit where monopiles cannot continue to be the dominant foundation structure, at least from an economic perspective. It is envisioned that floating wind turbines moored with anchors will become increasingly popular for foundations installed in the deepest seas. However, even so it is likely that a combination of monopiles and floating foundations will be deployed in the OWT industry, depending on water depth. Therefore, applications for monopiles remain relevant and are likely to continue playing a significant role in the development of offshore wind energy.

1.3 Loading conditions for offshore wind turbines

OWT foundations are subjected to a variety of loads induced by its self-weight, wind and wave actions and turbine operational processes as schematically shown in Figure 1-2(a).

At foundation level, these load components can be translated into horizontal loads *H*, vertical loads, *V* and Moment, *M*, which are depicted in Figure 1-2(a). Loading in offshore environments are rather unique in that several of these loading types are dynamic in nature. Loadings from the wind and wave are considered pseudo-random, increasing and decreasing at different magnitudes with time as depicted in Figure 1-2(b). Loadings from wind, waves and rotor operation are not only dynamic but also cyclic in that they repeat (in magnitude) periodically. This also has implications for monopile design. It is necessary for OWT designers to take into consideration all combinations of loading conditions when applying design techniques to such structures.

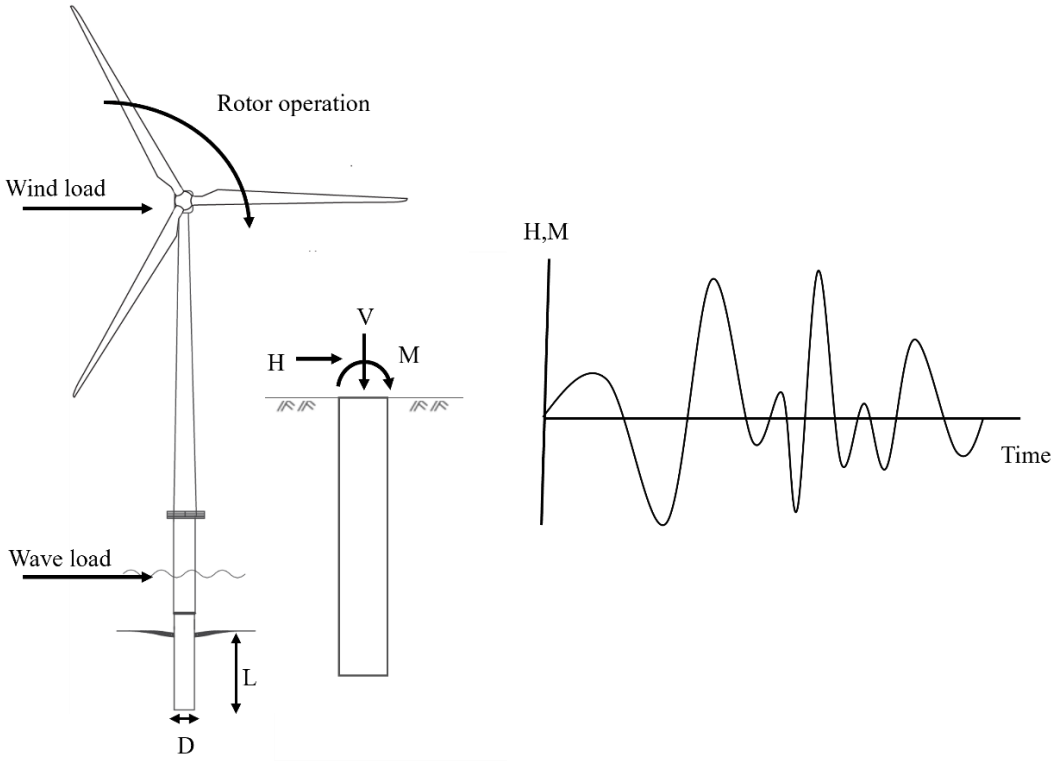


Figure 1-2 Typical OWT loading (a) Loads on an OWT, adapted from Byrne et al. (2017); and (b) Load amplitude with time

Monopile foundations are designed to resist environmental and operational loads, and to support the OWT. The optimisation of such monopiles requires careful choice of design parameters namely, the diameter, $D_{p,}$ embedded length, L_p and wall thickness of the monopile, t_W. Monopile dimensions are chosen to satisfy a variety of design limits. The D_p is generally constrained by the ultimate load state (ULS), the L_p is designed to limit the horizontal displacement, v_G and monopile rotation, θ_G to satisfy serviceability limit state (SLS) and t_W is typically designed to withstand material yield which is governed by the fatigue limit state (FLS). An additional consideration for offshore structures is that they are required to be designed to avoid resonance of the structure, a phenomenon that occurs if the f_0 of the structure coincides with the frequency bands of the rotor operation loads known as f_{1P} and f_{3P}. Therefore, several geotechnical analyses are required for robust OWT monopile design under these different loading conditions. This research focuses on OWT foundation design considerations under SLS and FLS conditions which are discussed further below.

1.4 Considerations for serviceability limit state design

The SLS design criterion refers to the ensuring that the serviceability of OWTs is maintained by limiting the v_G and θ_G. The evaluation methods for determining v_G and θ_G for monopiles are herein discussed.

1.4.1 API/DVNGL method

Historically, the design of offshore piles subjected to lateral loads has predominantly relied on the p-y method, which was initially developed for offshore oil and gas structures (Matlock 1970; Reese et al. 1974). In this approach, the pile is modelled as a series of beam-column elements supported by nonlinear independent springs at nodal points. The spring's resistance (p) is characterised as a function the lateral deflection (y), these are referred to as p-y curves. The displacement and stress distribution along the pile are

determined by solving a fourth-order differential equation derived from conventional beam theory:

$$EI\frac{d^4y}{dx^4} = E_s y \tag{1-1}$$

Where, EI is the flexural stiffness of the pile, *y* is the displacement of the monopile at a specific node, and $E_s = p/y$ denotes the stiffness of the soil extracted from p-y curves at different depths along the monopile. By adopting a finite difference approach, the fourth order differential equation can be solved iteratively. This method is recommended for foundation design by several offshore wind turbine standards (API 2010; DNVGL 2016). The recommended p-y curves from the offshore design standards were calibrated against a variety of large-scale field test conducted on piles with length to diameter ratios, $L_p/D_p > 34$. Monopiles however, typically have $L_p/D_p < 6$. Consequently, these existing curves do not accurately capture the expected behaviour of monopiles.

1.4.2 PISA Design methods

To address the short comings of the traditional *p-y* approach, the Pile Soil Analysis (PISA) project focused on developing improved design method for offshore monopiles under monotonic lateral loading. Led by DONG Energy, the project comprised medium-scale field testing, 3D finite element modelling, and 1D model development, resulting in a new design methodology for OWT monopiles under monotonic loading, Byrne et al. (2020); Burd et al. (2019). The findings from this project demonstrated that the geometry of the monopile provided the structure with greater ultimate capacity to monotonic loading compared to predictions from existing *p-y* methods, suggesting that the *p-y* method produced overconservative designs for OWT monopiles. The PISA design method was subsequently developed to account for the additional resistance provided by the monopile's geometry. Drawing from the *p-y* method, the PISA method also represents the monopile as a 1D beam model. However, the method incorporates additional resisting

components, distributed moment along the pile and a horizontal and moment acting at the pile base – this is illustrated in Figure 1-3(b) and (c). A conic function defines the soil reaction curves within the PISA design method, with the function parameters calibrated using site-specific 3D finite element analysis to accommodate different soil conditions and monopile geometries. The PISA project demonstrated substantial cost savings for offshore monopile design when applying this method for monotonic lateral loading.

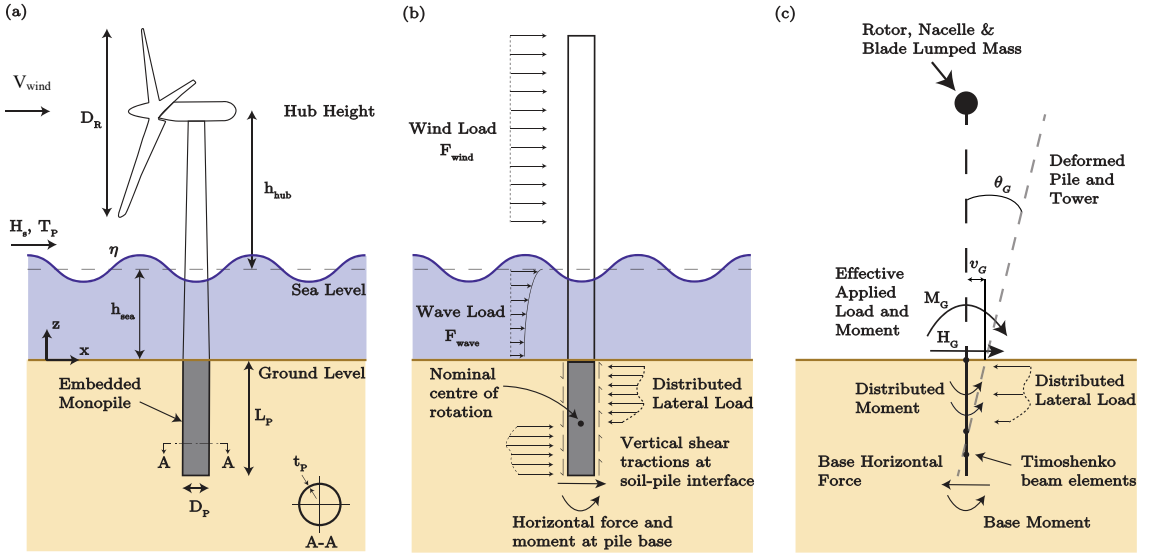


Figure 1-3 PISA design model (a) Geometry of an OWT with monopile foundation; (b) idealisation of soil components acting on foundation; and (c) 1-D implementation of model

1.4.3 PICASO project

As discussed, cyclic loading has been demonstrated as a prevalent loading condition for OWTs. Therefore, the next stage of research focuses on improved design methods for monopiles under cyclic loading. Part of the body of work from this thesis will contribute to the Pile Cyclic Analysis (PICASO) project, a collaborative endeavour between Ørsted and the University of Oxford that aims to develop design procedures that capture the cyclic loading behaviour of foundations. This is intended to be undertaken through theoretical advancements, laboratory testing, field testing, constitutive modelling, and application to design. The research presented in this thesis is related to the laboratory testing and characterisation of one of the test sites where medium-scale field tests of monopiles under cyclic loading will take place. The characterisation of the site involved

both onsite tests and a range of laboratory tests. Results from these activities produced several design parameters such as the initial shear stiffness, relative density and critical state parameters that are necessary inputs for advanced foundation modelling. A major part of this laboratory testing regime entailed an extensive investigation of the mechanical behaviour of cohesionless soils under cyclic loading. These experiments provided insights into the physical mechanisms that govern the cyclic behaviour of cohesionless soils. Incorporating these mechanisms into simple empirical models and more complex constitutive models has formed the final part of this research which aims to improve design methodologies of OWT foundations undergoing cyclic loading by connecting the behaviour of the soil at an element level to the medium-scale field tests and large-scale foundation behaviour.

1.5 Considerations for fatigue limit state design

In addition to the environmental loads (i.e., wind and waves), the rotational operation of OWT induce two further operational loads termed the 1P and 3P loads. The 1P vibrational load is mainly caused by mass and the aerodynamic imbalance of the rotor and the 3P vibrational load is mainly caused by wind shear and tower shadow effects as blades pass by the front of the tower. Repeated cycles of environmental and operational loads induce fatigue damage to the structure and therefore a key consideration for OWT designers is to improve the fatigue performance and prevent material yield. The eigenfrequency of the OWT, f_0, is a key aspect of the structure that influences the fatigue damage and FLS design. To prevent resonance and increase the fatigue performance of OWTs under continuous loads, the structure must be designed such that f_0 does not interfere with between the frequency bands of the 1P and 3P (f_{1P} and f_{3P}), whose values depend on turbine characteristics, nor the frequencies of the wind and wave loading, (Jonkman 2007; DNVGL 2016). Interference of f_0 with either environmental or operational frequency

cause increased fatigue damage to the OWT per cycle, therefore demonstrating the necessity of careful f_0 determination in FLS design. The excitation frequencies of the wind and wave loading are usually much lower than f_0 and thus the design of f_0 is typically constrained by f_{1P} and $f_{3P,}$ which is referred to as the "soft-stiff" region as illustrated in Figure 1-4.

The f_0 of the OWT is a function of the mass and structural geometry of the superstructure and substructure, material properties of the superstructure and substructure, loading eccentricity, position of water table and founding soil stiffness. Predictions of this value are typically obtained via such as using closed-form solutions proposed by Arany et al. (2017) or computed numerically using eigenvalue analysis, further discussed in Chapter 5.

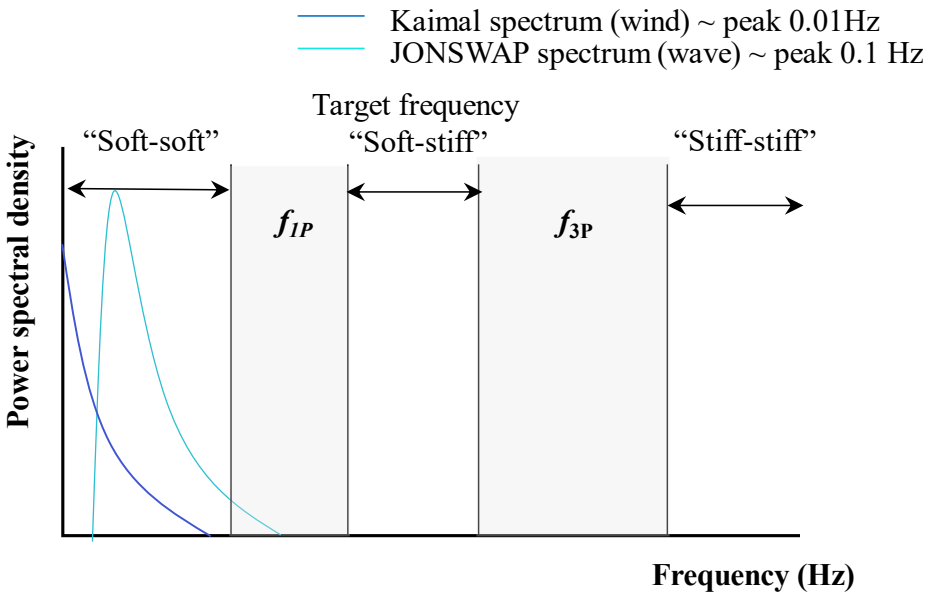


Figure 1-4 Operational excitation intervals of three bladed OWTs, areas shaded grey represent the f_{1P} and f_{3P} regions

1.6 Behaviour of cohesionless soils

Design methods for OWT foundations are, of course, largely governed by the behaviour of the founding soil. The following sections provide a comprehensive review of the theoretical aspects contributing to the mechanical behaviour of cohesionless soils and how this behaviour impacts the design of OWT foundations. It begins by introducing the

generalised behaviour of soils under monotonic shear loading. An explanation of current frameworks for characterising the monotonic behaviour of cohesionless soils is presented, with particular emphasis on the influence of drainage. Next, definitions of cyclic loading are provided, followed by a discussion of the key aspects of the cyclic behaviour of cohesionless soils and relevant literature in this area of study.

1.6.1 Generalised behaviour of cohesionless soils

The behaviour of cohesionless soils under monotonic shear loading largely depends on the 'initial state' of the soil and drainage conditions. These factors and their influence on the behaviour of cohesionless soil are explained in this section. A large suite of direct shear tests on cohesionless soils performed by Casagrande (1936) established general descriptions that characterise cohesionless soil behaviour under shear. These tests show that for densely compacted specimens, shearing causes the soil particles to interlock, leading the specimen to achieve a peak shear stress, denoted as $\tau_{peak.}$ Subsequent shearing acts to overcome this interlocking, causing τ to decline and eventually reach a residual shear stress, $\tau_{res,}$ as presented in Figure 1-5(a). During shearing, the volume of the specimen initially contracts due to the voids displaced from the shearing force and initial interlocking of soil particles. However, once interlocking is overcome, the specimen undergoes dilation until it reaches a critical state, where the volume change comes to a halt (See Figure 1-5(b)).

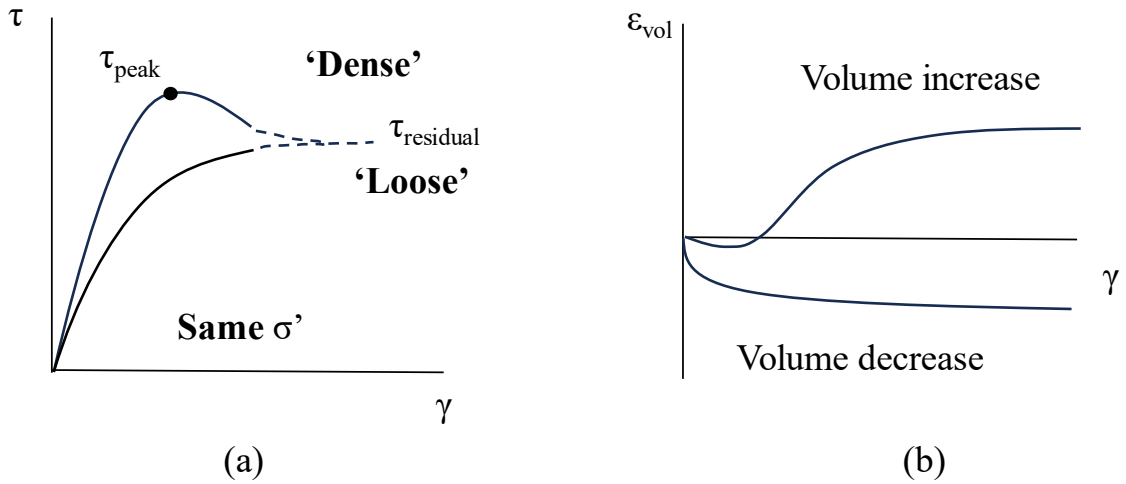


Figure 1-5 General behaviour of cohesionless soils undergoing shear loading (a) stress-strain; and (b) volume behaviour

For loosely compacted soil specimens, the specimen tends towards a maximum τ corresponding to τ_{res}. Only contraction during shearing is observed in loose specimen as the voids in the specimen are displaced from the shearing force, a process that continues until the specimen reaches its critical state.

1.6.2 Strength of soils

The strength of soil refers to its ability to withstand applied forces before failure. A satisfactory failure criterion should express the relationship between the principal stresses when the soil is in limiting equilibrium. The Mohr-Columb failure criterion is appropriate for characterising drained soil properties in terms of effective stress, whilst the Tresca failure criterion describes the undrained shear strength of soils, these criterions are illustrated in Figure 1-6(a) and (b) respectively.

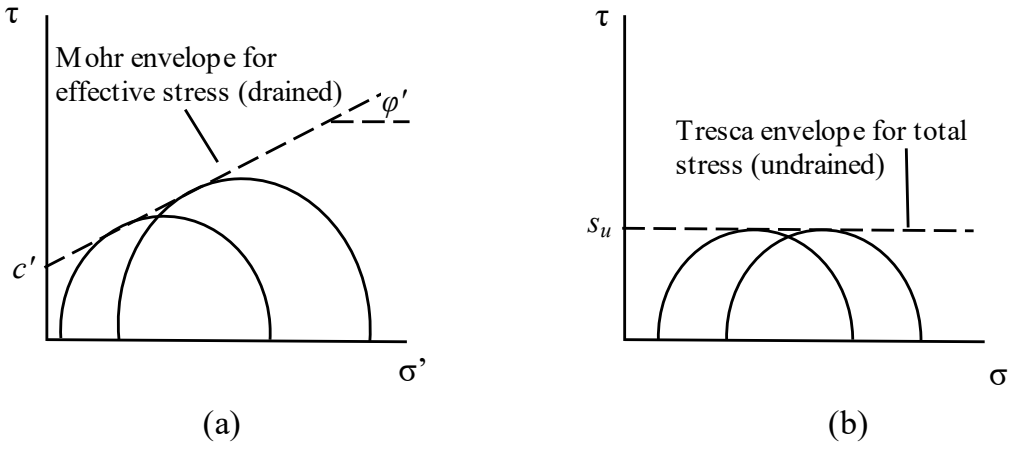


Figure 1-6 Idealised failure envelopes of a soil from *t*riaxial testing (a) example of drained consolidated test; and (b) example of undrained unconsolidated test

In Figure 1-6(a), the most marked feature that the failure criterion must consider is the increase in strength as the average effective stress increases, σ'. The failure envelope is controlled by the friction angle, φ', and apparent cohesion, c', which are intrinsic properties of the soil. In the Tresca framework in Figure 1-6(b), the failure envelope is independent of principle stresses for a particular soil and is characterised by a single parameter, the undrained shear strength, s_u.

Precise determination *in-situ* shear strength properties of cohesionless soil in the laboratory can be challenging, mainly due to difficulty in obtaining undisturbed samples. Cohesionless soils, such as sands and gravels, lose their natural structure and fabric during sampling and transportation. As a result, most laboratory tests on these soils are conducted on reconstituted specimens, which might misrepresent *in-situ* conditions.

1.6.2.1 Critical state framework

The concept of the critical state for soil, as defined by Roscoe et al. (1953), represents the state at which a soil continues to deform under constant stress and volume conditions. This constitutes the failure state of the soil specimen. As previously mentioned, Casagrande's direct shear tests on loose and dense cohesionless soils observed that, while dense specimens initially exhibited a τ_{peak}, they eventually converged towards the same τ_{res} as the loose specimen. Both loose and dense specimens reach a constant volume at the critical state that remains unchanged with further shearing. This suggests a distinct critical state exists in cohesionless soils regardless of initial density.

Conventional methods of charactering cohesionless soil as 'loose' or 'dense' rely on the concept of relative density, D_r, which is defined by:

$$\mathrm{D_r} = \frac{\mathrm{e_{max}} - \mathrm{e}}{\mathrm{e_{max}} - \mathrm{e_{min}}} \tag{1-2}$$

Where e_{min} and e_{max} refer to the minimum and maximum void ratios achievable for the soil, and e is the void ratio of the soil. Further discussion of D_r is presented in Section 2.2.

In a study by Verdugo and Ishihara (1996), the behaviour of cohesionless soil was investigated at the same void ratio but with varying initial confining stress, p'_0. The results indicated that the response of the soil was dependent on both p'_0 and e. Consequently, the state parameter, Ψ, was introduced to account for the coupled effects of p'_0 and e on the behaviour of cohesionless soil. The Ψ defined by Been et al. (1986) is the difference between the initial e of a specimen and e_{cs} at critical state for a given p'_0. As shown in Figure 1-(b) below, negative Ψ indicates 'denser than critical' and positive Ψ indicates 'looser than critical'. The Ψ relies on precise determination of the critical state line (CSL), typically obtained via triaxial tests, defined in the e, p' space (See 7(b)).

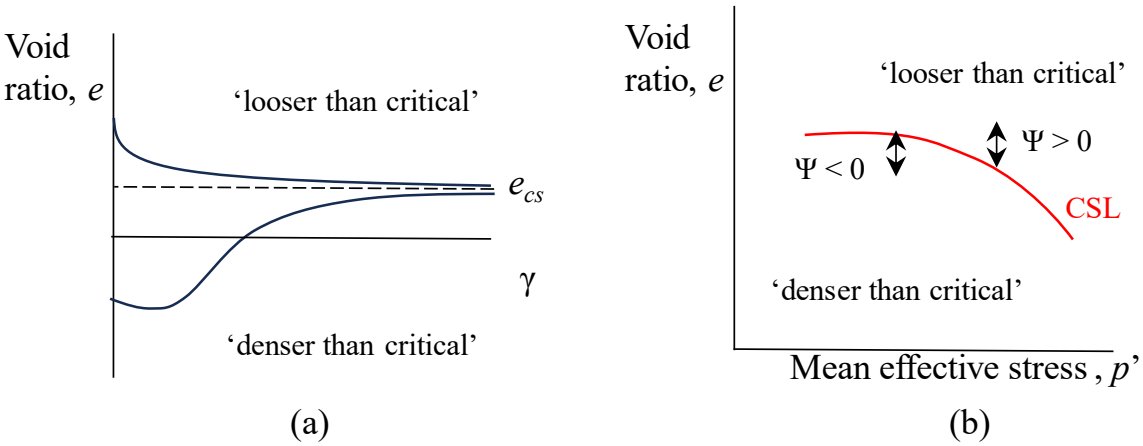


Figure 1-7 Illustration of Critical State Framework for cohesionless soils (a) e vs γ; and (b) e, p' space

For sand, the CSL exhibits nonlinearity and the power law suggested by Li et al. (1999) is routinely adopted in geotechnical practice as shown by the equation below:

$$e_{cs} = e_{ref} - \lambda \left(\frac{p'}{P_a}\right)^{\alpha} \alpha \tag{1-3}$$

Where p' is mean effective stress, P_a is the atmospheric pressure, e_{ref} is the reference void ratio at p' = 1kPa and λ and α are curve fitting parameters that control the shape of the CSL.

In conventional laboratory testing, obtaining the CSL for sands can be challenging, requiring special care during specimen preparation and throughout the triaxial test. The outcomes of the PISA project underscored these challenges, particularly in the suite of

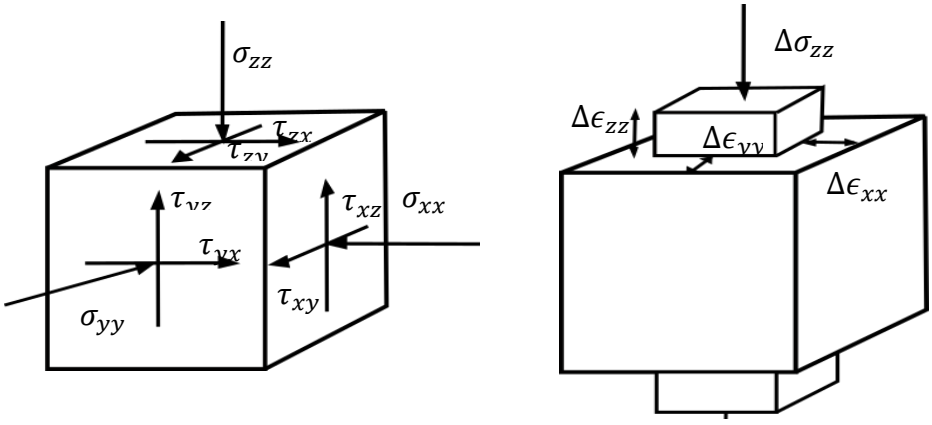
triaxial tests on Dunkirk Sand conducted by Liu et al. (2017). Results from loose specimens yielded a different CSL than dense specimens, revealing two distinct CSLs for the same material. Several triaxial tests conducted at lower confining stresses fell short of reaching the critical state due to premature strain localisation when shearing at lower stresses, Zdravković et al. (2020). Researchers have noted other soil properties that influence the position of the CSL for cohesionless soils, such as fabric, grain characteristics, particle size distribution, fines content (F.C), and gravel content (G.C), (Castro et al. 1982; Jeffries and Been 2006; Kang et al. 2019). This suggests that changes to soil specific properties may alter the position of the CSL.

1.6.3 Stiffness of soils

The stiffness of soil refers to its capacity to withstand deformation under loading, and its value evolves with further applied loading. At very small strains, the soil stiffness is linear elastic, where deformations are essentially recoverable. The governing equations to describe soil behaviour in such situations are discussed in Section 1.6.2.1 below.

1.6.3.1 Linear elastic stiffness

Considering a finite element of soil undergoing an increment of applied load, a depiction of the full principal stresses acting on this element is presented in Figure 1-8(a), and the corresponding strain that results in response to the load is shown in Figure 1-8(b).



(a) (b)

Figure 1-8 A 3D schematic of the (a) stresses; and (b) strain acting on an element of soil undergoing axial loading

For an increment of stress under vertical loading $\Delta\sigma_{zz}$ as presented in Figure 1-8(b), the following relationships can be assumed to describe the behaviour of the soil under linear elastic conditions:

$$\Delta\varepsilon_{zz} = \frac{\Delta\sigma_{zz}}{E} \tag{1-4}$$

$$\Delta\varepsilon_{xx} = \Delta\varepsilon_{yy} = -\nu \cdot \Delta\varepsilon_{zz} \tag{1-5}$$

Where *E* is the Young's modulus of the material. Independent increments of loading in the *x* and *y* plane causes the following:

$$\Delta\varepsilon_{zz} = -\nu \cdot \frac{\Delta\sigma_{xx}}{E} \tag{1-6}$$

$$\Delta\varepsilon_{zz} = -\nu \cdot \frac{\Delta\sigma_{yy}}{E} \tag{1-7}$$

Where *v* is the poisson ratio of the material. Therefore, by applying stress changes in all three directions and by superposition, the following strain equations can be established.

$$\Delta\varepsilon_{zz} = \frac{1}{E}\left(\Delta\sigma_{zz} - \nu \cdot \Delta\sigma_{xx} - \nu \cdot \Delta\sigma_{yy}\right) \tag{1-8}$$

$$\Delta\varepsilon_{xx} = \frac{1}{E}\left(\Delta\sigma_{xx} - \nu \cdot \Delta\sigma_{zz} - \nu \cdot \Delta\sigma_{yy}\right) \tag{1-9}$$

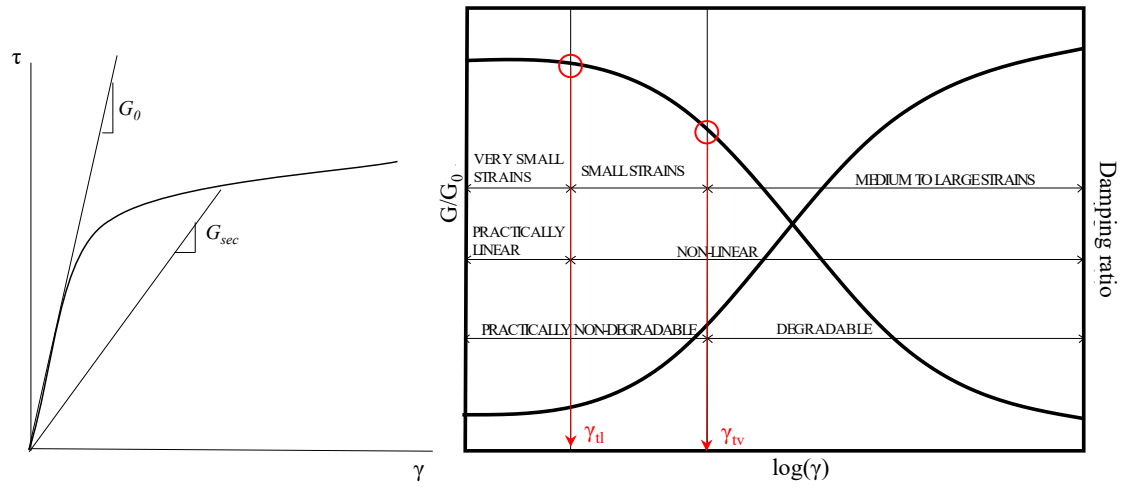
$$\Delta\varepsilon_{yy} = \frac{1}{E}\left(\Delta\sigma_{yy} - \nu \cdot \Delta\sigma_{zz} - \nu \cdot \Delta\sigma_{xx}\right) \tag{1-10}$$

The shear strain is pure distortion with no volume change. An increment of shear strain is related to shear stress by the following relationships, $\Delta\gamma_{xy} = \frac{\Delta\tau_{xy}}{G}$, $\Delta\gamma_{zx} = \frac{\Delta\tau_{zx}}{G}$, $\Delta\gamma_{yz} = \frac{\Delta\tau_{yz}}{G}$. The generalised relationship between stress and strain for a linear elastic material can therefore be expressed with the following matrix:

$$\begin{pmatrix} \delta\epsilon_{xx} \\ \delta\epsilon_{yy} \\ \delta\epsilon_{zz} \\ \delta\gamma_{yz} \\ \delta\gamma_{zx} \\ \delta\gamma_{xy} \end{pmatrix} = \begin{bmatrix} \frac{1}{E} & -\frac{\nu}{E} & -\frac{\nu}{E} & 0 & 0 & 0 \\ -\frac{\nu}{E} & \frac{1}{E} & -\frac{\nu}{E} & 0 & 0 & 0 \\ -\frac{\nu}{E} & -\frac{\nu}{E} & \frac{1}{E} & 0 & 0 & 0 \\ 0 & 0 & 0 & \frac{1}{G} & 0 & 0 \\ 0 & 0 & 0 & 0 & \frac{1}{G} & 0 \\ 0 & 0 & 0 & 0 & 0 & \frac{1}{G} \end{bmatrix} \cdot \begin{pmatrix} \delta\sigma_{xx} \\ \delta\sigma_{yy} \\ \delta\sigma_{zz} \\ \delta\tau_{yz} \\ \delta\tau_{zx} \\ \delta\tau_{xy} \end{pmatrix} \quad (1\text{-}11)$$

1.6.3.2 Stiffness across a wide strain range

This thesis focuses on shear stiffness, G which represents the soil's ability to resist shear loading. The initial shear stiffness, G_0, defined as $G_0 = \tau/\gamma$ at very small strains as illustrated in Figure 1-9(a), reflects the soil's behaviour when the assumption linear elasticity holds true. Soil stiffness is known to degrade with strain level, exhibiting some non-linearity even at small strains and is termed the secant shear stiffness, G_{sec} once this occurs. Many geotechnical analyses, e.g., Finite Element (FE), used to support offshore foundation design requires reliable information on both G_0 and stiffness degradation G/G_0. Furthermore, as discussed in Section 1.5, G_0 is a parameter that directly impacts the f_0 of OWTs, influencing the fatigue response of the structure.



(a) (b)

Figure 1-9 Typical soil behaviour under shear loading (a) τ,γ space; and (b) Stiffness degradation, G/G_0 with respect to γ adapted from Vucetic (1994)

Lo Presti (1991) and Vucetic (1994) introduced the concept of threshold strains to delineate the boundaries in the cyclic behaviour of soils at very small, small, and medium to large strains (see Figure 1-9(b)). At strains less than the linear cyclic threshold strain, $\gamma_{tl,}$ soils behave in a linear elastic manner. Between γ_{tl} and the volumetric cyclic threshold shear strain, $\gamma_{tv,}$ the soils begin to show non-linear behaviour, but the deformations are essentially recoverable even with the number of cycles. Beyond $\gamma_{tv,}$ the behaviour becomes significantly non-linear, and deformations are irrecoverable due to changes in the microstructure of the material. Past this point, both cohesive and cohesionless soils experience plastic strains and permanent stiffness degradation; Vucetic and Dobry (1988). The conceptual framework described by Jardine (1992) is also a useful tool for explaining observed soil behaviour across a wide range of strains. The framework is based on four nested yield surfaces with the first yield surface (Y1) limiting the region within which the response is linear elastic, analogous to $\gamma_{tl.}$ The second yield surface (Y2) limiting the elastic response, corresponding with γ_{tv}.

Hardin and Drnevich (1972b) showed that in clean sands, non-linear behaviour (and therefore the values of γ_{tl} and γ_{tv}) is controlled primarily by the strain amplitude, the mean effective confining pressure, p'_0 and the void ratio, $e.$ Relationships developed to capture the non-linear stiffness behaviour of cohesionless soils are discussed further in Chapter 3. From a practical perspective, the concept of threshold strain is an important input into constitutive models to replicate soil behaviour in FE analysis. The reference threshold strain $\gamma_{0.7,}$ the shear strain at which the shear stiffness has degraded to 70% of its original value, was introduced by Santos and Correia (2001), and is utilised in the hardening soil with small strain stiffness (HSS) model developed by Benz (2007) which is routinely used by industry. Complex constitutive models such as that described by

Papadimitriou and Bouckovalas (2002) control the boundary of elastic behaviour using a parameter that is physically associated with γ_{tv}.

Also presented on Figure 1-99(b) is the damping ratio with strain of a typical soil. Foundations and structures under dynamic or cyclic loading experience energy loss upon repeated loading. The foundation material's ability to dissipate energy is defined as the damping ratio. The damping ratio is inversely proportional to the soil's shear stiffness with increasing shear strain, (Seed and Idriss 1970; Chung et al. 1984; Menq 2003).

1.6.4 Drainage conditions

Much of the soil behaviour described thus far refers to that of cohesionless soils undergoing shearing in drained conditions. In the field, the drainage conditions depend on the loading rate, the permeability of the soil, and the drainage path (a function of foundation geometry and soil profile). When a load is applied quickly to soil, initially, the load is transferred to the porewater. The sudden loading does not allow for volume change in the soil medium, and instead, porewater pressure, u is generated. This is referred to undrained conditions. Once u dissipates, the loading is transferred from the porewater to the soil matrix, and changes to the soil volume occur; this state is referred to as drained. A drained response can also be induced at the onset of loading. In this situation, the load is applied directly to the soil matrix, allowing for the soil to deform and changes to the soil volume. Fine-grained cohesive soils exhibit low permeability, and most loading situations induce an undrained response. Cohesionless soils have higher permeability, and their behaviour is typically considered partially drained or drained.

In element testing, drained and undrained loading conditions can be induced. Generally, soil testing apparatuses control the drainage conditions by restricting the volume change of the specimen. The typical undrained behaviour of cohesionless soil can also be considered within the critical state framework. The Ψ of the specimen strongly

influences the undrained response of the soil. 'Looser than critical' specimens show contractive behaviour as u is generated upon shear loading and the effective stress reduces – this is typically referred to as the 'Flow condition'. In such cases, flow liquefaction occurs, which is a phenomenon where saturated soil rapidly loses a significant portion of its strength and stiffness due to undrained loading, such as during an earthquake (Kramer and Stewart 2024). This occurs when the shear stresses induced in the soil exceed its undrained shear strength, leading to sudden and catastrophic deformation. Conversely, 'Denser than critical' specimens exhibit dilative behaviour, where u is initially generated but then decreases with further shearing, causing p' to increase; this is referred to as the 'No-flow' condition. The typical undrained stress-strain response, stress paths and flow conditions are depicted in Figure 1-10(a) and (b) respectively.

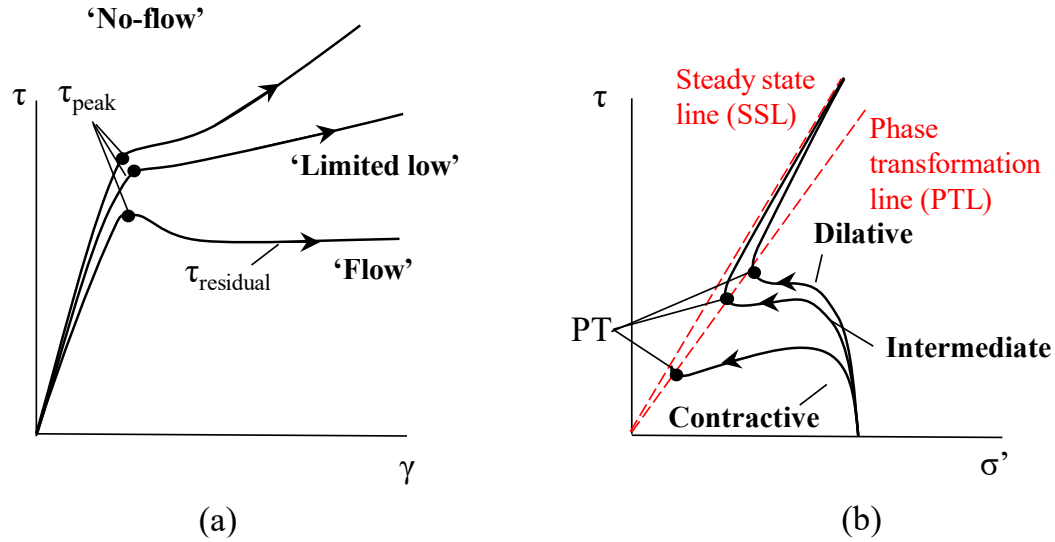


Figure 1-10 Definitions of flow and no-flow for undrained tests on cohesionless soil (adapted from Porcino et al. (2020)) (a) τ, γ space ; and (b) τ, σ' space

Although no volume change is permitted in undrained conditions, cohesionless soil specimens still exhibit 'denser' and 'looser' than critical behaviours, referred to as 'No-flow' and 'Flow' respectively. As seen in Figure 1-10(a), undrained shearing induces an initial peak shear stress, $\tau_{peak.}$, in all flow conditions. Subsequent post-peak behaviour is governed by the initial density of the specimen, with 'No-flow' and 'Flow' specimens producing post-peak strain hardening and softening respectively, see Figure 1-10(a). In

this thesis strain hardening refers to increase of stress with increasing strain whilst strain softening refers to a reduction in stress with increasing strain.

Figure 1-10(b) clearly demonstrates two 'states' of the soils on their stress path, referred to as the phase transformation (PT) and ultimate steady (SS) state. See Verdugo and Ishihara (1996) for details. The PT denotes the point at which the specimen changes from contractive to dilative behaviour, and the SS refers to the condition in which the mass is continuously deforming at constant volume, constant normal effective stress, constant shear stress, and constant velocity, as shown in Figure 1-10(b). The stress path of a 'looser than critical' specimen mostly exhibits contractive behaviour, while 'denser than critical' specimens experience contractive followed by dilative behaviour. Two lines can be obtained from the interpretation of these results: the phase transformation line (PTL) and the steady state line (SSL). Intellectually, for cohesionless soils, there appears to be little distinction between the critical and steady states (Jefferies and Been 2015). The term steady state and critical state are considered analogous in this thesis.

1.7 Cyclic loading

Cyclic loading refers to the repeated application of stress or strain, which is relevant to offshore environments. In element testing, the cyclic loading applied to the soil specimen is characterised by the average applied shear stress, $\tau_{ave,}$ and the cyclic shear stress, τ_{cyc}. The resultant average and cyclic shear strain induced in the specimen are denoted, $\gamma_{ave,}$ γ_{cyc} respectively. The cyclic definitions are presented on Figure 1-11.

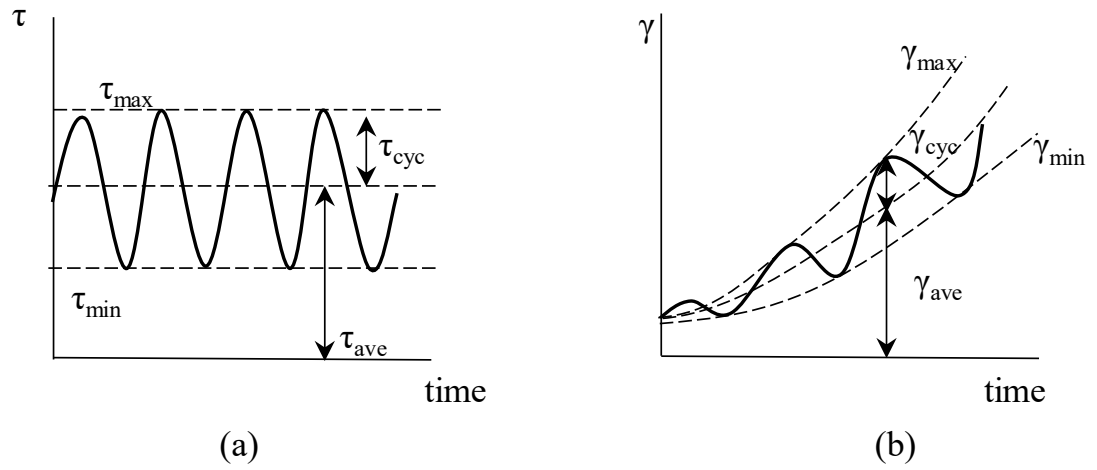


Figure 1-11 Cyclic stress and strain definitions (a) Cyclic stress, τ with time; and (b) Cyclic strain, γ with time

The maximum and minimum τ applied to the specimen are defined as:

$$\tau_{min} = \tau_{ave} - |\tau_{cyc}|, \qquad \tau_{max} = \tau_{ave} + |\tau_{cyc}| \tag{1-12}$$

In physical modelling tests, these cyclic parameters are typically characterised by the load amplitude ratio, ζ_b and load asymmetry, ζ_c as presented by Leblanc et al. (2010a); Richards (2019). These parameters refer to the magnitude of the load and the symmetry of loading. In element tests they are defined as:

$$\zeta_b = \tau_{max/\sigma_{REF}} \quad \zeta_c = \tau_{min}/\tau_{max} \tag{1-13}$$

$$\tau_{ave} = (\tau_{max} + \tau_{min})/2, \qquad \tau_{cyc} = (\tau_{max} - \tau_{min})/2 \tag{1-14}$$

Where σ_{REF} is the reference stress, taken to be $\tau_{residual}$ or τ_{peak} obtained from monotonic tests in this study. These cyclic definitions are schematically shown in Figure 1-12(a). Cyclic loading tests are classified into four categories based on the symmetry of loading referred to as two-way (ζ_c = -1), one-way (ζ_c = 0), partial-one way ($0 < \zeta_c < 1$) and partial two-way ($-1 < \zeta_c < 0$) and are illustrated in Figure 1-12(b).

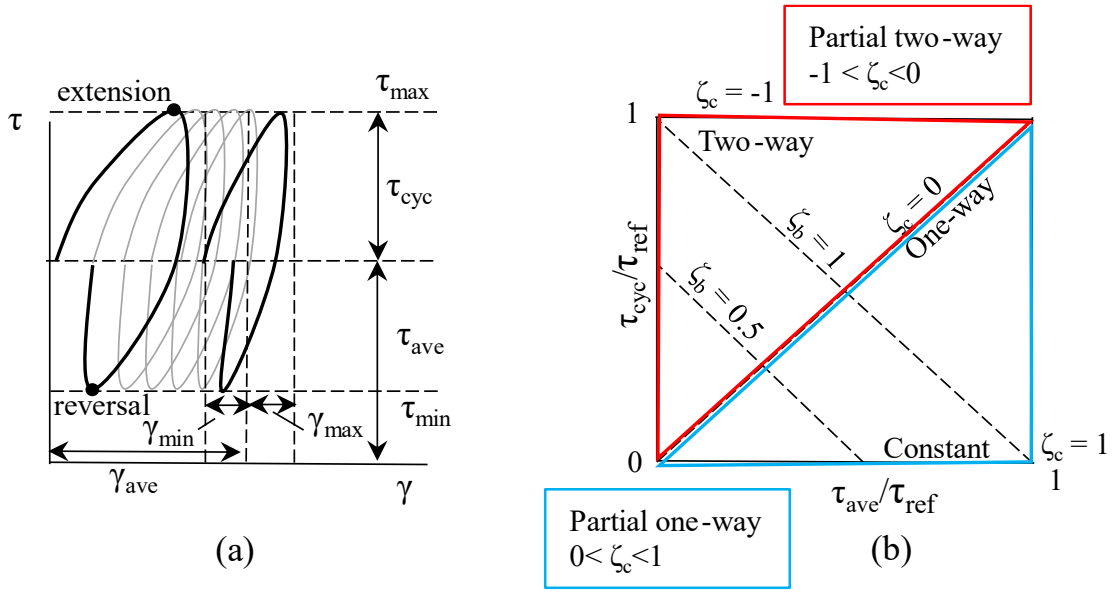


Figure 1-12 Cyclic definitions in this thesis (a) stress-strain response; and (b) graphical representation of ζ_b and ζ_c

1.7.1 Drainage considerations

The concept of drainage is particularly relevant when examining the cyclic behaviour of cohesionless soils. While it may be appropriate to assume that cyclic loading induces a fully undrained response in cohesive soils, this assumption may not be suitable for cohesionless soils. Instead, in cohesionless soils, the rate at which cyclic loading is applied significantly influences the drainage conditions. As mentioned in Section 1.6.4, if the loading applied to the soil is slow compared to the time required for *u* to dissipate, the loading condition is considered drained. In the case of cyclic loading, the rate at which the *u* dissipates is a function of drainage length (dependent on foundation geometry and soil layering) and the permeability of the soil. The cyclic loads applied to OWTs originate from several sources such as 1P/3P operational loads, wind, wave, and extreme storm events. Combined, such loading can induce different drainage conditions for OWTs over their lifetimes. While a drained loading situation is a common assumption for cohesionless soils, studies suggest that the typical diameters of modern offshore monopiles have the potential for *u* to develop, which will likely induce a partially drained response, (Zhang, et al. 2019; Jostad et al. 2020).

Cyclic loading in undrained conditions does not allow for volume change. Luong and Sidaner (1981) demonstrate the significance of the unique locus of stress states independent of the density of the sand and termed the characteristic threshold (CT) in p',q space. The term CT can be used interchangeably with the PT. The line dividubg the soil behaviour in stress space into two regions: the sub-characteristic region and super-characteristic region, as shown in Figure 1-13.

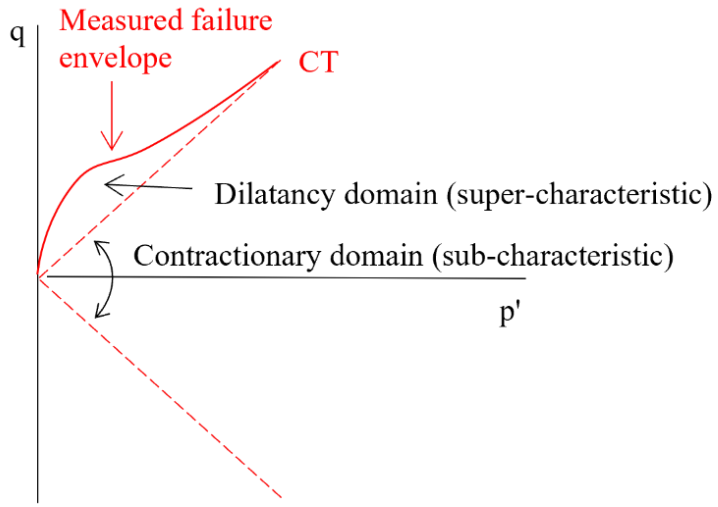


Figure 1-13 Schematic of the characteristic threshold (CT) line in p',q space (adapted from Chang and Whitman (1988) and Lade and Ibsen (1997))

The static stress of a soil specimen can be represented as a point in p',q space. Drained cyclic triaxial tests performed by Chang and Whitman (1988) observed that specimens at a static stress state below the CT line (sub-characteristic) would contract with cycles as water is expelled from the voids of the specimen, and the material would compress to a denser state—a phenomenon referred to herein as 'densification'. For specimens at a static stress state above the CT line (super-characteristic), cyclic loading would induce dilation with cycles. For specimens with a static stress state on the CT line, no volume change would occur with cycles.

In the direct cyclic simple shear device (DCSS), the static stress state of the specimen is unknown, as the horizontal stress applied on the specimen is not measured.

Previous studies imply that the static stress state within the DCSS is mostly sub-characteristic, as all published studies to date indicate densification with cycles under drained conditions (Kang et al. 2016; Bhaumik et al. 2017; Al Tarhouni and Hawlader 2021; Nong and Park 2021; Cui et al. 2019). The amount of densification is shown to be negatively correlated with D_r, p'_0 and load reversal and positively correlated with ζ_b and f from these studies.

For undrained tests, volume change is restricted, and no volume change occurs; instead, u is generated, reducing the specimen's effective stress. Mao and Fahey (2003) observed a clear cyclic phase transformation (PT_{cyc}) state which separates the stress path of individual cycles into contractive and dilative behaviour and is different from the PT state in monotonic tests. Qadimi and Coop (2007) demonstrated that the undrained cyclic behaviour of cohesionless soil is a function of the soil's initial state, Ψ in the critical state framework. Nong et al. (2020) demonstrated that increasing the loading frequency, f and D_r reduced the u accumulation and thus increased the soil's undrained resistance to cyclic loading.

As drainage conditions are seen to greatly influence both the monotonic and cyclic behaviour of cohesionless soils, it is postulated that drainage conditions will also largely dictate other salient features of cyclic loading, such as accumulated ratcheting, stiffness, and damping with cycles, which are also explored in this investigation. These cyclic features are discussed in the following sections.

1.7.2 Accumulated ratcheting

In all loading regimes except possibly in two-way loading, accumulated ratcheting (sometimes referred to as permanent strain in the literature) develops in the soil element. This phenomenon occurs as the soil specimen does not return to the original strain value, even though the same stress amplitudes in extension and reversal are applied. Instead,

some plastic strain accumulates in the direction of load bias, which further accumulates with more cycles. However, it is important to note that cyclic loading also induces changes to the soil stiffness, which will influence the mean shear strain with loading.

This effect has been observed in centrifuge model tests performed by Truong et al. (2018) and Bayton (2020) as well as 1g model tests performed by Leblanc et al. (2010b) and Richards et al. (2020). These studies found that accumulated ratcheting is influenced by D_r and ζ_b. Soils with a lower D_r and higher ζ_b produced more accumulated ratcheting than in the opposite situation. From the results of these experiments, a power-law relationship has been proposed and is commonly used to describe the accumulated ratcheting with cycles, with fitting parameters dependent on loading and soil characteristics. This research seeks to improve predictions of accumulated ratcheting of offshore foundations by investigating the mechanisms that influence ratcheting in the DCSS, which can be incorporated into constitutive models for cohesionless soils or into empirical correlations such as power-law relationships. Furthermore, model tests have been undertaken on either dry sand or have been loaded at a rate to ensure drained conditions. Therefore, the accumulated ratcheting behaviour in undrained conditions for cohesionless soils remains relatively unexplored in the context of model-scale testing.

Accumulated ratcheting in element testing has also been observed and examined by many researchers. Qiu (2023) performed a large suite of cyclic direct simple shear tests on a glacial clay also noting marked impact of ζ_b on accumulated ratcheting. Arangelovsk and Towhata (2004) conducted undrained one-way cyclic tests on cohesionless soil using the torsional shear apparatus and concluded that accumulated ratcheting was independent of loading rate and mostly a function of ζ_b. Wichtmann et al. (2005) and Wichtmann et al. (2011) performed a number of drained cyclic triaxial tests to explore strain accumulation, which is positively correlated to ζ_b and stress ratio and

negatively associated with p'_0, D_r, C_u. A high cycle strain model was subsequently developed to account for these features. The cyclic triaxial defines certain regions of soil movements around an OWT foundation, such as the compression and extension regions shown in Figure 1-14 whilst other regions appear to reflect soil behaviour captured in the VDDCSS, due to differences in loading direction and position of soil elements relative to the foundation.

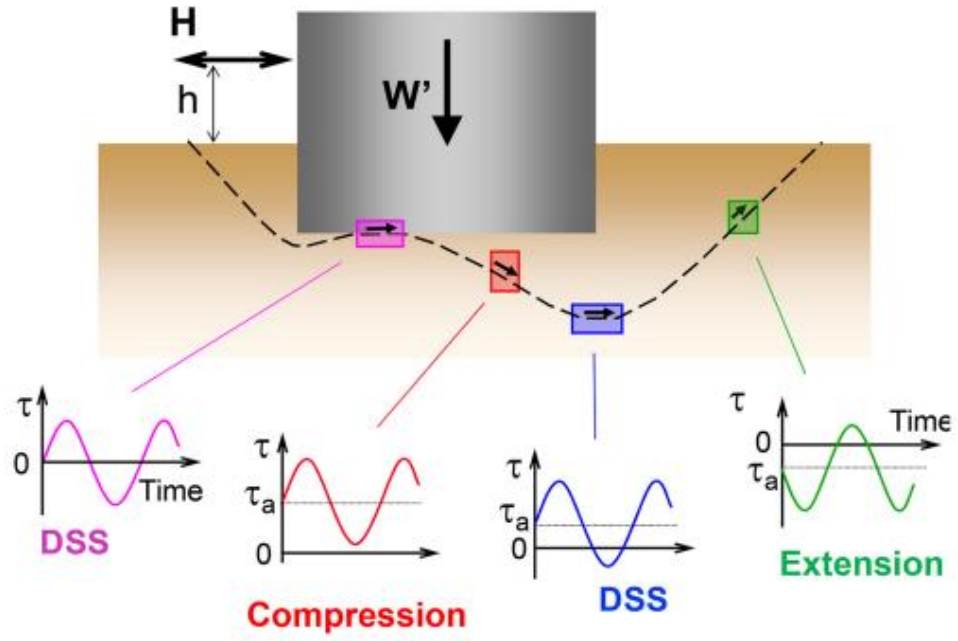


Figure 1-14 Simplified stress conditions for typical elements and potential failure beneath shallow foundation (from Andersen (2015))

Therefore, it is additionally of interest to examine the accumulated ratcheting in the direction of shearing and the mechanisms that influence this behaviour. Andersen (2015) proposed a method of determining cyclic properties of a material through contour diagrams developed from several laboratory tests, including cyclic direct simple shear as well as cyclic triaxial compression and extension tests. This is a practical method that predicts certain cyclic behaviours of offshore foundations. However, the physical mechanisms that occur during cyclic loading remain relatively unexplored.

1.7.3 Generation of excess porewater pressure

The generation of u develops under partially drained and undrained cyclic loading. This phenomenon also influences the performance of OWT foundations as it reduces the effective stress of the founding soil and can potentially cause liquefaction. The generation of u in cyclic loading has been extensively explored in the context of earthquake loading on saturated soils. The development of stress-based methods and energy-based methods for evaluating liquefaction potential demonstrates significant strides by researchers in assessing liquefaction potential in cohesionless soils. Stress-based methods typically rely on liquefaction charts based on empirical relationships developed from field and laboratory data collected from past seismic events (Seed and Idriss 1971). Energy-based methods focus on the energy balance during seismic loading and how soil properties affect the dissipation of this energy (Berrill and Davis 1985). However, both methods have been developed with the specific goal of assessing liquefaction potential and thus do not necessarily encapsulate the behaviour of soils prior to failure. In terms of OWT design, engineers additionally seek to understand the progressive behaviour of OWTs under operational conditions, not only the behaviour of soil at liquefaction.

Several researchers have explored the features that contribute to the progressive development of u with cycles (DeAlba et al. 1975; Lee and Albaisa 1974). Kokusho (2013) and Do et al. (2023) demonstrate the development of u is positively related with ζ_b and negative related with D_r. Cary (2011) additionally demonstrates that porewater pressure generation is positively related to loading frequency and moisture content.

1.7.4 Evolution of stiffness

Several researchers have observed that by applying cycles of loading to cohesionless soils in drained conditions, the stiffness of the soil increases with each cycle (Iwasaki et al. 1978; Nong and Park 2021; Richards et al. 2020). Stiffness improvement has been observed to be a function of the same parameters that influence the volume change during

cyclic loading, namely, D_r, p'_0, ζ_b, and f. Like the volume change, stiffness improvement with cycles is negatively correlated with D_r, p'_0 and positively correlated with ζ_b and f. It is therefore theorised that the increased stiffness is directly a response to densification, as denser specimens have greater shear resistance than loose specimens.

Results from element testing in undrained conditions show that the stiffness of cohesionless soils decreases with cycles as u develops, leading to a complete loss of stiffness when soils reach liquefaction (Li, Ling, et al. 2019; Nong et al. 2020; Dobry 1989; Le et al. 2024).

1.7.5 Evolution of energy dissipation

As mentioned in Section 1.6.3.2, the damping ratio represents the soil's capacity to dissipate energy under loading. In this thesis, this is referred to as energy dissipation, η.

Researchers considering liquefaction potential have previously noted a strong correlation between η and generation of u which inspired the development of energy based methods for evaluating liquefaction potential of cohesionless soil (Green et al. 2000; Figueroa et al. 1994; Mele et al. 2019). Tatsuoka et al. (1978) determined that energy dissipation of cohesionless soils is positively correlated with ζ_b and negatively correlated with p'_0 and the number of cycles, N. The influence of cohesionless soil type was found to be moderate and the effects of D_r, saturation and sample preparation method were minor. Doygun et al. (2021) additionally demonstrates that C_u and $F.C$ are positively related with energy dissipation whilst OCR is negatively related with energy dissipation.

1.8 Research Objectives

The experimental component of this research uses a combination of advanced soil element testing methods, including the Resonant Column Apparatus (RCA), Bender Elements (BE), and the Variable Direction Dynamic Cyclic Simple Shear (VDDCSS) device. This research seeks to develop the theoretical understanding of cohesionless soils under cyclic loading and to understand the physical mechanisms that control such

behaviour through an extensive experimental regime. In particular, the research focuses on small-strain stiffness, G_0 stiffness degradation, G/G_0 and the cyclic behaviour of cohesionless soils. The theoretical developments in these areas are expected to inform design practices for OWT foundations, particularly under Serviceability Limit State (SLS) and Fatigue Limit State (FLS) design criteria. The former is explored by linking the behaviour observed from element tests to model tests and pile behaviour, and the latter by considering the influence of G_0 on natural frequency and fatigue performance of OWTs. These aims are supported by the following objectives:

- Chapter 2 details the materials and experimental methods referenced in this study. This comprises *in*-situ and laboratory characterisation of test material, a detailed explanation of experimental apparatuses and equipment. Calibration procedures, test procedures, data interpretation and commissioning tests are also presented.
- An investigation of small-strain stiffness of cohesionless soils is the subject of Chapter 3. A critical examination of existing models that predict G_0 and G/G_0 is initially undertaken. Subsequently, an experimental study using the resonant column apparatus (RCA) and bender elements (BE) on three cohesionless soil types is presented. Several key physical factors impacting G_0 and G/G_0 in the elastic region are investigated. The applicability of the RCA for characterising stiffness degradation parameters, and a clear procedure for obtaining representative stiffness measurements, is also presented.
- Chapter 4 explores the monotonic and cyclic behaviour of two cohesionless soils as captured by the Variable direct dynamic cyclic simple shear device (VDDCSS). It is evident that the cyclic behaviour of soil varies significantly depending on drainage conditions. This research seeks to explore the limiting behaviours of drained and undrained cyclic behaviour across loading regimes and directions

representative of OWTs. The influence of cyclic amplitude, asymmetry, loading frequency, applied stresses, and relative density are also considered. The goal is to provide a deeper understanding of the physical mechanisms that occur during cyclic loading in cohesionless soil to improve analytical or constitutive models for such soils under cyclic loading.

- The application of the experimental results to offshore foundation design is discussed in Chapter 5. The experimental results obtained from Chapters 3 and 4 reveal insights into the stiffness of cohesionless soils, which are direct inputs for fatigue analysis of OWTs. A 1D numerical study is therefore undertaken to investigate the effects of G_0 on the fatigue performance of OWTs. The cyclic behaviour captured in Chapter 4 provides a direct point of comparison to 1g model pile tests obtained by other researchers at the University of Oxford. This chapter therefore also explores the link between key cyclic behaviours such as accumulated ratcheting, stiffness, and energy dissipation changes and, post-cyclic capacity which are evident in both element and model tests.
- Chapter 7 summarises the novel contributions of this thesis and provides suggestions for future work to develop the research presented herein.

No amount of experimentation can ever prove me right; a single experiment can prove me wrong – Albert Einstein

CHAPTER 2
Experimental methods

2.1 Introduction

This chapter introduces the experimental materials, apparatus, and procedures employed in this study. The research examines three cohesionless soils: two representing typical North Sea soil foundations, and a third, a common research soil serving as a reference material. The chapter first details the in-situ testing methods used in this research to obtain the characteristics of the test materials. It presents the origins, in-situ conditions, and preliminary characteristics of the soils tested.

The Resonant Column Apparatus (RCA) with bender elements (BE) and the Variable Dynamic Direct Cyclic Simple Shear device (VDDCSS) are the primary testing apparatuses used in this research. This chapter provides a comprehensive description of the testing apparatuses and equipment. It includes an overview of specimen preparation procedures, test procedures, and approaches to data interpretation from experimental results. A significant portion of this chapter discusses the commissioning process for the RCA, including calibration, validation, and the evaluation of best practice methods.

2.2 *In-situ* testing methods

Due to the difficulty of obtaining undisturbed specimens of cohesionless soil for laboratory testing, the exploration of such soils greatly benefits from in-situ testing. These tests provide important information about the soil's condition in the field, ensuring that subsequent laboratory tests are conducted on specimens that accurately reflect field conditions. This section describes the Cone Penetration Test with pore water pressure measurements (CPTu) and its interpretation methods, which have been used throughout this thesis as part of the site characterisation for the PICASO project, ensuring representative soil conditions for subsequent laboratory testing.

2.2.1 Cone penetration test

The Cone Penetration Test (CPT/CPTu) is a popular in-situ testing method used to identify and classify soil stratification. The CPT is conducted by inserting a cone attached to a series of rods into the ground at a constant rate. Continuous or intermittent measurements of cone tip resistance, q_s, sleeve friction, f_s and porewater pressure, u are taken which give indication of the soil's *in-situ* properties. Detailed information about the CPT and procedure can be found in Lunne et al. (1987). A summary of the main measurements is discussed below:

- q_s: Measured by load cells located behind the tapered cone. It represents the forces on the cone tip divided by the area normal to the tip.
- f_s: Measured by load cells embedded in the sleeve; it captures the force acting on the sleeve divided by the surface area of the sleeve.
- u: Measured from a porous element and a pressure transducer integrated into the cone penetrometer, which converts the pressure into an electrical signal.

In recent years, researchers have developed interpretation methods that allow geotechnical design parameters to be determined from CPT data via empirical relationships. Correlations between CPT parameters and D_r and G_0 are of particular

interest for cohesionless soils and have been referred to in this thesis. The following section discusses the empirical correlations developed by various researchers.

2.2.2 CPT-D_r correlations

2.2.2.1 Concept of D_r

The relative density, D_r of cohesionless soils is defined by its density relative to its loosest and densest states and has been defined in Equation (1-2). Determining the minimum and maximum densities (γ_{min} and γ_{max}) is therefore an essential component in the classification of cohesionless soils and typically performed through density tests in the laboratory. Various standards exist for these tests, including BS1377:1990 BS (1990), ASTM D4254-16 ASTM (2006), DIN 18126-1996-11 DIN (1996) as well as proprietary methods developed by organisations. Lunne et al. (2019) demonstrates that γ_{min} and γ_{max} are highly sensitive to testing methodology. Factors such as particle crushing susceptibility, differences in equipment, the volume of soil tested, and operator errors contribute to this sensitivity. To mitigate errors, Lunne et al. (2019) recommends using two test methods to determine γ_{min} and γ_{max}, ensuring more reliable and accurate results.

2.2.2.2 CPT correlations

In the field, D_r can be interpreted from CPT results via empirical correlations developed by several researchers. The original equation to describe the relationship between CPT parameters and D_r was proposed by Schmertmann (1976) as shown below.

$$D_r = \frac{1}{C_2} \cdot \ln \frac{q_c/P_a}{C_o(\sigma'/P_a)^{C_1}} \tag{2-1}$$

Where q_c is the cone tip resistance σ' is the mean effective stress, P_a is the atmospheric pressure and C_0, C_1 and C_2 are soil constants that require soil specific calibration.

Baldi et al. (1986) developed earlier calibrations of soil constants through statistical analyses of field and laboratory measurements for normally consolidated and

over-consolidated sand using Ticino sand. It was determined that C_0 = 157, C_1 = 0.55, C_2 = 2.41 for normally consolidated sand.

Kulhawy and Mayne (1990) determined a modified expression for D_r appropriate for young uncemented sands based on 24 calibration chamber tests. Their expression includes adjustments accounting for compressibility, overconsolidation and ageing.

$$D_r^2 = \frac{Q_{tn}}{Q_f \cdot Q_c \cdot Q_{OCR} \cdot Q_A} \tag{2-2}$$

Where, Q_f = 332, 305 and 278 for low, medium, and high compressibility sands respectively, Q_c is the compressibility factor ranging between 0.91 <Q_c < 1.2, Q_{OCR} = $OCR^{0.18}$ and, $Q_A = 1.2 + 0.05 \log \frac{t}{100}$ for t = time in years. Q_{tn} is the normalised cone tip resistance and is defined by the following equation:

$$Q_{tn} = \left[\frac{q_t - \sigma_v}{\sigma'_{ref}}\right] / \left[\frac{\sigma'}{\sigma'_{ref}}\right] \tag{2-3}$$

Where σ_v is the total vertical stress. Jamiolkowski et al. (2001) proposed a modified form of Equation (2-1) based on CPT and Dilatometer Tests (DT) in deposits of unaged, uncemented silica sands of low to moderate compressibility. Their expression is described below.

$$D_r = \frac{1}{C_2} \cdot \ln \frac{Q_{tn}}{\left(\sigma'/\sigma_{ref}\right)^{C_1}} - C_3 \tag{2-4}$$

Where soil constants C_2 and C_3 are determined as C_2 = 0.0375 and C_3 = 67.5.

Agaiby and Ahmed (2019) similarly adopts the Equation (2-1) however provides further correlations for soil constants C_2 and C_3 based on soil properties behaviour index, I_c as defined by Robertson (2009) and mean particle size, d_{50} as summarised below. These relationships were developed considering the undisturbed sand databased published by Mayne (2006).

$$C_2 = 1/(0.771 - 0.345I_c - 0.07 \ln d_{50}) \quad (2\text{-}5a)$$

$$C_3 = = \ -3.27 + 1.64I_c + 0.253 \ln d_{50} \quad (2\text{-}5b)$$

$$I_c = \sqrt{[3.47 - \log(Q_{tn})]^2 + [1.22 + \log(F_r)]^2} \quad (2\text{-}5c)$$

$$F_r = 100f_s/(q_c - \sigma_v) \quad (2\text{-}5d)$$

Where f_s is the skin friction.

Predictions by Baldi et al. (1986) typically produces the highest values of D_r due to its higher soil constant term and absence of the C_3 term. Solutions proposed by Kulhawy and Mayne (1990) is often a lower bound as, unlike the other relationships, their numerator includes a square root term. An evaluation of these correlations by Sadrekarimi (2016) deduced a large variance in D_r, thus advising caution when applying these relationships to general sand applications. Given the potential variability in predictions, it is crucial to understand the specific soil conditions when choosing a correlation method.

2.2.3 *CPT-G_0* correlations

Several correlations between CPT measurements and G_0 have been developed by researchers (Table 2-1).

Table 2-1 G_0/V_s and CPT relationships

CPT-V_s/CPT-G_0 correlations	**Required parameters**	**Reference**
1.V_s=0.0831Q_{tn}exp(1.7861I_c) (σ'_v/P_a)$^{0.25}$	I_c: Soil behaviour index	Hegazy and Mayne (2006)
2. V_s=18.5+118.81log(f_s)	f_s: Sleeve friction	Mayne (2006)
3. V_s = 2.27$q_t^{0.412}I_c^{0.989}z^{0.033}$	q_t: Cone tip resistance	Andrus et al. (2007)
4. G_0 =0.0188 [$10^{(0.55Ic+1.68)}$(q_t - σ_v)]	Q_{tn}: Normalised cone tip	Robertson (2009)
5. V_s=18.4$q_t^{0.144}I_c^{0.0832}z^{0.278}$	resistance	McGann et al. (2014)
	σ'_v: effective vertical stress	
6. G_0 = 6700 σ'_v exp(-1.4I_c)	σ_v: total vertical stress z: vertical depth below ground level	Ahmed et al. (2014)

Hegazy and Mayne (2006) developed a correlation between CPT parameters and V_s using statistical correlations applied to a database of soils including, quaternary clays, sands, mixed soil and mine tailings. Mayne (2006) developed a correlation between CPT parameters and V_s for quaternary soils based on regression of a large dataset from various sites worldwide. Andrus et al. (2007) and McGann et al. (2014) proposed the same general relationship between V_s and q_t, I_c and depth below ground level, z. However, they provide different calibration constants based on the soil examined with the former considering a range of soil covering Holocene, Pleistocene and Tertiary aged soil and the latter considering Christchurch and Springston formations (comprising gravels, sand, silt, clay and peat). Robertson (2009) developed a relationship between V_s and CPT measurements using a database of 1035 data pairs from predominantly Holocene and Pleistocene-age general soil sites of both cohesive and cohesionless soil constituents. Using the published data of undisturbed sand samples from Mayne (2006), Ahmed (2014) developed a relationship between G_0 and σ'_v and I_c.

The performance of the summarised correlations have been evaluated against four case studies in Ahmed (2017). The results show that relationships 1 through 4 produced significant errors in predicted G_0, up to 335% occurrence based on Table (2-7), a similar conclusion as Amoroso (2014). As such, it is generally advised that these empirical correlations should only be used for site-specific situations (Mola-Abasi et al. 2015).

The relationship by Ahmed et al. (2014) performed the most accurately of the 6 relationships. It is believed that one of the most important aspects in enhancing the correlation between I_c and $G_0/\sigma'v$ is to harmonise the stress dependency of both quantities. Consequently, the consistent normalisation scheme was anticipated to strengthen the correlation between these quantities which resulted in the relationship by Ahmed et al. (2014) predicting values of G_0 between $\pm$20% error.

2.3 Test Material

This section details the testing materials investigated in this research, Cuxhaven sand (CX), North England sand (NE) and Leighton Buzzard sand (LBS). The first two represent typical offshore sands in the North Sea although are sourced from onshore sites and the third sand is a commonly researched sand which serves as a reference material in this study. These sands are shown in Figure 2-1, and their locations are presented on a geological map in Figure 2-2. It is important to note that microscopy and a statistical analysis of morphological characteristics of the sand grains would be required to fully quantify the similarity between the sands.



(a) (b) (c)

Figure 2-1 Images of the soils tested in this study (a) CX sand (b) NE sand (c) LBS

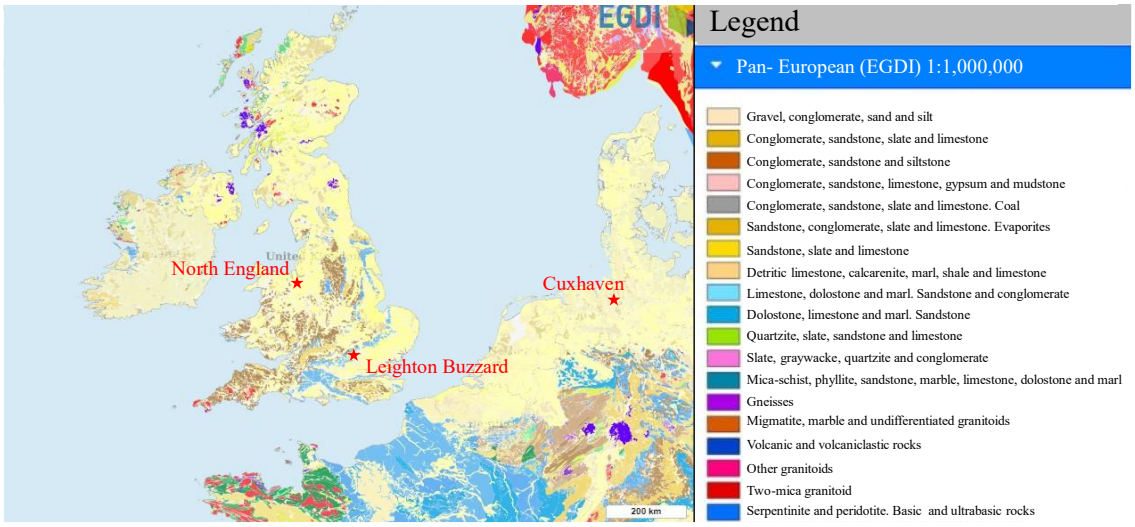


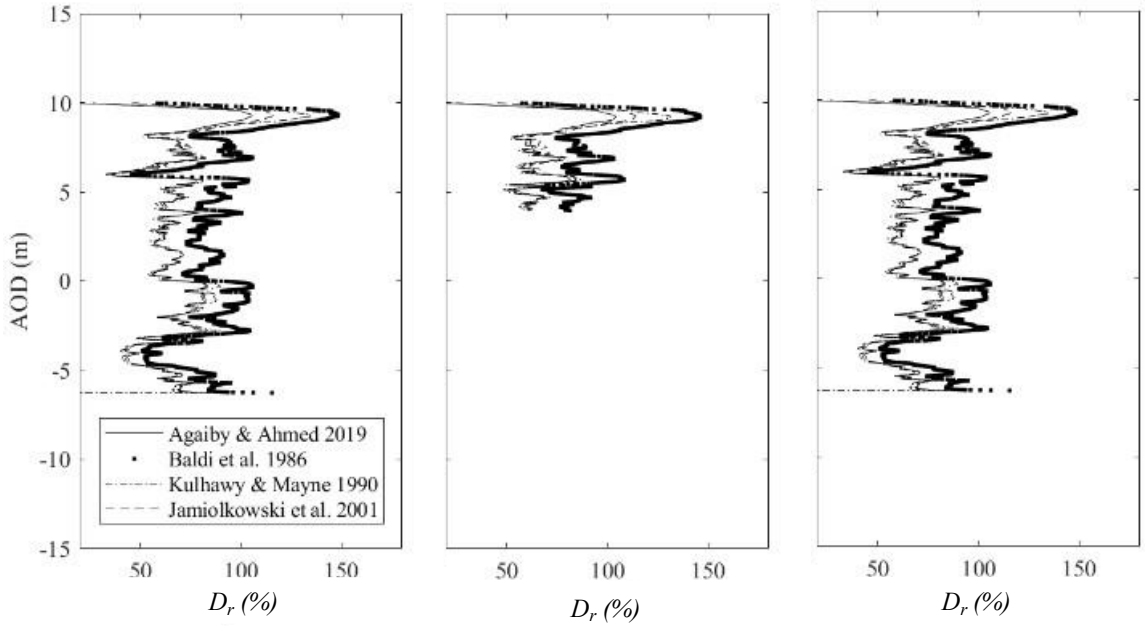
Figure 2-2 Pan-European Geological Units with locations of tested materials marked (source: (EGDI 2024))

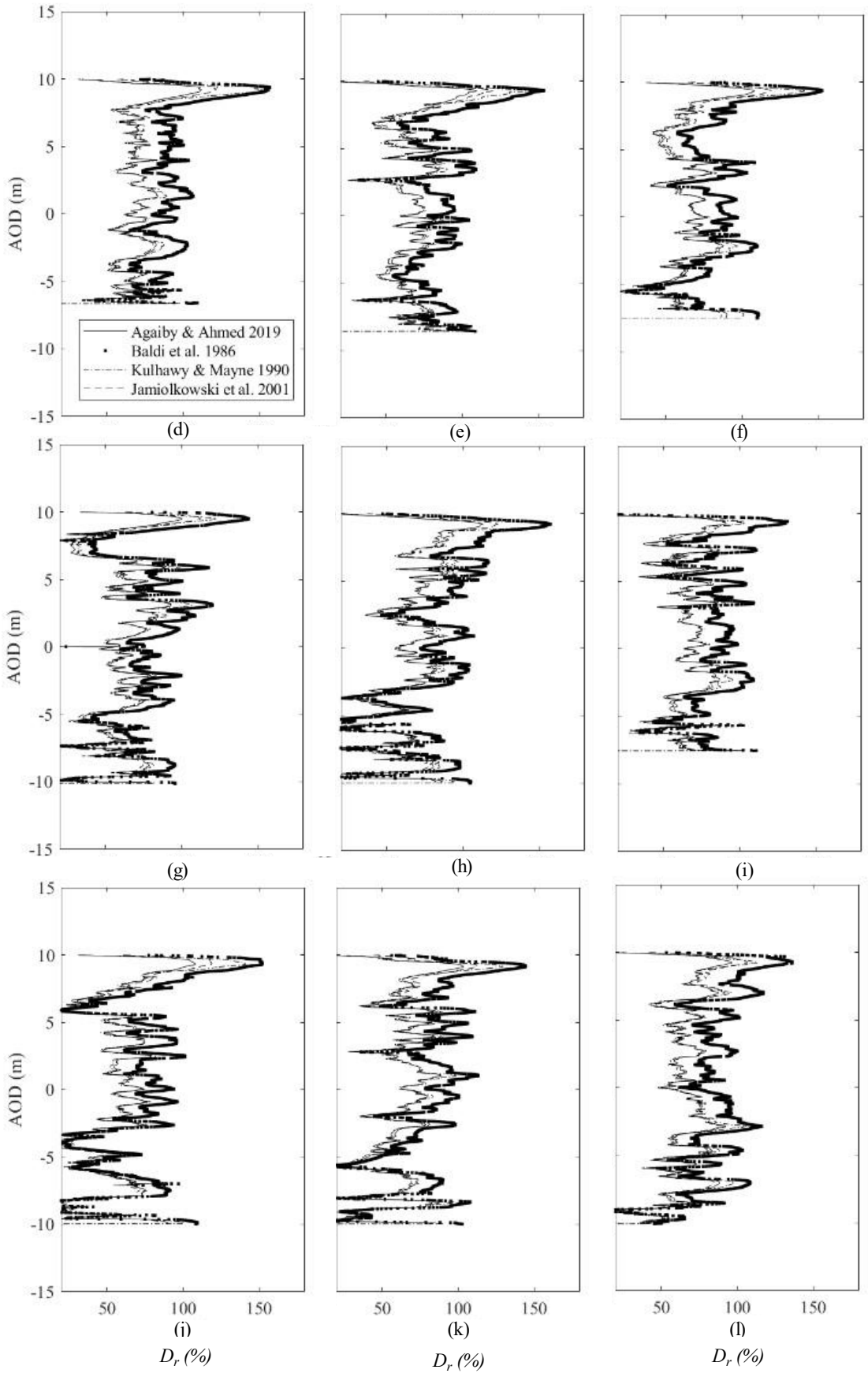
2.3.1 Cuxhaven sand

Cuxhaven sand (CX) is a grey, well-graded, fine silica sand. The sand is sub-rounded with traces of gravel and silt. The material used in this study was obtained via boreholes

from a test site 5 km south of Cuxhaven, Germany, and 6 km east of the North Sea coast. The site is part of an active sand quarry located in the Northwest German Basin, sometimes referred to as the Central European Basin System. The stratification comprises younger Quaternary sediments, mostly glacial deposits underlain by tertiary deposits of marine clayey sediments (Norden et al. 2023).

An extensive site investigation campaign has been conducted at the Cuxhaven site in preparation for medium-scale cyclic field tests for the PICASO project. Fifteen cone penetration tests (CPTs) were performed across the site, with exact locations documented in the site investigation report, ref. Geo-Engineering (2023). The D_r profile was interpreted from CPT results using the empirical correlations as described in Section 2.2.2. These are shown for all CPTs undertaken in Figure 2-3(a) to (o).




AOD (m)
15
10
5
0
-5
-10
-15
Agaiby & Ahmed 2019
Baldi et al. 1986
Kulhawy & Mayne 1990
Jamiolkowski et al. 2001
(d)
(e)
(f)
(g)
(h)
(i)
(j)
(k)
(l)
50
100
150
D_r (%)

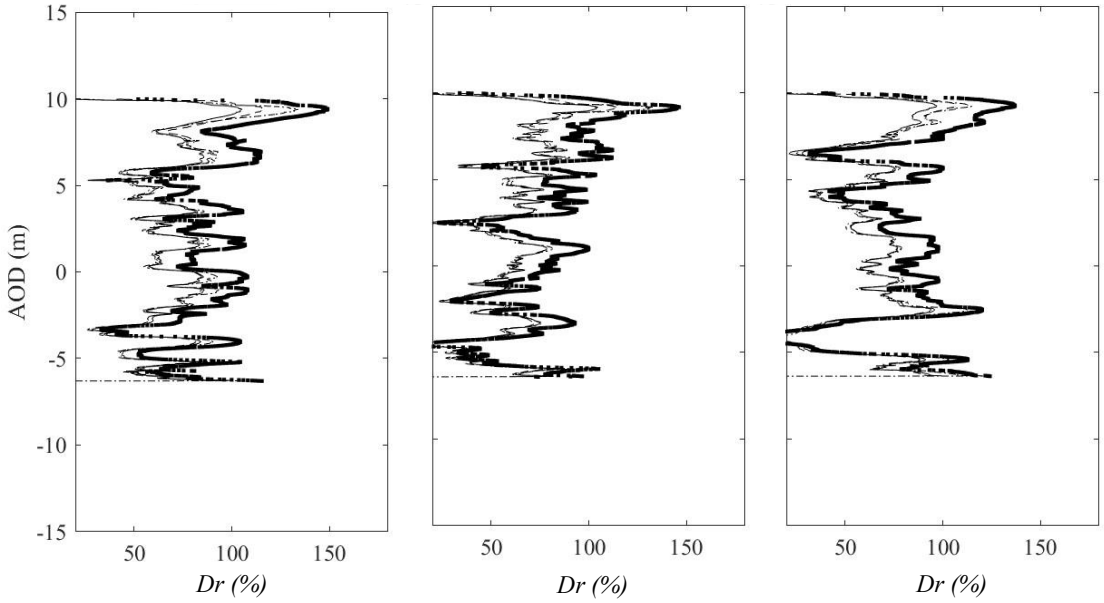


Figure 2-3 *CPT-D_r* correlations (a) CPTP01; (b)CPTP01T2; (c)CPTP01T2; (d)CPTP02; (e)CPTP3; (f) CPTP04; (g)CPTP05; (h)CPTP6; (i)CPTP07; (j)CPTP8; (k)CPTP09; (l)CPTP10; (m)CPTP11; (n)CPTP12; and (o)CPTP4

As expected, the correlation by Baldi et al. (1986) provides an upper bound (UB) estimate of the *in-situ* D_r and those by Kulhawy and Mayne (1990) provides a lower bound (LB), refer Section 2.2.2. The correlations by Jamiolkowski et al. (2001) and Agaiby and Ahemed (2019) are closer to the LB. Figure 2-4 shows the D_r profile interpreted from all CPTs on a single plot using the correlation by Jamiolkowski et al. (2001). This correlation was used as it consistently produced D_r values between UB and LB.

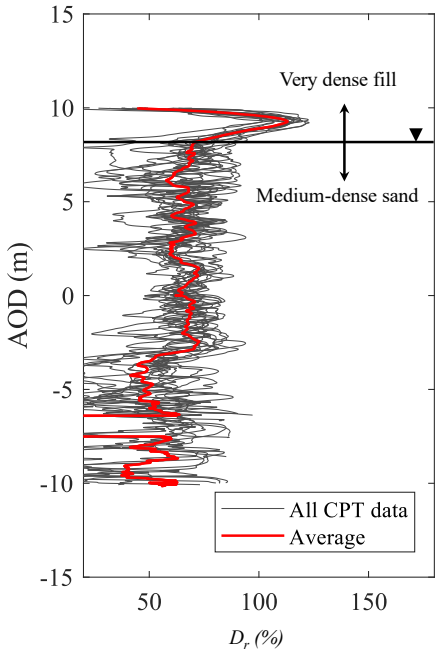


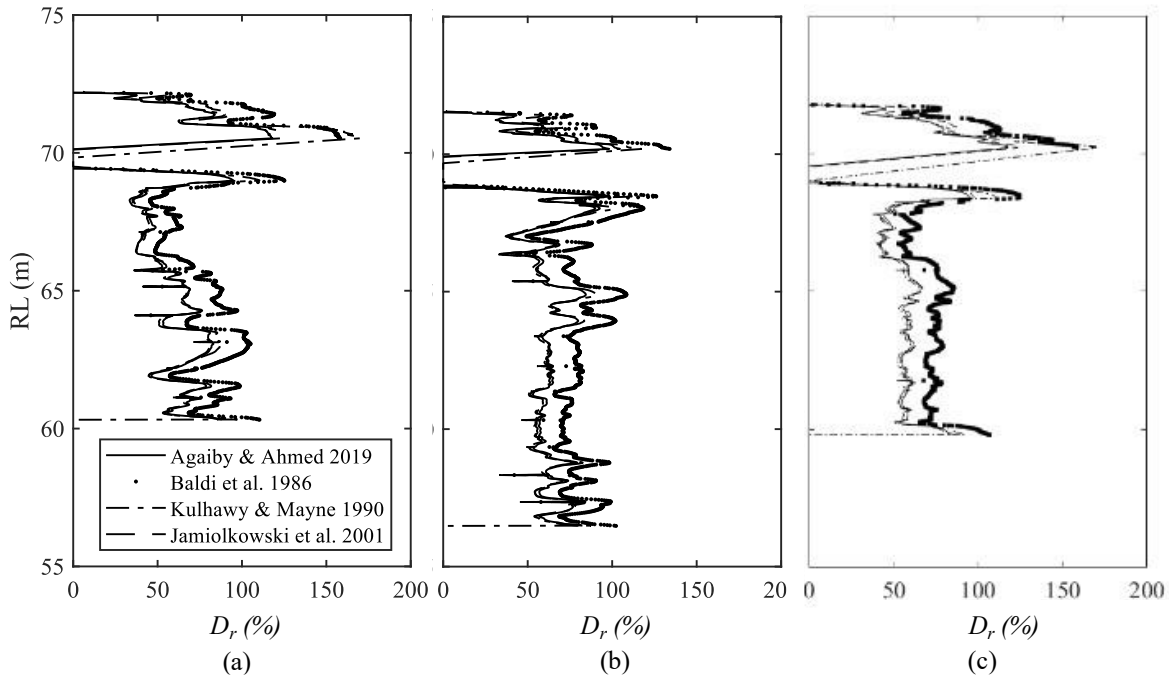
Figure 2-4 Interpreted D_r profile at Cuxhaven site using interpretation by Jamiolkowski et al. (2001)

Figure 2-4 indicates that the interpreted stratification of the soil profile is consistent across all CPT's. The profile exhibits a very dense layer of compacted fill underlain by medium dense sand. The water table is located approximately 2 m below ground level. Very little lateral variation is observed across the site. The average D_r within the medium dense sand is approximately D_r = 60% which is the target D_r for element tests conducted at *in-situ* soil conditions in Chapter 3 and 4.

2.3.2 North England sand

North England sand (NE sand) is a naturally occurring medium grained silica sand. The sand is sub-rounded to rounded with traces of gravel. Material in this study was recovered via test pits from a quarry located in the Northwest of England. According to the British Geological Survey (BGS) database, the quarry is situated within Devensian glaciofluvial deposits comprising sand and gravel, BGS (2022a).

Six CPTs were undertaken at the North England site, with exact locations detailed in OU (2022). The interpreted D_r profiles based on correlations discussed in Section 2.2.2 are presented in Figure 2-5(a) to (f).



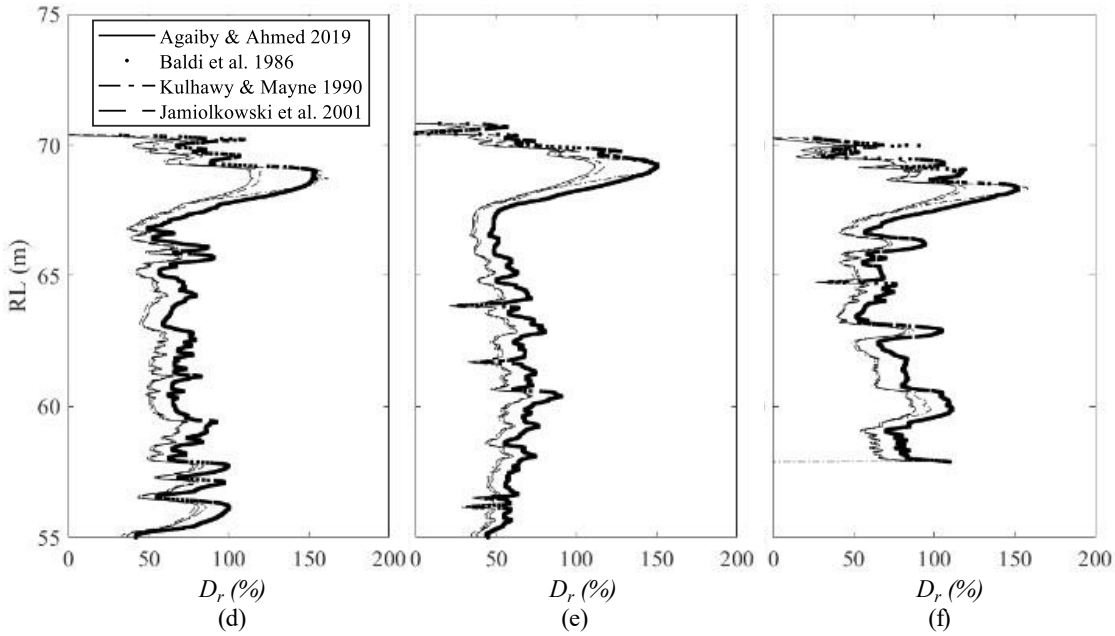


Figure 2-5 CPT-D_r interpretation (a) CPT1; (b) CPT2; (c) CPT3; (d) CPT4; (e) CPT5; and (f) CPT6

Like the results shown for the Cuxhaven profile, the correlation by Baldi et al. (1986) provides an upper bound estimate of in-situ D_r and those by Jamiolkowski et al. (2001) and Agaiby and Ahmed (2019) produce similar D_r values closer to the lower bound estimate by Kulhawy and Mayne (1990). Figure 2-6 shows the D_r profile interpreted from all CPT on a single plot using the correlation by Jamiolkowski et al. (2001).

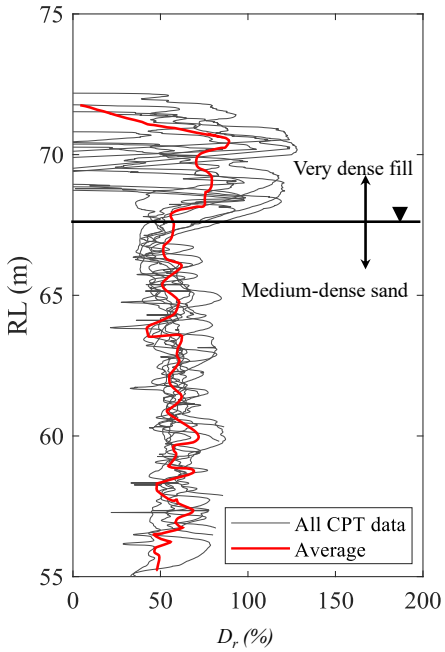


Figure 2-6 Interpreted D_r at North England site using interpretation by Jamiolkowski et al. (2001)

Figure 2-6 demonstrates a consistent soil stratum across the site with very little spatial variation. The profile comprises a very dense compacted fill underlain by medium dense sand. The water table is located at approximately an RL = 68m. The average *in-situ* D_r in the medium dense sand layer is approximately D_r = 60% and is the target density for element tests conducted at *in-situ* conditions in Chapter 3 and 4.

2.3.3 Leighton buzzard sand

Leighton buzzard sand (LBS) is a commercially available aggregate comprising of pure quartz and is described as coarse, sub rounded to subangular. The material is available in different fractions ranging from coarse (fraction A) to fine (fraction E). In this study LBS – fraction B sand was used, a poorly graded medium to coarse grained sand. The sand is a part of the Lower Greensand Formation encountered across southern England, BGS (2022b). The material used in this study is sourced from the Leighton Buzzard Beds from a quarry in southwest Bedfordshire.

2.3.4 Classification tests

Table 2-2 summarises the index properties the three cohesionless soils and Figure 2-7 presents the particle size distribution (PSD) curves of each material. The region shaded red outlines the variation of PSD curves measured from cohesionless soil samples collected from the North Sea as described by Fleischer et al. (2023).

Table 2-2 Particle size distribution properties of tested material

Material	**Fines (%)**	d_{50} **(mm)**	C_u^*	C_z^{**}	e_{min} **(-)**	e_{max} **(-)**	G_s **(kg/cm^3)**
CX sand	1	0.12	2.3	0.81	0.44	0.96	2.64
NE sand	2.2	0.09	2.4	0.94	0.45	0.9	2.62
LBS	<0.1	0.80	1.3	1.04	0.53	0.82	2.65

Note: $*C_u = \frac{D_{60}}{D_{10}}$, $**C_z = \frac{D_{30}^2}{D_{10} \times D_{60}}$

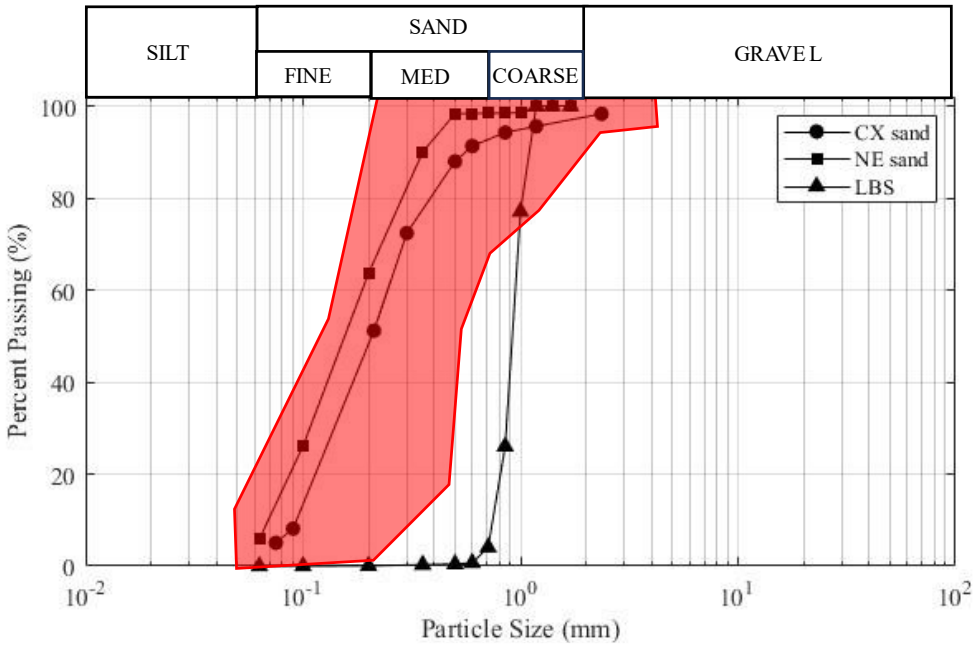


Figure 2-7 PSD of tested material, area shaded red refers to typical offshore sand gradings from Fleischer et al. (2023)

From Figure 2-7, the PSD of NE and CX sand are within the bounds of typical gradings of offshore sands. The LBS is much coarser, and more uniform compared to typical offshore sand gradings and NE and CX. LBS is included in this study as it is commonly used for research at laboratory model-scale experiments. It provides a point of reference to the other two offshore sands.

2.4 Bender Element test (BE)

The Bender Element (BE) method is a widely used technique to obtain the initial shear stiffness, G_0 at shear strains less than 10^{-4}%. The method first suggested by Shirley and Hampton (1978) establishes measurements of shear velocity which can then be converted to G_0. A bender element is a piezoceramic device that can generate and detect shear waves in the soil. Due to the small size of the BEs, the device can be set up within various laboratory devices such as triaxial, resonant column, oedometer and direct shear apparatuses. A BE is set up at each end of the soil specimen acting as a transmitter and receiver. A typical set up of the BE is presented in Figure 2-8.

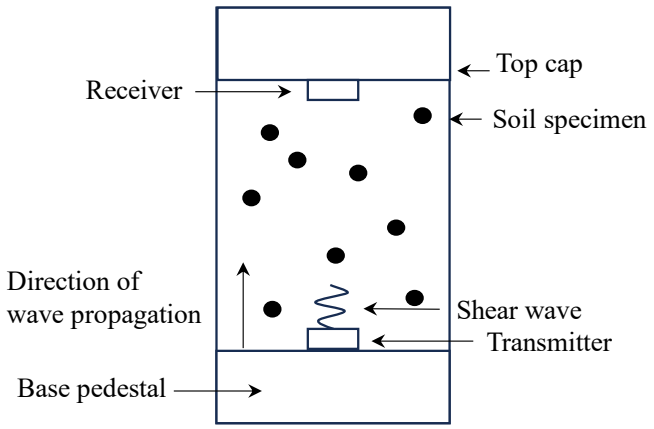


Figure 2-8 Typical BE Schematic installed within a soil specimen

A shear wave is propagated through the soil and the shear velocity is calculated as:

$$V_s = \frac{L_{tt}}{t_a} \tag{2-6}$$

Where L_{tt} is the is the tip-to-tip distance between the transmitter and receiver and t_a is the travel time of the wave. There are several methods for the determination of t_a. It has been found that adopting a different method for time arrival can drastically alter the measured V_s and subsequent G_0. These interpretation methods are herein discussed.

2.4.1 Characteristic points

In a typical bender element signal, there are a set of "characteristic" points that can represent t_a of the shear wave as indicated by points A, B and C in Figure 2-9.

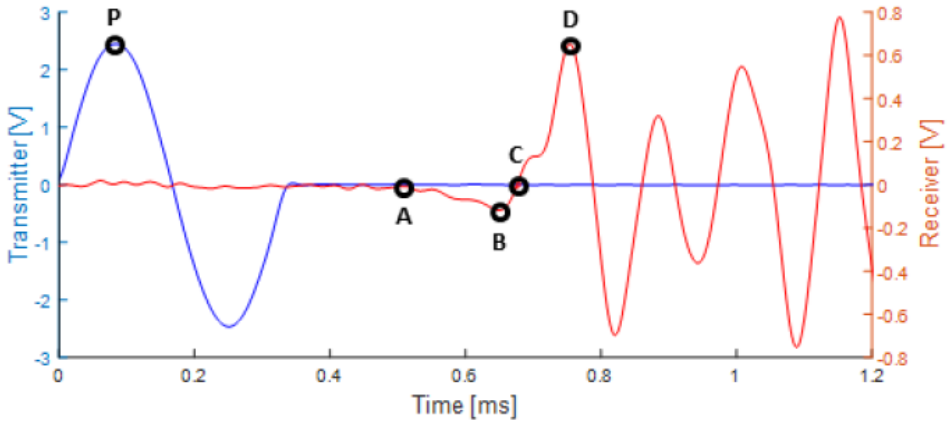


Figure 2-9 Typical BE output showing characteristic points taken for t_a (taken from Adamidis et al. (2017))

The points have been established as indicators of the first arrival: first deflection (A), first trough (B) and first zero crossing (C) (Leong et al. 2005; Gu et al. 2015; Ogino et al.

2015; Arulnathan et al. 1998). However, the identification of these points is highly subjective, and the identification of this point can be impacted by near-field effects.

The peak-to-peak method for determining time of first arrival is defined as the time difference between the peak input signal and that of the output signal, denoted by point D in Figure 2-9. As the output signal may have several peaks, it is common practice to take either the first peak or largest peak (Yang and Gu 2013).

2.4.2 Cross-correlation

The cross-correlation technique proposed by Viggiani and Atkinson (1995), is a time domain technique however calculations are executed in the frequency domain. The cross-correlation function of the input signal *(X(t)*) and output *(Y(t)*) is the measure of the degree of correlation of the two signals. The t_a can be detected by determining the peaks of this function. The cross-correlated function can be established via the following equations.

$$G(f) = FFT\big(X(t)\big), H(f) = FFT\big(Y(t)\big) \tag{2-7}$$

Where *G(f)* and *H(f)* are the frequency domain representative of the input and output signals respectively and *FFT* is the fast Fourier transform. The cross-correlated function can then be established as:

$$GCC(\tau) = IFFT\big(H^*(f)\big)G(f)) \tag{2-8}$$

Where $H^*(f)$ is the complex conjugate of *H(f)* and IFFT is the inverse Fourier transform. It has been observed from various researchers that there may be several peaks from the cross-correlated function that could correspond with the first arrival time. Ogino et al. (2015), found clearly identifiable peaks in soft soils with the maximum peak equating to the first peak. However, in sandy soils maximum and first peak did not coincide, and user identification is required to pick the correct peak corresponding with the first arrival. Airey and Mohsin (2013), observed the correct peak of the cross-correlated function is found to 'jump' unpredictably as the stress, waveforms, and frequency change. As such,

it was proposed that the time of maximum positive peak should be selected and the times of preceding maxima in the correlated signal should also be stored. This ultimately still requires the end user to pick the correct peak corresponding with the first arrival.

2.5 Resonant Column Apparatus (RCA)

The Resonant Column Apparatus (RCA) is a device capable of determining the dynamic properties of soil in the small-strain region, namely, G_0, G/G_0 and η. Since its inception in the 1960s, the device has been employed by many researchers to study shear stiffness and energy dissipation in the very small and small strain region (Hardin and Richart 1963; Hardin and Drnevich 1972b; Hardin and Black 1968; Lo Presti et al. 1997; Clayton et al. 2005).

Several configurations of the device have been created such as the 'fixed-free' type developed by Stokoe et al. (1980) or the 'fixed-fixed' developed by Hardin and Richard (1963). The former configuration allows the top of the specimen to rotate freely, while the latter restrains the top. The resonant column (RC) test is performed at small strains, where the assumption of elasticity holds true, 10−4% to 10−2%, (Ishihara 1996). A torsional vibration excitation is applied to a cylindrical soil specimen and the shear velocity, V_s is derived using the wave oscillation equations of motion, from which the elastic stiffness parameters E, G, ν of the soil can be obtained. The shear strain, γ is directly measured from the device. Once the material undergoes plastic deformation, the RCA is no longer reliable for describing the stiffness parameters.

2.5.1 Wave Equation for Torsional Oscillations

In the RCA, increasing amplitudes of torsional vibrations are applied to a soil specimen, and the resonant frequency, f_n of the specimen for a given amplitude is measured by the device. This section aims to derive the governing equations of the system that establish

the proportionality between shear velocity, V_s (a soil property) and the resonant angular frequency, ω_r (which is measured from the test).

This derivation makes use of the theory of wave propagation in an elastic, homogeneous, isotropic medium and assumes one-dimensional wave propagation as described in Richart (1970). The cylindrical specimen is idealised as a rod subjected to torsional vibrations and operates under a fixed-free system. Figure 2-10 below describes the components of a cylindrical coordinate system upon which the subsequent derivations are based.

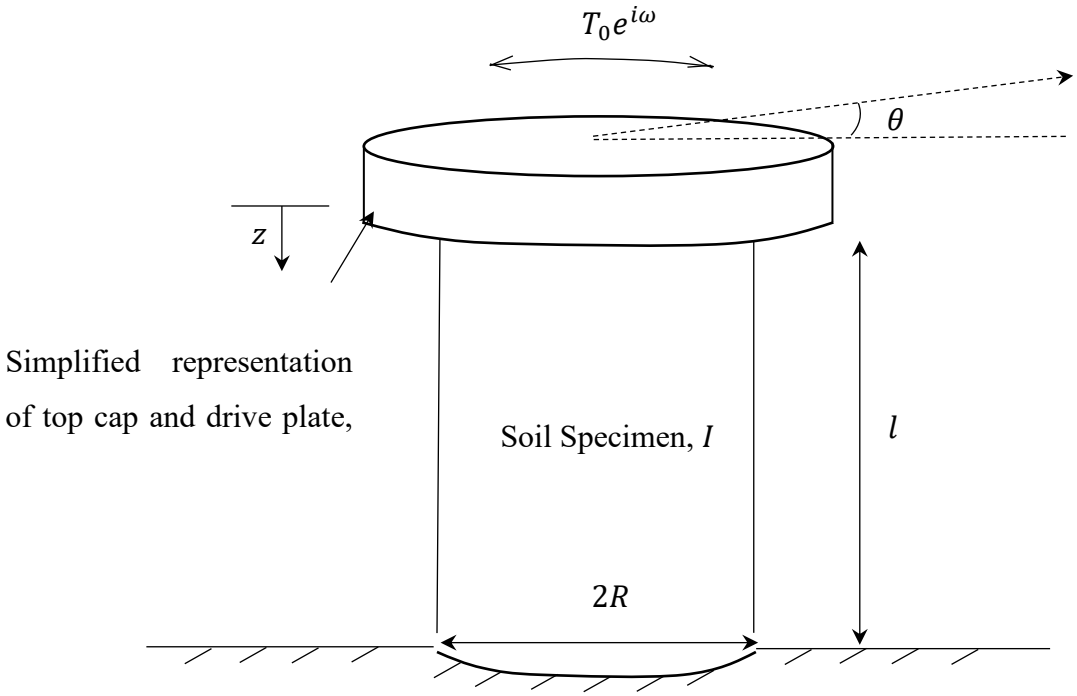


Figure 2-10 Simplified illustration of a fixed-free specimen within the RCA (modified after Ishihara (1996))

The wave equation by Richart (1970) for torsional motion can be expressed as:

$$\frac{\partial^2 \theta}{\partial t^2} = V_s^2 \cdot \frac{\partial^2 \theta}{\partial z^2} \tag{2-9}$$

Where, V_s is the shear velocity, θ is the rotational angle and z is the distance along the specimen. The rotational angle is a function of time and location along the height of the specimen. If the specimen is subjected to harmonic torque $T_0 e^{i\omega t}$, then the rotation angle can be expressed in the following form:

$$\theta(z,t) = f(z) \cdot e^{i\omega_r t} \tag{2-10}$$

Where, ω_r = angular frequency at resonant frequency $f(z)$ = the rotation amplitude along the length of the specimen. For a harmonic wave, the solution to Equation (2-10) can be written as a trigonometric function:

$$f(z) = A\cos\left(\frac{\omega_r z}{V_s}\right) + B\sin\left(\frac{\omega_r z}{V_s}\right) \tag{2-11}$$

The boundary condition of a fixed-free rod is that the displacement and subsequently rotation at the fixed end of the cylinder is 0 therefore $f(0) = 0$, substituting this into Equation (2-11) leads to $A = 0$.

$$f(z) = B\sin\left(\frac{\omega_r z}{V_s}\right) \tag{2-12}$$

The torque experienced on a transverse section of a cylindrical specimen such as that depicted in Figure 2-0 can be written as:

$$T = GJ\frac{\partial\theta}{\partial z} \tag{2-13}$$

Where, G is the shear modulus of the specimen, J is the polar moment of the specimen. For a cylindrical specimen, the mass polar moment, I can be related to the polar moment, J by $I = \rho l J$. This produces the following equation for torque:

$$T = \frac{GI}{\rho l}\frac{\partial\theta}{\partial z} \tag{2-14}$$

Torque is also a function of the rotational inertia exerted on the rod. In the RCA this is primarily influenced by the mass polar moment of the added mass (I_0):

$$T = I_0\frac{\partial^2\theta}{\partial t^2} \tag{2-15}$$

Equating both expressions of torque, one obtains:

$$T = GI\frac{\partial\theta}{\partial z} = \rho I_o l\frac{\partial^2\theta}{\partial t^2} \tag{2-16}$$

Using Equation (2-10) to obtain,

$$\frac{\partial\theta}{\partial z} = \frac{\partial f(z)}{\partial z} \cdot e^{i\omega_r t} \tag{2-17}$$

And

$$\frac{\partial^2\theta}{\partial t^2} = -\omega_r^2 \cdot f(z) \cdot e^{i\omega_r t} \tag{2-18}$$

Differentiating Equation (2-12) gives,

$$\frac{\partial f(z)}{\partial z} = \frac{\omega_r}{V_s} \cdot \ B\cos\left(\frac{\omega_r z}{V_s}\right) \tag{2-19}$$

Substituting these expressions into Equation (2-16) for $z = l$ gives:

$$GI \cdot \frac{\omega_r}{V_s} \cdot B\cos\left(\frac{\omega_r l}{V_s}\right) \cdot e^{i\omega_r t} = -\rho I_o l\omega_r^2 \cdot B\sin\left(\frac{\omega_r l}{V_s}\right) e^{i\omega_r t} \tag{2-20}$$

Rearranging the equation above and using the substituting $G = \rho V_s^2$, simplifies Equation (2-37) to the classical expression given by Richart (1970):

$$\frac{I}{I_0} = \frac{\omega_r l}{V_s}\tan(\frac{\omega_r l}{V_s}) \tag{2-21}$$

Where $\omega_r = 2\pi f_n$, l is the length of the specimen, I and I_0 are the mass polar moment of inertia of the soil specimen and the top cap and drive plate respectively and V_s is the shear velocity. The shear stiffness is found via $G = \rho V_s^2$ and ρ is the density of the soil specimen.

2.5.2 Derivation of Shear Strain

The shear strain due to torsional excitation in a cylindrical rod is non-uniform and varies with distance from the centre, with the strain increasing from zero at the centre to a maximum at the outer edge, as shown in Figure 2-11 below.

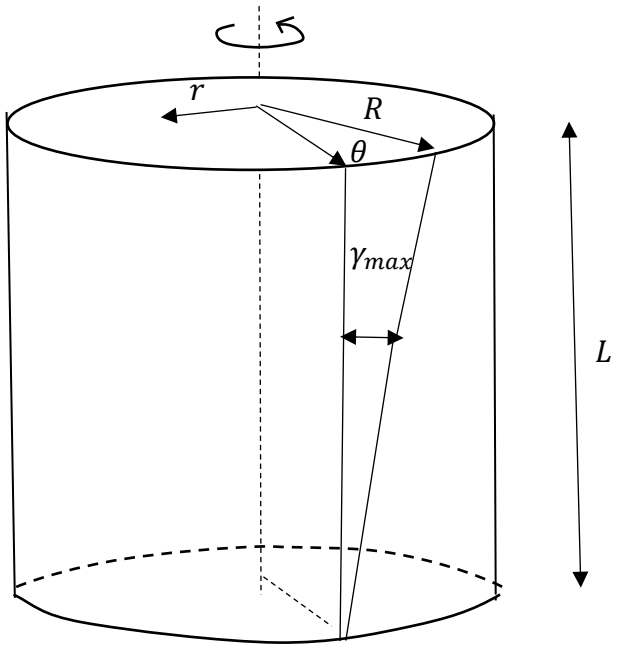


Figure 2-11 Schematic of shear strain developed in a cylindrical specimen subjected to torsional loading

The shear strain at the outer edge can be calculated via the following equation.

$$\gamma_{max} = \frac{R\theta}{L} \tag{2-22}$$

The equivalent radius concept to calculate average shear strain was developed by Chen and Stokoe (1979) to account for the non-uniform stress and strain distribution in solid soil specimens. This approach assumes that representative stress and strain occur at a specific radius called the equivalent radius, denoted r_{eq}. The equivalent radius approach incorporates an equivalent radius ratio, $R_{eq} = r_{eq}/R$ defined as the ratio of the equivalent radius to the outside radius of soil specimen. The measured strain is calculated by:

$$\gamma = R_{eq}\gamma_{max} \tag{2-23}$$

For a traditional fixed-free system, it is recommended that a $r_{eq} = 0.82$ should be used for strains less than 0.001% and 0.79 for strains up to 0.1% (Kim 1991; Hwang 1997).

2.5.3 Energy dissipation Calculation

The method of logarithmic decrement for attaining energy dissipation from the resonant column is now discussed. In a single degree of freedom (SDOF) system, the amplitude of motion under free vibration decays exponentially with time, as shown in Figure 2-12

below. The logarithmic decrement measures the decay amplitude of subsequent cycles:

$$\delta_{dec} = \frac{1}{n} \ln \frac{A_n}{A_{n+1}} \tag{2-24}$$

Where A_n and A_{n+1} is the measured shear strain amplitude at cycle n, and $n+1$. The damping ratio or energy loss factor is then determined by:

$$\eta = \sqrt{\frac{\delta_{dec}^2}{4\pi^2 + \delta_{dec}^2}} \tag{2-25}$$

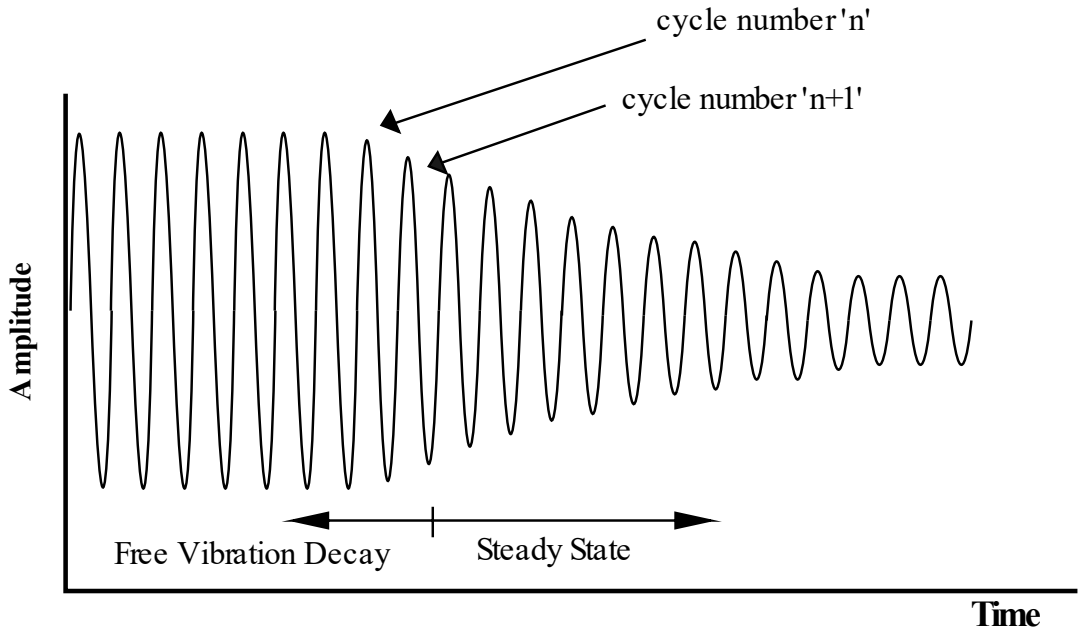
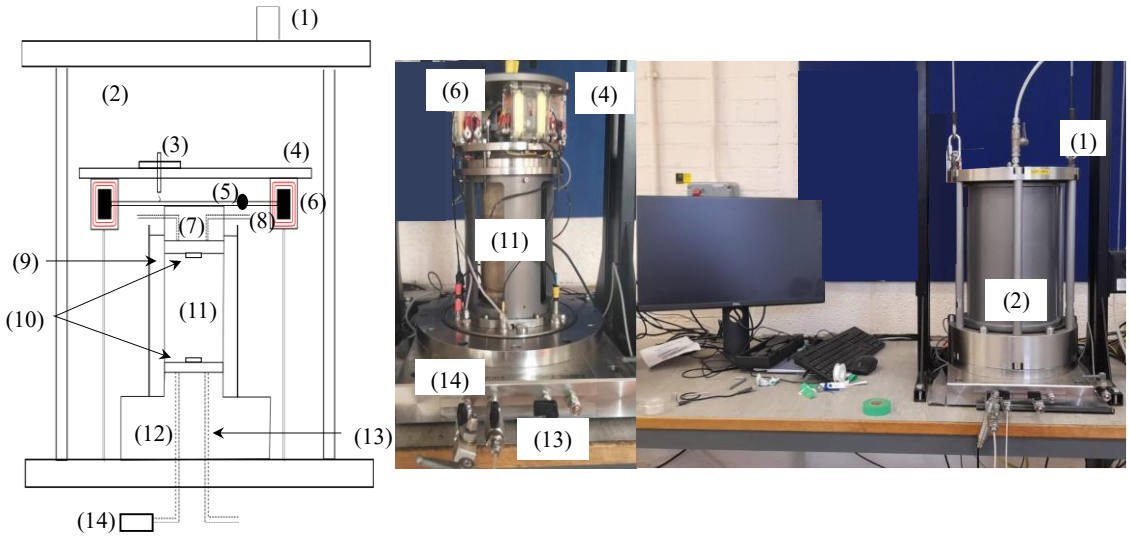


Figure 2-12 Schematic of the logarithmic decrement calculation from vibrational decay

2.5.4 Apparatus used in this study

This work uses the Stokoe-type RCA device manufactured by GDS Instruments Ltd. This device has a "fixed-free" boundary condition, assuming that the tested soil specimen is isotropic, homogeneous, and elastic. In this setup, the specimen rests on a fixed bottom platen, while the top is connected to a top platen and excited by a magnet coil system. A schematic of the apparatus is illustrated in Figure 2-13(a) below.



(1) Confining air inlet/outlet
(2) Pressure chamber
(3) Axial LVDT
(4) Drive plate
(5) Accelerometer
(6) Magnetic coils
(7) Top cap
(8) Top drainage
(9) Confining fluid
(10) Bender elements
(11) Soil specimen
(12) Fixed based pedestal
(13) Bottom drainage
(14) Porewater pressure transducer

Figure 2-13 (a) Schematic of Stokoe Type RCA, (after Stokoe & Santamarina (2000)); (b) Image of the RCA with cell up; and (c) Image of RCA with cell down

Depending on the properties required from the experiment, either axial force or torque can be applied to the specimen. This study primarily focuses on investigating the shear properties of soil, so the techniques described herein refer to torsional vibrations. The device is equipped with an electromagnetic driving head with four precision-mounted magnet coils that induce torsional oscillations within a solid cylindrical soil specimen. An accelerometer located within the drive head records the response during dynamic vibration. The base of the specimen is fixed onto a pedestal where no rotation is allowed. The pedestal is anchored and must have a mass polar inertia, I_p, of at least 100 times the specimen's rotational mass inertia ASTM (2015). An active end platen with rotational inertia, I_0, is composed of a top cap, magnetic coil, and drive plate and is located on the top of the soil specimen. This platen is rotated by a magnet-coil system fixed to the apparatus. An axial linear variable differential transformer (LVDT) is placed at the top of the specimen to measure axial strain. The pore water pressure is measured using a pore pressure transducer attached to the base of the cell.

2.5.5 Test procedure

A preliminary set of RCA tests was conducted to commission the device and establish the optimal testing procedures. This initial phase compared two methods of sand preparation: moist tamping and wet pluviation. The specimen geometry in these preliminary tests had a diameter of 50 mm and a target height of 100 mm. Based on the preliminary results, the main series of tests adopted the moist tamping technique exclusively. This decision was made to prevent the loss of fines associated with the wet pluviation method and to achieve lower specimen densities. These subsequent tests were performed on specimens with a diameter of 100 mm and a target height of 200 mm. The larger specimen size was selected to minimise boundary effects in the interpretation of BE tests and to ensure the specimens were representative for the RCA. The detailed test procedures are discussed below.

2.5.5.1 Sample preparation

Wet pluviation (WP): this technique is analogous to the underwater depositional processes that occur in natural oceanic environments (Lade and Duncan 1973). In this technique, a measured quantity of dry sand is mixed with water. The sand-water mixture is deposited into a mould to a specified height to achieve the desired density. The water acts as a dispersing medium, preventing segregation and ensuring a uniform distribution of sand particles as they settle. After the sand has settled, excess water is drained from the mould by carefully decanting the water from the top. Additional compaction may be necessary to achieve a very dense specimen by gently tapping the sides of the mould or using a weight on the top of the specimen.

Moist tamping (MT): In this method, wet sand is deposited in layers into a mould and compacted to a specified height to achieve a target density for each layer. The sand is typically compacted at its optimal moisture content to ensure effective compaction. To overcome the nonuniformity produced by compaction layers (where compaction of each succeeding layer can further densify the sand below it), Ladd's method of under-

compaction was followed. This approach involves compacting the base layers to a lower density than the succeeding layers, resulting in a more uniform overall density. This technique ensures that each layer contributes appropriately to the final desired density, enhancing the consistency and reliability of the prepared sand sample (Ladd 1978).

2.5.5.2 Saturation

The saturation stage ensures all the voids within the specimen are filled with water and that the drainage lines are de-aired. Initially, gaseous CO_2 was introduced to the specimen through the bottom drain, pushing the lighter air through the top drainage lines. This was conducted over 30 minutes ensuring complete replacement of air with CO_2. De-aired water was then introduced through the specimen until the volume of the water that passed through the specimen was equal to or greater than the volume of voids. The cell pressure and back pressure were ramped to 300kPa and 290kPa, respectively at a rate of 60kN/m^2 per hour. To ensure full saturation of the specimen, a calculation of Skempton's B-value was conducted. A B-value of > 0.95 was assumed to confirm saturation.

2.5.5.3 Consolidation

Specimen were consolidated to the target effective stress required at a rate of 60kN/m^2 per hour. The effective stress p'_0 is defined as $p'_0 = p - u$ where p is the total confining stress and u is the porewater pressure. To ensure that excess u was fully dissipated, and the effects of creep were negligible, BE and RC tests were not conducted until creep strains reduced to < 0.002% per day following Zdravković et al. (2020).

2.5.5.4 Bender element stage

After completing the consolidation process to reach the target stress, the next step involved conducting a BE stage to derive G_0. In this study the peak-to-peak method, as described in Section 2.4, was used to determine t_a due to its consistent outcomes compared to other interpretation methods. Identifying characteristic points from the output signal presented challenges, as they were not always distinctly identifiable.

Additionally, consistent determination of t_a using the cross-correlation method was challenging because this method often produced multiple peak detections, reintroducing subjectivity into BE interpretation.

2.5.5.5 Resonance Stage

The RCA is limited to measuring the stiffness response of soils within the elastic region only. It is expected that no porewater pressure develops in the elastic region so that the response characterised in the resonance stage is independent of drainage conditions.

In this study, the resonance stage was conducted under drained conditions. Initially, very small amplitude oscillations were induced in the sample across a range of frequencies. The frequency that produced the highest strain within the specimen was taken to be the resonant frequency, f_n and then converted to V_s using Equation (2-21) for wave oscillations, subsequently converted to G via:

$$G = \rho V_s^2 \tag{2-26}$$

The first computed value of G was taken as G_0. The induced shear strain measured by the accelerometer was also recorded for each increase in oscillation amplitude. Incremental increases in amplitude of oscillations were induced until the G decreased to $< 0.99G_0$, indicating non-linearity; γ_{tl} was taken as the average measured strain between this point and the preceding point. Beyond this value, "small strain checks" were performed after each increase in oscillation amplitude to ensure that the specimen had not undergone permanent reduction of G_0. The small strain checks were completed by inducing very small amplitude oscillations in the sample and recording the computed value of G (i.e., repeating the first step of this test). If the value of G corresponded to G_0 ± 1%, elastic behaviour of the soil could be assumed, as no permanent degradation of the soil stiffness had been induced. The test process continued with further increases in oscillation amplitudes. If the small strain check produced a value $G < 0.99G_0$, this

indicated the soil had undergone permanent degradation and corresponded with the onset of non-elastic soil behaviour. γ_{tv} would be taken as the average of this point and the preceding point. The procedure is schematically depicted in Figure 2-14.

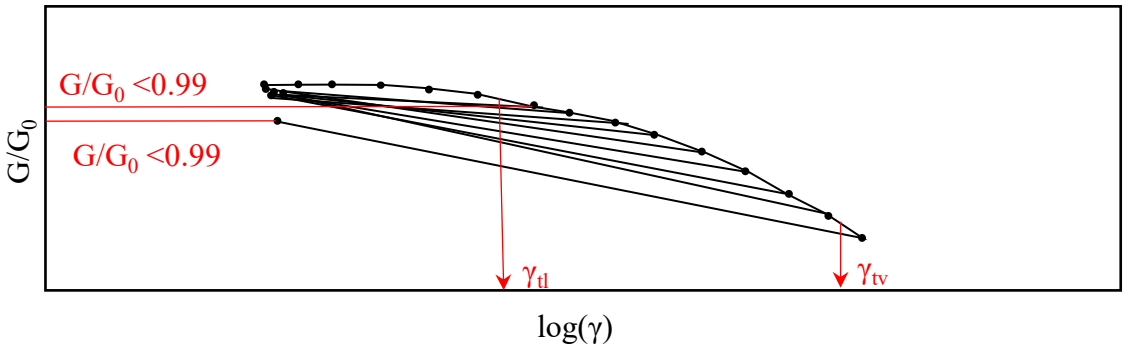


Figure 2-14 Schematic illustrating the procedure of small-strain checks and the determination of, γ_{tl} and γ_{tv}

2.5.5.6 Damping stage

A damping stage was conducted successively after each resonance stage (i.e., after each increase in oscillation amplitude). The damping stage was undertaken by oscillating the specimen once at the same amplitude and f_n measured in the preceding resonance stage. The measured motion and decay in the specimen induced by the oscillation recorded by the RCA allow for Equations (2-24) and (2-25) to be applied to determine the damping ratio/energy dissipation factor, η.

2.5.6 Limitations of System

Depending on the boundary conditions of the RCA system, different limitations apply. The Stokoe-type 'fixed-free' configuration is limited to isotropic consolidation and cannot subject specimens to anisotropic stress conditions. Soils often exhibit anisotropy in the field, which cannot be replicated in the Stokoe-type apparatus, affecting the accuracy in representing realistic soil conditions. The Hardin 'fixed-fixed' RCA configuration can apply anisotropic stress conditions.

Another limitation of all RCA types is that stress and strain non-uniformities can develop in solid cylindrical samples under substantial torsional loads, limiting the applicability of results at high strain levels. To obtain accurate results, torsional shear tests should be

conducted on hollow specimens. The Hollow Cylinder Apparatus has been developed to allow for torsional loading at medium to large strains (Hight et al. 1983).

2.6 Commissioning of the RCA

The performance of the RCA hardware required calibration of the device and a series of commissioning tests to ensure the consistency and accuracy of the results obtained from the RCA. These commissioning tests were undertaken on LBS – Fraction B.

2.6.1 Calibration of RCA device

The value of the rotational inertia of the active end platen, I_0, is a required input for Equation (2-21), to convert the measured f_n to V_s. Due to the complex geometry of the drive system, it is necessary to calibrate I_0 experimentally.

In this study calibration of this value was undertaken following the added mass method outlined in ASTM D4015, (ASTM 2015). I_0 was calibrated using three aluminium calibration bars and stainless-steel masses with known weights and geometries. The behaviour of the RCA can be modelled as a harmonic vibrating system, where the drive system acts as the pendulum mass and the specimen as a torsional spring. An appropriate expression for the system can be written as:

$$\omega_r = \sqrt{\frac{k}{I}} \tag{2-27}$$

where ω_r is the angular velocity, k is the stiffness of the system, and I is the total mass polar moment. Equation (2-27) can be re-written in the form:

$$I_{am} = \frac{k}{\omega_r^2} - I_0 \tag{2-28}$$

Where I_{am} is the mass polar inertia of one or more added masses on the calibration bar. One can plot $1/\omega^2$ with respect to I_{am}, and I_0 can simply be found as the y-intercept of the plot. The results from the calibration process obtained in this study for two specimen size diameters, D = 50 mm and 100 mm is represented in Figure 2-15 below.

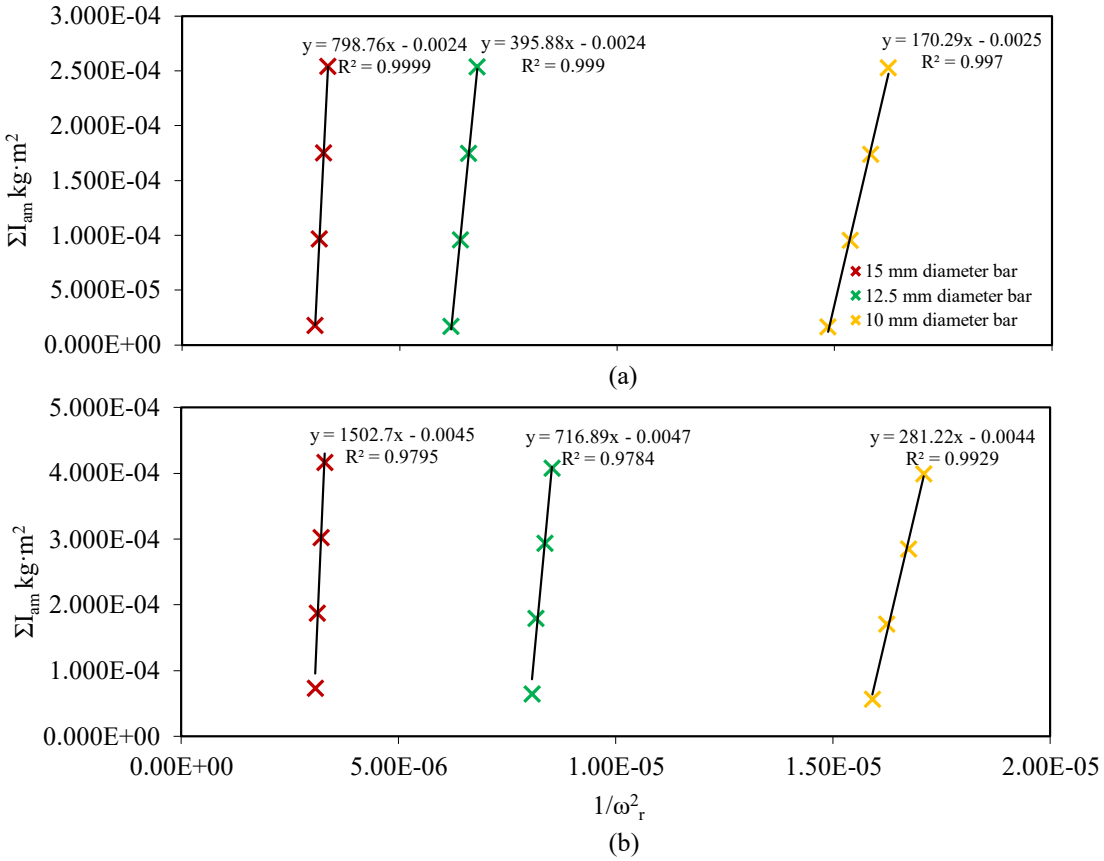


Figure 2-15 Variation of I_{am} with $1/\omega^2_r$ for calibration bars and added masses (a) 50 mm diameter; and (b) 100 mm diameter

Over the range of calibration bars investigated, the computed value for I_0 of the RCA system is computed as 0.00246kg·m^2 and 0.00408kg·m^2 for the 50 mm diameter and 100 mm diameter base respectively. Rieman et al. (2024) present a new calibration method for Stokoe and Hardin type RCA that accommodates drive system compliance, particularly important for stiff samples.

2.6.2 Comparison of measured data with results obtained by others

A series of BE and RC tests on LBS were undertaken to compare measurements from the RCA with previous data obtained by others. The G_0 measurements were validated against BE test results from White (2020) and empirical relationships developed by Hardin and Black (1968). A summary of the validation tests conditions and computed values of G_0 are presented in Table 2-3 below. The G_0 measurements from the validation study with respect to p'_0 are presented in Figure 2-16.

Table 2-3 Summary of validation tests

Test ID	Test Type	p'_0 (kPa)	D_r(%)	G_0 (MPa) This study	G_0 (MPa) White (2020)
BE_1	BE	25	81	125	135
BE_2	BE	51	81	165	172
BE_3	BE	77	81	175	179
BE_4	BE	198	81	280	297
RC_1	RCA	51	81	158	172
RC_2	RCA	198	81	252	297

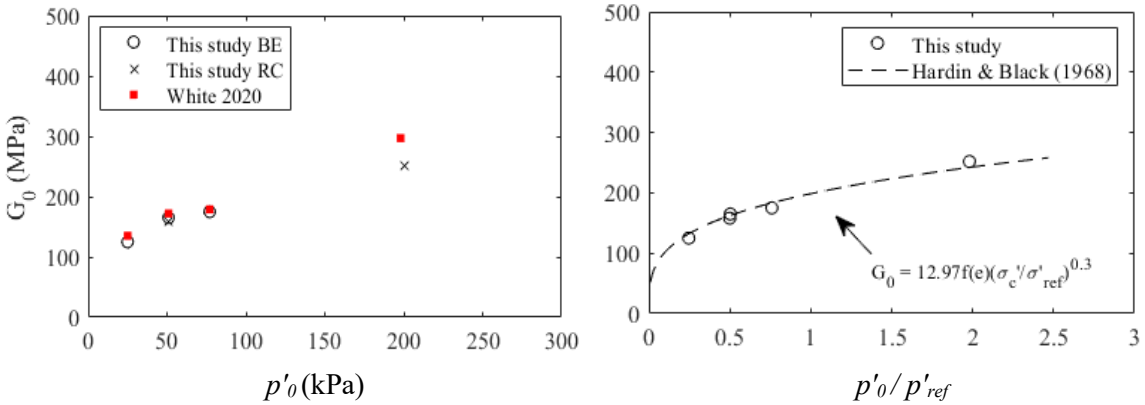


Figure 2-16 Validation of Comparison with G_0 (a) measurements by White (2020); and (b) empirical fit

Figure 2-16(a) shows computed values of G_0 are in close proximity to those measured by White (2020); however, measurements in this study are slightly lower by 3 to 8%. These discrepancies likely stem from size effects due to the differences in specimen geometry between their study and this one (Arroyo et al. 2006). White (2020) conducted testing on specimens with a diameter of 100 mm, while in this study, preliminary tests were undertaken on 50 mm diameter specimens, which might lead to differences in BE results. Figure 2-16(b) demonstrate that G_0 values in this study were in very close agreement with theoretical predictions by Hardin and Black (1968).

2.6.3 Repeatability tests

A total of four repeatability tests were conducted at two confining stresses p'_0 = 50.9kPa and 198.1kPa. Tests were prepared using the moist tamping method. A BE and RC test were conducted at each p'_0. The results summarised in Table 2-4 below and presented in Figure 2-17.

Table 2-4 Summary of repeatability tests on LBS, D_r = 81%

Test ID	p'_0 (kPa)	$G_{0,BE}$ (MPa)	$G_{0,RC}$ (MPa)	γ_{tv} (%)
RC_1	51	175	157	3.6×10^{-2}
RC_2	51	171	159	3.9×10^{-2}
RC_3	198	280	252	8.8×10^{-2}
RC_4	198	252	247	9.0×10^{-2}

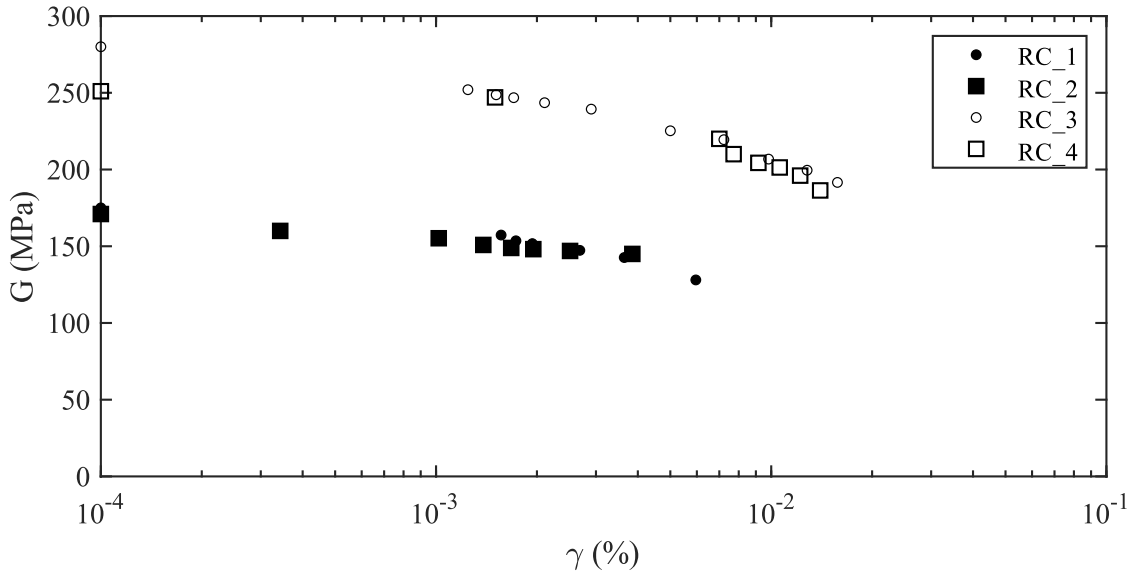


Figure 2-17 Repeatability tests showing measured G_0 and G/G_0 from BE and RCA tests, LBS, D_r = 81%

Table 2-4 and Figure 2-17 demonstrate the consistency of measurements across repeatability tests. Measured values of G_0 are within 2 to 10% across BE tests and 1 to 2% from RC tests. Measured values of γ_{tv} are between 2 and 7% across repeatability tests. These results demonstrate that repeatable results can be achieved from the RCA.

2.6.4 Effects of specimen preparation

The moist tamping (MT) and wet pluviation (WP) reconstitution methods were compared to quantify possible differences in measurements from the RCA due to sample preparation methods. Results are presented in Table 2-5 and Figure 2-18.

Table 2-5 Summary of specimen preparation tests on LBS, D_r = 81%

Test ID	Preparation method	p'_0 (kPa)	$G_{0,BE}$ (MPa)	$G_{0,RC}$ (MPa)	γ_{tv} (%)
RC_1	MT	50.9	175	157	4.2×10^{-3}
RC_2	MT	198.1	280	252	9.5×10^{-3}
RC_5	WP	50.9	171	123	6.8×10^{-3}
RC_6	WP	198.1	268	229	1.0×10^{-2}

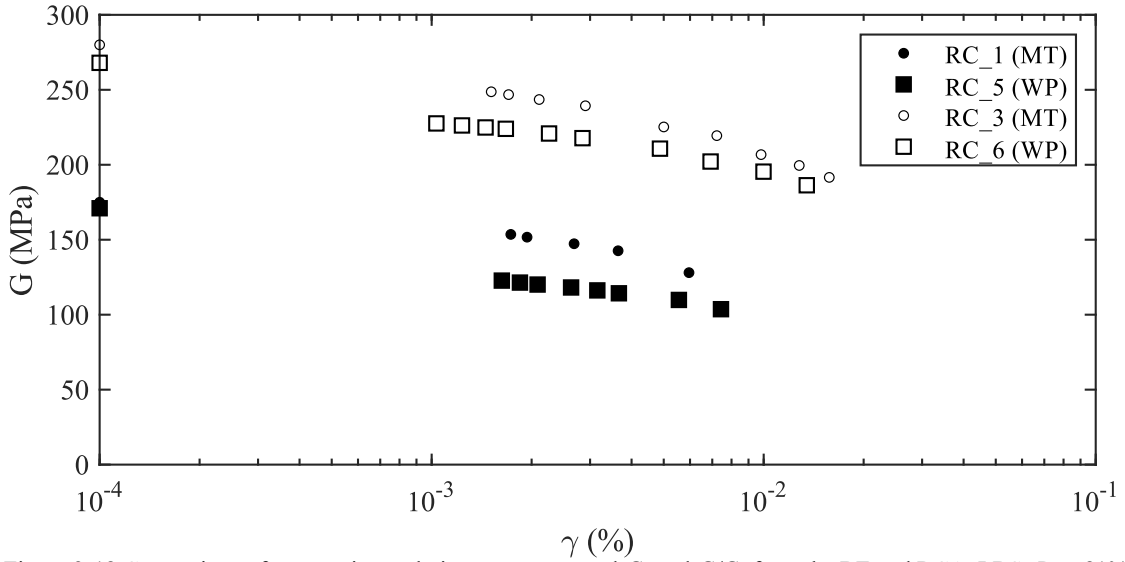


Figure 2-18 Comparison of preparation techniques on measured G_0 and G/G_0 from the BE and RCA, LBS, D_r = 81%

Several notable differences in G_0 and γ_{tv} obtained from the two preparation methods are observed. The WP method reduced nominal values of G_0 by approximately 5%, consistent with previous research relating to sample preparation effects (Gu et al. 2015). The γ_{tv} values obtained from the WP method ranged from 5 to 30% higher than those measured using the MT method. The challenge with the WP technique is related to achieving low D_r values and the loss of fines in naturally occurring sands. Consequently, the tests in the main body of this work rely on the MT technique. The primary focus of research using the RCA in this study is to examine trends through a parametric study. Consistency in sample preparation allows for reliable comparison of results, despite potential discrepancies in nominal values due to the choice of sample preparation.

2.7 Variable Dynamic Direct Cyclic Simple Shear (VDDCSS)

The direct shear device was developed to study the shear strength properties of soils as described in Section 1.7 and can determine the medium to large strain stiffness response

of soils as described in Section 1.6.3. The device applies a vertical load to the specimen and subsequently shears the specimen horizontally.

Early iterations of the direct shear device (DSS) include the shear box which causes specimens to fail along a pre-determined plane due to the configuration of the shear box, Roscoe (1953). The direct simple shear device has since been developed such that the soil confined by a stack of steel rings and is sheared uniformly across the specimen, allowing for the specimen to shear at its weakest point, Bjerrum and Landva (1966). Therefore, the shear strength determined from this test is more representative of the material and soil conditions. Furthermore, the test allows for control of drainage condition of the test to be altered. In recent years, the device has been modified to allow for cyclic and multidirectional loading, such that the cyclic behaviours discussed in Section 1.7 can be readily measured herein referred to as the Variable Dynamic Direct Simple Shear (VDDCSS) device.

The VDDCSS apparatus can induce medium to large shear strains to an element of soil. The shearing of the specimen takes place along a failure plane in line with the direction of shearing. The interpretations, definitions, assumptions, and failure state of the VDDCSS apparatus are now discussed.

2.7.1 Stress-strain response in the VDDCSS

In the VDDCSS cannot deform freely in 3D space as the specimen is constrained radially by a stack of confining rings. These rings bound the soil and restrict the specimen from changing cross-sectional area during shearing. To consolidate the specimen, a vertical stress is applied on top of the specimen and the coefficient of lateral pressure, K_0 conditions are imposed by the confining rings. However, radial stresses from the confining rings and thus the nominal value of K_0 are unknown during the test unless stress sensors are used. A simplified 2D representation of the motion an element of soil

in the VDDCSS test is presented in Figure 2-19(b).

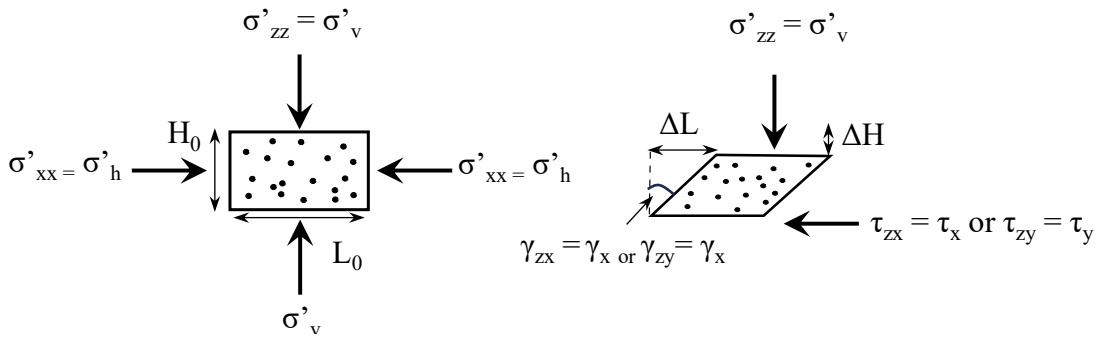


Figure 2-19 Stress-strain distribution of an element of soil in the VDDCSS in drained conditions (a) static state; and (b) sheared state

The shear stress parameters derived from the tests are described by the following:

$$\sigma'_v = \sigma'_{zz} = \frac{F_z}{A}, \tau_{zx} = \frac{F_x}{A}, \tau_{zy} = \frac{F_y}{A} \tag{2-29}$$

Where F_z is the applied vertical load, F_x and F_y are the applied horizontal load in the x and y direction respectively and A is the cross-sectional area of the specimen. Since A remains constant, the volumetric strain ε_{vol} is synonymous with the axial strain ε_z in this test. The strains measured in the test are determined via the following relationships:

$$\varepsilon_{vol} = \varepsilon_z = \frac{\Delta H}{H_0}, \gamma = \frac{\Delta L}{H_0} \tag{2-30}$$

The behaviour described in Figure 2-19(b) refers to tests undertaken in 'drained' conditions where the height and thus volume of the specimen are free to change with loading. For the duration of shearing, the specimen is subject to a constant stress of fixed σ'_v, see Figure 2-20(a) and (c). The device also has capabilities of shearing the specimen in 'undrained' conditions where the height and thus volume of the specimen remains fixed during shearing and instead changes to σ'_v occur during cycling, this is shown in Figure 2-20(a) and (b). In such scenarios, Equation (2-29) remain governing soil behaviour, however $\varepsilon_{vol} = 0$ and $\Delta\sigma'_v$ is assumed synonymous with Δu (Dyvik et al. 1987; Bjerrum and Landva 1966).

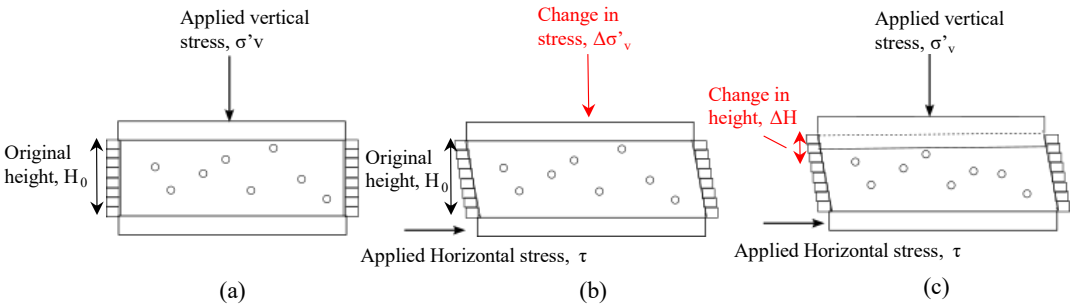


Figure 2-20 Schematic of the motion in the VDDCSS (a) initial condition; (b) undrained test; and (c) drained test

2.7.2 Failure states in the VDDCSS

Three types of failure modes can describe the failure state of a soil specimen within the VDDCSS. The first one is the assumption that the horizontal planes are planes of maximum stress obliquity as seen in Figure 2-21(a), this is the failure state referred to in latter chapters of this thesis. The second approach is to assume that the horizontal planes are planes of maximum shear stress as shown in Figure 2-21(b). Finally, the third assumes that failure in simple shear could occur either by sliding on horizontal planes or sliding in conjunction with rotations on vertical planes. But, if the boundary conditions are such that both modes of failure are equally possible, the sample will choose the one with the least resistance, as shown in the latter model by De Josselin de Jong (1971) as shown in Figure 2-21(c).

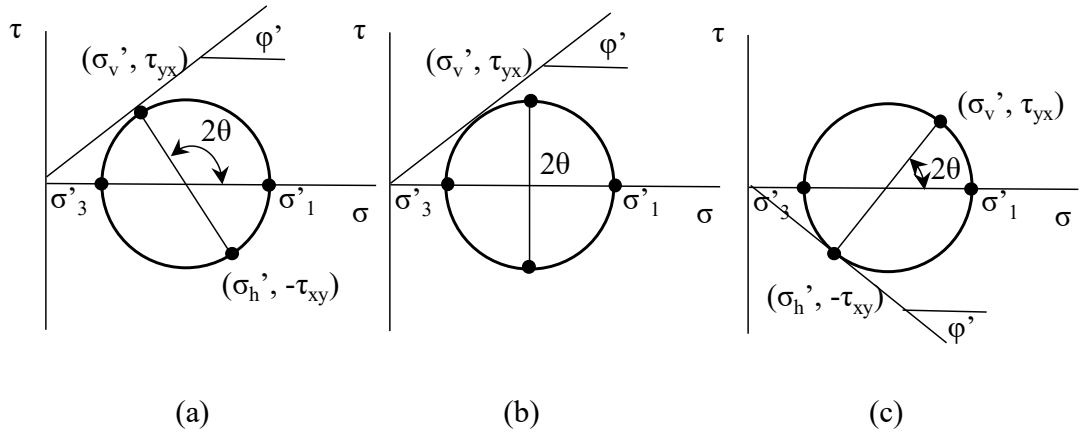


Figure 2-21 Mohr's circle failure modes from the VDDCSS, modified from Budhu (2011)

2.7.3 Cyclic definitions

The following definitions have been used in this thesis to interpret the salient cyclic features as obtained from the VDDCSS.

2.7.3.1 Accumulated ratcheting

In the VDDCSS, accumulated ratcheting develops in the direction of loading, simultaneously the stiffness of the soil is also changing. It is therefore important to decouple the effects of accumulated ratcheting and changes in stiffness of the specimen. Definitions that describe the average shear strain in a cycle, γ_{ave} and the accumulated shear strain with cycles γ_{acc} that attempt to minimise the coupled effects of stiffness change and strain accumulation are shown in Equation (2-31) and (2-32). This is also illustrated Figure 2-22(a):

$$\gamma_{ave} = \frac{1}{2}\left(\gamma(a_n) + \gamma(b_n)\right) \tag{2-31}$$

$$\gamma_{acc} = \frac{1}{2}\left(\gamma(a_n) + \gamma(b_n) - \gamma(a_0) + \gamma(b_0)\right) \tag{2-32}$$

2.7.3.2 Evolution of stiffness and energy dissipation

The secant stiffness, G_{sec} of a material under cyclic loading is generally defined as the slope between the minimum stress, strain point τ_{min}, γ_{min} and the maximum stress, strain point τ_{max}, γ_{max}. While this is well defined for closed hysteresis loops, as mentioned previously, for cycles that induce permanent strain, it is challenging to decouple the stiffness change with ratcheting. The central cycle stiffness is therefore used in this study to minimise this coupling as described in Equation (2-33) and illustrated in Figure 2-22(a):

$$G_{sec} = \frac{\tau(a_0) - \tau(b_0)}{\gamma(a_0) - \frac{1}{2}(\gamma(b_0) + \gamma(b_1))} \tag{2-33}$$

Energy dissipation, η is the ratio between hysteretic energy loss, E_H to maximum stored energy per cycle E_E as illustrated in Figure 2-22(b). For closed hysteric loops (e.g., two-way loading), the energy dissipation factor and energy stored per cycle are well defined by the following equations:

$$\eta = \frac{1}{2\pi}\frac{E_H}{E_E} \tag{2-34}$$

$$E_E = \frac{1}{2}[\tau(u_1) \times \gamma(u_1)] = \frac{\tau(u_1)^2}{2k_{sec}} \tag{2-35}$$

$$E_H = \oint \tau d\gamma \tag{2-36}$$

However, like the definitions for accumulated strain and secant stiffness, modifications to the above equations are required for non-closing loops which occur when ratcheting occurs during one-way or partial one-way loading. In such situations, one may use following equations to describe the energy loss and energy stored:

$$E_E = \frac{1}{2}\left[\frac{1}{2}\left(\tau(u_1) - \tau(r_1)\right) \times \frac{1}{2}\left(\gamma(r_1) + \gamma(r_2)\right)\right] = \frac{(\tau(u_1) - \tau(r_1))^2}{8k_{sec}} \tag{2-37}$$

$$E_H = \int_{r_i}^{u_i} \tau d\gamma + \int_{u_i}^{r_{i+1}} \tau d\gamma \tag{2-38}$$

Subsequently, the energy dissipation factor for non-closing loops can be expressed as:

$$\eta = \frac{4k_{sec}}{\pi((\tau(u_1) - \tau(r_1))^2}\left(\int_{r_i}^{u_i} \tau d\gamma + \int_{u_i}^{r_{i+1}} \tau d\gamma\right) \tag{2-39}$$

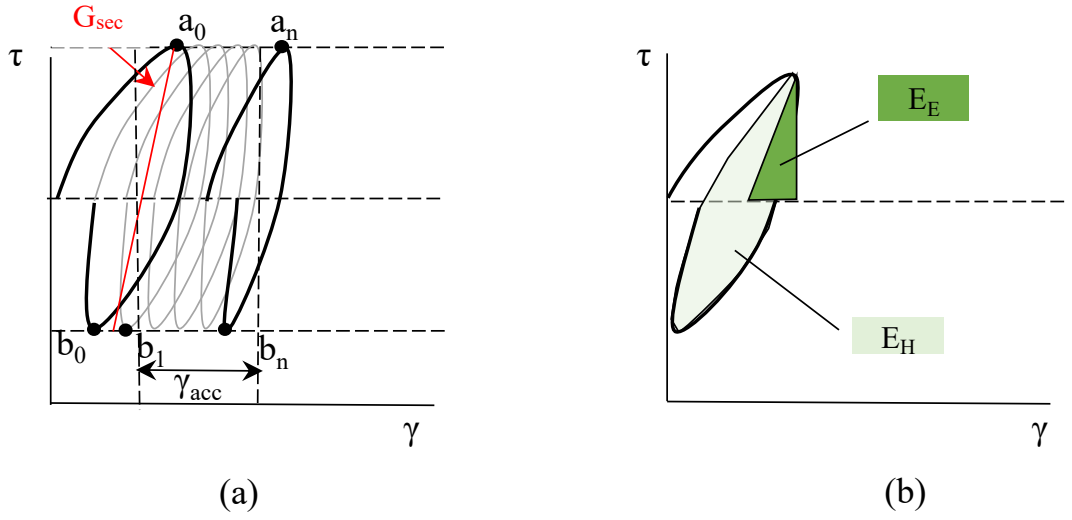


Figure 2-22 Graphical representation of (a) γ_{acc} and G_{sec}; and (b) η

2.7.4 Loading asymmetry

The cyclic loading applied to OWT structures is often asymmetrical by nature, and the measure of asymmetry is determined by the parameter ζ_c. Analysis of wind data typically

reveals a bias or prevailing wind direction, commonly represented in engineering practice through tools such as wind roses. This load bias suggests that asymmetrical loading on OWTs is typical in the field.

The contour diagrams proposed by Andersen (2015) are an effective method that represent the combined effects of ζ_b and ζ_c on key cyclic features like, accumulated ratcheting in drained conditions and number of cycles to liquefaction in undrained conditions for a particular material and are based on experimental results from the cyclic direct simple shear device (CDSS). Cui et al. (2019) using Discrete Element Modelling (DEM) of CDSS tests note that loading asymmetry influences the densification of soils with lower ζ_c increasing the densification. However, they note that the cyclic soil behaviour is only dominated by loading asymmetry for the first hundred cycles and subsequent cyclic behaviour is dominated by loading amplitude. Pan et al. (2022) examines the failure mechanisms of sands in undrained loading under asymmetrical loading and notes that asymmetry can both increase and decrease the specimen's resistance to liquefaction depending on its initial static stress condition.

Dry 1g model tests of a monopile founded in LBS by Richards (2020) demonstrate that the rate of accumulation is negatively correlated with ζ_c for $-0.75 < \zeta_c < 0$, results are broadly in line with Leblanc et al. (2010b) and Truong et al. (2018). These findings highlight the importance of capturing the effects of ζ_c in monopile design.

2.7.5 Multidirectional loading

In addition to asymmetry, offshore locations often experience a greater degree of variability in wind and wave direction. This spatial variability of loading results from factors such as coastal geography, atmospheric conditions, and seasonal weather patterns.

Furthermore, seismic loading from earthquakes and extreme storm events are generally multidirectional. Thus, the design of foundations in offshore conditions additionally requires consideration of multidirectional loading.

Multidirectional loading can manifest in various patterns in the field. Commonly studied patterns include, Perpendicular, Elliptical, Spiral, Figure-8, and Fan-shaped loading as illustrated in Figure 2-23 (a) to (f) throughout.

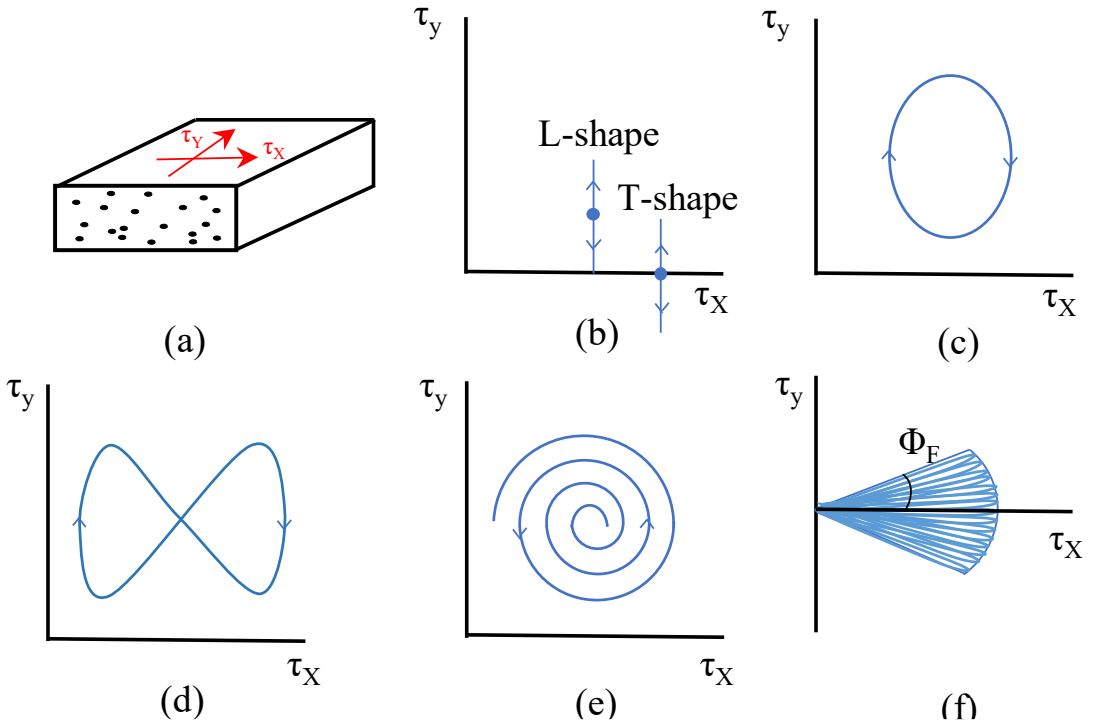


Figure 2-23 Multidirectional loading (a) 3D representation of soil specimen; (b) Perpendicular loading; (c) Elliptical loading; (d) Figure-8 loading; (e) Spiral loading; and (f) Fan-type loading

Ishihara and Yamazaki (1980) developed a modified direct simple shear testing apparatus capable of applying multidirectional cyclic loading on soil specimens. They conducted several unidirectional and multidirectional tests on saturated sands in undrained conditions. Their results demonstrate significantly higher accumulated ratcheting and reduction of shear strength for multidirectional tests compared with corresponding unidirectional tests. Boulanger and Seed (1995) performed undrained perpendicular cyclic tests in the simple shear device. The results demonstrate lower liquefaction resistance of specimens under perpendicular loading compared to unidirectional with

results attributed to the amount of principal stress rotation and shear stress reversal that occurs in such conditions. Kammerer (2002) investigated the undrained response of saturated sands under multidirectional loading investigating Elliptical and Figure-8 multidirectional loading and notes that the development of u under such loading is quicker than corresponding unidirectional loading. Matsuda et al. (2004) demonstrated that multidirectional loading increases the generation of u and accumulated ratcheting compared to unidirectional loading. Li et al. (2017) conducted a suite of undrained multidirectional monotonic tests on cohesionless soils investigating the impact of orientation and magnitude of shear stress applied during consolidation. They note smaller angles between the horizontal consolidation stresses lead to a more brittle response and higher peak strength while a ductile response is seen for higher angles. Le and Rackwitz (2020) performed a suite of drained cyclic simple shear tests under multidirectional loading, where the direction of the cyclic load rotates by 90° at least once during cycling. Specimen exposed to changes in direction during cyclic loading developed a significant amount of ratcheting immediately after rotation in the direction of loading, causing a temporary increase in strain rate. They also observe a reduction in stiffness, at the onset of rotation in loading direction. Bhaumik et al. (2023) demonstrated that multidirectional elliptical and Figure-8 cyclic loading induce greater densification than unidirectional cyclic loading.

Dry 1g model tests of a monopile installed in LBS by Richards (2020) demonstrated that multidirectional perpendicular loading impacts the rate of accumulated ratcheting for the first 100 cycles. However, perpendicular tests converge to the ratcheting of the unidirectional test after 100 cycles. Results indicate that strain accumulates in the direction of average stress for T-shaped perpendicular tests and at an angle to the direction of average stress in L-shaped perpendicular tests depending on the cyclic amplitude.

Furthermore, the results show that for Fan-type loading, the spread angle, Φ_F controls the magnitude of ratcheting.

2.7.6 Apparatus used in this study

This research makes use of the NGI-style VDDCSS apparatus, manufactured by GDS Instruments. The VDDCSS device is a modified type of simple shear device that enables shearing of the soil specimen in orthogonal directions using two high-accuracy actuators. It has the capability to apply monotonic or cyclic loading to the specimen, with loading options including stress control or strain control. Different loading frequencies, f, amplitudes, ζ_b, and loading symmetries as discussed in Section 1.7 for cyclic loading can be applied using the device. A schematic of the apparatus is presented in Figure 2-24(a), with images from the apparatus shown in Figure 2-24(b) and (c).

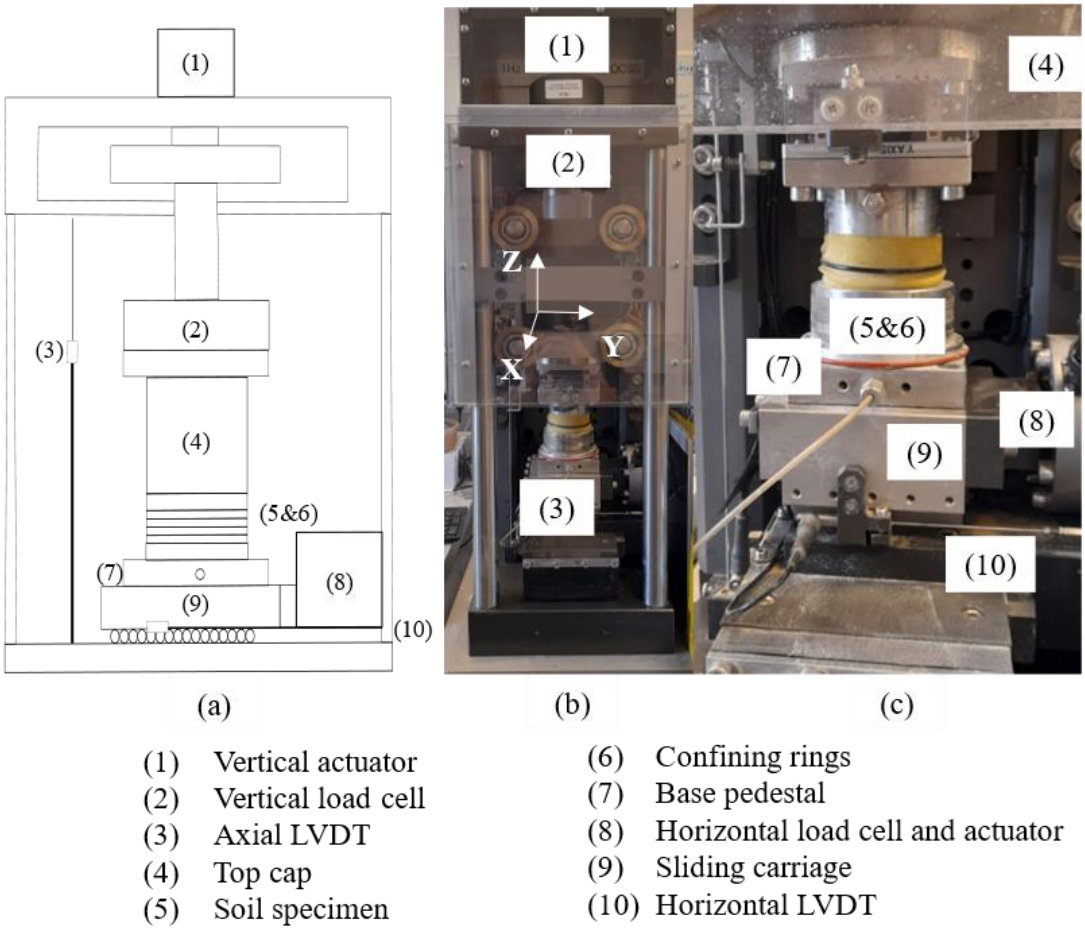


Figure 2-24(a) VDDCSS Schematic; (b) Full image of VDDCSS; and (c) Close up image of the VDDCSS set-up

In the device, the soil specimen sits within a latex membrane that attached to the base pedestals via o-rings. The specimen and membrane are confined by a stack of Teflon coated rings. The top cap sits on top of the specimen and is attached to the top of the specimen via o-rings attached to the protruding membrane. A vertical load cell that applies vertical stress to the top cap and has a 5kN capacity. Two horizontal load cells sit in-line with the base pedestal and have the capability to apply shear loading to the specimen in orthogonal directions. The horizontal load cells have a maximum capacity of 2kN. Axial and horizontal LVDTs measure the specimen throughout the test.

2.7.7 Test procedure

2.7.7.1 Specimen preparation

Soil specimens were prepared using MT, following the procedure outlined in Section 2.5.5, however only three layers were used. The geometry of the specimen tested was diameter, D_{spec} = 70 mm and height, H_{spec} = 17mm with a D_{spec}/H_{spec} ratio of 4 to avoid nonuniform stress and strain distributions, following Boulanger and Seed (1995) and Li et al. (2017).

2.7.7.2 Saturation and consolidation

Specimens were saturated using deaired water through a back line in the device. Since the device does not directly measure *u*, *B-value* checks are not possible to evaluate saturation. The specimen was then consolidated to a target vertical stress, σ'_v at 100kPa/hour and left to consolidate until creep strains reduced to < 0.002%/day.

2.7.7.3 Pre-shear cyclic stage

Andersen (2015) states for cohesionless soils a pre-shear cycling stage may be introduced before cyclic loading if the founding soil is expected to undergo small cyclic loads before the main storm design event. In this study, it was observed that pre-shearing led to specimen densification up to D_r = 90-100%, values higher than its *in-situ* D_r.

Furthermore, since this research is concerned with understanding the progressive behaviour of soil during cyclic loading during OWT operation and not exclusively designing for a storm event, the pre-shearing stage was omitted.

2.7.7.4 Monotonic shear

Samples were sheared either at constant volume (undrained) or constant vertical stress (drained) conditions. Monotonic tests were conducted via strain control and specimens were sheared at fixed strain rate of 0.06%/min.

2.7.7.5 Cyclic shear

The cyclic loading tests were designed to explore the physical mechanisms influencing cyclic behaviour for cohesionless soils. Therefore, tests were carried out under a range of σ'_v, f, ζ_b and ζ_c in both undrained and drained conditions. Cyclic tests were stress-controlled where target shear load was applied to the specimen. Tests were subjected to 3000 cycles or failure. The failure criterion for drained tests was when γ_{ave} reached 15% shear strain. The failure criterion for undrained tests was when $\Delta u > 90\%$.

2.7.7.6 Post-cyclic shear

A post-cyclic monotonic shear stage was introduced for specimens that did not reach failure to evaluate the influence of cyclic loading on the monotonic capacity. Specimens were sheared at fixed strain rate of 0.06%/min during this stage in the same drainage conditions as the cyclic stage.

2.7.8 Limitations of apparatus

A major limitation of the DSS is that the stress state of the specimen during shearing is unknown. This is because the horizontal stresses (σ'_x and σ'_y) applied by the confining rings are unknown, and the average stress of the specimen is also unknown (i.e., $\sigma'_m = (\sigma'_v + \sigma'_x + \sigma'_y)/3$). This makes it difficult to compare the behaviour obtained from this apparatus with that from other devices such as the RCA and triaxial, as it cannot be

verified whether the tests were undertaken at the same stress states. Qiu (2023) installed thin flexible piezoresistive force sensors to modify the original system to enable direct measurements of the lateral stresses, σ'_x and σ'_y within the specimen during shearing. Such modifications were allowed for accurate measurements of stress state of the specimen. Another limitation of the device stems from the measurement of *u.* In the DSS, *u* is not directly measured, and interpretation of test results assume that changes in $\Delta\sigma'_v$ are synonymous with Δu. This is not necessarily a precise measurement of the value.

Finally, a major issue reported by several researchers is that no form of DSS device can impose true simple shear conditions, as they are unable to generate the required complementary shear stress on the vertical boundaries (Boulanger and Seed 1995; Franke et al. 1979; Madhusudhan 2022). This results in a complex non-uniform stress and strain in the specimen. Shen et al. (1978) undertook finite element analysis (FEA), simulating a 3D element of soil in the cyclic DSS for different specimen geometries. Their results demonstrate that a higher specimen diameter to height (D_{spec}/H_{spec}) ratio results in reduced nonuniform stress and strain distributions. They explain that for the same amount of horizontal displacement imposed on the specimen, a smaller external moment develops within the thinner specimen (larger D_{spec}/H_{spec} ratio), producing a more uniform shear state. The effects of stress and strain nonuniformities on have been evaluated experimentally by varying the D_{spec}/H_{spec} ratios of circular specimens in the DSS, (Amer et al. 1987; Kovacs and Leo 1981; Carroll 1979). The results reiterate the importance of increasing D_{spec}/H_{spec} ratio to reduce nonuniformities in DSS testing. More recently, Doherty and Fahey (2011) showed through a 3D FEA of the DSS tests that imposing certain boundary conditions can lead to ideal simple shear conditions, with details explained in their paper. From a practical standpoint, the specimen is assumed to be close

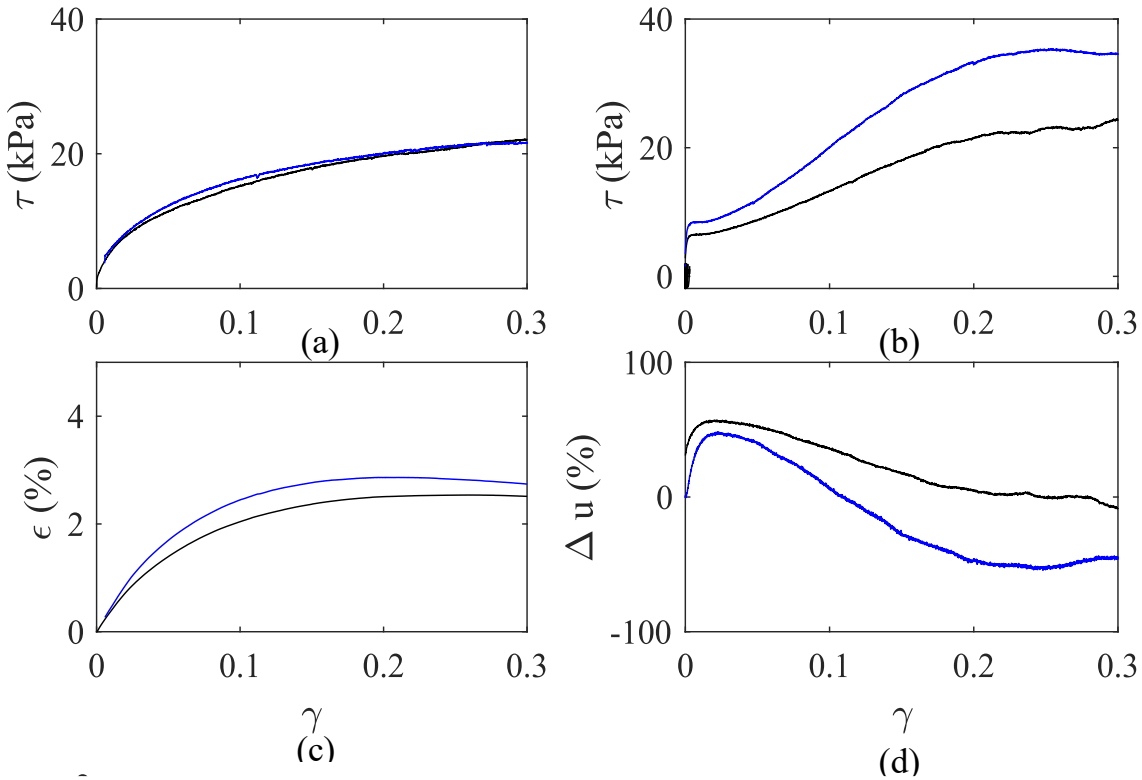
enough to the pure shear stress state to justify the interpretation of results in the later chapters of this thesis.

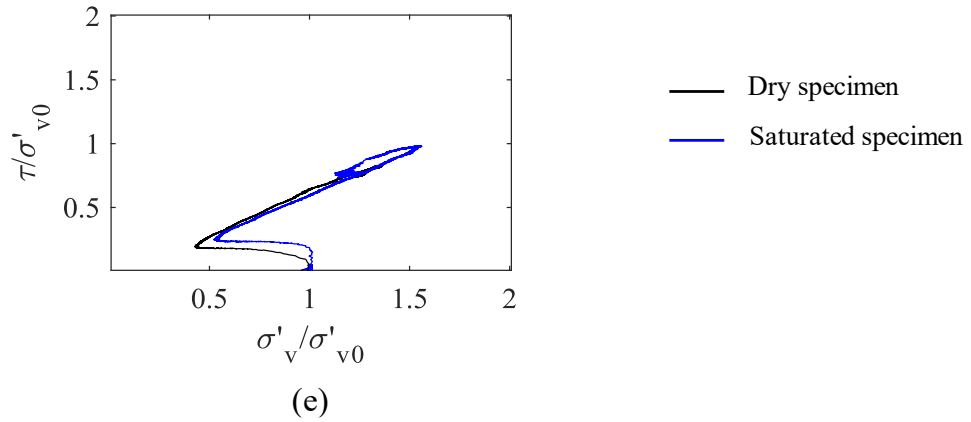
2.8 Commissioning of the VDDCSS

Significant commissioning tests on the VDDCSS used in this study were conducted by Qiu (2023). In this study, a smaller suite of preliminary tests was undertaken on CX to determine the best practice procedures using the device and to ensure that reliable results could be obtained from the apparatus. The focus of these preliminary tests was to evaluate the effects of soil saturation on monotonic and cyclic responses.

2.8.1 Monotonic tests

The monotonic responses of the dry and saturated samples are presented in Figure 2-25(a) to (e) throughout. For drained tests specimen were prepared to D_r = 60% and σ'_v = 36kPa, for undrained tests they were prepared to D_r = 90% and σ'_v = 36kPa.





(e)

Figure 2-25 Influence of saturation on monotonic behaviour (a) Stress-strain, drained; (b) Stress-strain, undrained; (c) Axial strain, drained; (d) Porewater pressure, undrained; and (e) Stress path, undrained

The dry and saturated specimens exhibited no significant differences in monotonic behaviour. The drained tests show that both dry and saturated specimens reached similar τ_{max} and exhibited similar levels of axial strain during shearing. Since fluids cannot resist shear stresses, it is unsurprising that the shear resistance of both dry and saturated soils is identical under drained conditions. There was also little difference in the undrained behaviour of the dry and saturated tests. Both specimens experienced a similar τpeak followed by strain hardening, although more porewater pressure developed in the saturated specimen compared to the dry specimen.

2.8.2 Cyclic tests

Cyclic tests were undertaken at $\zeta_b = 0.3$, $\zeta_c = 0$, $D_r = 60\%$ $\sigma'_v = 36$kPa, on both dry and saturated specimens in both drained and undrained test conditions. The cyclic stress-strain curves are shown in Figure 2-26 and other cyclic features are presented in Figure 2-27.

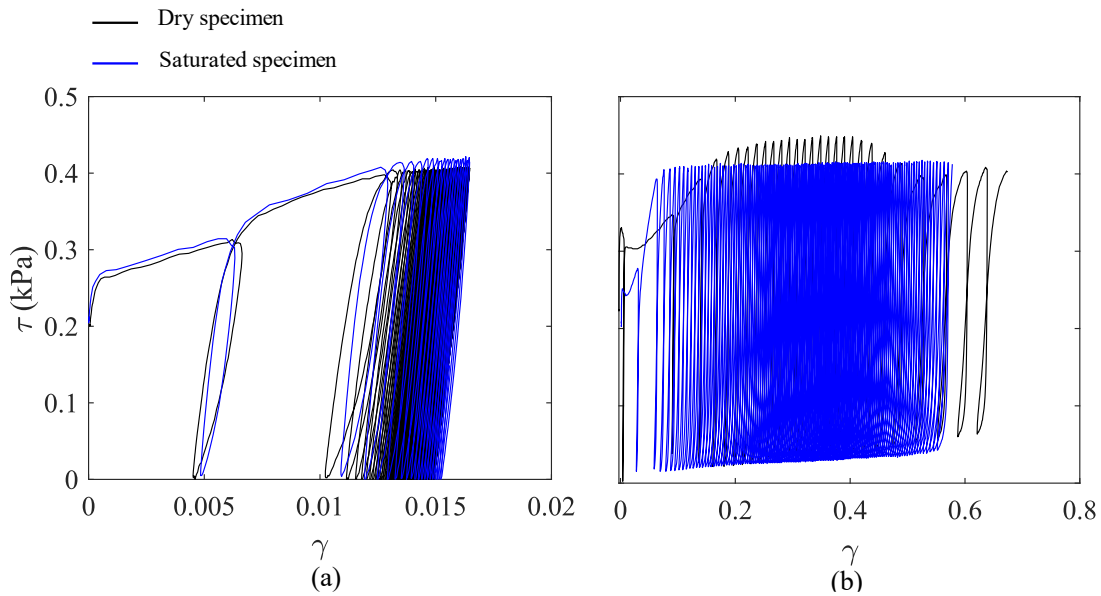
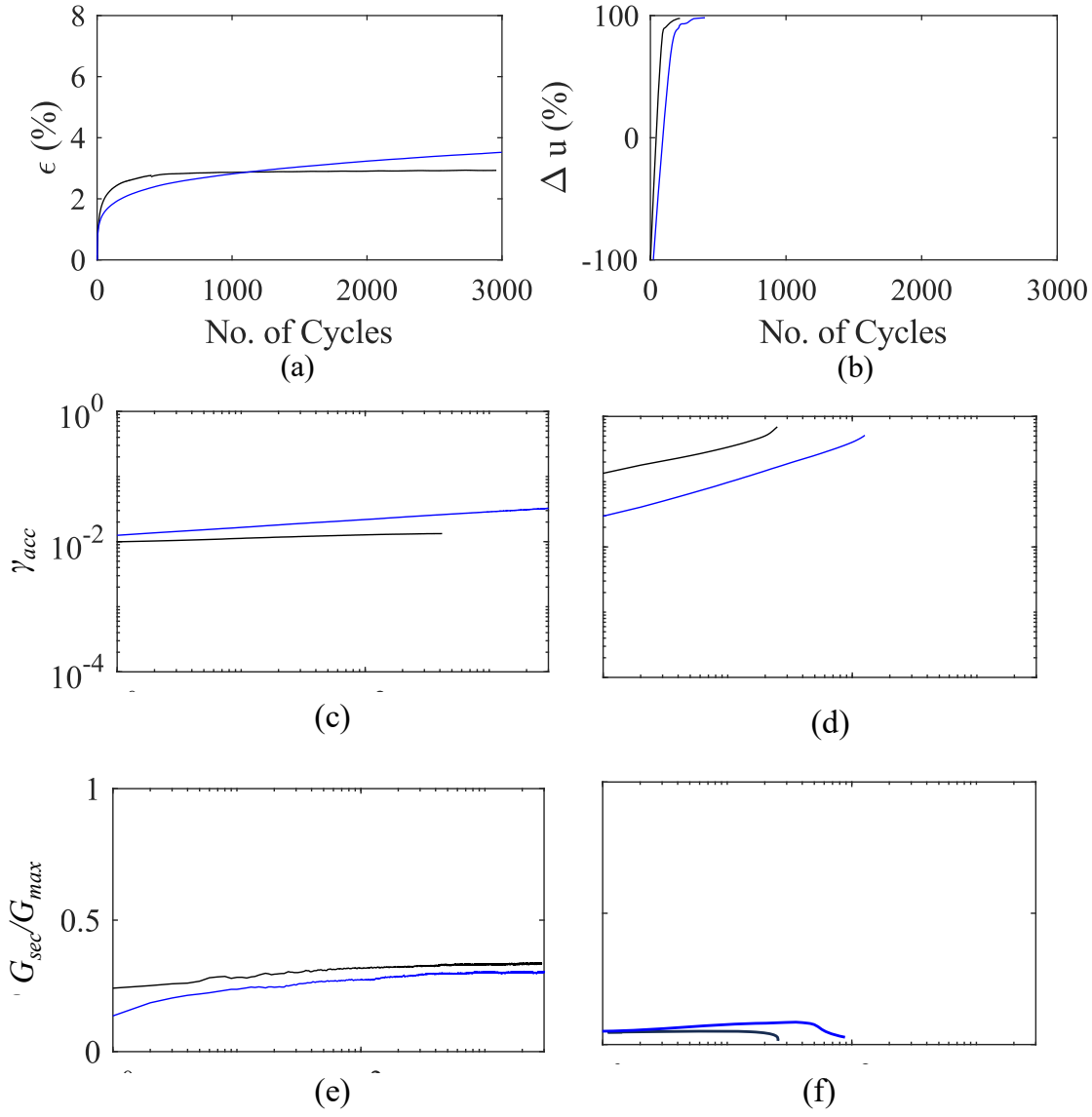


Figure 2-26 Stress-strain cyclic behaviour comparing dry and saturated responses (a) drained; and (b) undrained



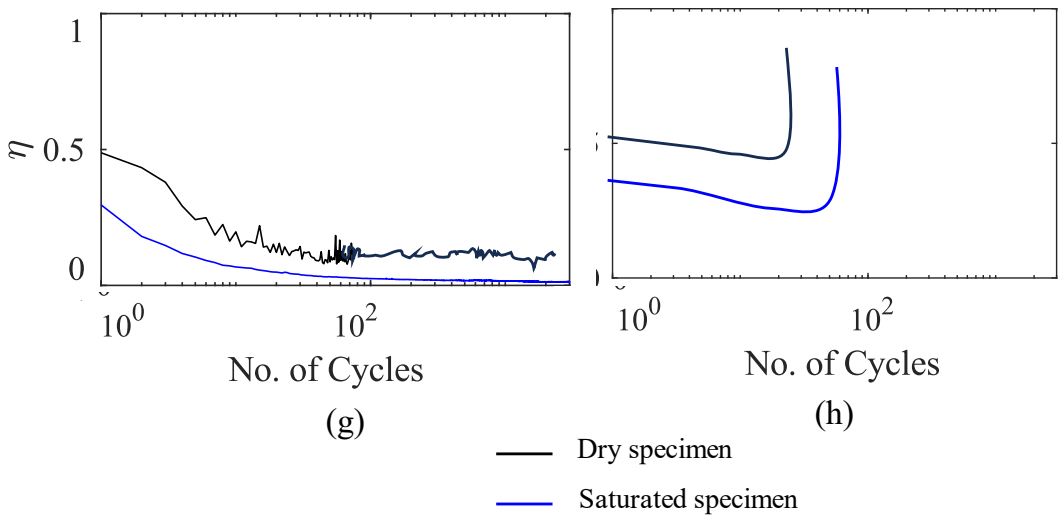


Figure 2-27 Influence of saturation on cyclic behaviour (a) Axial strain, drained; (b) Porewater pressured, undrained; (c) Accumulated strain, drained; (d) Accumulated strain, undrained; (e) Normalised stiffness, drained; (f) Normalised stiffness, undrained; (g) Energy dissipation, drained; and (h) Energy dissipation, undrained

Very little difference was observed between the dry and saturated cyclic behaviour. In drained tests, both dry and saturated specimens exhibited similar levels of densification from cycles, accumulated similar ratcheting in the direction of cycling, and produced similar values of normalised stiffness and energy dissipation with cycles. Similarly, in undrained tests, the dry and saturated specimens showed similar levels of porewater generation, accumulated ratcheting, normalised stiffness, and energy dissipation. The number of cycles required to fail the dry specimen was lower, $N_f = 28$ compared to the saturated specimen $N_f = 108$. However, failure in both specimens is seen to be characterised by the rapid changes in Δu, γ_{acc}, G_{sec} and η.

This investigation indicates that the saturation of cohesionless soils does not greatly affect the monotonic or cyclic behaviour captured in the VDDCSS. Both fully saturated and fully dry specimens showed similar drained and undrained responses. Consequently, all subsequent tests in the main testing regime were conducted on fully saturated specimens.

Like sands through the hourglass, so are the days of our lives – Socrates

CHAPTER 3

Small-strain stiffness of cohesionless soils

3.1 Introduction

The concept of initial shear modulus, G_0, shear modulus degradation, G/G_0 and threshold shear strains and their relevance to geotechnical design have been described in Section 1.6.3. G_0 and G/G_0 degradation parameters are routinely used in geotechnical analyses e.g. in the calibration of constitutive soil models and provide key details about soil behaviour across different strain regions, such as the limit of linearity, elasticity, and rate of G/G_0 degradation. Moreover, the typical strain levels around geotechnical structures fall in the range where changes to soil shear modulus are the most dramatic with strain (Clayton 2011).

Previous research suggests that G_0, G/G_0 and threshold reference strains are primarily dependent on D_r, p'_0, C_u, and d_{50}, (Menq 2003; Wichtmann and Triantafyllidis 2009; Oztoprak and Bolton 2013; Payan et al. 2016; Senetakis et al. 2016; Upreti and Leong 2019). There is common consensus that G_0 is positively related with D_r and p'_0 whilst the rate of G/G_0 degradation is negatively proportional to D_r and p'_0. However, conclusions from studies investigating C_u and d_{50} have been contradictory. Wichtmann

and Triantafyllidis (2009) performed RC tests on clean sands and found that G_0 was independent from d_{50} and decreased with C_u, as supported by Yang and Gu (2013) who performed BE tests on glass beads of various sand sizes and Gu et al. (2021) who performed BE tests on glass beads and a clean sand. However, Chen et al (2019) who performed Hollow Cylinder tests on different sand-gravel mixtures and Gabryś et al. (2021) who conducted BE experiments on a range of coarse sands noted a positive relationship between C_u and G_0. Additionally, Menq (2003) who studied clean sands and sand-gravel mixtures observed a positive relationship between d_{50} and G_0. Similarly contradictory findings have been reported for G/G_0. RC tests performed by Wichtmann and Triantafyllidis (2013) on clean sands demonstrated that increasing C_u increased the rate of G/G_0 degradation (i.e., reduce reference shear strain, γ_r) whilst results from Chen et al. (2019) indicated that γ_r was relatively independent of C_u for C_u >10. Arrango (2006) and Liu et al. (2018) showed that G_0 of carbonate soils was higher than that of silica sands and the rate of G/G_0 degradation was faster in carbonate soils than in silica soils despite both exhibiting identical particle size distribution and being tested under identical conditions. These contradictory findings indicate that G_0 and G/G_0 are influenced by factors beyond D_r, p'_0, C_u, and d_{50} alone.

Recently, several researchers including, Menq (2003), Wichtmann and Triantafyllidis (2009), Payan et al. (2016), Oztoprak and Bolton (2013), Senetakis (2013) and Upreti and Leong (2020) have proposed empirical models to predict G_0 and G/G_0. Such models have developed based on published stiffness data, relying on relationships between model parameters and soil properties, D_r, p'_0, C_u, and d_{50}. Oztoprak and Bolton (2013) additionally considered a term describing soil elasticity in their model. However, conflicting experimental findings suggest that careful consideration of these models when applied to wide range of cohesionless soils is necessary in practice. A literature survey

was therefore undertaken to investigate the main mechanisms governing G_0, G/G_0 and threshold strains of cohesionless soil and offers explanation for discrepancies in published literature, thus providing guidance on the models' applicability for different soils.

The review of existing databases and correlations indicate that G_0 and G/G_0 across a wide strain range are predominantly affected by D_r, p'_0, C_u, and d_{50}, these are discussed in detail in Section 3.2.2 and Section 3.2.3. However, the stiffness behaviour within the small-strain region requires investigation, in particular the bounds of linearity and elasticity of such soils remain relatively unexplored and often overlooked in G/G_0 models. This study presents an experimental investigation using the RCA on three cohesionless soil types: two representing typical offshore sands and one quarry sand, serving as a reference. The influence of D_r, p'_0, and material type on G_0, G/G_0, γ_{tl} and γ_{tv} are explored and the suitability of the existing empirical models to examined sands are discussed. The aim of this work is to provide a deeper understanding of the mechanisms that influence in the small-strain stiffness region and to assess how these findings impact the calibration of empirical models and the determination of constitutive model inputs, which are essential for geotechnical design applications.

3.2 Review of published trends

The development of the RCA and other measurement techniques have allowed for reliable determination of G_0 and G/G_0 of soils in the small-strain range. Medium to large strain stiffness behaviour can be precisely assessed using element testing apparatuses such as Torsional Shear (TS), Torsional Simple Shear (TSS), Triaxial (TXT), and Direct Simple Shear (DSS). A comprehensive review of published experimental trends conducted by other researchers utilising these devices has informed the focus of investigation in this study. G_0 and G/G_0 are considered separately with the aim of determining the physical

mechanisms that govern each parameter and reviewing the performance of existing empirical models that describe them.

3.2.1 Database of stiffness tests

In this study, 840 test results from 53 references were digitised and collated to create a database of stiffness behaviour. The stiffness database builds upon the database by Oztoprak and Bolton (2013), including more recent experimental data that have been published. However, several references in the original database were not included due to difficulty with sourcing original data. A summary of the references with selected information from the database is presented in Table 3-1. The database includes tests conducted on silica and carbonate sands and across a large range of sand/gravel gradings – totalling 108 unique sand and gravel types. Specimens were prepared using several preparation techniques including, moist tamping, dry tamping, wet pluviation, air pluviaion and vibration, some specimens were also tested undisturbed using advanced sampling methods. Chapter 2 highlights the impact of sample preparation G_0 and G/G_0 which should be considered when analysis the results of the database. Such tests were tested under differing testing conditions and with different equipment. Although data was predominantly sourced from the RCA and the TS, DSS and TX devices are also often used to characterise G_0 and G/G_0 and are also included on this study. Figure 3-1(a) to (i) throughout illustrate the scope of the database in this research and presents a comparison with the stiffness database collated by Oztoprak and Bolton (2013). The tests collated in this study mostly fell within the parameter space investigated by Oztoprak and Bolton (2013). However, this database included significantly more fines, fine-mixtures, gravel, and gravel-mixtures, therefore, a greater range of C_u and d_{50} are investigated compared to the original database, see Figure 3-1(a), (d) and (i).

Table 3-1 Summary of database used in this study

Material	Test type/conditions	Investigated parameters	Sample preparation	Reference
Ottawa sand 20/30	RCT+TST dry	D_r OCR, stress ratio, p'_0	Air pluviation	Alarcon-Guzman et al. (1989)
Toyura sand	TST saturated	D_r, p'_0	Air pluviation	Altun and Goktepe (2006)
Berlin sand	RCT	D_r, OCR, no. cycles, p'_0	Dry tamping/Air pluviation	Bai (2010)
Clean sand	BE dry + saturated	D_r, d_{50}, saturation	-	Bartake and Singh (2007)
Leighton buzzard sand	RCT+CLTST dry	D_r, p'_0, test method	Air pluviation	Cavallaro et al. (2001)
Siliceous and carbonate sands	RCT, dry	D_r, p'_0	Air pluviation	Cataño-Arango (2006)
Sand and gravel mix	RCT saturated	D_r, e, $F.C$, $G.C$ K_0 p'_0	Moist tamping	Chen et al. (2019)
Monterey No.0 sand	RCT + HCT dry	p'_0, test method	Dry tamping	Chung et al. (1984)
Natural sands	RCT dry	D_r, e, p'_0	Air pluviation	Dammala et al. (2017)
Fontainebleau sand	RCT + CLTXT	p'_0	Air pluviation	Delfosse-Ribay et al. (2004)
Hime gravel	MLTXT	D_r, d_{50}, C_u	Dry tamping	Dong (1994)
Toyura sand + silica sands	RCT dry + saturated	D_r, sand types, viscosity	Air pluviation	Ellis et al. (2000)
Quiou sand	RCT saturated	D_r	-	Fioravante et al. (1994)
Quartz sand	RCT saturated	p'_0, d_{50}, C_u	Moist tamping	Gabryś et al. (2021)
Gravel	CLTXT	D_r, sample quality	Unidsturbed	Goto et al. (1992)
Rhein sand	TXT saturated	e, grain shape, stress state, p'_0	Air pluviation	Gu et al. (2021)
Clean sands	CLSST dry	p'_0	-	Hardin and Drnevich (1972b)
Clean sands	CLSST dry	p'_0	-	Hardin and Drnevich (1972a)

Ottawa sand	RCT dry + saturated	D_r, p'_0, G.C,		Hardin and Kalinski (2005)
Monterey No.0 sand, Ohgi-shima sand, Toyura sand	RCT+TST dry + saturated	D_r, p'_0	Moist tamping/Air pluviation.	Iwasaki et al. (1978)
Ottawa sand	BE dry + saturated	D_r, p'_0, saturation		Kim et al. (2021)
Toyura sand	CLTXT saturated	p'_0 G.C,	Vibration	Kokusho (1980)
Toyura sand	CLTXT saturated	p'_0	-	Kokusho and Esashi (1981)
Sand	DSST, dry	D_r, p'_0, OCR	-	Lanzo et al. (1997)
Leighton buzzard sand	RCT saturated	D_r, no. cycles, p'_0	Air pluviation	Li and Cai (1999)
Siliceous sands	RCT saturated	D_{50}, sand types, p'_0	Moist tamping	Liang et al. (2021)
Siliceous and carbonate sands	RCT saturated	D_r, sand types, p'_0	Dry tamping	Liu et al. (2020)
Toyura sand	DSST dry	e, OCR, p'_0	Air pluviation	Lo Presti et al. (1997)
Ottawa sand	RCT+CLTXT	D_r, p'_0	Dry tamping	Maher et al. (1994)
Ottawa sand	RCT+CLTXT saturated	p'_0	Air pluviation	El Mohtar et al. (2013)
Gravelly sands	RCT saturated	C_u, c_{50}, e	Moist tamping	Menq (2003)
Natural sands	RCT+TST saturated	sand types, p'_0	Air pluviation	Molina-Gómez et al. (2020)
Ottawa sands	RCT saturated	D_r, e, p'_0	Moist tamping	Patiño et al. (2020)
Sydney sand	RCT dry	C_u, D_r, e, p'_0	Vibration	Payan, Senetakis, et al. (2016)
Clean coral sand	RCT saturated	D_r, e, F.C, p'_0	Air pluviation	Qi et al. (2022)
Sand and gravelly sand	RCT, saturated	D_r, p'_0	-	Rollins et al. (1998)
Monterey sand	RCT, saturated	D_r, p'_0	Dry tamping	Saxena et al. (1988)
Gravel	CLTXT	D_r	-	Seed et al. (1986)
				Senetakis et al. (2013)

Higashi-Ohgijima	CLTXT	p'_0, sampling depth	Undisturbed	Shibuya et al. (1992)
Clean sand	TXT	D_r, p'_0, d_{50}, C_u	Air pluvitation	Tika et al. (2003)
Clean sand	CLTXT, dry	D_{50}	Air pluviation and dry tamping	Upreti and Leong (2020)
Metramo silty sand	RCT, saturated	D_r, saturation		Vinale et al. (1999)
Ottawa sand, Toyura sand	RCT dry	Ageing, D_r, e, p'_0	Moist tamping	Wang and Tsui (2009)
Doresten sand	RCT dry	D_r, p'_0, Cu	Air pluviation	Wichtmann and Triantafyllidis (2013)
Dorsten sand	RCT dry	D_r, p'_0, d_{50}, C_u	Air pluviation	Wichtmann et al. (2015)
Gigashi-Ohgishima sand	CLTXT+CLTST	Drainage, p'_0	-	Yamashita et al. (1997)
Toyura sand	RCT, saturated	D_r, e, p'_0	Moist tamping	Yang and Liu (2016)
Gravels	CLTSST	p'_0	Dry tamping	Yasuda and Matsumoto (1993)
Gravels	CLTXT	D_r, p'_0, d_{50}, C_u	Vibration	Yasuda and Matsumoto (1994)
Gravels	MLTXT, CLTXT	p'_0	Unidsturbed	Yasuda et al. (1996)

*CL – Cyclic loading ML – Monotonic loading BE – Bender element RCT – Resonant column Test, TSST – Torsional simple shear test, TST – torsional shear test, TXT – triaxial test, SST – Simple shear test

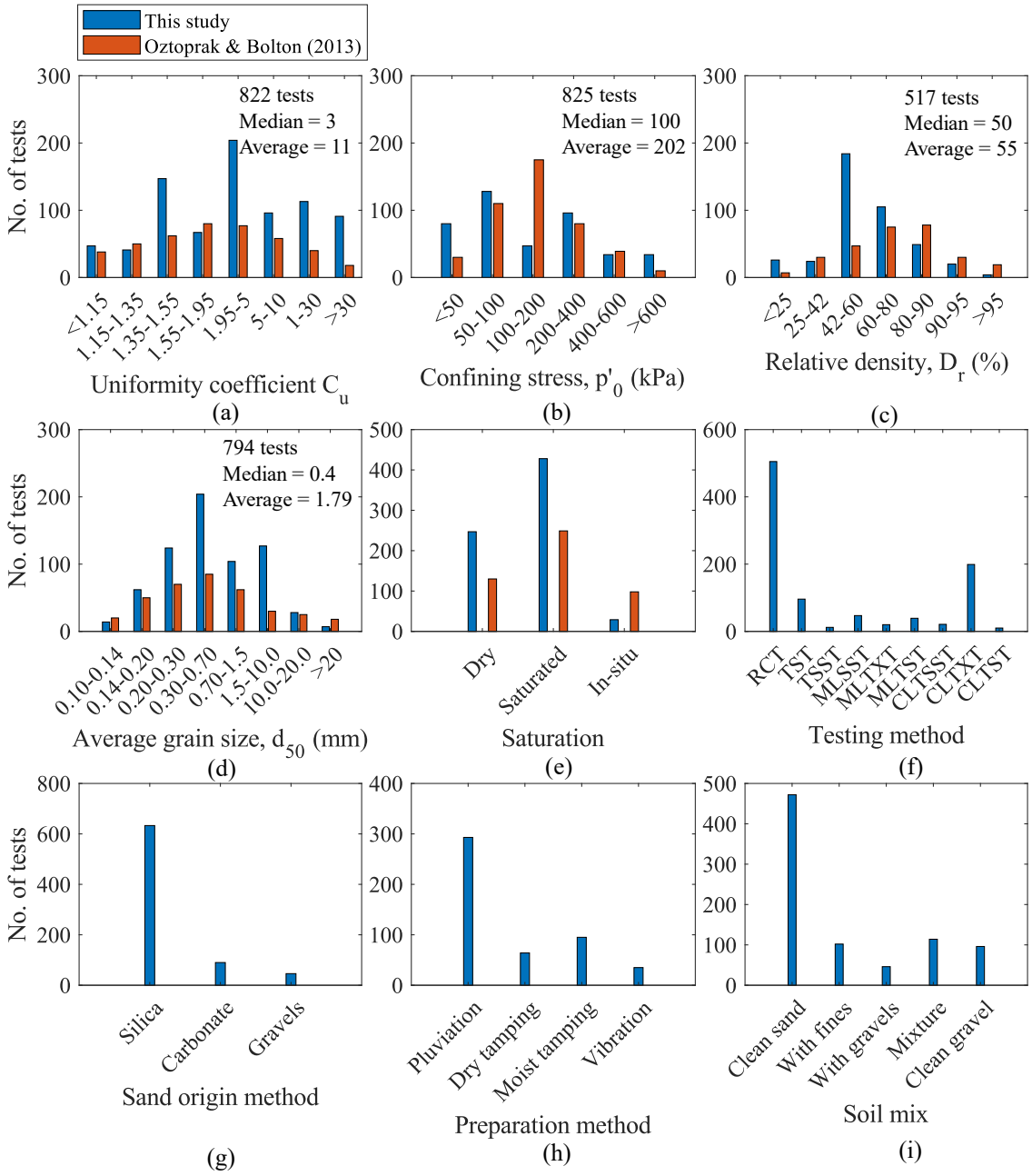


Figure 3-1 Statistical information from database (a) C_u; (b) p'_0; (c) D_r; (d) d_{50}; (e) saturation (f) testing method; (g) sand origin; (h) preparation method; and (i) soil grading

Key parameters extracted were G_0 and, $\gamma_{0.7}$, representing initial shear stiffness and a threshold strain parameter that describes the degradation rate respectively. γ_{tl} and γ_{tv} were not always published but were collected where applicable. The influence of confining pressure, p'_0, relative density D_r, coefficient of uniformity C_u and average grain size d_{50} on the stiffness parameters of cohesionless soils is recognised and these quantities have been recorded, See Figure 3-2(a) to (h) throughout for the trends in the database.

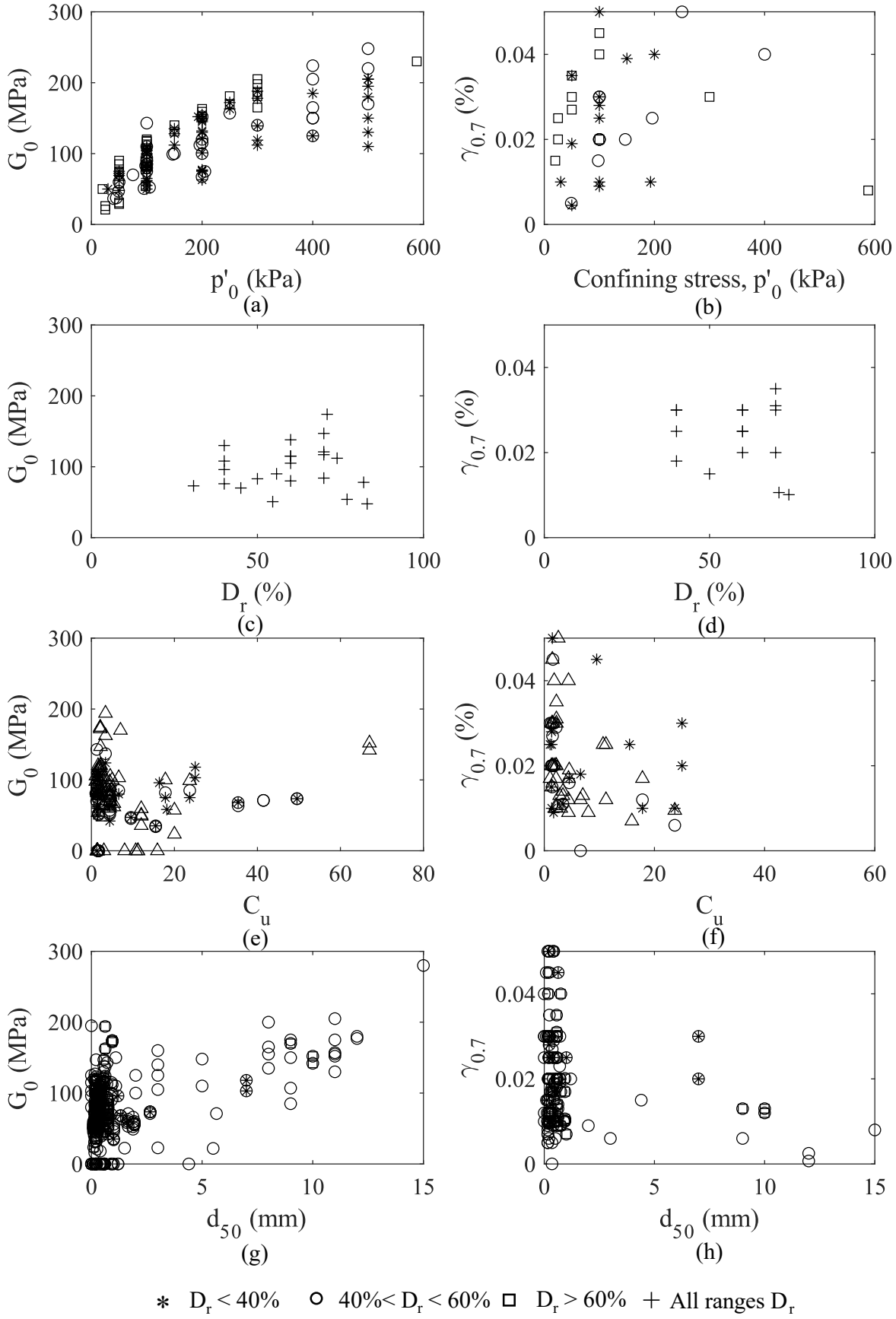


Figure 3-2 Trends in G_0 from the database (a) G_0 with p'_0 ; (b) $\gamma_{0.7}$ with p'_0; (c) G_0 with D_r; (d) $\gamma_{0.7}$ with D_r; (e) G_0 with C_u ; (f) $\gamma_{0.7}$ with C_u ; (e) G_0 with d_{50} ; and (d) $\gamma_{0.7}$ with d_{50}

Although less studies have been focused on investigating anisotropy, characterised by K_0, gravel content, *G.C* and fines content, *F.C*, they are also seen to have marked influence stiffness parameters, see Figure 3-3(a) to (d) throughout for trends associated with these parameters, G_0 has been normalised with p'_0 to reduce scatter in the figures.

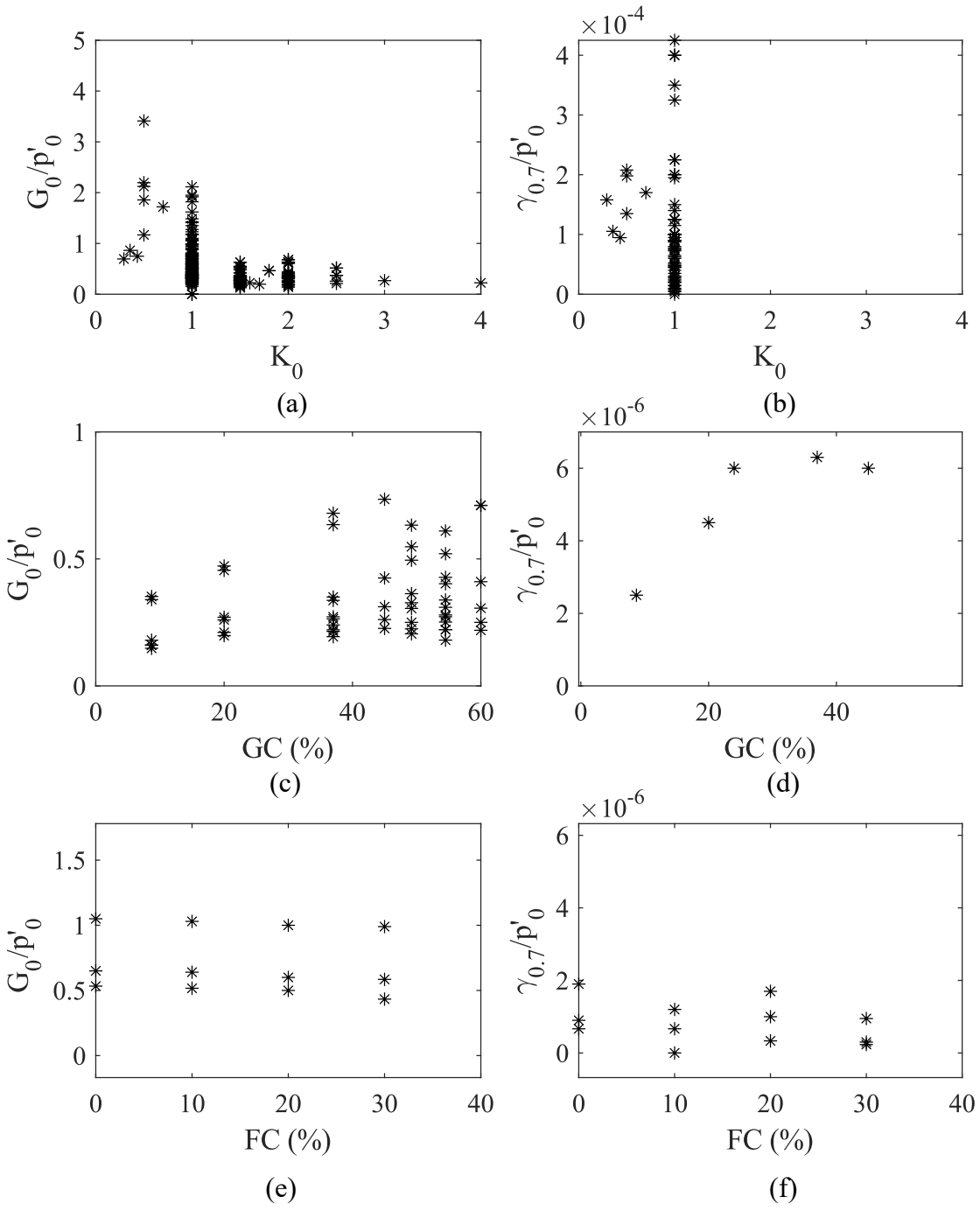


Figure 3-3 Trends G_0/p'_0 from database (a) G_0/p_0 with K_0; (b) $\gamma_{0.7}$ with p'_0; (c) G_0/p'_0 with *F.C*; (d) $\gamma_{0.7}$ with *G.C*; (e) G_0 with *F.C* ; and (f) $\gamma_{0.7}$ with *F.C*

A degree of scatter is evident in the trends above. G_0 shows a positive correlation with p'_0, D_r, $G.C$ and negatively correlated with $F.C$ and K_0. G_0 is negatively correlated with C_u for C_u< 10 however for C_u < 10, a positive relationship between the parameters is seen. G_0 is relatively independent of d_{50} for d_{50} < 3 however a strong positive correlation exists for and d_{50} > 3. The degradation parameter, $\gamma_{0.7}$ shows a large amount of scatter against all examined properties. A positive relationship between $\gamma_{0.7}$ with p'_0 and a negative relationship between $\gamma_{0.7}$ and $F.C$ can be confidently deduced. Although the variation of $\gamma_{0.7}$ with C_u is generally negative, considerable scatter is present. It appears $\gamma_{0.7}$ is independent of d_{50} for d_{50} < 3 however, a negative relationship between the two parameters is evident for d_{50} > 3. To understand the mechanisms that influence G_0 and G/G_0 in more detail. The relevant studies, their findings and current proposed empirical models for practice are herein discussed.

3.2.2 Parametric study on G_0

G_0 is a critical geotechnical design parameter and has been the focus on many previous studies. Hardin and Black (1966) demonstrated the influence of p'_0, e on G_0 and proposed the following empirical equation:

$$G_0 = A \cdot F(e) \cdot \left(\frac{p'_0}{P_a}\right)^m \tag{3-1}$$

Where p'_0 is the mean effective stress, P_a is a reference stress, generally taken as ambient atmospheric pressure, $F(e)$ is a function that describes e and A and m are soil specific fitting parameters derived from linear regression applied to experimental results.

Natural sands tend to include a certain amount of fines content $(F.C)$ and gravel content $(G.C)$ that can impact on their stiffness behaviour but is not captured by Equation (3-1). Controlled experimental studies by Wichtmann et al. (2015) and Yang and Liu (2016) suggest that $F.C$ has a negative correlation with G_0. Chen et al. (2019) and Xu et al. (2019) demonstrate that $G.C$ has a positive correlation with G_0, these trends are consistent with those in the stiffness database (See Figure 3-3(b) and (c)).

Equally G_0 can be influenced by the particle size distribution of cohesionless soils typically characterised by, d_{50} and C_u. Studies investigating the influence of C_u and d_{50} exhibit a complex relationship between these parameters and G_0. Wichtmann and Triantafyllidis (2009) found that for clean sands G_0 was independent of d_{50} for 0.1 mm < d_{50} < 6 mm and observed a negative relationship between G_0 with C_u, a conclusion corroborated by BE experiments on glass beads by Yang and Gu (2013) and glass beads and clean sands by Gu et al. (2021). Studies by Menq (2003) and by Gabryś et al. (2021) demonstrate that whilst this conclusion is appropriate for cohesionless soils with particle sizes within the sand gradation only, for sand-gravel mixtures, d_{50} and C_u is positively correlated with G_0 as the introduction of gravels (which in turn increases d_{50} and C_u) in a cohesionless soil mix acts to increase G_0 as previously mentioned – this also corroborates trends in this database, see Figure 3-2.

Results from previous experimental programmes have been used to propose new $F(e)$ functions for cohesionless soils. Additionally, there have been attempts to connect the fitting parameters from Equation (3-1) to these additional soil properties. A summary of these proposed functions is presented in Table 3-2 below. The original Hardin and Richart (1963) formulation is also shown here for comparison. The overall trends of G_0 based on these functions are presented in Figure 3-4(a) to (d) throughout, the corresponding data from this database is also shown on the figures.

Table 3-2 Proposed empirical equations for G_0

Material	**F(e)**	**A***	**m**	**Reference**
Crushed	$(2.97-e)^2/(1+e)$	3300	0.5	Hardin and Richart (1963)
Ottawa sand	$(2.17-e)^2/(1+e)$	7000	0.5	
Sand/gravel	$e^{-1}-(d_{50}/20)^{0.75}$	$6710C_u^{-0.2}$	$0.48C_u^{0.09}$	Menq (2003)
Quartz	$1.94e^{-0.066Cu}$	$1563+3.13C_u^{2.89}$	$0.4C_u^{0.18}$	Witchtmann and Triantafyllidis (2009)
General	$e^{-1.29}$	$8400C_u^{-0.14\rho 0.68}$	$C_u^{0.12}(-0.23\rho+0.59)$	Payan, Khoshghalb, et al. (2016)

* In kPA

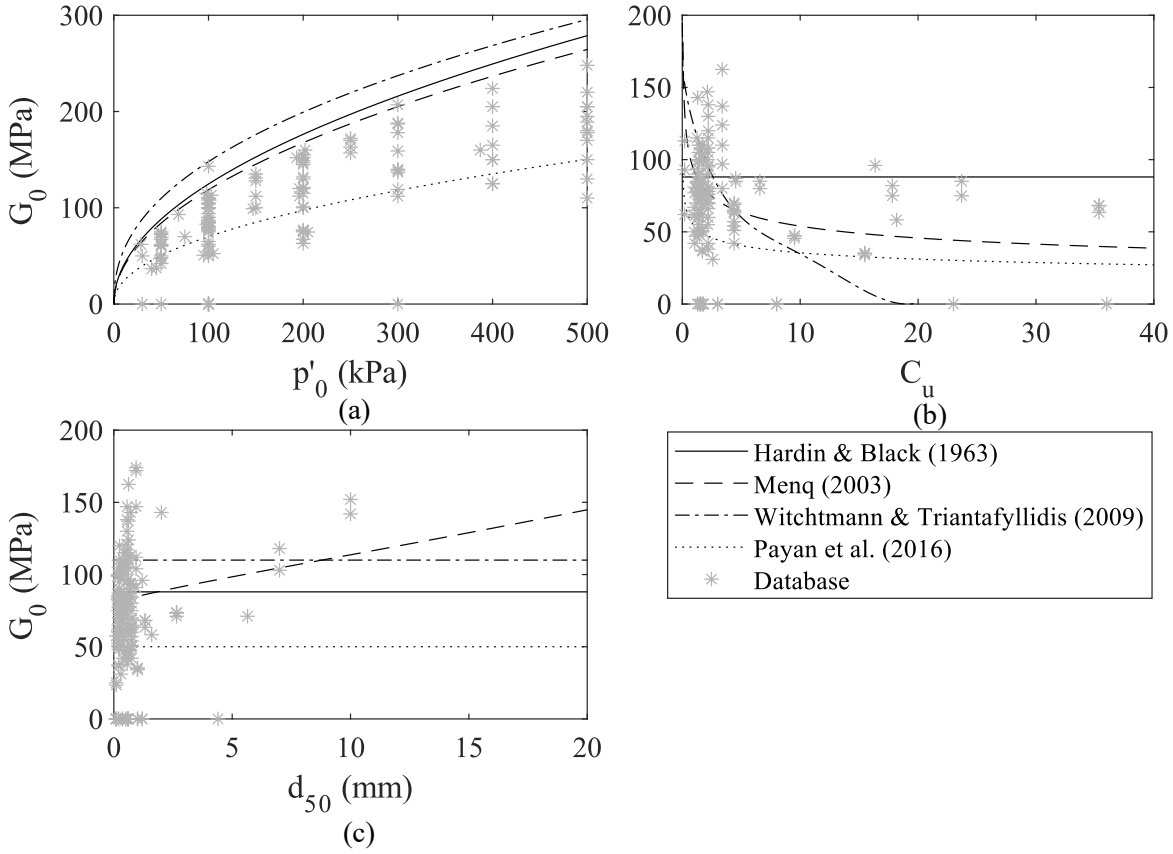


Figure 3-4 Proposed trends in G_0 from database with respect with (a) p'_0 (for $D_r < 65\%$, $d_{50} < 2$ and $C_u < 2$) ; (b) C_u; (for $D_r < 65\%$, $d_{50} < 2$ and $p'_0 < 150$kPa) and (c) d_{50} (for $D_r < 65\%$, $c_u < 2$ and $p'_0 < 150$kPa)

It appears that the original Hardin and Black (1966) equation for describing G_0 does not adequately describe the variation of G_0 across the parameter space in the database, see Table 3-2. Most notably, the function cannot capture the variance in G_0 due to C_u, see Figure 3-4(b). The recently developed functions more adequately describe the variation by incorporating the effects of C_u, and all three functions perform better than the original equation. It is worth remembering here that increasing C_u can be achieved by increasing $G.C$ or $F.C$, with the former increasing G_0 and the latter decreasing G_0. Following this line of thought, increasing C_u can therefore have both a positive and negative influence with $G0$ depending on whether the sand's constituents are fines or gravels. This delineation is not accounted for in any of these relationships which only display a negative relationship between C_u and G_0.

However, the function by Menq (2003) does show variation in G_0 with d_{50} which attempts to take into the account of $G.C$ of the soil mixture. A slight positive correlation

between d_{50} and G_0 is shown in Figure 3-4(c) which follows the trends in the stiffness database. It appears the consensus reached by previous researchers is that G_0 is independent of d_{50} which seems to be valid for clean sands but not for sand mixtures.

Whilst the above empirical relationships may be appropriate to describe cohesionless soils mostly within the sand grading, they likely are not well calibrated to natural sands across a wide grading. This effect is explored further by examining more data from this stiffness database. Several forms of $F(e)$ have been developed for cohesionless soils. The G_0 data from the stiffness database were fitted to the functions of $F(e)$ in Table 3-2 and normalised against the equation that produced the highest R^2 value corresponding with $F(e) = e^{-1.29}$. The variation of $G_0/F(e)$ with p'_0, C_u and d_{50} from all the data from the stiffness database is displayed in Figure 3-5(a) to (d) throughout.

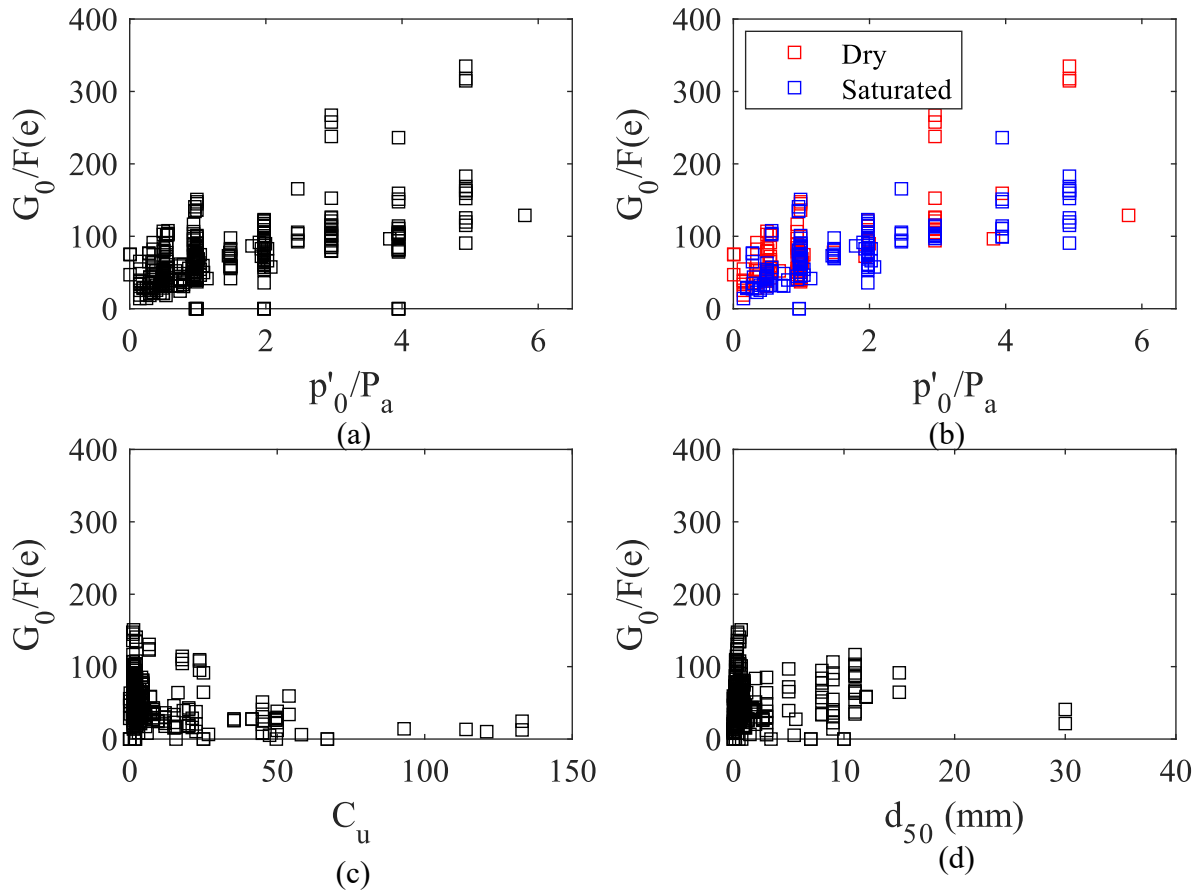


Figure 3-5 $G_0/F(e)$ with respect with (a) p'_0; (b) p'_0 showing effects of saturation; (c) C_u; and (d) d_{50}

Despite normalisation of G_0 with $F(e)$, results from Figure 3-5 display a fair amount of scatter

in trends associated with $G_0/F(e)$ from different tests. This indicates that G_0 is a function of more than p'_0, and e alone, reiterating that the general equation that describes G_0 is not sufficient. Figure 3-5(b) shows that $G_0/F(e)$ measurements obtained dry conditions are slightly higher than those from saturated conditions, however the effects are minor. Studies by Bartake and Singh (2007) and Kim et al. (2021) have compared the dry and saturated response and have also observed higher G_0 measurements for specimen tested in dry conditions compared to saturated. Although, a general negative trend between $G_0/F(e)$ and C_u can be observed from Figure 3-5 (c), however there is a fair amount of scatter, and a high C_u value is often associated with a high G_0 Figure 3-5(d) shows that $G_0/F(e)$ is mostly independent of d_{50} for $d_{50} < 2$ however there a positive relationship between the two exist for $d_{50} > 2$. Data collected outside the parameter space of the functions in Table 3-2, particularly sand-gravel mixtures do not follow the trends by Wichtmann and Triantafyllidis (2009) and Payan et al. (2016). The relationship by Menq (2003) attempts to account for differences in stiffness behaviours of sand-gravel mixtures by incorporating a term for d_{50}. Despite so, all proposed functions input C_u as a continuous parameter do not delineate the effects of $F.C$ and $G.C$ which both increase C_u but have contradicting impact on G_0.

Results demonstrate that caution should be taken when applying previously developed empirical equations for G_0 outside the parameter space of the individual studies. Consideration towards the sand's origin and characteristics is necessary, and re-calibration of Equation (3-1) may be required for cohesionless soils that have properties outside the parameter space of the previous studies, especially natural sands with gravel and/or fine content and carbonate sands.

3.2.3 Parametric study on stiffness degradation

Relationships describing G/G_0 degradation have also been developed in the scientific community. Stiffness degradation is generally expressed through a normalised stiffness value

that develops with shear strain. Hardin and Drnevich (1972b), proposed the following hyperbolic model to describe G/G_0 degradation:

$$\frac{G}{G_0} = \frac{1}{1 + \frac{\gamma}{\gamma_{ref}}} \tag{3-2}$$

Where, G/G_0 = the normalised shear stiffness, γ = applied shear strain, $\gamma_{ref} = \tau_{max}/G_0$ and represents the shear strain at failure. More recently, researchers have recommended a modified hyperbolic function raised to an exponent α to allow for a more accurate experimental fit (Vardanega and Bolton 2013; Menq 2003; Okur and Ansal 2007; Darendeli 2001; Zhang et al. 2005). The modified hyperbolic function takes the following form:

$$\frac{G}{G_0} = \frac{1}{1 + \left(\frac{\gamma}{\gamma_r}\right)^{\alpha}} \tag{3-3}$$

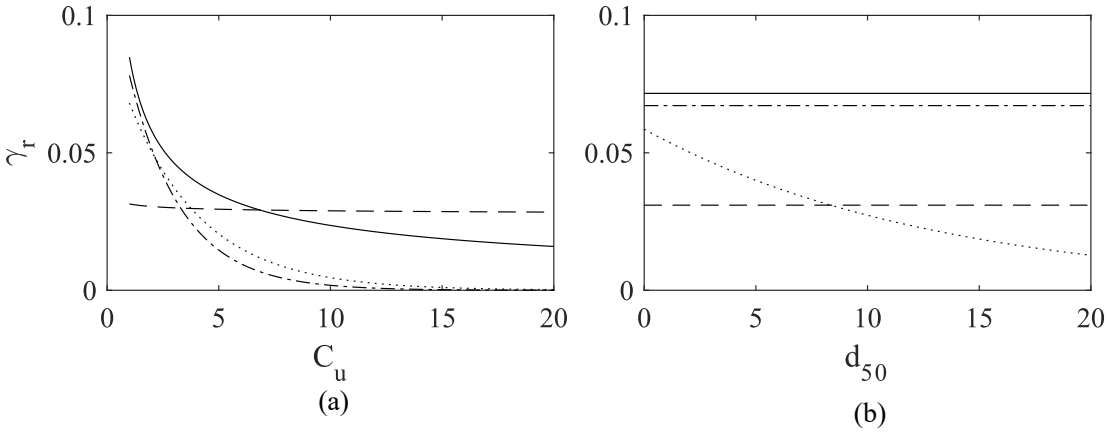
Where, γ_r = the reference strain and is equal to the strain at $G/G_0 = 0.5$. Substantial literature has focused on measuring the stiffness degradation of cohesionless soils to produce correlations between the γ_r and α with sand properties, C_u, d_{50}, e and D_r.

Menq (2003) undertook 59 resonant column tests on sands and gravels and observed a negative relationship between C_u and G/G_0. Wichtmann and Triantafyllidis (2013) conducted a series of experiments on 27 clean sands and likewise concluded a negative correlation between C_u and G/G_0 and a slight negative correlation between d_{50} and G/G_0. Oztoprak and Bolton (2013) developed a new hyperbolic model using a stiffness database of 454 tests on sand, similarly noting the same influence of C_u and also a positive relationship between D_r and G/G_0. Upreti and Leong (2019) concluded a negative correlation between d_{50} and G/G_0. Across all research activities, a clear positive relationship between p'_0 and G/G_0 was identified. Following from these experimental and data driven studies, several empirical relationships between sand specific properties and model parameters, γ_r and α have been developed. A

summary of these proposed empirical stiffness degradation models presented in Table 3-3-3 below. The trends captured by these models are presented in Figure 3-6(a) to (d) throughout.

Table 3-3-3 Proposed empirical models for stiffness degradation

Material	Form of equation	Parameter	Reference
Sand	$\frac{G}{G_0}=\frac{1}{1+\frac{\gamma}{\gamma_{ref}}}$	$\gamma_{ref}=\tau_{max}/G_0$ where τ_{max} is the maximum shear strength	Hardin and Drenvich (1972)
Sand/gravel	$\frac{G}{G_0}=\frac{1}{1+\left(\frac{\gamma}{\gamma_r}\right)^a}$	$\gamma_r=0.12\times C_u^{-0.6}\times\left(\frac{p'_0}{P_a}\right)^{0.5\times C_u^{-0.15}}$ $a=0.86+0.1\times\log\left(\frac{p'_0}{P_a}\right)$	(Menq 2003)
Sands	$\frac{G}{G_0}=\frac{1}{1+\left(\frac{\gamma-\gamma_e}{\gamma_r}\right)^\alpha}$	$\gamma_r=0.01C_u^{-0.3}\left(\frac{p'_0}{P_a}\right)+0.08eD_r$ $\gamma_{tv}=0.0002+0.0012\gamma_r$ $\alpha=C^{-0.075}$	Oztoprak and Bolton (2013)
Quartz sand	$\frac{G}{G_0}=\frac{1}{1+\frac{\gamma}{\gamma_r}}$	$\gamma_r=0.159\exp(-0.419C_u)\left(\frac{p'_0}{P_a}\right)^{0.42}$	Senetakis et al. (2013)
Sands	$\frac{G}{G_0}=\frac{1}{1+\left(\frac{\gamma}{\gamma_r}\right)^\alpha}$	$\gamma_r=0.13e^{-7640\left(\frac{d_{50}}{\frac{P_a}{\gamma_w}}\right)-0.3C_u}\left(\frac{p'_0}{P_a}\right)^{0.5}$ $\alpha=0.32-0.17\log\left(\frac{p_0{}'}{P_a}\right)$	Upreti and Leong (2019)



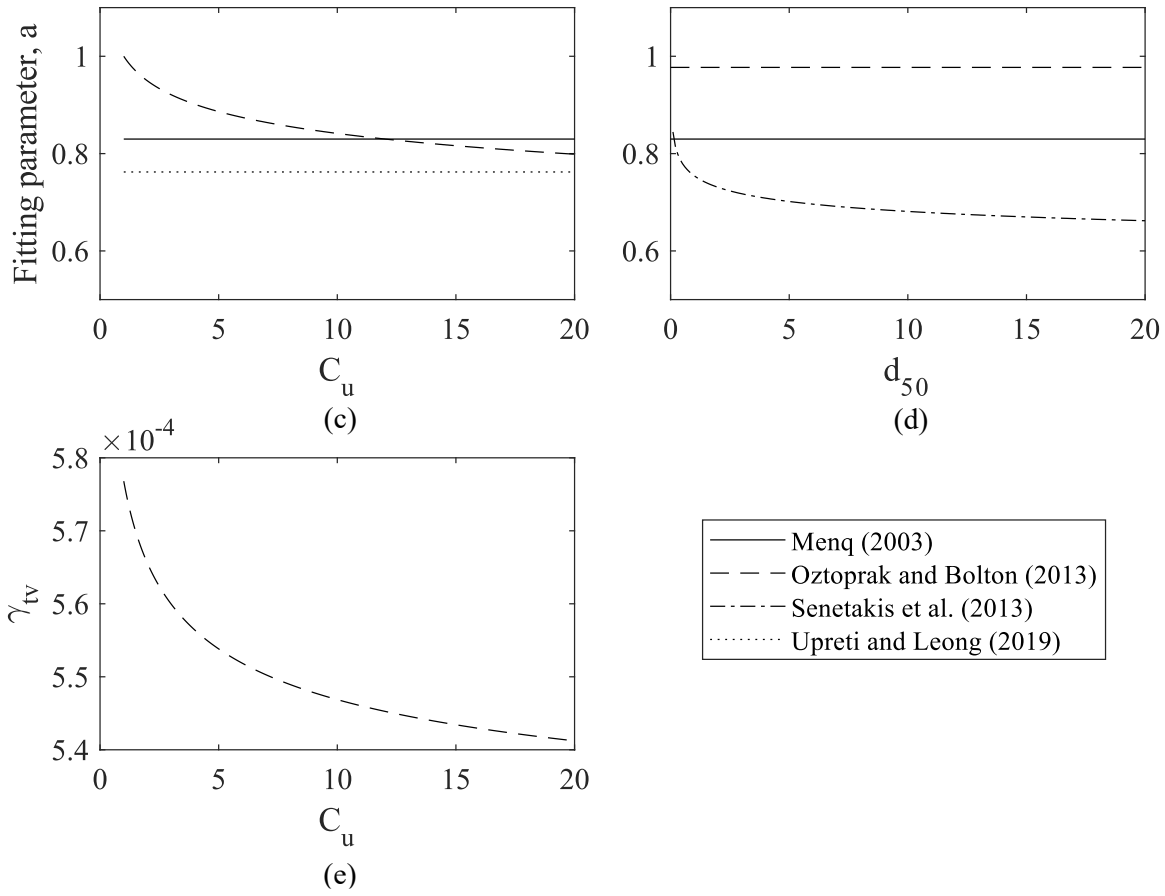


Figure 3-6 Variation of G/G_0 degradation model parameters by previous researchers (a) γ_r with respect to C_u; (b) γ_r with respect to d_{50}; (c) a with respect to C_u; (d) a with respect to d_{50}; and (e) γ_{tv} with respect to C_u

The original form of the equation to describe G/G_0 by Hardin and Drenvich (1972b) does not consider the influence soil properties on the degradation response and would require calibration for each new soil type and thus is not presented in Figure 3-6. Recent expressions for G/G_0 demonstrate a negative trend between C_u and rate of G/G_0 degradation. Oztoprak and Bolton (2013) presents an additional fitting term to their expression, the elastic threshold strain, γ_{tv} which enables the expression to cover cementation and interlocking effects at small strains. The expression by Upreti and Leong (2019) includes d_{50} in empirical relationships for γ_r and α and demonstrates a negative relationship between d_{50} and the rate of G/G_0 degradation, which is not accounted for by other models, this trend is also seen for certain parameter spaces in the stiffness database of this study (See Figure 3-2(g)).

The γ_r could not be consistently obtained for many of the tests in the stiffness database as most RCA tests were terminated at $G/G_0 > 0.5$ and many studies did not publish a. Therefore, it is difficult to assess the performance of models presented in Table 3-3 against the stiffness database in this study. Trends in $\gamma_{0.7}$ have already been presented and discussed in Section 3.2.2 (see Figure 3-2 and Figure 3-3). The trends mostly coincide with expected behaviour captured by empirical models. Despite so, several interesting inconsistencies between published stiffness trends and theoretical stiffness behaviour were identified and herein discussed.

3.2.4 Key observations

Chen et al. (2019) experimentally investigated the influence of $G.C$ on G_0 and G/G_0. Results from their study indicated a negative correlation between C_u and γ_r. However, for $C_u > 10$, values of γ_r appeared independent of C_u. This is contradictory to behaviour published in Wichtmann and Triantafyllidis (2013). A clear difference between the two studies was that the former changed C_u by increase $F.C$ and/or $G.C$ whilst the latter artificially altered C_u without by changing *F.C or G.C.* Similar conclusions from Section 3.2.2 can be reiterated here, that the delineation between clean sands and natural sands with $F.C$ and $G.C$ are not adequately addressed in G_0 and G/G_0 models as much of the stiffness data published refers to sands with $C_u < 5$. Thus, behaviour across a larger range of C_u, particularly when $G.C$ and $F.C$ are varied, is relatively non-conclusive.

Studies by Arango (2006) and Liu et al. (2021) demonstrate the importance of the chemical constituents of sand for G_0 and G/G_0 degradation measurements. Both studies investigated two sands (siliceous and carbonate), maintaining p'_0, C_u, D_r, and testing conditions constant. They observed the G/G_0 degradation response of the siliceous and carbonate varied. In both studies, the siliceous sand produced a lower nominal value of G_0 and a higher $\gamma_{0.7}$ value. Observations from stiffness database show that carbonate sands typically have a higher specific gravity, ($G_s \sim 2.8$) compared to siliceous sands ($G_s \sim 2.6$) which could be a potential reason for

the discrepancy in G_0 and G/G_0 degradation. This suggests that the properties used to calibrate the empirical models may not be sufficient to capture stiffness behaviour when used outside their calibration space.

Bai (2010) investigated the G/G_0 degradation of Berlin sand across p'_0 and D_r. For a constant D_r it was observed that a higher p'_0 produced lower values of γ_{tv} on several occasions. Similarly, experiments by Qi et al. (2022) and Liang et al. (2021) show that for sands tested constant D_r, increasing p'_0 did not consistently increase $\gamma_{0.7}$ as expected and suggests that $\gamma_{0.7}$ is independent of p'_0. These studies demonstrate trends inconsistent to expected behaviour from current theoretical frameworks, however it is not clear why this is the case.

The results published by various researchers indicate that certain experimental results (approximately 20% of this database) obtained a stiffness response that did not precisely reflect theoretical predictions by the models summarised in Table 3-2 and Table 3-3. These discrepancies can be accounted for due to differences in the test material, i.e., vastly different grading of sands (sand mixtures versus clean sands) and different chemical constituents. However, in other situations, the sources of these discrepancies remain unclear and require further investigation.

This suggests that the empirical models describing G_0 and G/G_0 by Menq (2003), Wichtmann and Trianfyddlis (2009), Senetakis et al. (2013), Payal et al. (2016) and Upreti and Leong (2020) are limited to the calibration space of their respective studies. It has been shown in Section 3.2.2 and 3.2.3, that outside the parameter spaces of these models, they do not necessarily accurately predict the G_0 and G/G_0 response.

The generalised models describing G/G_0 by Oztoprak and Bolton (2013) are an improvement on these models as they can be applied on a wider range of soil and account for soil elasticity. The model was developed considering large stiffness data from a range of published data on cohesionless soils. Whilst the models on average have been proven to

perform well against experimental data, there are several aspects that these models do not account for and are summarised below:

1. Sand-gravel and sand-fines are included in the stiffness database that the expressions were calibrated to, however, there is no delineation between clean sands or natural sands (i.e., sands with varying *F.C* and *G.C*) in the model or terms of the model. The model only uses a singular parameter, C_u to consider particle size distribution, however it has been shown in Section 3.2.2, depending on whether the soil examined is a clean sand or sand-gravel mixture, increasing C_u has a different impact on the stiffness response. This suggests there could be some skew or biases in calibrated parameters.
2. Likewise, stiffness data from both carbonate and siliceous sands are included in the development of this model however, no distinction between sand origin is included in the model or their parameters despite the chemical constituents having a large impact on G/G_0 degradation.
3. Discrepancies in stiffness measurements and theoretical behaviour have been observed in literature as discussed above. This suggests possible experimental errors which could also skew the data or suggests additional physics that have not been accounted for.

The limitations of the empirical models describing G_0 and G/G_0 has motivated the proposed elemental testing activities presented in this Chapter which specifically seek to investigate point 3 of above. A series of RCA tests across p'_0 and D_r of three siliceous cohesionless soils has been investigated to determine the applicability of the RCA in calibrating empirical models.

3.3 Test schedule and results

The nomenclature used to identify all tests carried out in this investigation is described below and further explained in Table 3-4.

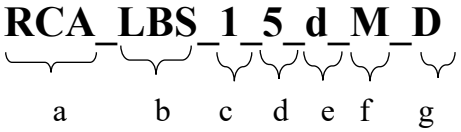


Table 3-4 Nomenclature used to identify tests

Key	Description	Nomenclature
a	Testing apparatus	RC: Resonant column
		VDDCSS: Variable direction dynamic cyclic simple shear
b	Material used	CX: Cuxhaven sand
		NE: North England sand
		LBS: Leighton Buzzard sand
c	Relative density (D_r)	Numerical value (in percent)
d	Effective confining stress or applied stress (p'_0 for RC, σ_v' for VDDCSS)	Numerical value (in kPa)
e	Saturation	s: saturated
		d: dry
f	Loading type (VDDCSS only)	M: Monotonic
		UTW: Unidirectional two way
		UOW: Unidirectional one way
		U1P: Unidirectional partial one way
		U2P_D: Unidirectional partial two way
		MD: Multidirectional
g	Drainage (VDDCSS only)	D: Drained
		U: Undrained

A total of 89 RC and 52 BE tests have been performed on three cohesionless soils at several p'_0 and D_r in this investigation. A summary of the tests and results obtained from the RC and BE tests are presented in Table 3-5. Conditions of laboratory tests RC_CX_65_10_s to RC_CX_65_10_s were undertaken at D_r = 65% to represent the sand's *in-situ* condition corroborated by CPTs from the site where the material was obtained. A range of p'_0 were tested to represent typical in-situ confining stresses experienced by offshore monopiles. Tests were undertaken at two other densities, D_r = 45% and D_r = 75%, across a similar range of p'_0 to

investigate the influence of relative density and initial state on the stiffness and degradation values of CX sand. Tests on NE sand and LBS were largely conducted under identical conditions to the tests on CX sand to facilitate a direct comparison of stiffness behaviour across the three soil types. LBS were also conducted under both dry and saturated conditions to investigate the effects of saturation. Experimental methods described in Chapter 2 were generally adopted in all RC/BE tests. However, tests RC_NE_60_10_s to RC_NE_60_150_s was carried out until the physical limit of the RCA to establish the difference between the γ_{tv} and the maximum allowable shear strain that could be induced by the RCA. Subsequent tests were terminated upon the onset of non-elastic behaviour, $\gamma = \gamma_{tv}$.

Table 3-5 Summary of resonant column and bender element test results

Test ID	$G_{0,BE}$ **(MPa)**	$G_{0,RC}$ **(MPa)**	γ_{tl} **(%)**	γ_{tv} **(%)**	G/G_0^*	**Reduction (%)**
RC_CX_45_10_s	24.3	18	0.001500	0.000020	0.93	7
RC_CX_45_20_s	30	23	0.000826	0.000014	0.94	6
RC_CX_45_30_s	39	27	0.000380	0.000042	0.87	13
RC_CX_45_40_s	46	33	0.000320	0.000019	0.90	10
RC_CX_45_50_s	49	35	0.000334	0.000036	0.89	11
RC_CX_45_80_s	57	51	0.000244	0.000040	0.90	10
RC_CX_45_100_s	62	56.5	0.000597	0.000029	0.94	6
RC_CX_45_120_s	68	62	0.000550	0.000028	0.94	6
RC_CX_45_140_s	75	66.1	0.000812	0.000027	0.95	5
RC_CX_45_160_s	77	70.4	0.001100	0.000035	0.93	7
RC_NE_45_30_s	16	14	0.00190	0.0091	0.96	4
RC_NE_45_40_s	22	21.17	0.00072	0.0057	0.93	7
RC_NE_45_50_s	27.9	24.6	0.00044	0.0037	0.92	8
RC_NE_45_60_s	30.267	28.5	0.00090	0.002	0.92	8
RC_NE_45_70_s	33.8238	31	0.00041	0.0009	0.84	16
RC_NE_45_80_s	38.02364	32.779	0.00037	-	0.85	15
RC_NE_45_100_s	40.658	35.05	0.00036	0.0029	0.87	13
RC_NE_45_110_s	42.18	37	0.00033	0.0020	0.96	4

RC_NE_45_120_s	45.3096	39.06	0.00030	0.0017	0.96	4
RC_NE_45_130_s	49.88	43	0.00041	0.0020	0.88	12
RC_NE_60_10_s	31	30	0.00085	0.0010	0.96	4
RC_NE_60_30_s	40	33.4	0.00090	0.0025	0.93	7
RC_NE_60_40_s	45	34	0.00092	0.0030	0.92	8
RC_NE_60_50_s	50	40.6	0.00093	0.0035	0.92	8
RC_NE_60_60_s	53	43	0.000100	0.0077	0.84	16
RC_NE_60_70_s	59	46	0.00110	0.0069	0.85	15
RC_NE_60_80_s	66	51	0.00098	0.0055	0.87	13
RC_NE_60_100_s	69	54	0.00099	0.0012	0.96	4
RC_NE_60_120_s	70	59	0.00098	0.0009	0.96	4
RC_NE_60_130_s	72	60	0.00053	0.0032	0.88	12
RC_NE_60_150_s	80	62	0.00034	0.0007	0.96	4
RC_NE_75_20_s	48	38.4	0.00065	0.0050	0.81	19
RC_NE_75_40_s	56	44.8	0.00070	0.0051	0.82	17.6
RC_NE_75_50_s	68	54.4	0.00088	0.0190	0.69	31
RC_NE_75_80_s	92	73.6	0.00100	0.0088	0.82	18.35
RC_NE_75_100_s	100	80	0.00100	0.0005	0.78	22
RC_LBS_28_5_d	-	18.4	0.00022	0.001	0.9	10
RC_LBS_28_10_d	-	23.7	0.00020	0.0024	0.84	16.4
RC_LBS_28_30_d	-	36.7	0.00041	0.0022	0.91	8.8
RC_LBS_28_40_d	-	40.18	0.00040	0.0030	0.89	11.3
RC_LBS_28_50_d	-	43.6	0.00070	0.0035	0.88	12
RC_LBS_28_8_d	-	53	0.00026	0.0027	0.91	9
RC_LBS_28_100_d	-	57	0.00026	0.0020	0.93	7
RC_LBS_28_150_d	-	65.7	0.00028	0.0020	0.90	10
RC_LBS_28_200_d	-	81.3	0.00051	0.0058	0.80	20
RC_LBS_45_5_s	-	10.7	0.00020	0.0028	0.87	13.5
RC_LBS_45_10_s	-	13.2	0.00093	0.0030	0.90	10.3
RC_LBS_45_20_s	-	17.9	0.00035	0.0051	0.85	15.5
RC_LBS_45_40_s	-	18.1	0.00049	0.0069	0.77	23

RC_LBS_45_50_s	-	19.9	0.00025	0.0033	0.85	15
RC_LBS_45_80_s	-	21.1	0.00020	0.0060	0.79	21
RC_LBS_45_100_s	-	22.2	0.00012	0.0026	0.86	14
RC_LBS_45_150_s	-	25.6	0.00002	0.0010	0.95	5
RC_LBS_45_200_s	-	27.7	0.00018	0.0090	0.87	13
RC_LBS_45_300_s	-	31	0.00028	0.0021	0.86	13.6
RC_LBS_45_5_d	-	42.3	0.00025	0.0018	0.88	12
RC_LBS_45_10_d	-	42.7	0.00025	0.0018	0.90	10
RC_LBS_45_20_d	-	43.8	0.00023	0.0017	0.9	10
RC_LBS_45_30_d	-	54	0.00030	0.0024	0.9	10
RC_LBS_45_50_d	-	59.7	0.00044	0.0020	0.9	10
RC_LBS_45_80_d	-	71.2	0.00048	0.0031	0.90	10.1
RC_LBS_45_100_d	-	79.7	0.00027	0.0017	0.88	12
RC_LBS_45_150_d	-	91.8	0.00028	0.0026	0.89	11
RC_LBS_45_200_d	-	118	0.00015	0.0007	0.94	6.2
RC_LBS_60_5_s	-	31	0.00025	0.0018	0.86	13
RC_LBS_60_10_s	-	11.4	0.00025	0.0018	0.91	13.6
RC_LBS_60_20_s	-	37.6	0.00025	0.0018	0.95	8.7
RC_LBS_60_30_s	-	49.6	0.00025	0.0018	0.88	5.5
RC_LBS_60_50_s	-	58.9	0.00023	0.00170	0.88	12
RC_LBS_60_80_s	-	69.5	0.00030	0.0024	0.94	12.5
RC_LBS_60_100_s	-	75	0.00044	0.0020	0.92	5.7
RC_LBS_60_150_s	-	88.6	0.00048	0.0031	0.95	8
RC_LBS_60_200_s	-	116	0.00027	0.0017	0.91	5.3
RC_LBS_60_300_s	-	119	0.00028	0.0026	0.92	9
RC_LBS_75_10_s	90	87.7	0.00098	0.0080	0.85	15
RC_LBS_75_20_s	116.4	116.3	0.0014	0.0037	0.92	8
RC_LBS_75_40_s	127.4	126.31	0.0013	0.0024	0.95	5
RC_LBS_75_50_s	145.6	145	0.0012	0.0028	0.96	4
RC_LBS_75_80_s	155.1	152	0.00079	0.0021	0.96	4
RC_LBS_75_100_s	170.5	166.5	0.00054	0.0046	0.92	8

RC_LBS_75_150_s	180.7	177.4	0.0017	0.0060	0.93	7
RC_LBS_75_200_s	221.5	203	0.000945	0.0038	0.96	4
RC_LBS_81_50_s**	145	134	-	0.0015	0.93	7
RC_LBS_81_200_s**	310	295	0.00088	0.0020	0.90	10
RC_LBS_81_50_s***	167	151	0.00016	0.0037	0.91	8.9
RC_LBS_81_200_s***	250	227	0.00012	0.0029	0.95	5

Note: * Value of G/G_0 at γ_{tv} **Moist tamping ***Wet pluviation

3.4 G_0 results

3.4.1 General observations

To reiterate, NE and CX represent typical natural offshore sands, which are well graded fine sands with some silt whilst LBS is a clean uniform and coarse sand. It is expected that there will be deviations in G_0 and G/G_0 of the NE/CX compared to the LBS. All three soils are silica sands with $C_u < 2$ and $d_{50} <$ 1mm, which fall directly within the parameter space of the stiffness database discussed in Section 3.2. Figure 3-7(a) to (d) throughout present measurements of G_0 from the RCA in this study with respect to p'_0 and includes the data from the stiffness database.

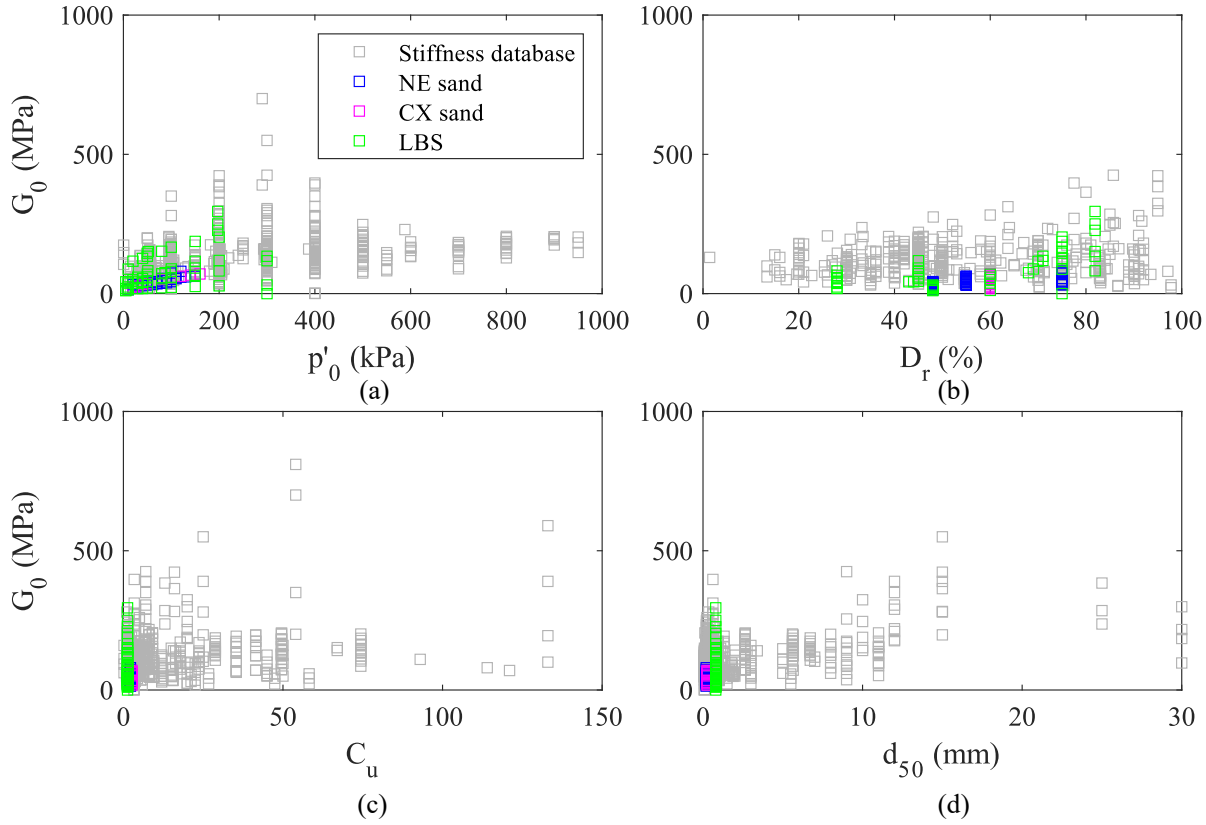


Figure 3-7 G_0 measurements from the RCA in study with respect to (a) p'_0; (b) D_r; (c) C_u; and (d) d_{50}

As the three soils studied here are all siliceous sands with 1.1 <C_u < 2 and d_{50} < 1 mm, they fall within the parameter space of the stiffness database, and it is unsurprising that the measurements of G_0 from the RCA in this study closely align with the database measurements. There are no significant deviations or outliers, indicating strong consistency between findings from this study and existing data and reliability of test results.

3.4.2 Discussion of measurement techniques

The BE and RCA are known to produce slightly different measurements of G_0. Yang and Gu (2013) found that these discrepancies mostly occurred from the complex waveforms generated by BE in granular materials, especially noting that a decrease in particle size can result in high-frequency components in the output signal. The waveforms generated in fine granular specimens display a small-amplitude peak preceding the largest peak which could distort determination of the correct t_a. Gu et al. (2015) demonstrated a coupled effect between the impact of sample preparation and testing method. The study found that for specimens prepared

under moist tamping, BE produced measurements of G_0 14% higher than RC tests whilst specimen prepared via air pluviation and dry tamping exhibited only a 3% increase between BE and RC tests. They theorised the effect was due to the difference in compaction energy used in these sample preparation methods and the difference in the principles involved in these test methods (i.e., BE tests measure the local stiffness of a specimen, whereas RC and TS tests measure the global stiffness of the specimen).

This section compares the measurements and discrepancies in G_0 from the BE and RC on the soils investigated in this study. Figure 3-8(a) presents the variation of G_0 with p'_0 from the two test methods and Figure 3-8(b) shows the error in G_0 values between test methods.

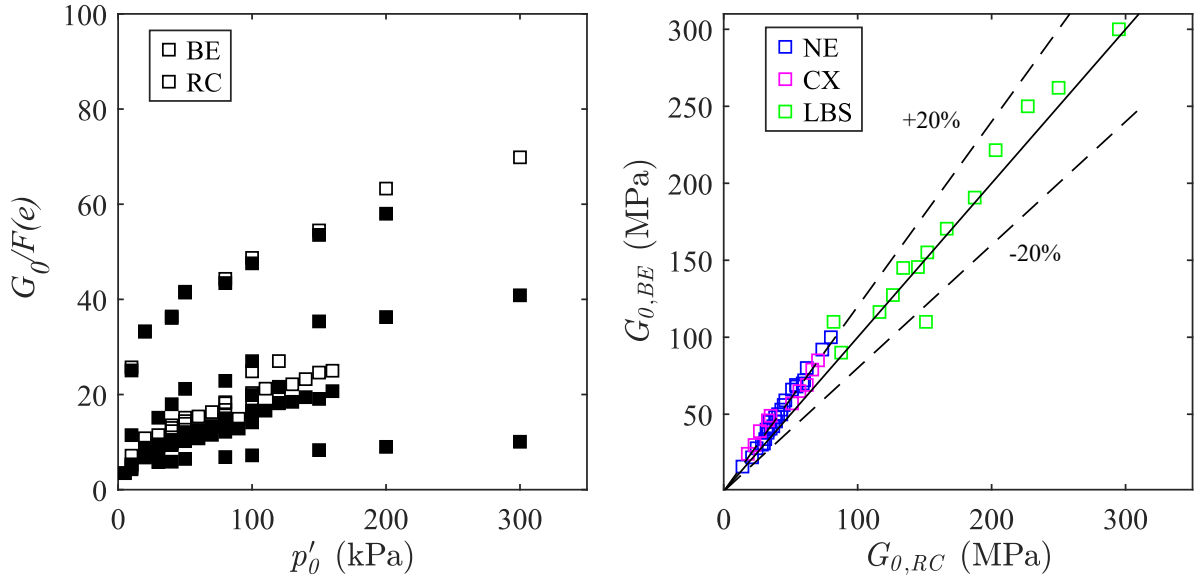


Figure 3-8 Differences between test methods (a) p'_0 vs G_0; and (b) error in testing methods

Here it is clear that G_0 computed from the BE test were consistently higher than RCA tests. The deviation between test methods is the smallest for the LBS material, with errors averaging 5% whilst for NE and CX material, the errors between test method averaged 18%. These results confirm observations by Yang and Gu (2013) and Gu et al. (2015). The discrepancies between test methods are hypothesised to stem particle size of the soils investigated. As LBS is a clean uniform coarse sand, the BE output signals through the material were clearer than the finer NE and CX soils. Thus, the interpretation of the BE tests for LBS were less subjective and more reliable than the NE and CX soils.

3.4.3 G_0 measurements

Most G_0 measurements were obtained via BE and the RCA on the same specimen. However, subsequent discussion of key trends in G_0 refer to measurements from the RCA only to avoid the errors that could arise from BE interpretation as discussed in the previous section. The variation of G_0 with p'_0 was empirically fit with the relationships developed by previous researchers and summarised in Table 3-2. It was observed that $F(e)=(2.97-e)^2/(1+e)$ best described the test results across all densities and soil types, corresponding with the highest R^2 value and lowest root mean squared (RMS) value. The fitting parameters for the test results are summarised in Table 3-6.

Table 3-6 Curve fitting parameters for G_0

Relative density, D_r (%)	Soil type	Fitting parameters		R^2	RMS
		A	m		
65	CX	17	0.55	0.99	0.53
45	NE	13	0.44	0.99	0.27
60	NE	16	0.50	0.99	0.45
75	NE	19	0.60	0.95	1.33
45	LBS	7	0.25	0.99	0.19
60	LBS	26	0.43	0.97	2.17
75	LBS	47	0.27	0.98	1.44

The values of A and m summarised in Table 3-8 are not constant per material type. The general equation proposed by Hardin and Black (1966) in Equation 3-1 suggests that these material constants should be density independent due to the $F(e)$ accounting for changes in void ratio and hence density, for a given material. However, it can be seen that to obtain close fits, quite different fitting parameters were obtained within a material type highlighting that a completely different form of $F(e)$ may be required for the tested soils.

The variation of G_0 with p'_0 from all RC tests and resulting fits using the parameters computed in Table 3-6 is presented in Figure 3-9(a) to (c) throughout. Figure 3-9(d) presents the variation of G_0 with p'_0 of the three soils at D_r = 60%.

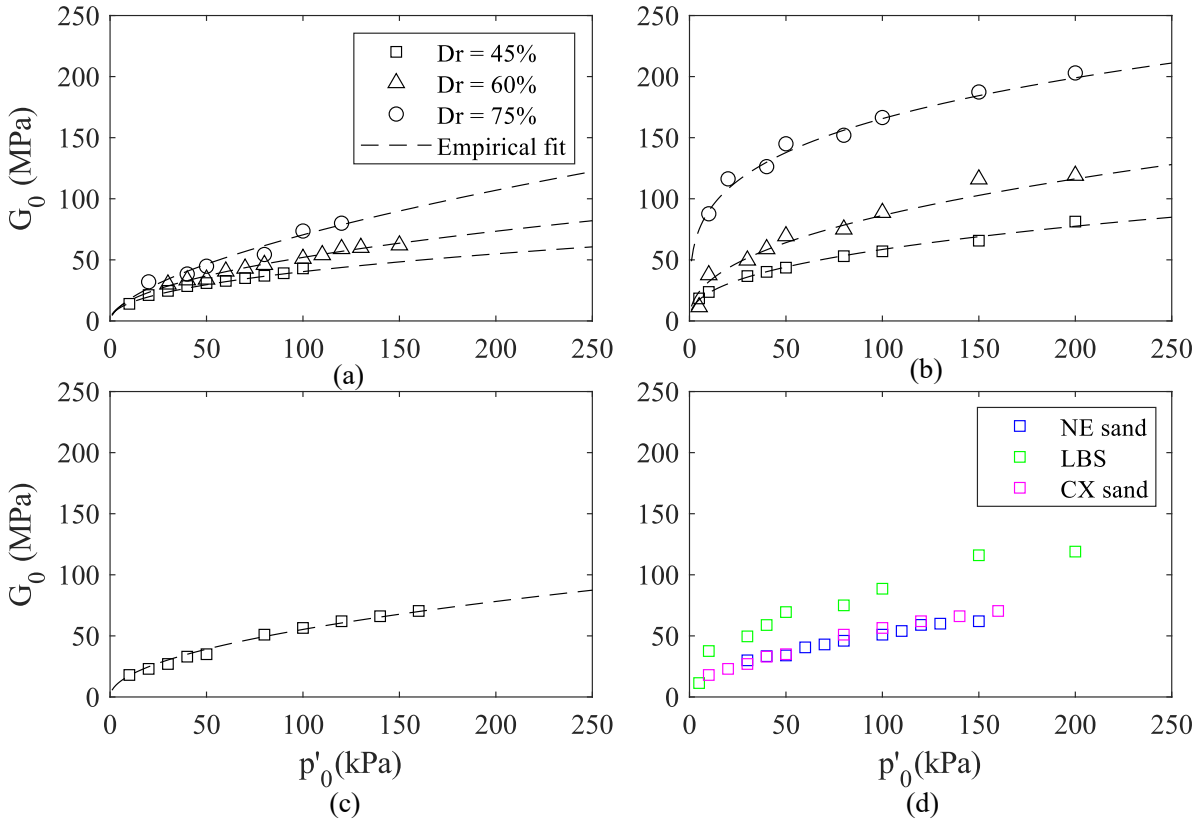


Figure 3-9 G_0 measurements with p'_0 (a) NE sand; (b) LBS; (c) CX sand; and (d) Measurements at D_r = 60%

The trends in G_0 with p'_0 for all soil types precisely followed the conventional power function developed for G_0 as described in Equation (3-1). All test data obtained a high R^2 value and low RMS when fit to the power law demonstrating significant correlation between experimental data to the power function. Moreover, the effect of applying different functions of $F(e)$ was minor with all forms $F(e)$ displaying high statistical correlation with test results, suggesting that all $F(e)$ in Table 3-2 are practically appropriate to describe G_0 for soils tested in this study.

For constant D_r and p'_0, LBS produced the highest G_0, approximately 90% higher than NE and CX sand which both exhibited similar measurements in G_0, see Figure 3-9(d). The variation for G_0 is highly sensitive to D_r for LBS which exhibited the greatest variation in G_0 measurements of roughly 300% between the highest and lowest D_r, see Figure 3-9(b). NE sand is less sensitive to changes to D_r and exhibits roughly 90% difference across the same D_r range, see Figure 3-9(a). For constant D_r and p'_0, NE and CX obtained very similar values of G_0 and an almost identical variation with p'_0 as shown in Figure 3-9(d). The similarities can be

attributed to likeliness in the two sands origin and grain characteristics. Both NE and CX sand are naturally occurring silica sands with similar values of d_{50} and C_u. Conversely, LBS is a uniform quarry material from a single faction and is coarser than the other two soils. These grain characteristics have been demonstrated to have a correlation with G_0 as discussed in Section 3.2.2.

3.4.4 Saturated vs dry response

The limiting conditions of fully saturated and dry conditions on the measured G_0 was briefly explored. RC_LBS_45_5_s to RC_LBS_45_200_s and RC_LBS_45_5_d to RC_LBS_45_200_d were identical RC tests undertaken on LBS under saturated dry conditions respectively. The test data alongside the empirical fits are presented in Figure 3-10 below.

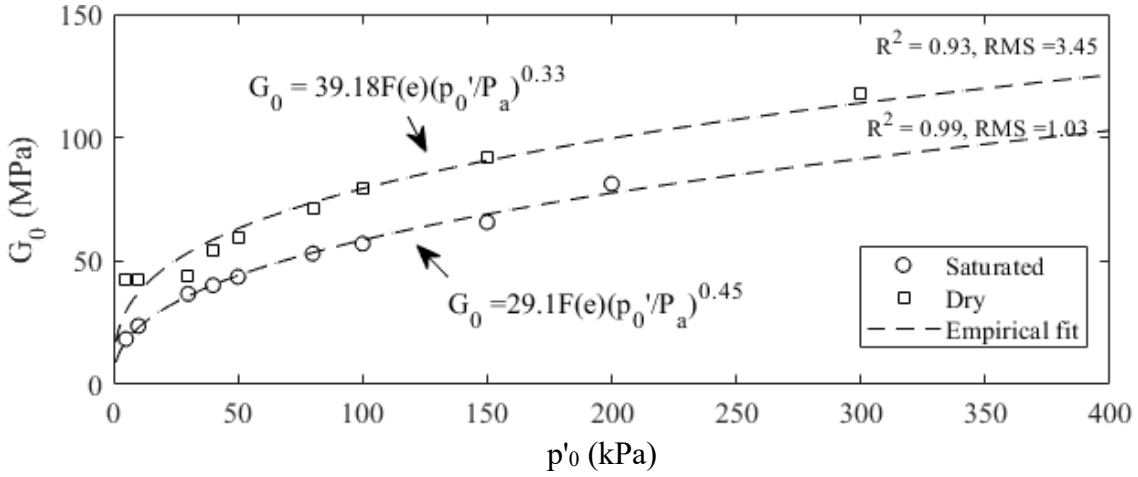


Figure 3-10 Effects of saturation on G_0 variation for LBS sand, D_r = 45%

Under the same testing conditions, the saturated specimen consistently produced lower nominal values of G_0 compared to the dry specimen. This aligns with findings from Bartake and Singh (2007), who studied quartz sand with C_u = 1.41 to 1.97 and Kim et al. (2021), who studied Ottawa sand with C_u = 1.97. Both of these studies involve silica sands with similar particle size distribution to the material used in this study. Menq (2003) observed higher shear velocity values, V_s for dry compared to saturated specimen however noted that G_0 were almost identical for dry and saturated specimen, however it should be noted that the tested material in this study was a gravelly sand with C_u= 15.7 which likely has a different behaviour than the fine silica

sand tested in this study. This behaviour is attributed to stronger intergranular contacts present in dry specimens, where the absence of pore fluid allows for more efficient load transfer between soil particles. Conversely, the presence of pore fluid in saturated specimens reduces intergranular contact. Additionally, the capillary force in unsaturated conditions further enhances stiffness, a contribution that is diminished in saturated conditions. Both dry and saturated specimens exhibit similar trends in G_0 variation with p'_0, indicating that saturation it does not alter the fundamental relationship between G_0 and p'_0.

3.4.5 Soil stiffness profile of NE and CX sand

The NE and CX are naturally occurring silica sands and obtained from two separate sites with conditions representative of offshore soils. Site investigation including trial pits and CPTs were undertaken at both sites. In particular, the Cuxhaven test site was selected as part of the PICASO project and represent a typical offshore sand profile in the North Sea (Quinteros et al. 2018). RCA tests were undertaken on NE and CX sand samples at across p'_0 values representative of *in-situ* stresses experienced by OWT monopiles and at the *in-situ* average D_r of the soil profile (D_r = 60%). By applying the empirical fit as described in Table 3-2, the following equations were adopted to describe soil stiffness profile at the two test sites.

$$\mathrm{G_0} = 32 \cdot \mathrm{f(e)} \sqrt{\frac{\mathrm{p'_a}}{\mathrm{p_{ref}}}}, \qquad \mathrm{G_0} = 35 \cdot \mathrm{f(e)} \sqrt{\frac{\mathrm{p'_a}}{\mathrm{p_{ref}}}} \tag{3-4a,b}$$

The G_0 profile of NE and CX sand measured via the RCA and predictions from calibrated Equation 3-2(a) and (b) are presented in Figure 3-11(a) and (b) respectively. Of the correlations discussed in 2.6.2, the model by Ahmed et al. (2014) produced a fit most closely aligning measured G_0 profile and the resultant fit is also presented on the figures.

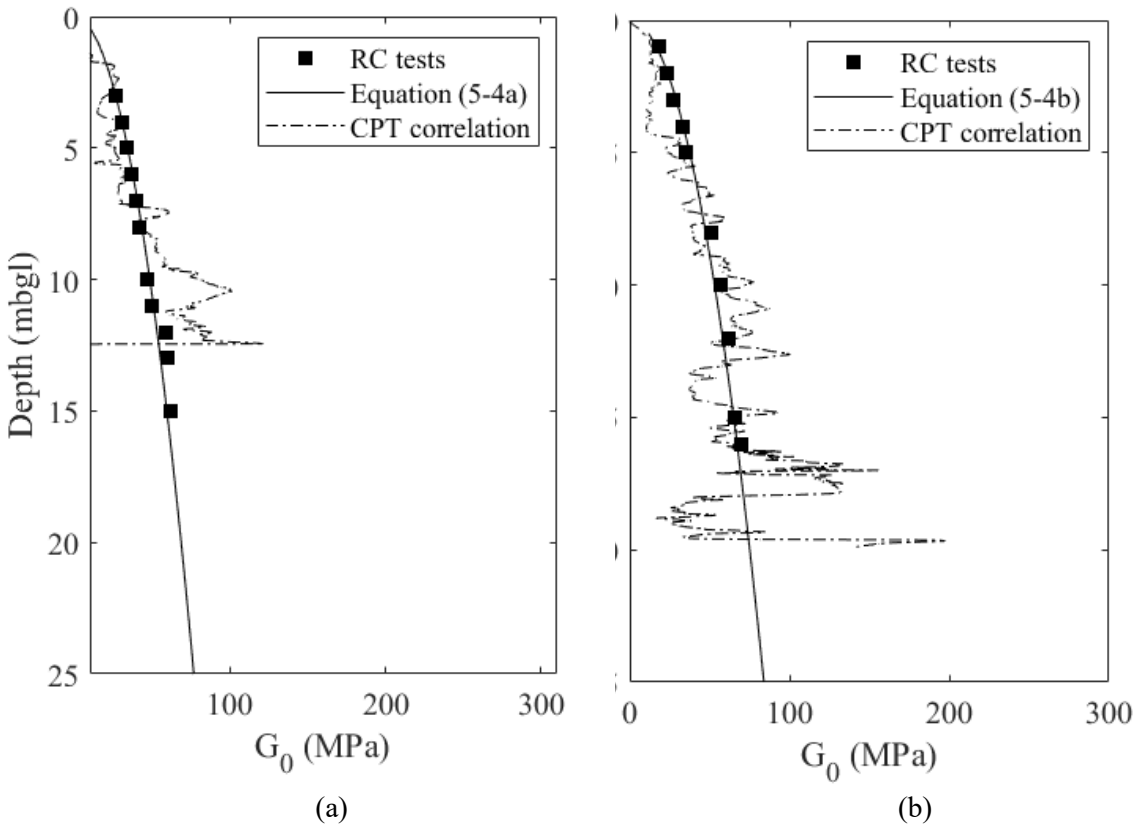


Figure 3-11 G_0 profile from measured laboratory values and CPT correlations (a) NE site; and (b) CX site

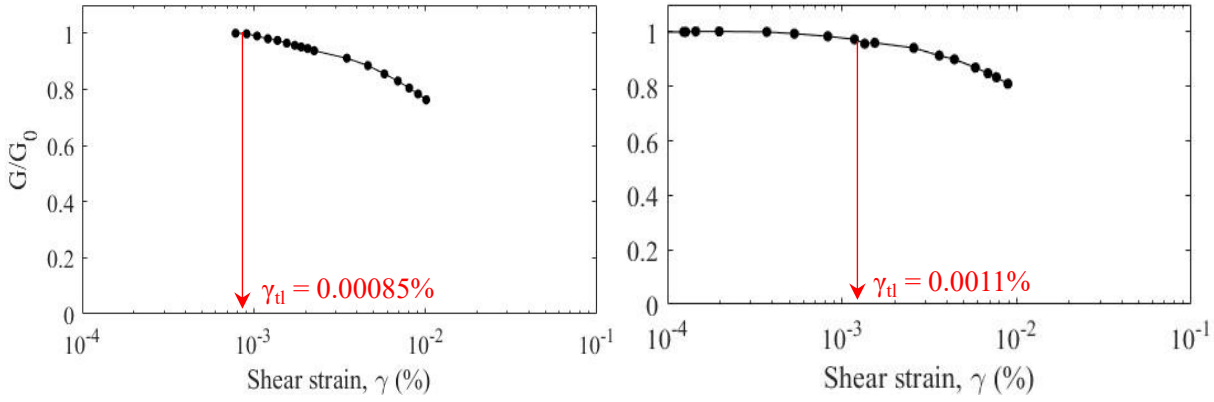
3.5 Obtaining representative stiffness parameters via the RCA

Prior to examining the nonlinear stiffness response of soils, a preliminary study related to G/G_0 degradation within the elastic bounds of soil was undertaken to establish the limit of elastic behaviour for cohesionless soils. These tests were undertaken on NE sands only and at a single density D_r = 60%, (RC_NE_60_10_s to RC_NE_60_150). Results were used to determine the best testing approaching using RCA and demonstrate the applicability of the RCA in obtaining stiffness degradation parameters in the small-strain range. Whilst values of G_0, G/G_0, γ_{tl} and γ_{tv} were typically obtained following the test procedure described in Section 2.5.5, in this smaller series of tests, tests were carried out until the limit of the RCA which in all cases exceeded $\gamma = \gamma_{tv}$. The results and findings were used to inform the testing procedures described in Chapter 2.

3.5.1 Elastic degradation of soil

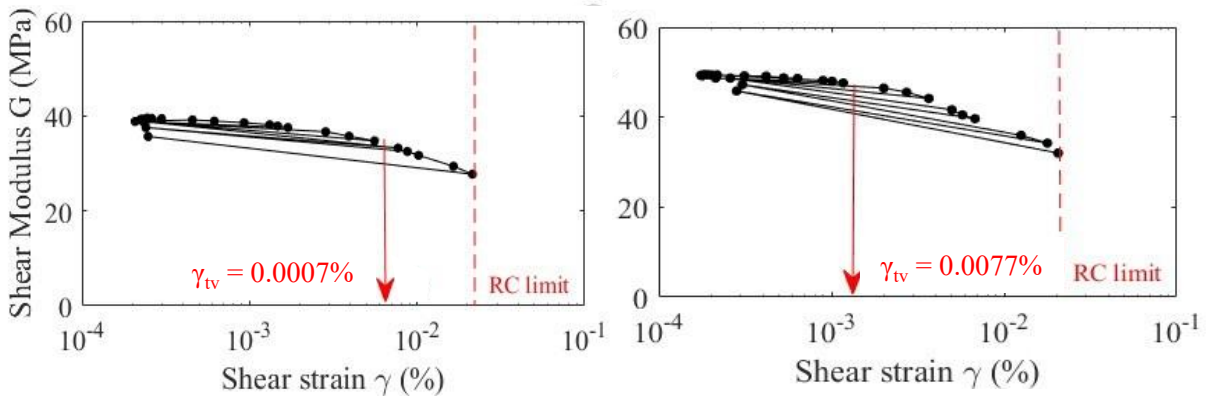
A summary of the G_0 and G/G_0 degradation parameters is presented in Table 3-1 and several examples are shown below. The range of measured γ_{tl} was narrow ranging between 0.00085%

to 0.0011%, RC_NE_60_10_s and RC_NE_60_100_s respectively, as shown in Figure 3-12. The G/G_0 degradation and small strain checks from these tests is presented in Figure 3-13(a) and (b) below. The value of measured γ_{tv} is also marked on the figures. The dotted red line represents the maximum allowable strain that can be safely induced in the RCA corresponding to ~0.023% and was the value of γ at which the test was terminated. The RCA is physically capable to generate $\gamma > 0.023\%$, however, tests were ceased prior to avoid damage to the RCA.



(a) (b)

Figure 3-12 Normalised stiffness response (a) RC_NE_60_60_10_s; and (b) RC_NE_60_100_s



(a) (b)

Figure 3-13 Shear degradation and small-strain checks (a) RC_NE_60_40_s; and (b) RC_NE_60_80_s

As discussed in Chapter 2, the interpretation of RCA test results is based on the theory of elastic wave propagation. Thus, behaviour at strains that induce non-elastic behaviour (i.e., $\gamma > \gamma_{tv}$) cannot be precisely interpreted via this interpretation method. In this investigation, γ_{tv} corresponded to a value significantly less than maximum allowable γ that could be induced by the RCA. This effect is further highlighted in below.

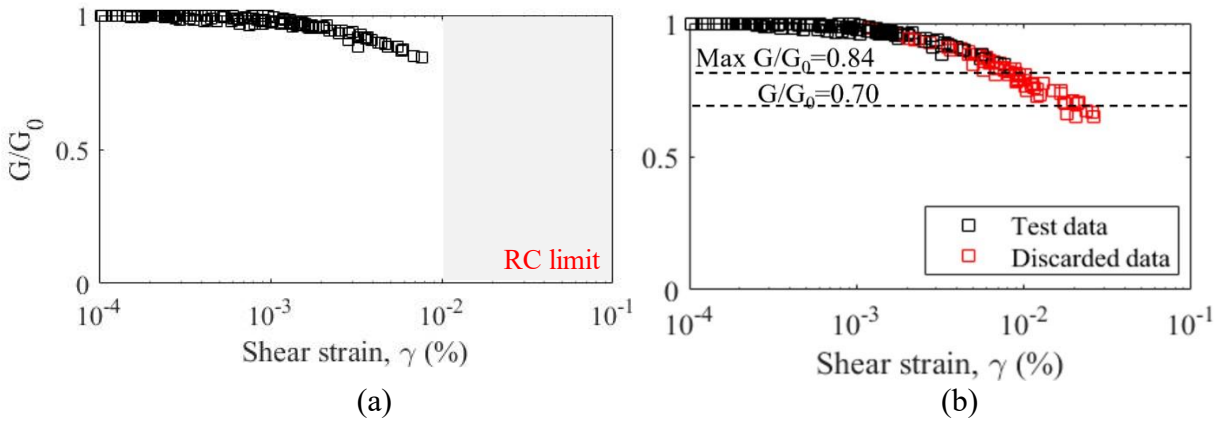


Figure 3-14 Normalised stiffness degradation from RC_NE_60_10_s to RC_NE_60_150_s Test data; and (b) Test data and discarded data

Figure 3-14(a) demonstrates that γ_{tv} is an order of magnitude lower than the RCA limit. Again, the dotted red line represents the physical limit of the RCA, the shaded grey region indicates the range of γ that can be induced by RCA. Consequently, a significant portion (more than half of soil behaviour measured by the RCA in this investigation was discarded due to the onset of plastic soil behaviour, as highlighted by the red data points in (b).

3.5.2 Discussion and implications for design

Whilst the RCA has capabilities of inducing shear strains ranging up to 10^{-2}% to 10^{-1}%, the volumetric threshold strains, γ_{tv} computed in this study were substantially lower (maximum of 7.7×10^{-3}%). Results from this investigation demonstrated the necessity for small strain checks in routine RC testing to ensure reliable test data. These small-strain checks were adopted in all RC experiments within this research regime. The maximum elastic degradation observed for the NE sand corresponded to values of G/G_0 = 0.84 respectively which is above the value of G/G_0 = 0.70 which is required to determine $\gamma_{0.7}$, a reference threshold strain used in the calibration of several constitutive soil models such as HS-small. This also raises concerns relating to the accuracy of stiffness data collected in Section 3.2.3 and offers some explanation for the discrepancies in experimental data to theoretical behaviour as discussed in Section 3.2.4. All data collated from previous RCA experiments included values of $\gamma_{0.7}$, however, it is unclear whether small-strain checks were undertaken to confirm elastic soil behaviour. Commonly

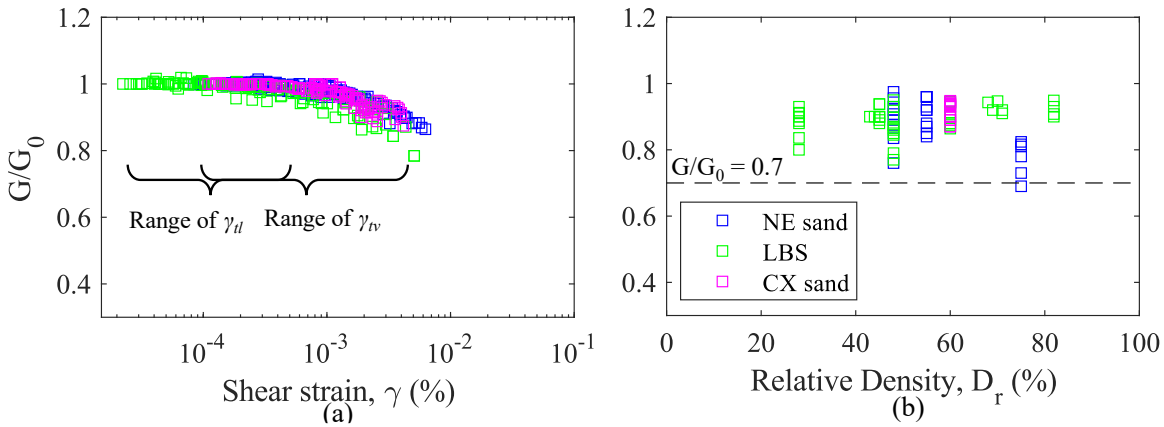
used relationships that describe G/G_0 in cohesionless soils (e.g. Oztoprak and Bolton (2013)), utilise a range of testing methods including the RCA but also rarely state whether such small-strain checks have been completed. Caution is advised relating to the sole use of the RCA for determining constitutive model parameters and the development of empirical stiffness degradation models such as those presented in Table 3-2.

3.6 Stiffness degradation parameters of cohesionless soils

It is of interest to explore the implications of Section 3.5 across a range of cohesionless soil types and testing conditions to ensure consistent conclusions regarding elastic soil behaviour can be drawn. Additionally, such an activity generates useful reference data that can be used in geotechnical design applications for cohesionless soils. A summary of the key findings related to G/G_0 degradation captured by the RCA across three cohesionless soils and a range of p'_0 and D_r are herein discussed.

3.6.1 Stiffness degradation

All measurements of G/G_0 degradation from RCA of the three soils are presented in Figure 3-15(a), the range of measured values γ_{tl} and γ_{tv} are also indicated on the figure. The G/G_0 value at termination of all RC tests are presented in Figure 3-15(b). The values of γ_{tv} with respect to D_r are shown in Figure 3-15(c) and comparison with $\gamma_{0.7}$ values from the stiffness database is shown in Figure 3-15(d).



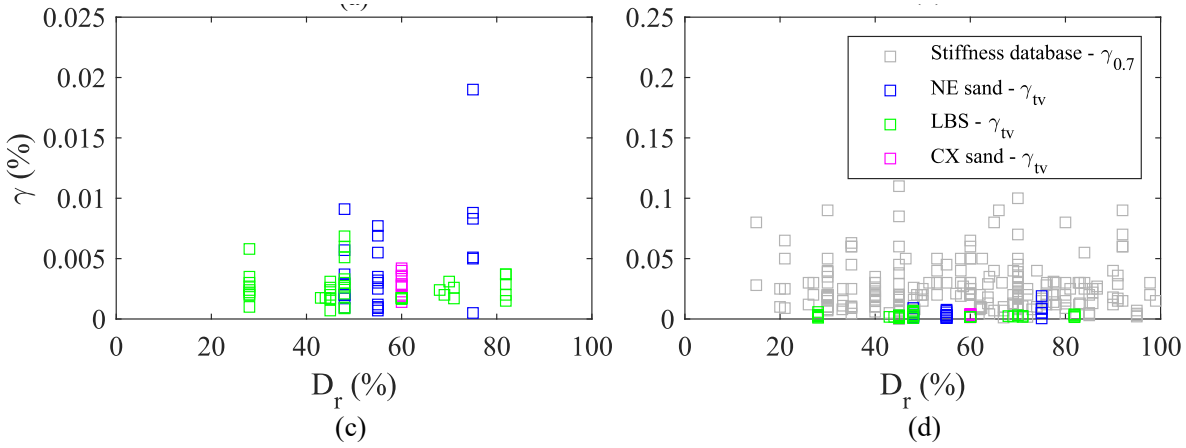


Figure 3-15 Stiffness degradation (a) G/G_0 of all cohesionless soils; (b) G/G_0 with respect to D_r at end of the test; (c) Measured γ_{tv} with respect to D_r; and (d) Measured γ_{tv} with respect to D_r with comparisons to $\gamma_{0.7}$ from database

The computed values of γ_{tl} ranged from 10^{-5} to 10^{-3}% and γ_{tv} ranged from 10^{-4} to 10^{-3}% across all three sand types, again reinforcing that valid test data obtained via the RCA were at least a magnitude lower than the limit of the RCA. The average elastic degradation for NE sand, LBS and CX sand were measured as G/G_0= 0.86, 0.89 and 0.91 respectively. Only one test result in this study computed a value of G/G_0 < 0.70, indicating that most of the elastic stiffness degradation response captured by the RC for cohesionless soils were above the level required to obtain $\gamma_{0.7}$. As mentioned in Section 3.5.2, most previous researchers that have investigated the stiffness degradation of cohesionless soils have presented the stiffness response captured by the RCA at strains exceeding 10^{-2} % corresponding to G/G_0 < 0.70. The results from this study suggest that the onset of plastic soil behaviour occurs at strains <10^{-3}% at G/G_0 > 0.7 for the cohesionless soils considered.

These results suggest that whilst the RCA can reliably measure γ_{tl} and γ_{tv}, the RCA alone is not satisfactory for measuring other reference threshold strains such as $\gamma_{0.7}$, or for calibrating empirical G/G_0 degradation models across the entire strain range. A combination of test methods (e.g., RC combined with local gauges in the triaxial or hollow cylinder testing), is thus recommended.

3.6.2 Effect of p'_0

(a) to (d) throughout displays the G/G_0 degradation for the three soils at D_r = 60%. The variation of stiffness degradation parameters γ_{tl} and γ_{tv} with respect to p'_0 are presented in Figure 3-16(a) and (b) respectively. The trend for γ_{tv} from Oztoprak and Bolton (2013) is also shown on Figure 3-17(b).

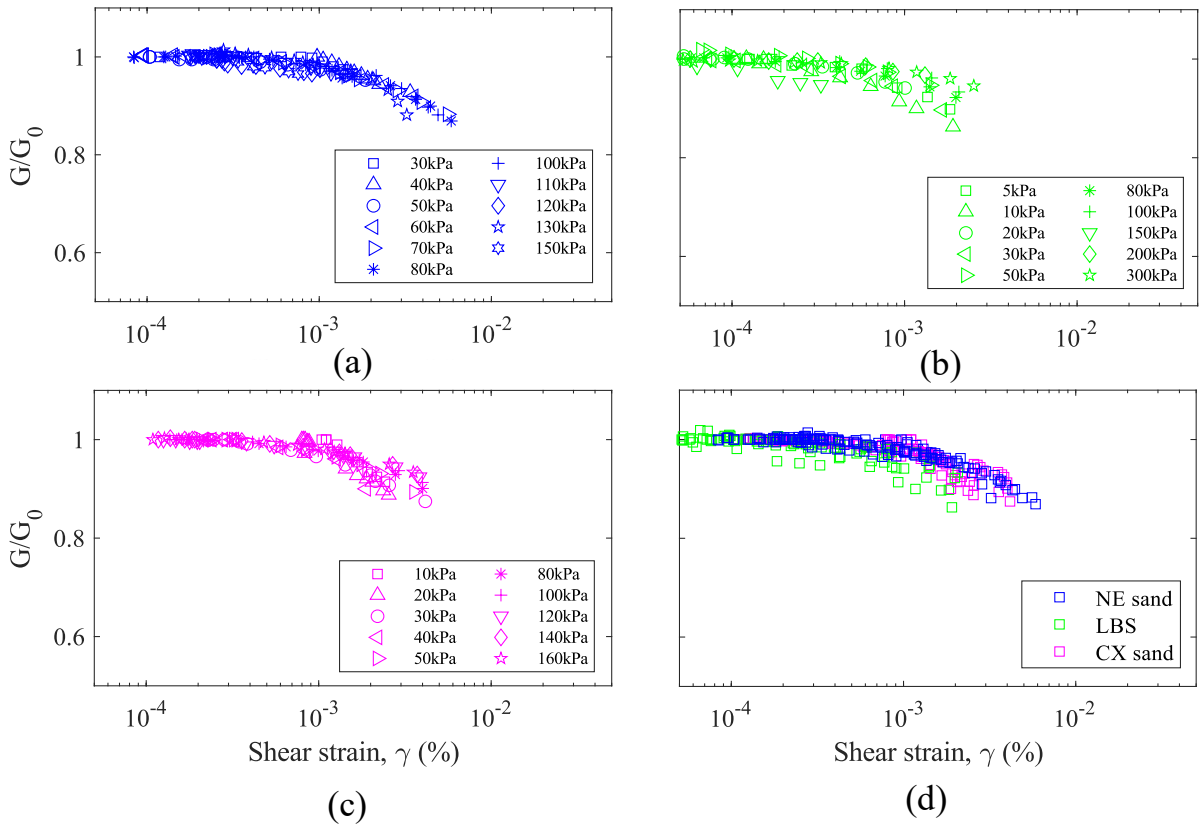


Figure 3-16 *G/G0* degradation measured from the RCA at D_r =60%(a) NE; (b) LBS; (c) CX; and (d) all soils

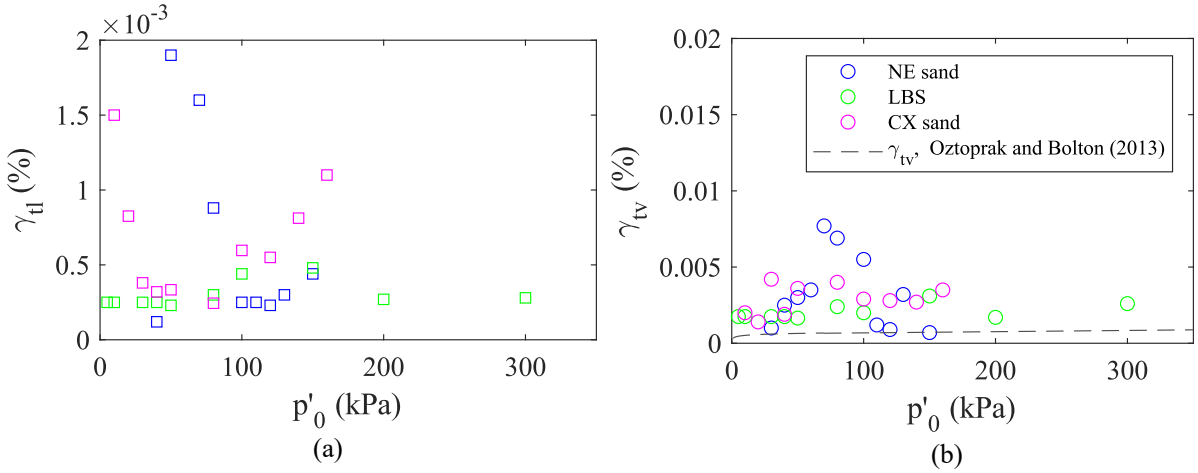
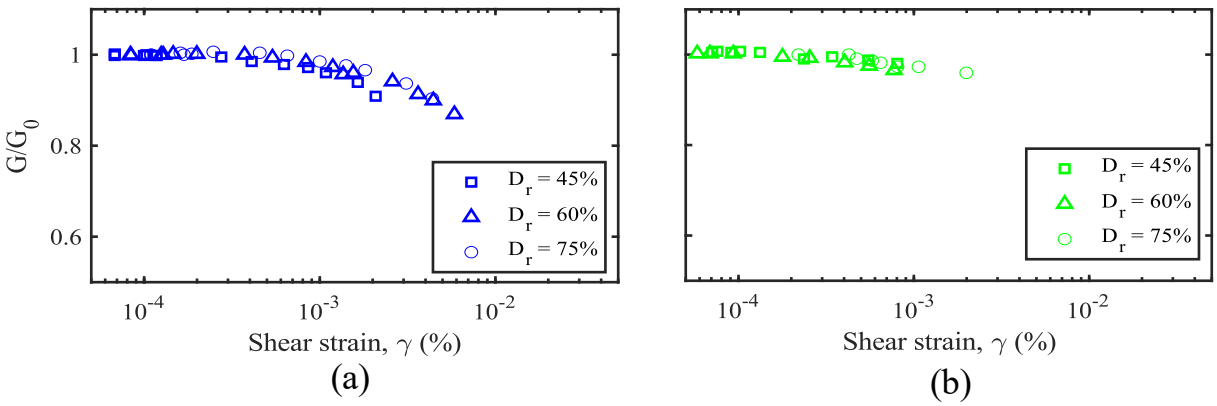


Figure 3-17 Stiffness degradation parameters with p'_0 for tests undertaken at D_r = 60% (a) γ_{tl}; and (b) γ_{tv}

In this investigation, tests have been conducted between $10 < p'_0 < 300$ kPa. Within this relatively limited range, G/G_0 appears independent of p'_0 across soil types. Figure 3-16(d) indicates no significant variation in G/G_0 apparent. A large amount of scatter is seen in Figure 3-17(a), indicating that γ_{tl} is independent of p'_0. Figure 3-17(b) shows less variance in γ_{tv} however, no consistent relationship between γ_{tv} and p'_0 can be drawn. This is contrary to trends described in Oztoprak and Bolton (2013) which suggest a positive relationship between the two parameters, also shown in Figure 3-17(b). Furthermore, measured γ_{tv} values in this study are on average triple the predictions by Oztoprak and Bolton (2013). Whilst Section 3.2 suggests that p'_0 is positively correlated to $\gamma_{0.7}$ and $\gamma_{0.5}$, experimental findings here show the relative independence of γ_{tl} and γ_{tv} to p'_0. This provides a possible explanation for the deviating behaviour as discussed in Section 3.2.4. Since $\gamma_{0.7}$ and $\gamma_{0.5}$ occur at strains where the soil is no longer elastic, the influence of p'_0 on G/G_0 appears more pronounced at the onset of plastic soil behaviour and suggests that the G/G_0 cannot be correlated with p'_0 in the elastic region of soil behaviour.

3.6.3 Effect of D_r

Figure 3-18(a) to (d) throughout displays the G/G_0 degradation for the three soils at p'_0 = 100kPa. The variation of stiffness degradation parameters γ_{tl} and γ_{tv} with respect to D_r are presented in Figure 3-19(a) and (b) respectively.



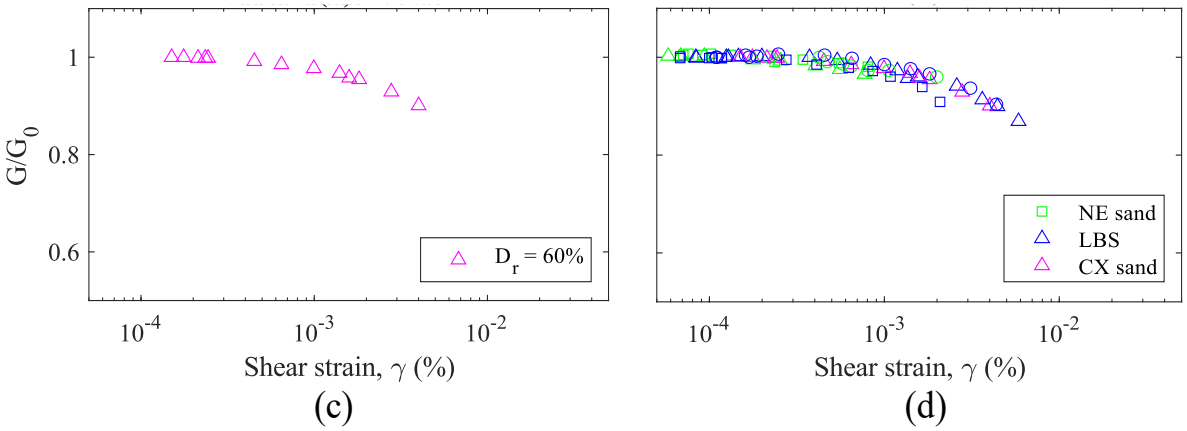


Figure 3-18 Small-strain stiffness degradation G/G_0 measured from the RCA at p'_0 =100kPa (a) NE response (b) LBS response (c) CX response (d) all soils

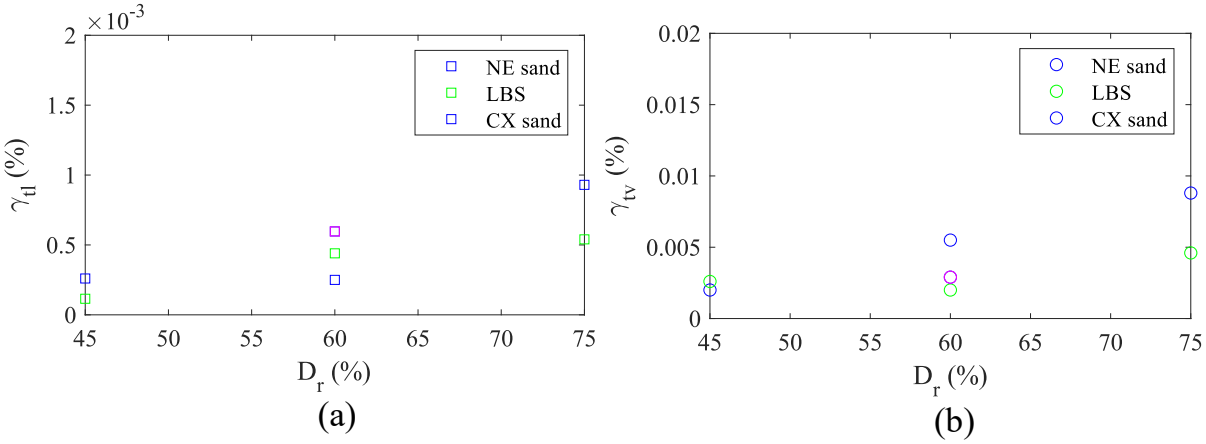


Figure 3-19 Stiffness degradation parameters with D_r for tests undertaken at p'_0 = 100kPa (a) γ_{tl} (b) γ_{tv}

The results are in alignment with expected behaviour in the literature as denser specimens produce a marginally stiffer response to looser specimens. Figure 3-18(d) demonstrates limited variation of stiffness degradation across soil types and for different values of D_r.

Figure 3-19(a) and (b) demonstrates a distinct positive relationship between γ_{tl} and γ_{tv} with D_r suggesting higher densities of soil increases the limit of linear and elastic soil behaviour. Generally, NE and CX sand obtain higher values of both parameters than LBS. This is likely due to the high C_u values such soils relative to uniform LBS material, corroborating observations by Wichtmann and Triantafyllidis (2013).

3.7 Conclusions

Accurate measurements of the shear modulus within the small-strain region have historically proved difficult due to equipment limitations. Conventional apparatuses developed to capture

soil behaviour such as the TX and DSS cannot accurately capture small-strain stiffness and specialised equipment such as BE, RCA or local strain gauges is required. In this study, a method in which representative stiffness degradation parameters can be obtained from the RCA is presented, and the measured G_0 and elastic G/G_0 of three cohesionless soils are presented. The key trends and conclusion are discussed below:

1. A review of existing trends on G_0 and G/G_0 highlight the importance of evaluating the parameter space of proposed empirical relationships when extrapolating them to new soils. Observations suggest that sand-gravel/sand-fines mixtures and carbonate sands may require separate parameter calibrations or even the development of new models, highlighting potential inaccuracies when applying existing models beyond their designated calibration space.
2. This study examined three cohesionless soils within the parameter space of the empirical models. The influence of p'_0, D_r and d_{50} on G_0 are line with findings from previous literature and empirical models for sands within their calibration space.
3. Saturation influences nominal values of G_0, with dry specimens computing higher values compared to saturated counterparts. However, saturation does not affect the variation of G_0 with respect to p'_0. This highlights a notable gap in reviewed models of G_0, as they do not account for saturation effects.
4. The RCA has capabilities of inducing strains up to 10^{-1}%, at least a magnitude of order higher than γ_{tv}, the limit of elastic behaviour measured for the cohesionless soils studied. This highlighted the need for small strain checks to be incorporated in routine RCA testing to ensure accurate stiffness measurements.
5. On average, for the three soil types examined, measured values of γ_{tv} (corresponding with G/G_0 = 0.88) are an order of magnitude lower than $\gamma_{0.7}$ in the stiffness database, highlighting the need of combined testing methods to capture relevant stiffness

degradation parameters, such as $\gamma_{0.7}$ or $\gamma_{0.5}$ that are inputs into constitutive models and for the calibration of G/G_0 models.

6. The measured G/G_0 across soil types and testing conditions is narrow within the elastic region. Interestingly, within the examined range of p'_0, γ_{tl} and γ_{tv} were found to be independent of p'_0. A slight positive relationship between D_r and γ_{tl} and γ_{tv} is observed.
7. Notably, the sand's PSD had a pronounced impact on G_0 and G/G_0, with the NE and CX sands producing lower nominal values of G_0 but a slower rate of G/G_0 compared to LBS. This distinction is attributed to their grain characteristics as both NE and CX sands are well-graded fine sands whereas LBS is a uniform coarse sand. This suggests that C_u and d_{50} are important parameters that influence bounds of linear and elastic behaviour for cohesionless soils.

生生之谓易 – The repeated coming into existence is the essence of nature, Yi Chinese Proverb

CHAPTER 4

Cyclic behaviour of cohesionless soils

4.1 Introduction

This chapter explores the monotonic and cyclic behaviour of cohesionless soils using the VDDCSS. Firstly, the drained and undrained monotonic behaviour of two soils is presented. The monotonic response of the soil provides the reference shear stresses, τ_{max} and τ_{peak}, used to normalise the subsequent cyclic responses. Monotonic tests are also used to characterise the critical state line in σ'_v, τ, and σ'_v, e space, required for the interpretation of cyclic behaviour.

As mentioned in Section 2.3, several notable features characterise the cyclic behaviour of cohesionless soils and foundations founded in cohesionless soils. These include volumetric strain (densification), accumulated lateral displacement and rotation (ratcheting), generation of excess porewater pressure, and changes to stiffness and energy dissipation with cycles. Previous research investigating the cyclic response of cohesionless soils has been undertaken through cyclic simple shear, cyclic triaxial, and cyclic torsional shear tests. In drained conditions, much research has focused on the factors describing densification. It is established that densification has a positive relationship with ζ_b and f whilst exhibiting a negative

relationship between densification and D_r and p'_0 (Chang and Whitman 1988; Kang et al. 2016; Bhaumik et al. 2017; Al Tarhouni and Hawlader 2021; Nong and Park 2021).

Others have investigated accumulated ratcheting and determined a positive relationship between ratcheting and ζ_b and a negative relationship between ratcheting and p'_0, D_r, C_u in the cyclic triaxial apparatus, (Chang and Whitman 1988; Arangelovsk and Towhata 2004; Wichtmann et al. 2005). Accumulated ratcheting in the cyclic triaxial refers to deformation in compression and extension, which is different from accumulated ratcheting described in this chapter, which refers to deformation in the direction of shearing. Thus, accumulated deformation models developed from triaxial data, such as those by Wichtmann et al. (2011), may not necessarily be applied to all loading scenarios for an element of soil.

In terms of undrained cyclic loading, many researchers have investigated the generation of excess porewater pressure, which is positively related to ζ_b and f and negatively related to D_r (Cary 2011; Kokusho 2013; Do et al. 2023). Energy dissipation of cohesionless soils has been studied by Mele et al. (2019), who demonstrated a strong correlation between energy dissipation and porewater pressure generation. Andersen (2015) presents a large set of VDDCSS tests that indicate that D_r is negatively correlated to ratcheting and positively correlated to number of cycles to failure, N_f, in undrained conditions and notes that N_f is additionally a function of ζ_b and ζ_c. An empirical approach for determining the failure envelope of soils of different origins is proposed from these experimental studies.

These studies highlight several key parameters that impact certain cyclic features such as D_r, ζ_b, and p'_0/σ'_v, however, most studies have investigated an isolated cyclic feature and not all aspects in tandem. For example, less attention has been dedicated to exploring changes to stiffness, energy dissipation, and post-cyclic behaviour of cohesionless soils, despite their importance in understanding the mechanisms of cyclic soil behaviour. Furthermore, although

Andersen (2015) presents the behaviour of asymmetrical cyclic tests, most studies to date focus on symmetric unidirectional two-way loading, and multidirectional tests are even less common.

Finally, cyclic loading is expected to induce a partially drained response in offshore conditions, a state between the drained and undrained conditions. It is therefore of interest to explore the limiting behaviours of drained and undrained cyclic soil behaviour to develop the understanding of the mechanisms that govern each condition. This chapter explores the physical factors that contribute to the cyclic features of cohesionless soils under the two drainage conditions. The study focuses on two cohesionless soils: LBS and CX sand. LBS was chosen due to the extensive history of physical model tests conducted on this material, including those by Richards (2020), which are discussed further in Chapter 5 of this thesis. CX sand was selected as it is the founding material where medium-scale field tests site in Germany for the PICAS project. This investigation builds upon previous cyclic experiments on cohesionless soils via four main contributions:

1. Investigation of physical factors controlling accumulated ratcheting, changes to stiffness, energy dissipation and post-cyclic response in drained conditions
2. Investigation of physical factors controlling porewater pressure generation, changes to stiffness, energy dissipation, stress paths and post-cyclic response in undrained conditions
3. Exploring the effects of asymmetry and multidirectional loading in both conditions
4. Providing plausible justification for drained cyclic behaviour based on experimental observations and theoretical understanding of soil mechanics.

This research aims to develop the current understanding of the mechanisms that govern cyclic soil behaviour. A particular emphasis on investigating limiting cases of drained and undrained behaviour is undertaken and the implications on OWT foundation design are also discussed.

4.2 Monotonic behaviour of soil

As described in Chapter 1, the critical state framework is commonly adopted to describe the monotonic behaviour of cohesionless soils. The soil's CSL is typically defined by triaxial tests and refers to the failure line of the material either in p', e or p' q space where p',e and q refer to the confining effective stress, void ratio and deviatoric stress respectively. An equivalent CSL can be obtained from the VDDCSS, presented in σ'_v, e and σ'_v, τ space where σ'_v and, τ refer to the applied vertical effective stress and shear stress respectively, Jefferies and Been (2015).

This section presents the monotonic tests of CX and LBS materials. Two relative densities, D_r were investigated, representing 'looser' than critical (D_r = 60%) and 'denser' than critical (D_r = 90%), herein referred to as 'loose' and 'dense'. Furthermore, two σ'_v representative of pile tip stresses at the Cuxhaven PICASO test site, were investigated, σ'_v = 36kPa and 74kPa such that meaningful comparison between laboratory behaviour and field behaviour can be drawn. The τ_{peak} and $\tau_{residual}$, as well as G_{max} obtained from these tests are used for the normalisation of cyclic tests in Sections 4.3 and 4.4. Key geotechnical parameters extracted from the monotonic behaviour of soil are presented.

4.2.1 Test schedule and results

A total of 4 VDDCSS monotonic tests were conducted on LBS and 12 on CX. LBS tests were conducted in drained conditions to allow for a meaningful comparison with physical tests by Richards (2020). Tests on CX material were conducted in both drained and undrained conditions to ensure comparative results with medium-scale field tests, which are likely to exhibit a range of drainage conditions. A summary of testing conditions and results is presented in Table 4-1. The naming convention follows the nomenclature described in Section 3.3.

Table 4-1 Monotonic VDDCSS test results

Test ID	σ'_v (kPa)[1]	D_r (%)	e_0	e_f	τ_{peak} (kPa)[2]	τ_{res} (kPa)[3]	G_{max} (kPa)[4]
VDDCSS_LBS_60_36_d_M_D	36	60	0.69	0.62	24	24	4400

VDDCSS_LBS_90_36_d_M_D	36	90	0.56	0.62	28	28	4700
VDDCSS_LBS_60_74_d_M_D	74	60	0.7	-	51	51	7000
VDDCSS_LBS_90_74_d_M_D	74	90	0.54	-	60	60	9000
VDDCSS_CX_60_36_i_M_D	36	60	0.64	0.61	22	22	2800
VDDCSS_CX_60_36_i_M_U	36	60	0.67	0.67	6	2	10000
VDDCSS_CX_100_36_i_M_D	36	100	0.60	0.61	30	30	3800
VDDCSS_CX_100_36_i_M_U	36	100	0.58	0.58	8	-	11000
VDDCSS_CX_60_74_i_M_D	74	60	0.60	0.57	44	44	8400
VDDCSS_CX_60_74_i_M_U	74	60	0.65	0.65	7	4	10500
VDDCSS_CX_100_74_i_M_D	74	100	0.60	0.56	48	48	8800
VDDCSS_CX_100_74_i_M_U	74	100	0.59	0.59	13	-	11300
VDDCSS_CX_60_110_i_M_D	110	60	0.55	0.50	58	58	11000
VDDCSS_CX_60_110_i_M_U	110	60	0.67	0.67	15	8	10800
VDDCSS_CX_100_110_i_M_D	110	100	0.48	0.47	68	68	11300
VDDCSS_CX_100_110_i_M_U	110	100	0.56	0.56	22	-	11000

Note: 1. σ'_v for VDDCSS tests 2. τ_{peak}, peak shear stress 3. τ_{res}, residual shear stress 4. Value taken at $\gamma = 0.0001$

The G_{max} of monotonic tests was taken to be the shear stiffness at very small strains, $\gamma = 0.0001$. The values reported in Table 4-1 (ranging from 2.8MPa to 11.3MPa) are significantly lower than the G_0 values measured from BE and RCA tests (ranging from 18 to 305 MPa). This is likely because the BE and RCA can measure the G values at very small strains whilst in the VDDCSS, the captured response is typically within the medium to large strain region where G has already degraded. Additionally, the BE and RCA were undertaken on specimen isotopically consolidated at a certain p'_0 whilst, the VDDCSS tests only apply a vertical stress σ'_v. The horizontal stress provided by the confining rings in VDDCSS tests is unknown and is likely much lower than σ'_v potentially contributing to the differences in initial shear stiffness values.

4.2.2 Monotonic response of soils

Figure 4-1 and Figure 4-2 present the monotonic drained response of LBS and CX respectively.

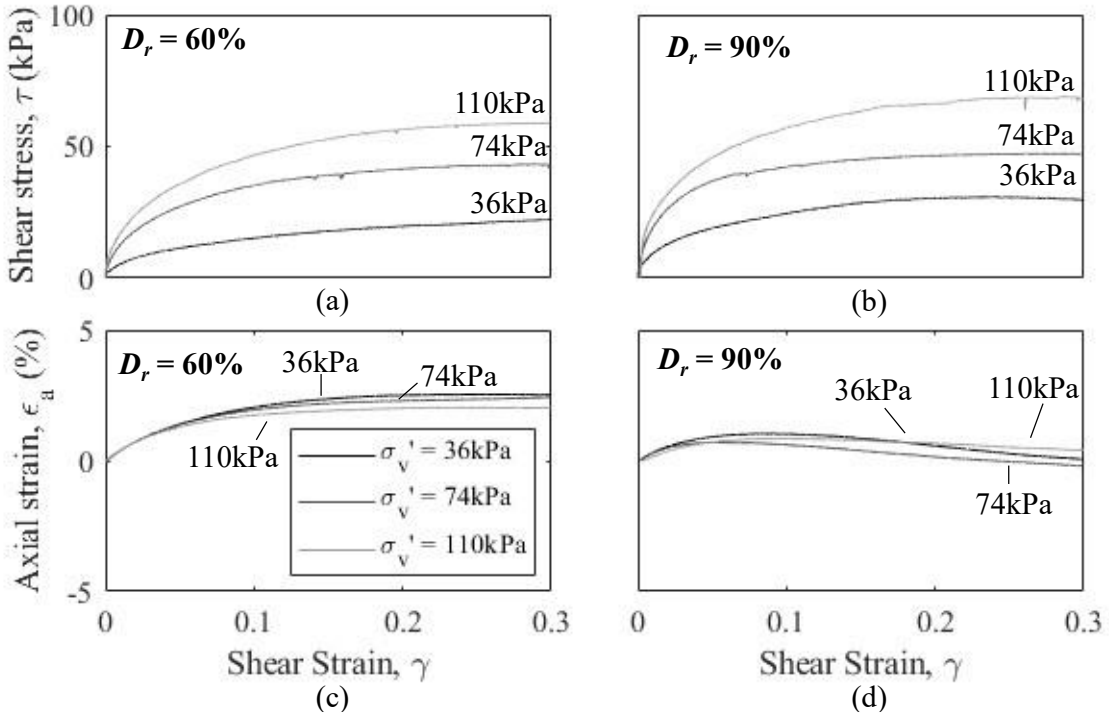


Figure 4-1 Monotonic behaviour drained of LBS (a) Stress-strain, D_r = 60%;(b)Stress-strain, D_r = 90%; (c) Axial strain, D_r = 60%; and (d) Axial strain D_r =90%

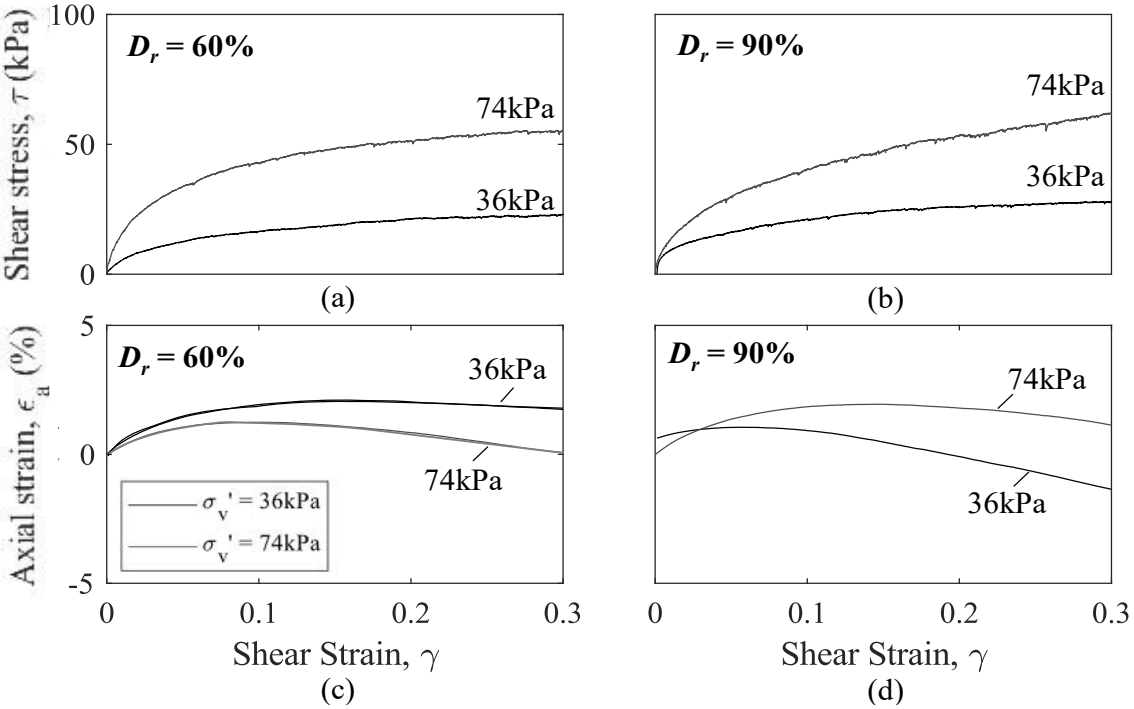


Figure 4-2 Monotonic drained response of CX (a) Stress-strain D_r = 60%; (b) Stress-strain, D_r = 90%; (c) Axial strain D_r = 60%; and (d) Axial strain, D_r =90%

For all tests, the specimen approaches a maximum shear stress, τ_{max}, but no peak is observed, see Figure 4-1(1) and (b) and Figure 4-2(a) and (b). D_r and σ'_v act to increase, τ_{max}. As discussed in Chapter 1, under conventional critical state theory, 'looser' than critical soil tend towards

τ_{max} and 'denser' than critical approaches τ_{peak} and subsequently experience strain softening. At a fixed σ'_v, both 'looser' and 'denser' than critical specimens eventually tend to the same τ_{res} at critical state irrespective of initial density. The results slightly deviate from this as neither 'looser' or 'denser' than critical specimens observe a τ_{peak}, and both tend directly towards τ_{max} which is slightly lower for the 'loose' specimen. However, this behaviour is seen in other studies using the VDDCSS, such as Al Tarhouni (2021) and Tohidvand et al. (2022).

All CX specimens compacted to D_r = 60% exhibit 'looser' than critical behaviour, exhibiting contraction only. Similarly, the LBS specimen compacted to D_r = 60% and σ'_v = 36kPa also exhibits contractive behaviour however specimens consolidated to σ'_v = 74kPa shows contractive followed by dilative behaviour. All specimens from both CX and LBS compacted to D_r = 90% exhibit 'denser' than critical behaviour, displaying contractive followed by dilative behaviour, (see Figure 4-1(d) and Figure 4-2(d)), LBS specimens continue to dilate after 30% strain, whilst CX specimens reach an equilibrium.

An equivalent suite of undrained monotonic tests was undertaken on CX. Figure 4-3 presents the undrained monotonic response of CX sand.

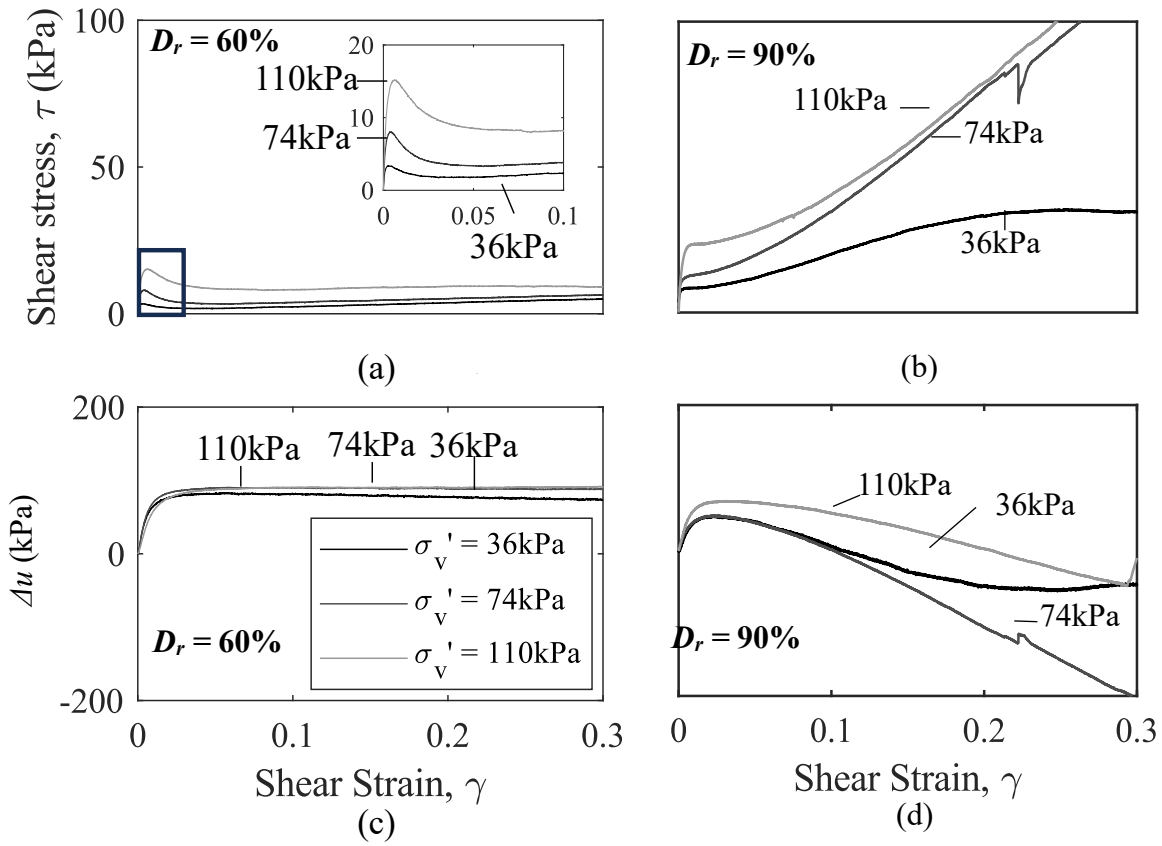


Figure 4-3 Monotonic undrained behaviour of CX material (a) Stress-strain, D_r = 60%; (b) Stress-strain, D_r = 90%; (c) Porewater pressure, D_r = 60%; and (d) Porewater pressure, D_r = 90%

The undrained response differs greatly to the drained response as all specimens reach a peak shear stress, τ_{peak}, followed by strain softening or strain hardening. The value of τ_{peak} is positively related to σ'_v and D_r. Loose specimens exhibit contractive behaviour evidenced by post-peak strain-softening and by the increase in Δu in Figure 4-3(a) and (c). The point at which τ_{peak} is overcome for 'loose' specimens corresponds to liquefaction and rapid increase in Δu of approximately 90%. Dense specimens exhibit dilative behaviour, where post peak strain-hardening is evident and Δu decreases with further large strains. The point at which τ_{peak} is overcome for 'dense' specimens corresponds to when the transition of contractive to dilative behaviour (i.e., change in Δu from positive to negative) occurs. The normalised stress-path and stress-strain response from the undrained tests is presented in Figure 4-4(a) and (b).

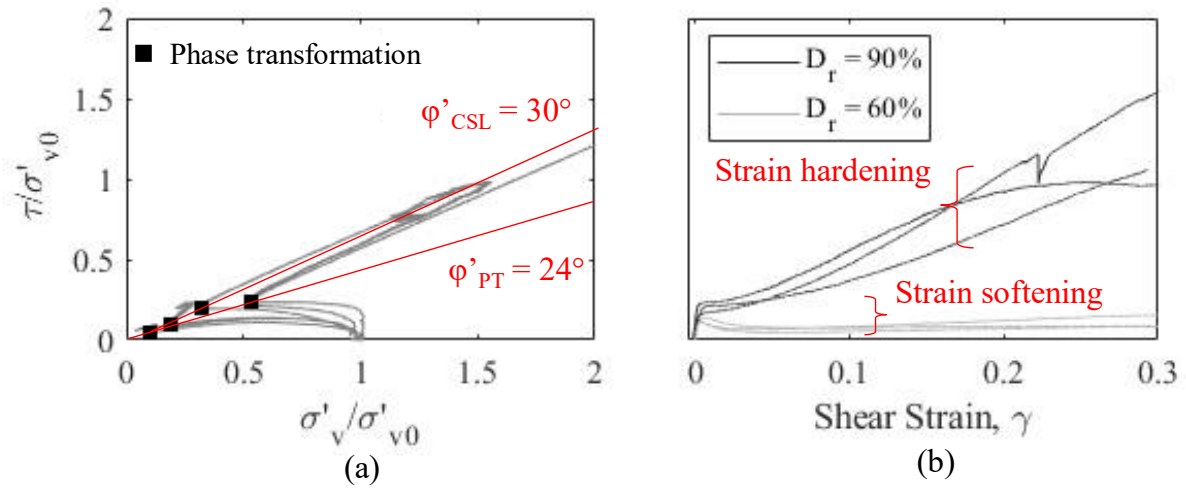


Figure 4-4 Monotonic characterisation of CX (a) Normalised stress-path; and (b) Normalised undrained response

4.2.3 Discussion

The interpreted mobilised phase transformation and critical state friction angles for CX are φ'_{PT} = 24° and φ'_{CS} = 30°. The monotonic behaviour of two cohesionless soils has been presented in this section. The monotonic capacity of both cohesionless soils is a function of σ'_v, D_r, and drainage conditions. Drainage conditions are seen to significantly alter the monotonic response of the cohesionless soil. In fully drained conditions, σ'_v and D_r are positively related to the monotonic capacity of soil and soils tend directly towards τ_{max}. Such trends that are in line with other experimental observations from the VDDCSS, (Al Tarhouni 2021; Tohidvand et al. 2022). In fully undrained conditions, both loose and dense experience an initial τ_{peak} which is positively related to σ'_v and D_r. The post-peak response of soil in undrained conditions is mostly governed by D_r with 'loose' specimens exhibiting the 'flow' condition and 'dense' specimens exhibiting 'limited' or 'no flow' as defined in Chapter 1. The undrained response, including the stress-strain response, stress-path and Δu behaviour, follows behaviour established by experimental observations from the VDDCSS and TX that have examined undrained behaviour of cohesionless soils, (Cubrinovski and Rees 2008; Li et al. 2017; Mahmoudi et al. 2018; Porcino et al. 2020).

4.3 Drained cyclic VDDCSS tests

This section presents constant stress cyclic VDDCSS tests undertaken on CX and LBS, i.e., drained cyclic tests. The conditions of LBS tests were designed to match testing conditions of 1g model tests outlined in Richards (2020). Tests undertaken on CX material were designed to investigate physical factors that impact cyclic behaviour including, load amplitude ratio, ζ_b, load asymmetry, ζ_c, frequency, f, applied vertical stress, σ'_v and relative density, D_r. Two vertical stresses, σ'_v = 36kPa and 74kPa and two relative densities were examined, D_r = 60% and D_r = 90%. ζ_b and ζ_c were varied within ranges related to design loads of typical OWT, as presented in Leblanc et al. (2010a). Four frequencies were investigated, 0.01, 0.1, 0.5 and 1Hz representative of typical wind, wave, and seismic frequencies applied to OWTs.

4.3.1 Test schedule and results

A total of 9 LBS and 36 CX cyclic tests were conducted using the VDDCSS in constant stress conditions. All tests were subjected to a maximum of 3000 cycles of loading. Unidirectional two-way, one-way, partial one-way tests, partial two-way, as well as multidirectional loading arrangements were explored. A summary of cyclic drained tests conditions and results are presented in Table 4-2.

Table 4-2 VDDCSS Constant stress test schedule

Test ID	ζ_b	ζ_c	f **(Hz)**	σ'_v **(kPa)**	$D_{r,\,initial}$ **(%)**	$D_{r,\,final}$ **(%)**	τ_{post}/τ_{max}
Two-way							
VDDCSS_LBS_60_36_UTW_D	0.4	-1	0.1	36	60	75	1.01
VDDCSS_LBS_90_36_UTW_D	0.4	-1	0.1	36	90	99	1.10
VDDCSS_CX_60_36_i_UTW_D1	0.2	-1	0.1	36	60	63	1.13
VDDCSS_CX_60_36_i_UTW_D2*	0.4	-1	0.1	36	60	71.5	1.36
VDDCSS_CX_60_36_i_UTW_D3	0.8	-1	0.1	36	60	100	2.41
VDDCSS_CX_60_36_i_UTW_D4	0.4	-1	0.01	36	60	77	1.45
VDDCSS_CX_60_36_i_UTW_D5	0.4	-1	0.5	36	60	80	1.50

VDDCSS_CX_60_36_i_UTW_D6	0.4	-1	1	36	60	82	1.8
VDDCSS_CX_100_36_i_UTW_D	0.4	-1	0.1	36	90	93	1.50
VDDCSS_CX_60_74_i_UTW_D	0.4	-1	0.1	74	60	84.4	2.00
One-way							
VDDCSS_LBS_60_36_d_UOW_D1	0.2	0	0.1	36	60	65	-
VDDCSS_LBS_60_36_d_UOW_D2	0.4	0	0.1	36	60	70	1.02
VDDCSS_LBS_90_36_d_UOW_D	0.4	0	0.1	36	90	95	-
VDDCSS_CX_60_36_i_UOW_D1	0.2	0	0.1	36	60	66	1.50
VDDCSS_CX_60_36_i_UOW_D3*	0.4	0	0.1	36	60	71	1.80
VDDCSS_CX_60_36_i_UOW_D4	0.8	0	0.1	36	60	81	2.23
VDDCSS_CX_60_36_i_UOW_D5	0.4	0	0.01	36	60	17	1.57
VDDCSS_CX_60_36_i_UOW_D6	0.4	0	0.5	36	60	66	1.67
VDDCSS_CX_60_36_i_UOW_D7	0.4	0	1	36	60	69	1.72
VDDCSS_CX_100_36_i_UOW_D	0.4	0	0.1	36	90	96	1.8
VDDCSS_CX_60_74_UOW_D	0.4	0	0.1	74	60	70	1.67
Partial one-way and two-way							
VDDCSS_LBS_60_36_U1P_D1	0.6	0.33	0.1	36	60	75	-
VDDCSS_LBS_90_36_U1P_D1	0.6	0.33	0.1	36	90	95	-
VDDCSS_CX_60_36_i_U1P_D1	0.3	0.3	0.1	36	60	63	1.40
VDDCSS_CX_60_36_i_U1P_D2	0.5	0.6	0.1	36	60	63	1.50
VDDCSS_CX_60_36_i_U1P_D3	0.6	0.3	0.1	36	60	72	1.90
VDDCSS_CX_60_36_i_U1P_D4	0.7	0.7	0.1	36	60	72	1.73
VDDCSS_CX_60_36_i_U1P_D5	0.8	0.5	0.1	36	60	70	2.04
VDDCSS_CX_60_36_i_U2P_D1*	0.6	-0.3	0.1	36	60	80	2.00
VDDCSS_CX_60_36_i_U2P_D2	0.8	-0.5	0.1	36	60	88	2.55
VDDCSS_CX_60_36_i_U2P_D3	0.6	-0.3	0.01	36	60	78	2.16
VDDCSS_CX_60_36_i_U2P_D4	0.6	-0.3	0.5	36	60	80	1.99
VDDCSS_CX_60_36_i_U2P_D5.	0.6	-0.3	1	36	60	81	2.10
VDDCSS_CX_100_36_i_U2P_D	0.6	-0.3	0.1	36	90	100	2.27
VDDCSS_CX_60_74_i_U2P_D	0.6	-0.3	0.1	74	60	100	2.90

Multidirectional							
VDDCSS_LBS_60_36_d_MD1_D (x)	0.2	1	0.1	36	60	64	1.60
VDDCSS_LBS_60_36_d_MD1_D (y)	0.2	-1					
VDDCSS_LBS_90_36_d_MD1_D (x)	0.2	1	0.1	36	90	93	-
VDDCSS_LBS_90_36_d_MD1_D (y)	0.2	-1					
VDDCSS_CX_60_74_i_MD1_D (x)	0.2	1	0.1	74	60	65	1.80
VDDCSS_CX_60_74_i_MD1_D (y)	0.2	-1					
VDDCSS_CX_60_74_i_MD2_D (x)	0.4	1	0.1	74	60	72	2.11
VDDCSS_CX_60_74_i_MD2_D (y)	0.2	-1					
VDDCSS_CX_60_74_i_MD3_D (x)	0.2	1	0.1	74	60	70	1.60
VDDCSS_CX_60_74_i_MD3_D (y)	0.4	0					
VDDCSS_CX_60_74_i_MD4_D (x)	0.4	1	0.1	74	60	87	-
VDDCSS_CX_60_74_i_MD4_D (y)	0.6	0.33					
VDDCSS_CX_100_74_i_MD1_D (x)	0.2	1	0.1	74	100	94	1.10
VDDCSS_CX_100_74_i_MD1_D (y)	0.2	-1					
VDDCSS_CX_100_74_i_MD2_D (x)	0.4	1	0.1	74	100	95	2.10
VDDCSS_CX_100_74_i_MD2_D (y)	0.2	-1					
VDDCSS_CX_100_74_i_MD3_D (x)	0.2	1	0.1	74	100	96	1.50
VDDCSS_CX_100_74_i_MD3_D (y)	0.4	0					
VDDCSS_CX_100_74_i_MD4_D (x)	0.4	1	0.1	74	100	99	-
VDDCSS_CX_100_74_i_MD4_D (y)	0.6	0.33					

Note: * Test was repeated with post-cyclic tests undertaken in the transverse direction to cyclic loading - No post-cyclic test was undertaken

Of the 41 drained VDDCSS tests, none of the specimens experienced failure within 3000 cycles of loading. Selected cyclic drained stress-strain responses are presented in Figure 4-5(a) to (f) throughout.

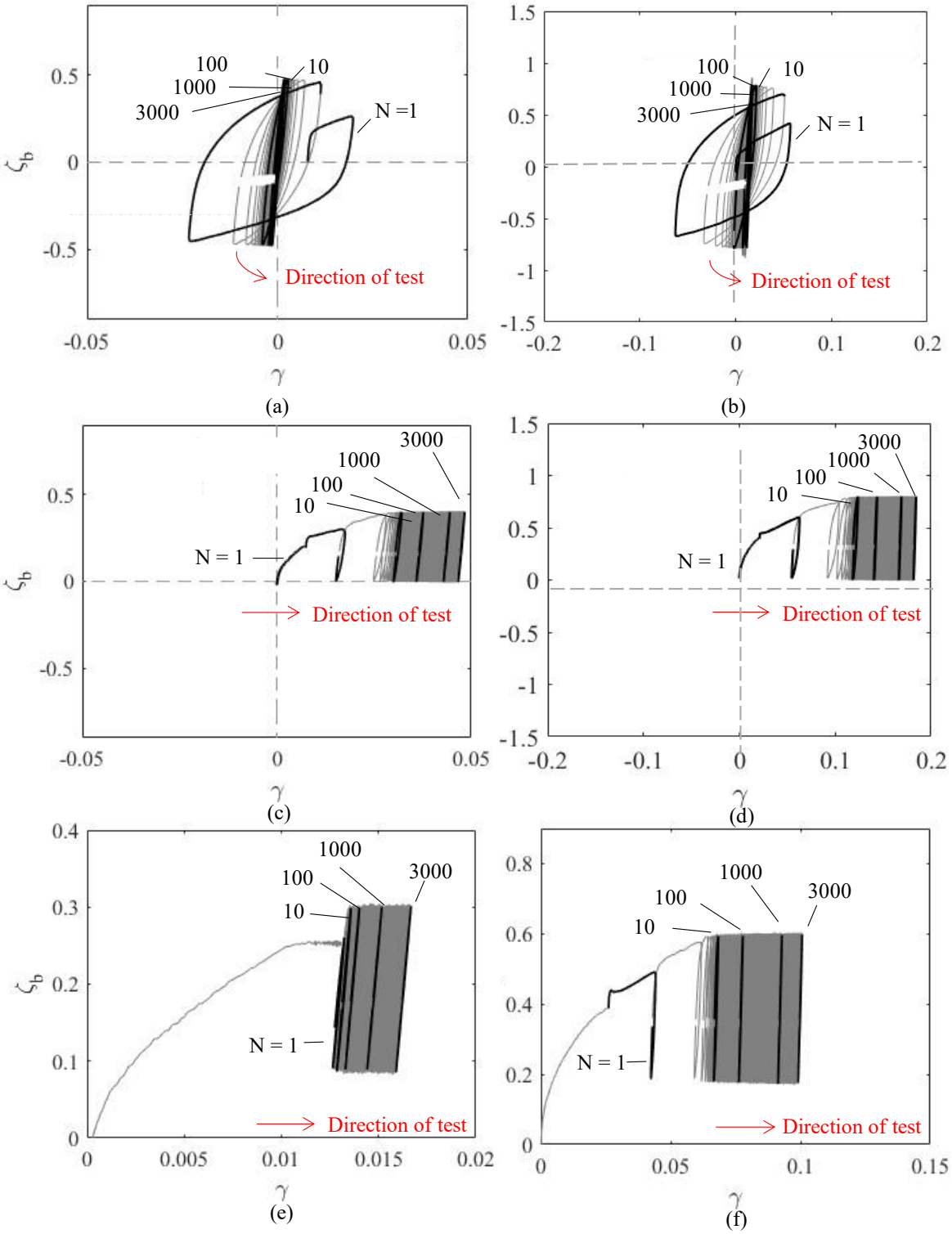


Figure 4-5 Drained cyclic behaviour of various tests at D_r = 60% (a) ζ_b = 0.4, ζ_c -1; (b) ζ_b = 0.8, ζ_c -1; (c) ζ_b = 0.4, ζ_c = 0; (d) ζ_b = 0.8, ζ_c = 0; (e) ζ_b = 0.3, ζ_c = 0.3; and (f) ζ_b = 0.5, ζ_c = 0.6

An observation across all tests undertaken using the VDDCSS was that the first cycle applied to the specimen always fell short of the target amplitude. This could be due to the device having trouble in achieving the desired precision during the initial target phase.

The following sections evaluates the significance of ζ_b, ζ_c f, D_r, and σ'_v on prominent cyclic features. Previous researchers have demonstrated the clear importance of ζ_b, ζ_c, D_r and σ'_v on the cyclic behaviour of cohesionless soil in the VDDCSS device (Andersen 2015; Kang et al. 2016; Bhaumik et al 2017; Cui et al. 2019; Al Tarhouni and Hawlader 2021; Nong and Park 2021; Andersen et al. 2023). The f was varied to determine whether drainage conditions could be altered in the VDDCSS through the loading frequency, i.e., whether very quick loading could simulate undrained conditions.

4.3.2 Densification with cycles

This section examines the densification of soil specimens under different cyclic load scenarios. For each loading scenario, the effect of ζ_b, f, D_r and σ'_v are considered against a reference base case, summarised in Table 4-3. The base case parameters were selected to match the anticipated soil condition and loading regime expected in medium-scale field tests.

Table 4-3 Base case test condition

	Unidirectional two-way	Unidirectional one-way	Unidirectional partial two-way
ζ_b	0.4	0.4	0.6
ζ_c	-1	0	-0.3
f (Hz)	0.1	0.1	0.1
D_r (%)	60	60	60
σ'_v (kPa)	36	36	36

In the VDDCSS, the cross-sectional area of the specimen is constrained and therefore, changes to the height directly corresponds to changes in volume and, hence, the densification of the specimen. Figure 4-6(a), (b), and (c) present the change in D_r with respect to the number of cycles under two-way, one-way, and partial two-way loading, respectively. The base case for each loading regime is represented by the thick black solid line.

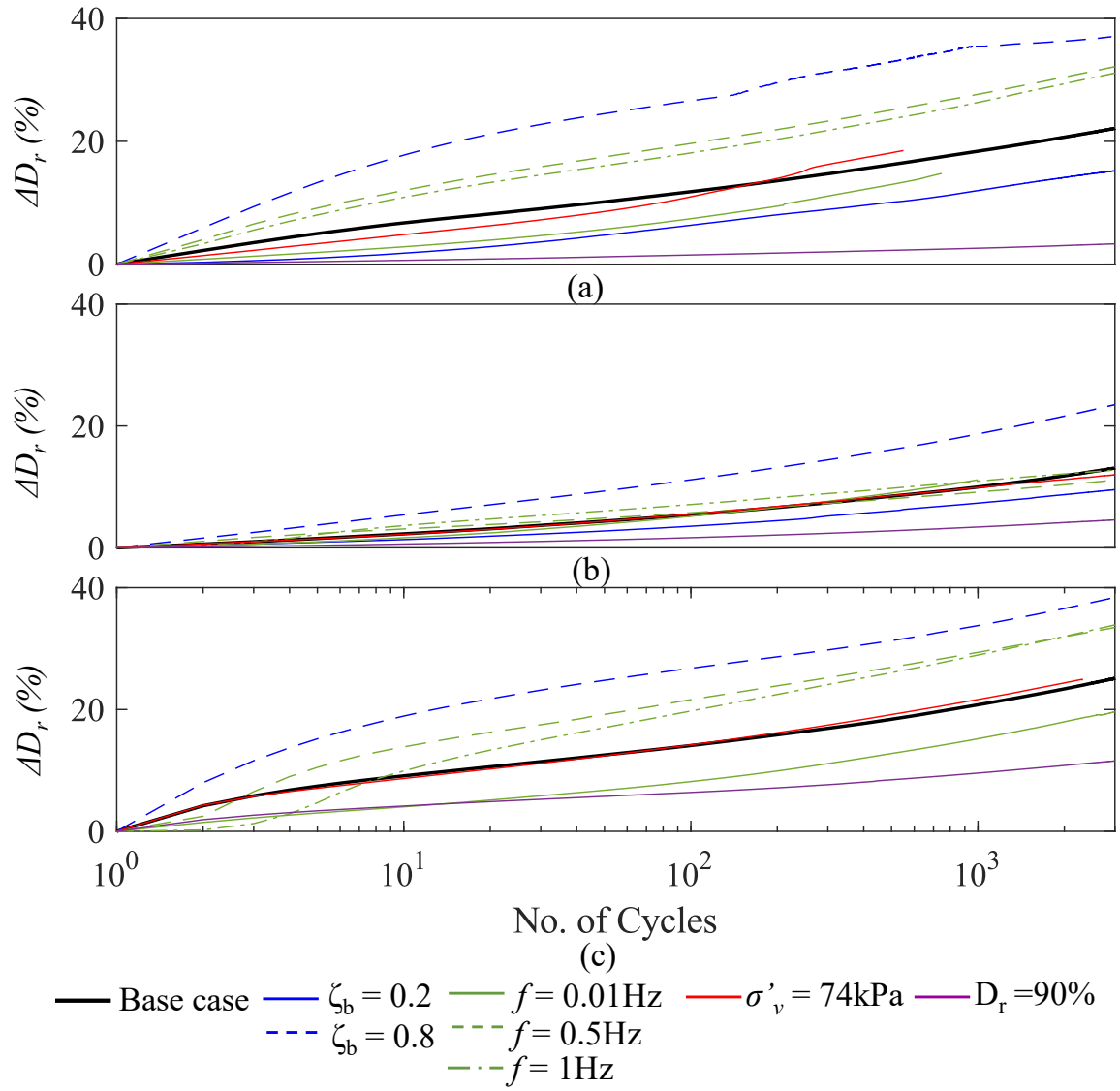


Figure 4-6 Change in D_r with cycles under drained loading(a) Two-way, base case condition: ζ_b = 0.4, ζ_c = -1 f = 0.1Hz σ'_v = 36kPa, D_r = 60%; (b) One-way, base case condition: ζ_b = 0.4, ζ_c = 0, f = 0.1Hz σ'_v = 36kPa, D_r = 60%; and (c) Partial two-way, base case condition: ζ_b = 0.6, ζ_c = -0.3 f = 0.1Hz, σ'_v = 36kPa, D_r = 60%

Since all drained tests induced densification with cycles, it can be said that the specimens were initially at a sub-characteristic stress-state, as described in Chang and Whitman (1988) and discussed in Section 1.7. The amount of densification varies considerably across the test cases. The two-way, and partial two-way loading regimes induce more densification than one-way loading. ζ_b is positively correlated with densification, as the highest ζ_b produces the most densification and vice versa across all loading conditions, supporting observations by Kang et al. (2016) and Bhaumik et al. (2017).

The influence of *f* has a marginal impact on densification for one-way loading, as all four tested frequencies induce a similar amount of densification. For two-way and partial two-way loading, *f* is positively correlated with densification. σ'_v has marginal impact on densification with the σ'_v = 74kPa producing an almost identical response to the base case when the cyclic load amplitude is normalised with the monotonic response. D_r is negatively correlated with densification as the specimen compacted to a higher D_r experience less densification compared lower D_r, an observation consistent with those of the conclusions of Chang and Whitman (1988), Kang et al. (2016) and Bhaumik et al. (2017).

The relationship between ζ_c and amount of densification for two-way and one-way loading is examined and presented in Figure 4-7 below.

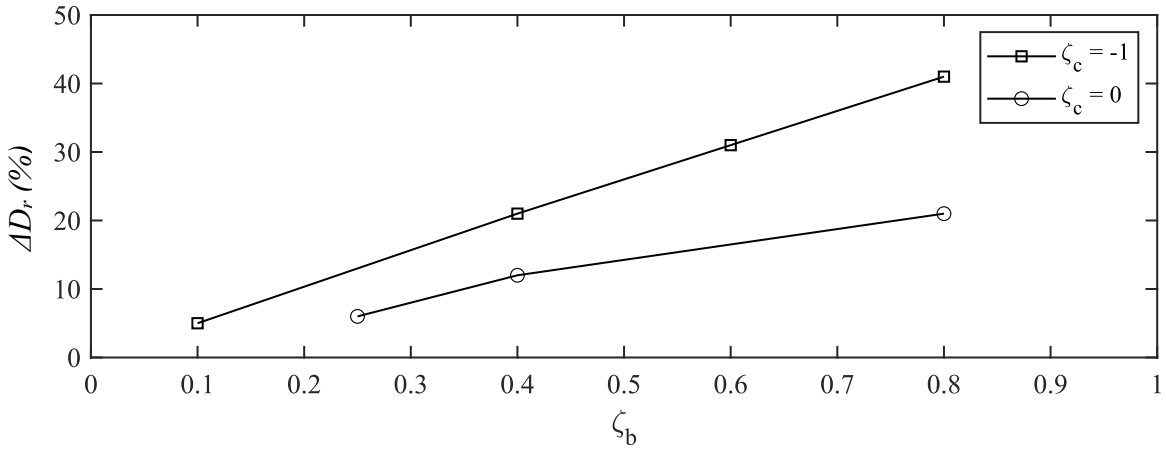


Figure 4-7 The influence of ζ_c on densification for two-way and one-way tests in drained condition

Here, a near linear relationship exists between ζ_b and densification induced in the specimen. Two-way loading approximately doubles the amount of densification compared to one-way loading, highlighting the importance of ζ_c on densification in cohesionless soils. This observation is in line with observations by Cui et al. (2019) who also observed a negative relationship between load reversal and change in void ratio. This relationship is theorised to occur due to the greater movement in soil grains that occur with high ζ_b which allows for greater expulsion of voids and densification.

The effects of ζ_b and ζ_c are further investigated by plotting a contour diagram of final densification after 3000 cycles for drained cyclic tests undertaken at σ'_v = 36kPa, D_r = 60% and f = 0.1 Hz in Figure 4-8 below.

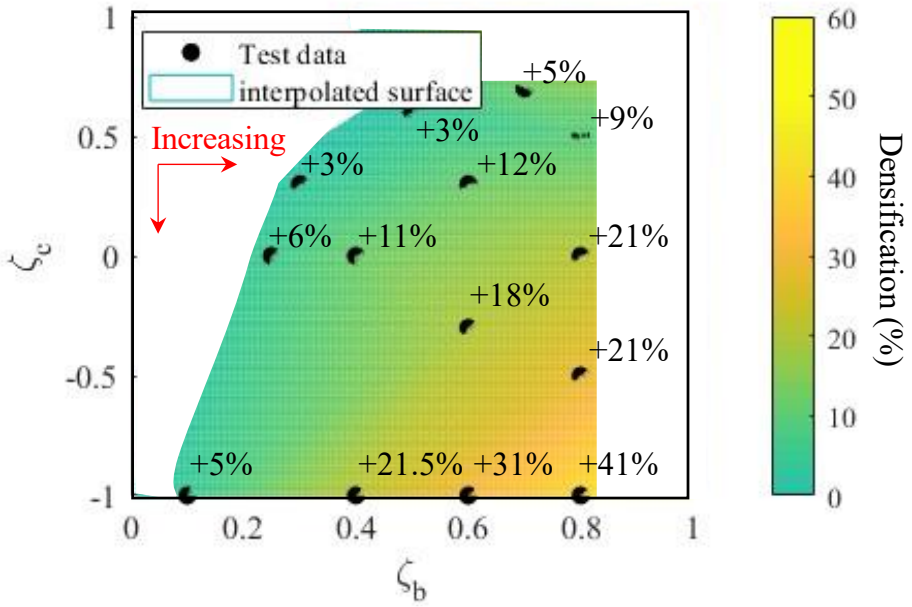


Figure 4-8 Final densification after 3000 cycles with respect to ζ_b and ζ_c (for σ'_v = 36kPa, D_r = 60% and f = 0.1 Hz)

Figure 4-8 demonstrates the combined impact of ζ_b and ζ_c on densification. Densification is positively correlated with ζ_b and negatively correlated with ζ_c. It is postulated that this is because higher extension and reversal loads induce greater movement in the soil specimen. For all investigated loading regimes, the specimen experiences most of the densification within the first 100 cycles, after which the rate of densification plateaus with cycles.

4.3.3 Accumulated ratcheting with cycles

For one-way, partial one-way and partial two-way loading, accumulated ratcheting, γ_{acc} is induced in the direction of load bias as the shear strain does not return to the original position upon unloading. The effect of ζ_b, f, D_r and σ'_v on γ_{acc} for one-way and partial two-way loading is presented in Figure 4-9 below.

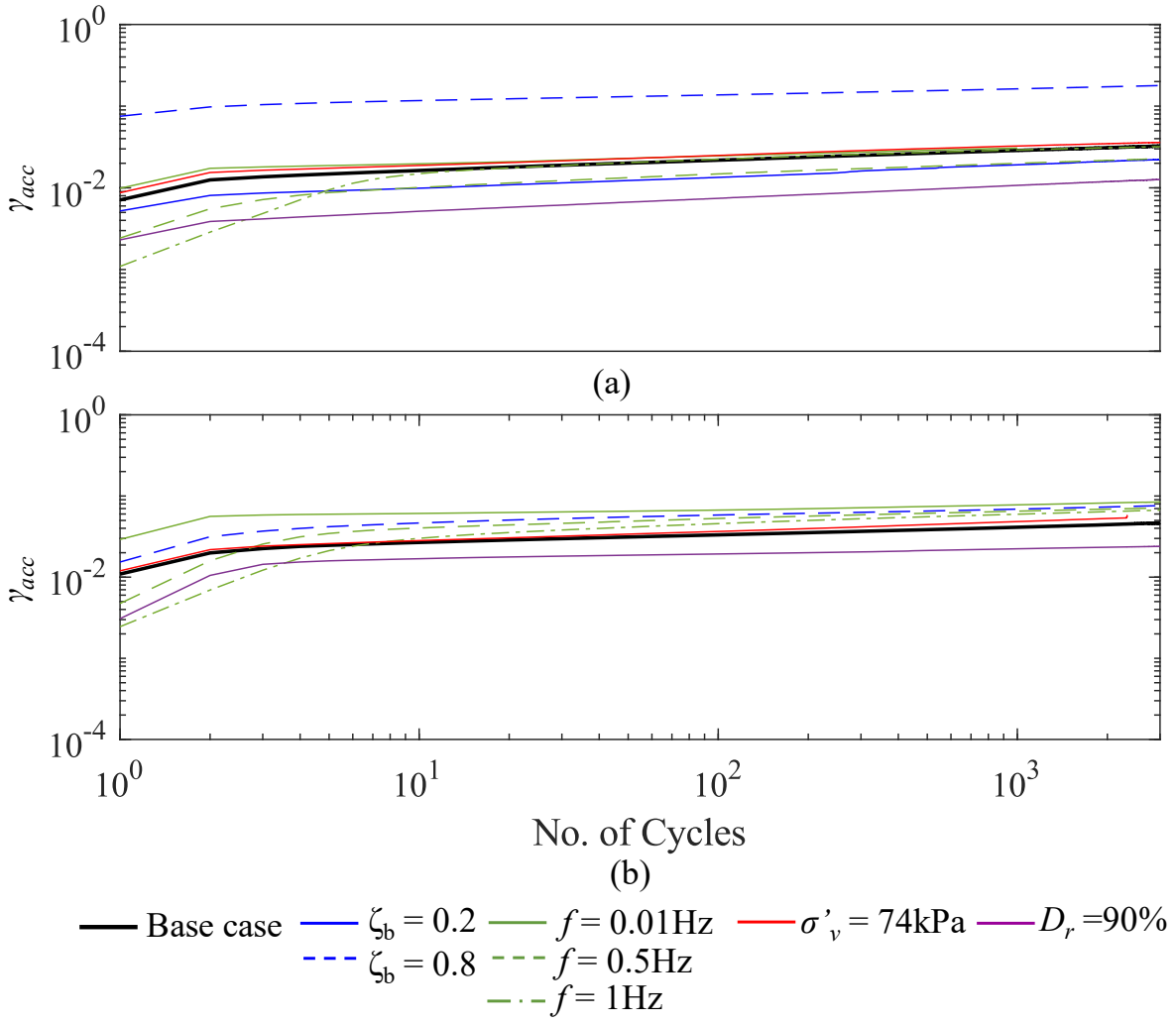


Figure 4-9 γ_{acc} with cycles under drained loading (a) One-way, base case condition: $\zeta_b = 0.4$, $\zeta_c = 0$ $f = 0.1$Hz $\sigma'_v = 36$kPa, $D_r = 60\%$; and (b) Partial two-way, base case condition: $\zeta_b = 0.6$, $\zeta_c = -0.3$ $f = 0.1$Hz, $\sigma'_v = 36$kPa, $D_r = 60\%$

The accumulated ratcheting for both loading regimes investigated has a log-linear relationship with cycles, indicating that each cycle produces less ratcheting than the cycle before. The effects of investigated parameters on accumulated ratcheting are more pronounced for one-way loading than for partial two-way loading. In both loading cases, ζ_b is positively related to accumulated ratcheting. The higher frequencies f = 0.5Hz and 1Hz experience less ratcheting for the first 10 cycles compared to the lower frequencies f = 0.01Hz and 0.1Hz, however, eventually, all f tends toward the same final value of accumulated ratcheting, indicating that accumulated ratcheting is relatively independent to f, coinciding with experimental conclusions by Arangelovsk and Towhata (2004). Once again, within the relatively small range of applied stresses investigated, σ'_v has a marginal impact on accumulated ratcheting, from both Figure

4-10(a) and (b) the response for the σ'_v = 74kPa case is practically identical to the base case due to the normalisation of loads by the monotonic response. Finally, D_r is negatively correlated with accumulated ratcheting, as for both loading regimes, denser specimen experiences less ratcheting, consistent with Wichtmann et al. (2005).

A contour plot displaying the combined impact of ζ_b and ζ_c on the final value of ratcheting, defined as $\gamma_{acc,3000}$ for drained cyclic tests undertaken at σ'_v = 36kPa, D_r = 60% and f = 0.1 Hz is shown on Figure 4-10 below.

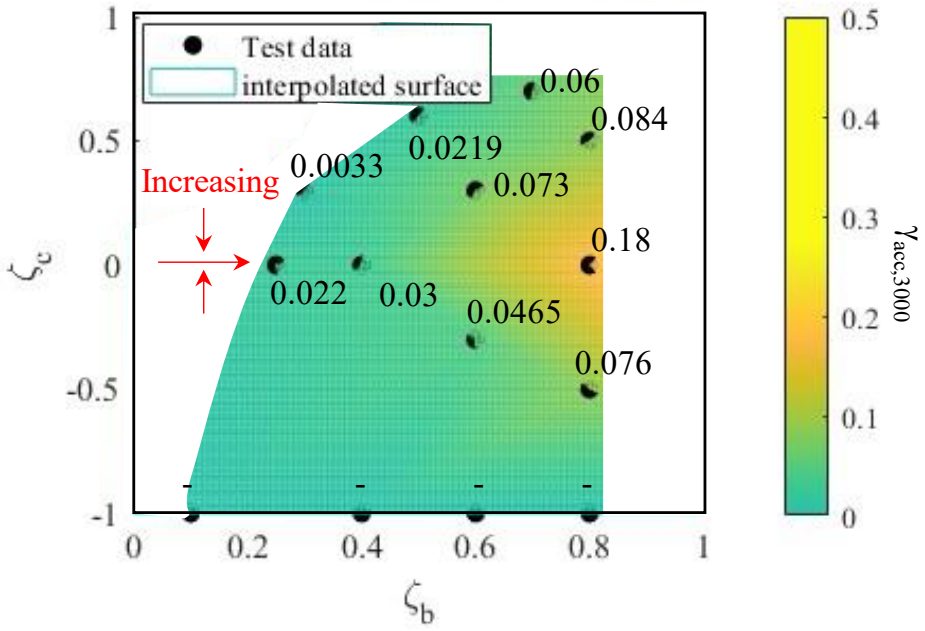


Figure 4-10 Final γ_{acc} after 3000 cycles with respect to ζ_b and ζ_c (for σ'_v = 36kPa, D_r = 60% and f = 0.1 Hz)

Here, ζ_b is positively correlated with γ_{acc}. However, the relationship between ζ_c and γ_{acc} is less clear. For constant ζ_b, ζ_c = 0 produces the greatest γ_{acc}. For ζ_c > 0, a negative relationship between ζ_c and γ_{acc} is deduced while for ζ_c < 0 it is likely that a positive relationship between ζ_c and γ_{acc} exists. For the same ζ_b, ζ_c > 0 induces higher γ_{acc} than the equivalent tests with ζ_c < 0. This is thought to be because the higher reversal load pushes the soil grains in the opposite direction to the load bias, inducing permanent strains which acts to 'undo' the ratcheting induced by the extension load.

4.3.4 Stiffness and energy dissipation with cycles

Cyclic loading induces changes in stiffness, G_{sec} and energy dissipation, η with cycles. The effect of ζ_b, f, D_r and σ'_v to changes to G_{sec} and η for two-way loading, one-way loading, and partial two-way loading are presented in Figure 4-11(a) to (f) throughout. The stiffness response is normalised with G_{max} obtained from monotonic tests in Section 4.2.

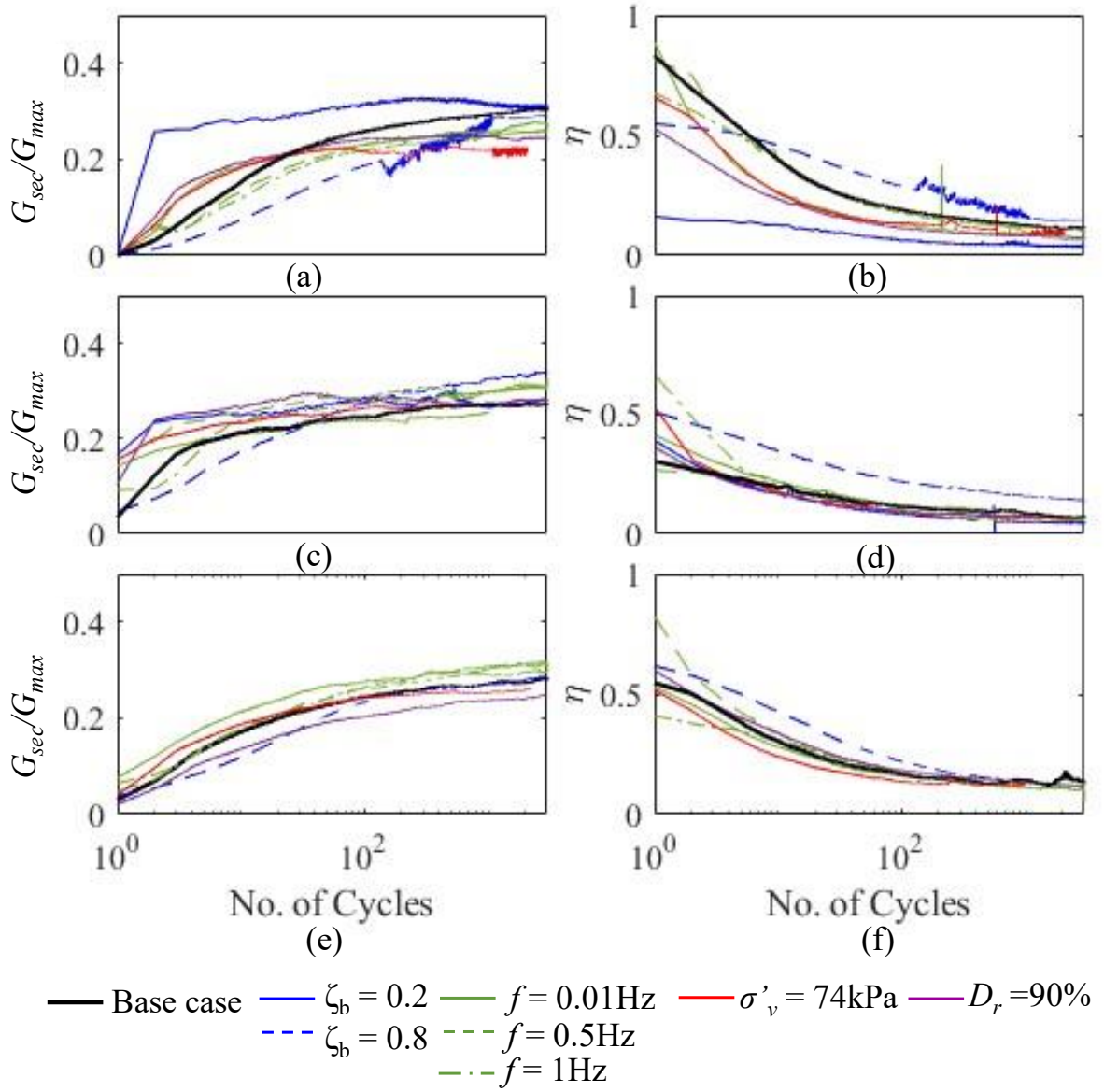


Figure 4-11 G_{sec}/G_{max} (left column) and η (right column) with cycles under drained loading (a)(b) Two-way, base case condition: ζ_b = 0.4, ζ_c = -1 f = 0.1Hz σ'_v = 36kPa, D_r = 60%; (c) (d) One-way, base case condition: ζ_b = 0.4, ζ_c = 0, f = 0.1Hz σ'_v = 36kPa, D_r = 60%; and (e) and (f) Partial two-way, base case condition: ζ_b = 0.6, ζ_c = -0.3 f = 0.1Hz, σ'_v = 36kPa, D_r = 60%

It is observed that G_{sec} increases whilst η decreases with cycles and the evolution of both parameters are inversely proportional, suggesting that cyclic loading acts to increase the resistance of the specimen. The two-way tests, (Figure 4-11(a)) display the most variation in

G_{sec} and η across the examined parameters, exhibiting a more varied spread of values compared to the one-way and partial two-way tests (Figure 4-11(c) and (e)) which show a limited variation in G_{sec} and η across all parameters examined. Nominal values of G_{sec} are negatively correlated ζ_b while η is positively correlated with ζ_b as the specimen produces a stiffer response at low cyclic amplitudes. The influence of f, σ'_v and D_r are negligible on the evolution of G_{sec} and η as all varied parameters produce responses in proximity across all loading regimes.

The amount of change to G_{sec} and η diminish with cycles and eventually the rate of changes of both parameters plateaus. This plateau is reached quicker for lower ζ_b. For a relatively low ζ_b (such as the case of $\zeta_b = 0.1$ and $\zeta_c = -1$), equilibrium of stiffness improvement is reached within 3000 cycles. This is not the case for equivalent tests at high ζ_b (e.g., $\zeta_b = 0.8$ and $\zeta_c = -1$) where it appears that further cycling could increase the stiffness further.

To explore this, the combined effects of ζ_b and ζ_c on stiffness improvement, defined as the final stiffness value, $G_{sec,3000}$ divided by the first stiffness value, $G_{sec,1}$ is shown on the contour plot presented in Figure 4-12 below.

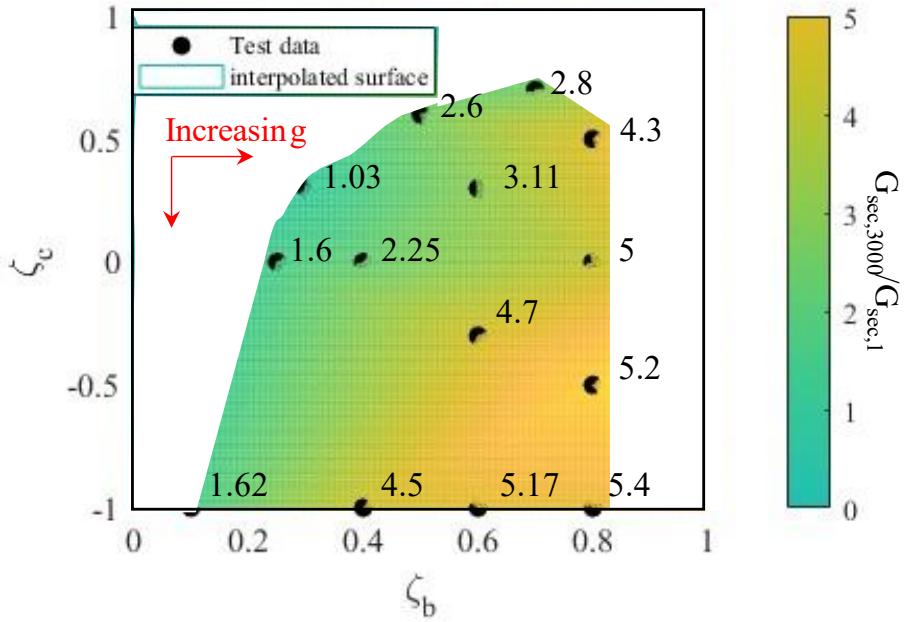


Figure 4-12 $G_{sec,3000}/G_{sec,1}$ with respect to ζ_b and ζ_c (for specimen prepared to σ'_v = 36kPa, D_r = 60% and f = 0.1 Hz)

Stiffness improvement is positively corelated with ζ_b and negatively correlated with ζ_c, consistent with observations by Nong and Park (2021). It is postulated that two phenomena

generate this increase in resistance. First is the densification of the specimen as shown in Section 4.2. Secondly, cyclic loading brings soil grains closer together, inducing 'interlocking' where the soil particles become tightly compacted, further strengthening the specimen.

To explore the effect of densification on stiffness increase, the amount of stiffness increases with respect to ΔD_r is presented in Figure 4-13.

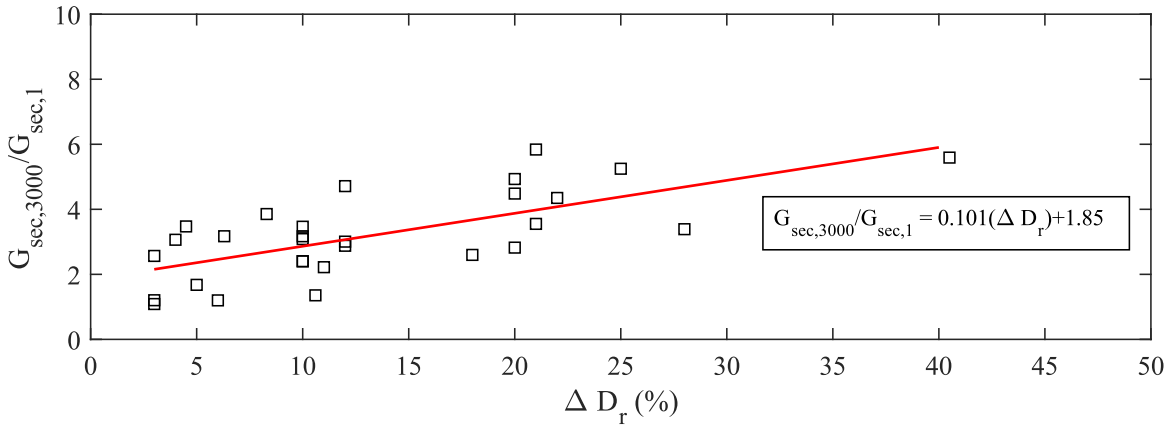


Figure 4-13 The effect of densification on stiffness improvement from drained tests

The trends in Figure 4-13 suggest that the increase in stiffness is directly proportional to densification induced by cyclic loading. This observation suggests a correlation between densification and the increase in G_{sec}.

4.3.5 Post-cyclic behaviour

The 'post-cyclic' behaviour of the specimen, i.e., the monotonic response of the specimen after cyclic loading has been induced is explored in this section. The effect of ζ_b, f, D_r and σ'_v on post-cyclic behaviour for two-way loading, one-way loading, and partial two-way loading are shown in Figure 4-14(a) to (c) throughout and summarised in Table 4-2.

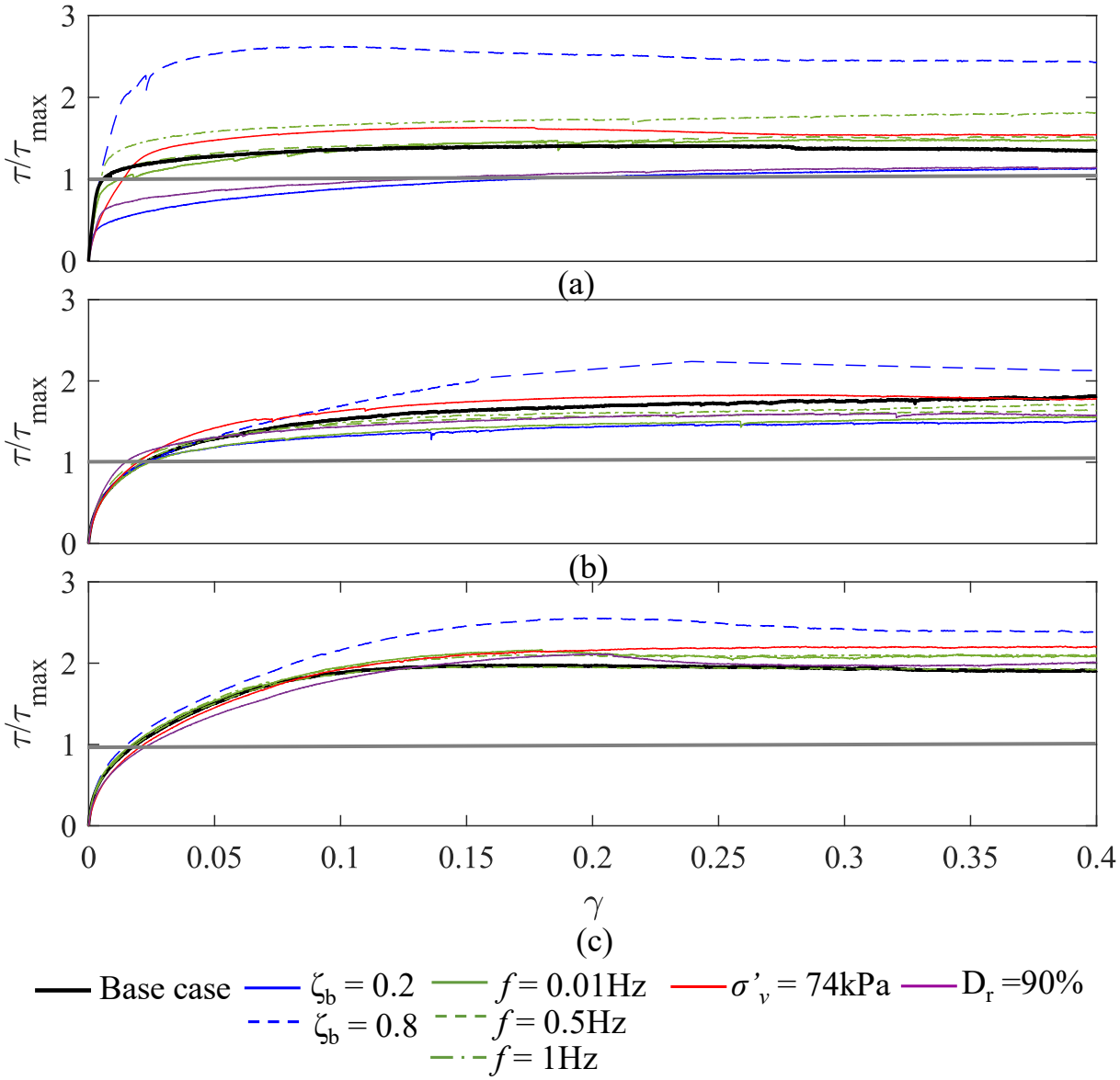


Figure 4-14 Post-cyclic drained behaviour, grey dashed line represents where $\tau/\tau_{max} = 1$ (a) Two-way, base case condition: $\zeta_b = 0.4$, $\zeta_c = -1$ $f = 0.1$Hz $\sigma'_v = 36$kPa, $D_r = 60\%$; (b) One-way, base case condition: $\zeta_b = 0.4$, $\zeta_c = 0$, $f = 0.1$Hz $\sigma'_v = 36$kPa, $D_r = 60\%$; and (c) Partial two-way, base case condition: $\zeta_b = 0.6$, $\zeta_c = -0.3$ $f = 0.1$Hz, $\sigma'_v = 36$kPa, $D_r = 60\%$

The post-cyclic behaviour of all drained specimens exhibits an increase from the original monotonic capacity, ranging from 1.1 to 2.5 times. Notably, the same physical factors that influence densification and stiffness improvement in Section 4.3.2 and 4.3.4 are observed here. This suggests a close link between densification, stiffness improvement and post-cyclic capacity increase. For example, the same ζ_b, ζ_c and f that induced the most densification and stiffness increase is associated with the greatest post-cyclic capacity here. Additionally, D_r is negatively related to both densification and post-cyclic capacity increase and like densification, post-cyclic capacity is relatively independent of σ'_v when the cyclic amplitude is normalised by

its monotonic response. These results indicate that it is likely that the same mechanisms that contribute to densification and stiffness increase also increase post-cyclic capacity of cohesionless soils.

The post-cyclic response of soils is explored further by examining the combined effects of ζ_b and ζ_c on increase in post-cyclic strength and post-cyclic stiffness (defined as $\tau_{postcyc}/\tau_{max}$ and $G_{max,\text{postcyc}}/G_{max,mono}$ respectively). Contour plots showing the variation of $\tau_{postcyc}/\tau_{max}$ and $G_{max,postcyc}/G_{max,mono}$ for tests undertaken at σ'_v = 36kPa, D_r = 60% and f = 0.1 Hz in Figure 4-15(a) and (b) respectively.

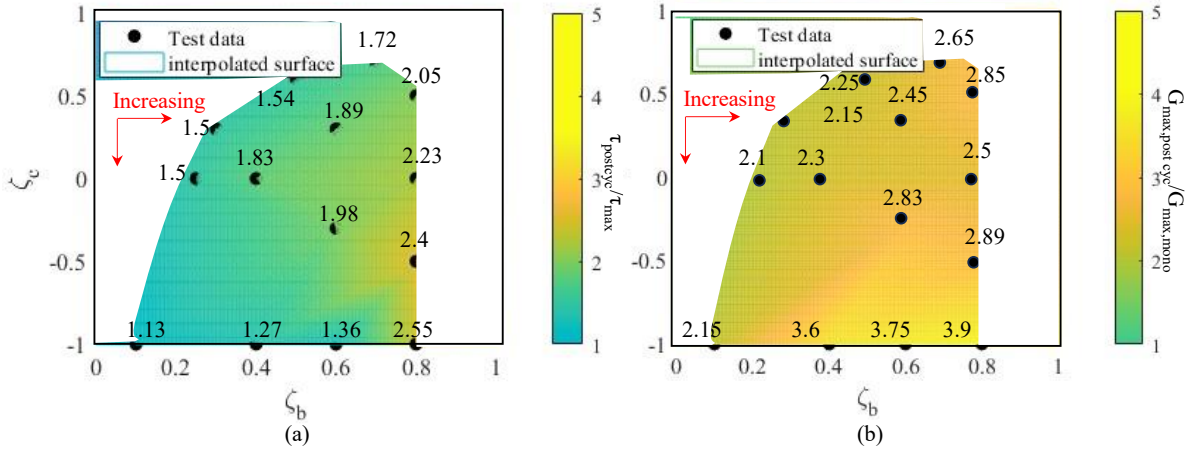


Figure 4-16 Post-cyclic strength increase with respect to change in D_r, red line shows line of best fit

Similarities between the trends in densification and post-cyclic behaviour can be observed, as the combination of ζ_b and ζ_c influence the post-cyclic behaviour in the same way they influence densification. The increase in post-cyclic capacity and post-cyclic stiffness is positively correlated with ζ_b and negatively correlated with ζ_c.

These increases are theorised to arise from densification and 'interlocking'. Figure 4-16 displays the post-cyclic capacity increase of all tests as a function of ΔD_r from cyclic loading.

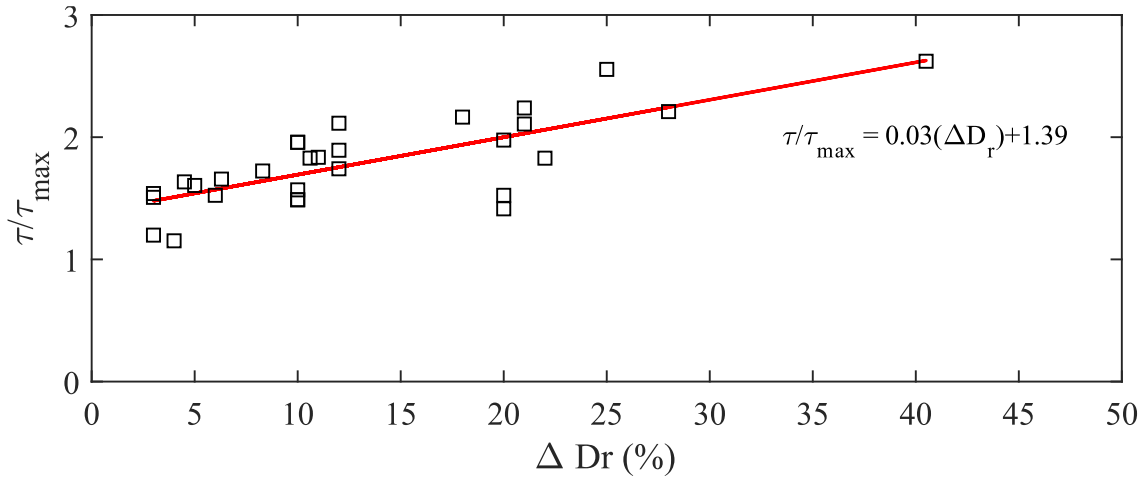


Figure 4-15 Effect of ζ_b and ζ_c on post-cyclic drained behaviour (a) post-cyclic strength; and (b) post-cyclic initial stiffness

There is a clear positive relationship between ΔD_r and post-cyclic capacity, suggesting that densification of the specimen directly contributes to increased shear strength. As the post-cyclic capacity exceeds those derived from monotonic tests of even the densest specimen, part of the increased capacity is attributed to 'interlocking'.

Conventional critical state theory suggests that at a fixed σ'_v, both 'loose' and 'dense' sands tend to the same τ_{res} at critical state irrespective of the density of the specimen. Results from the post-cyclic tests show a large range of τ_{res} values, despite being undertaken at the same σ'_v, most likely due to 'interlocking'. These results indicate that conventional critical state theory does not necessarily fully encapsulate all cyclic loading effects. Figure 4-17 presents the axial strain behaviour of post-cyclic drained tests.

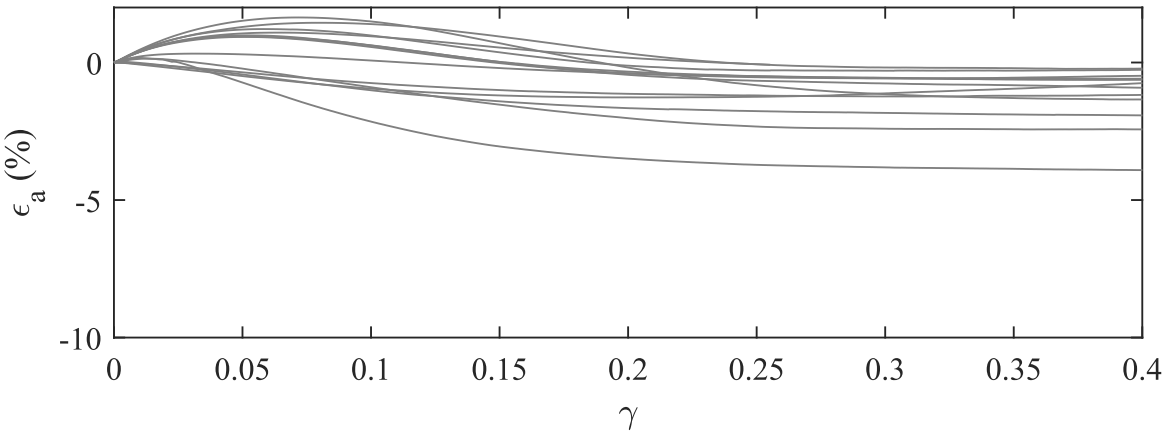


Figure 4-17 Post-cyclic axial strain of all drained cyclic tests on CX material

All drained post-cyclic tests exhibit initially contractive followed by dilative behaviour, associated with 'dense' soils. This demonstrates that cyclic loading alters the state of cohesionless soils from a 'loose' to 'dense' in the VDDCSS after approximately 100 cycles.

4.3.6 Multidirectional cyclic loading

So far, the cyclic loading regimes discussed have been associated with unidirectional loading. The VDDCSS allows for multidirectional cyclic loading, a more realistic condition for OWT as discussed in Section 2.7.4 and 2.7.5. This section explores the multidirectional cyclic response of soils in in drained condition. Multidirectional tests are undertaken considering perpendicular loading, which involve loading at constant stress along one axis (x-direction) and cycling in the orthogonal axis (y-axis), under two-way, one-way, or partial one-way loading conditions. Figure 4-18 presents the multidirectional strain response for the multidirectional tests as described in Table 4-2 at two relative densities, D_r = 60% and D_r = 90% respectively.

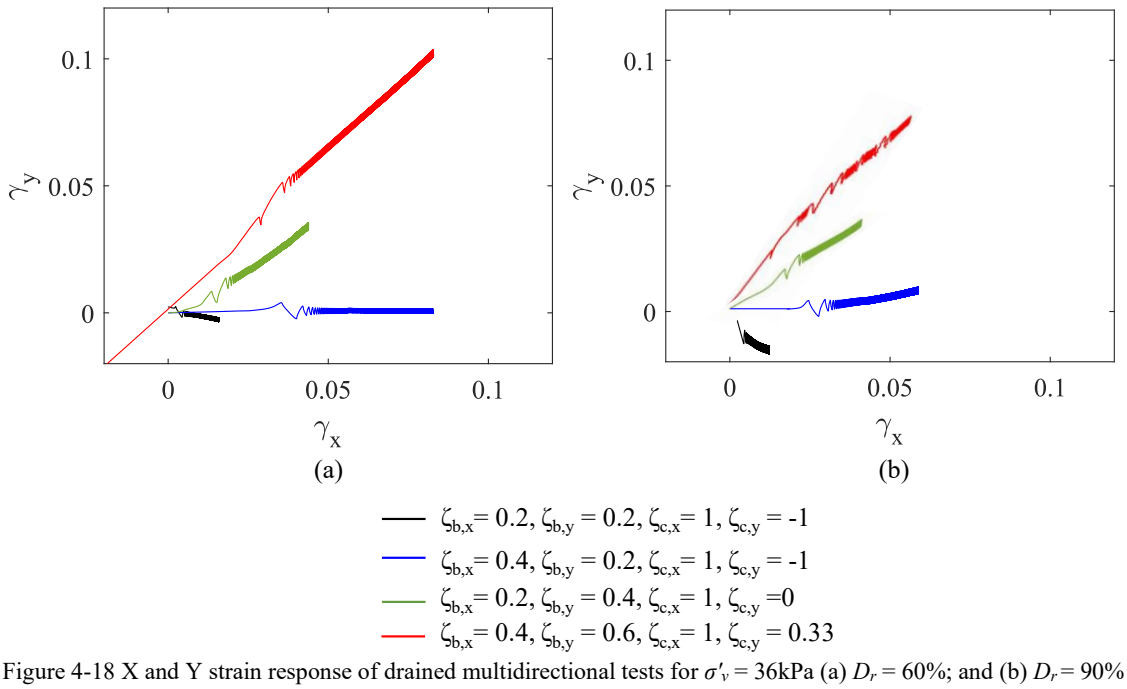


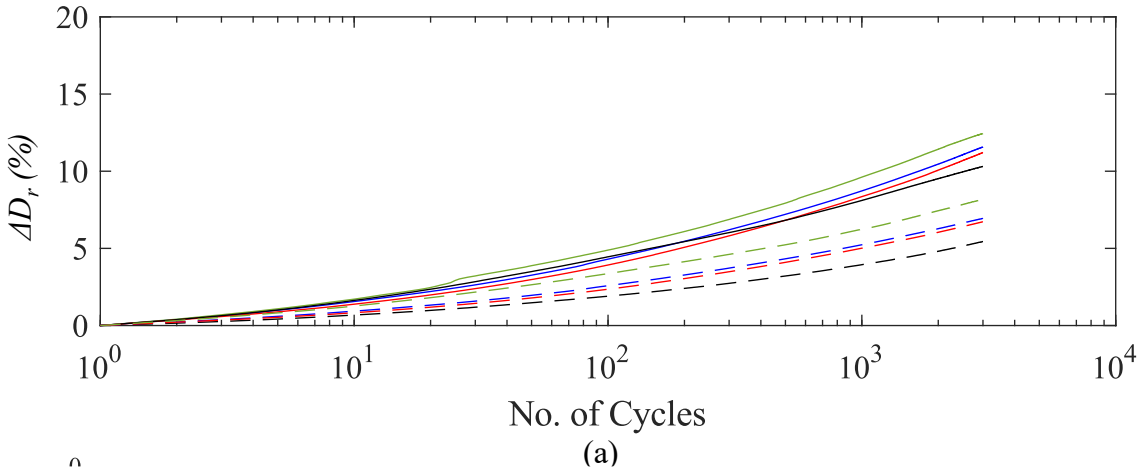
Figure 4-18 X and Y strain response of drained multidirectional tests for σ'_v = 36kPa (a) D_r = 60%; and (b) D_r = 90%

For two-way cyclic tests, strain accumulates in the direction of constant stress (x-direction). Under one-way and partial one-way tests, the direction of the resultant strain accumulates at an angle (θ_{multi}) to the x-axis. Across both densities investigated, θ_{multi} is positively correlated to

the constant stress value in the x-direction and cyclic amplitude in the y-direction. Overall, the specimen compacted to D_r = 90% experiences less ratcheting than the D_r =60% specimen across the same number of cycles.

In multidirectional tests (both drained and undrained), ratcheting is defined as the strain accumulated in the direction of loading which is in the x-direction for two-way tests and in both x and y directions for one-way and partial one-way tests. The nominal secant stiffness with cycles is normalised with the maximum shear stiffness determined in Section 4.2. Post-cyclic tests were sheared along the axis of constant stress, i.e., the x-axis, and normalised with maximum shear stress value obtained in Section 4.2.

The densification, accumulated ratcheting and normalised secant stiffness and energy dissipation with cycles and post-cyclic response from the multidirectional drained tests are presented in Figure 4-19.



(a)

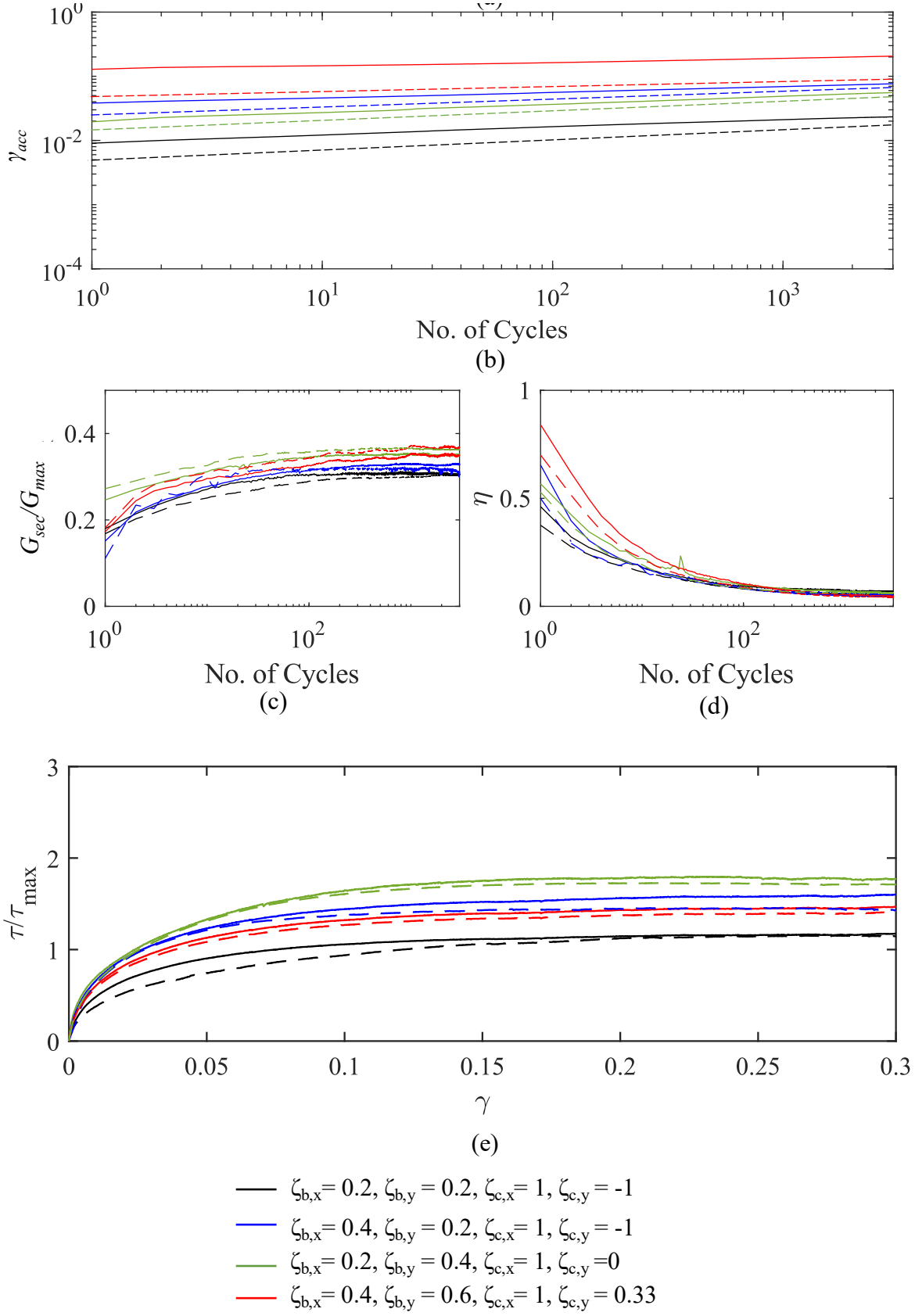


Figure 4-19 Multidirectional drained cyclic behaviour, solid lines D_r = 60%, dashed lines D_r = 90% (a) Densification; (b) Accumulated ratcheting; (c) Normalised stiffness; (d) Energy dissipation; and (e) Post-cyclic behaviour

Results from multidirectional tests echo conclusions drawn in previous sections. However, multidirectional tests additionally observe that higher constant stress amplitudes ($\zeta_{b,x}$) in the x-axis act to increase the accumulated ratcheting. Higher cycling amplitudes ($\zeta_{c,y}$) act to increase the θ to the x-axis for one-way and partial one-way tests.

All tests experience an increase in G_{sec}, the dense specimens achieve higher nominal values of G_{sec} however experience less stiffness increase compared to their loose counterparts after cycling. Like the unidirectional tests, stiffness increase is positively proportional to ζ_b and negatively proportional to ζ_c. Energy dissipation values are higher for the looser specimens, indicating lower shear resistance compared to denser counterparts.

Finally, the post-cyclic capacity of all multidirectional tests increases from the monotonic capacity. The greatest post-cyclic capacity corresponds to the specimen with the highest $\zeta_{b,x}$. This can be attributed to the 'interlocking' that develops in the direction of constant stress. Since post-cyclic tests were sheared in the direction of constant stress, specimens with greater constant stress amplitudes would presumably produce more 'interlocking'.

This effect is explored further by considering the impact of post-cyclic behaviour sheared in the transverse direction, as all post-cyclic tests thus far refer to those sheared in the direction of load bias. Several tests from Section 4.3.1 were repeated with the post-cyclic load applied in the orthogonal plane to the cyclic loading to examine the transverse post-cyclic behaviour of the specimen. Figure 4-20 presents the post-cyclic capacity of specimens sheared in the y-axis and the corresponding tests sheared in the x-direction.

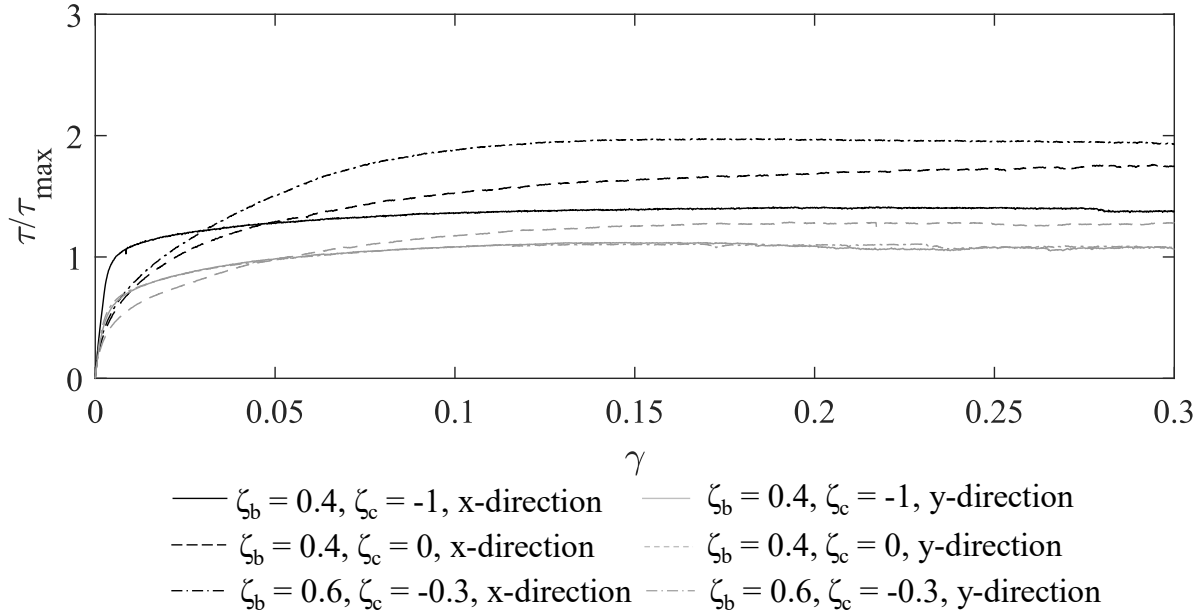


Figure 4-20 Post-cyclic drained behaviour of selected two-way, one-way, and partial two-way tests, black and grey lines denote the post-cyclic capacity in direction of loading an orthogonal direction respectively.

While post-cyclic tests in the transverse direction exhibit an increase in capacity compared to monotonic tests, Figure 4-20 clearly illustrates that this increase is less pronounced than post-cyclic tests on specimens subjected to shearing in the direction of loading. This observation suggests that densification cannot solely explain the increase in post-cyclic capacity, as both longitudinal and transverse tests were conducted on specimens with the same D_r. As mentioned earlier, the interlocking of grains is an additional factor that contributes to the increase in post-cyclic capacity. It is likely that the interlocking effect is more significant in the direction of cyclic loading compared to the orthogonal direction, offering a plausible explanation for the behaviour observed in Figure 4-20.

4.4 Undrained VDDCSS tests

This section presents and discusses the undrained VDDCSS tests conducted on CX material, i.e., undrained test conditions. Section 4.3 has identified and discussed several significant physical properties affecting cyclic behaviour in drained conditions. This investigation extends their impact on undrained cyclic behaviour, focusing on understanding the influence of ζ_b, ζ_c, σ'_v and D_r on undrained cyclic behaviour is presented. The effect of loading frequency is not considered as here it has been investigated by Nong and Park (2021). For constant volume tests

ζ_b is the ratio of applied shear stress with respect to the peak τ_{peak} obtained from corresponding monotonic tests in at the same stress level.

4.4.1 Test results schedule and results

A total of 23 undrained VDDCSS tests were completed in this investigation. All tests were subjected to a maximum of 3000 cycles of loading unless specimen failure occurred prior to reaching 3000 cycles. A summary of the undrained cyclic test conditions and key results from the tests are presented in Table 4-4 below.

Table 4-4 VDDCSS Constant volume test schedule

Test ID	Soil	ζ_b	ζ_c	f (Hz)	σ'_v (kPa)	D_r (%)	$\gamma_{av,10}$ (%)	$\gamma_{av,100}$ (%)	$\gamma_{av,1000}$ (%)	N_f [-]	τ_{post}/τ_{peak}
Unidirectional two-way tests											
VDDCSS_CX_60_36_i_UTW_U1	CX	0.1	-1	0.1	36	60	-	-	-	-	0.7
VDDCSS_CX_60_36_i_UTW_U3	CX	0.4	-1	0.1	36	60	-	-	-	108	-
VDDCSS_CX_60_36_i_UTW_U4	CX	0.4	-1	0.1	36	60	-	-	-	5	-
VDDCSS_CX_90_36_i_UTW_U	CX	0.4	-1	0.1	36	90	-	-	-	-	0.4
VDDCSS_CX_60_74_i_UTW_U	CX	0.4	-1	0.1	74	60	-	-	-	150	-
Unidirectional one-way tests											
VDDCSS_CX_60_36_i_UOW_U1	CX	0.2	0	0.1	36	60	0.086	0.100	12	1980	-
VDDCSS_CX_60_36_i_UOW_U2	CX	0.4	0	0.1	36	60	12.5	43.6	-	1370	-
VDDCSS_CX_60_36_i_UOW_U3	CX	0.8	0	0.1	36	60	25.8	-	-	26	-
VDDCSS_CX_90_36_i_UOW_U	CX	0.4	0	0.1	36	90	0.160	0.200	0.310	-	0.95
VDDCSS_CX_60_74_i_UOW_U	CX	0.4	0	0.1	74	60	21.3	48.9	-	10	-
Unidirectional partial one-way tests											
VDDCSS_CX_60_36_i_U1PW_U1	CX	0.3	0.3	0.1	36	60	0.039	0.057	9	1300	-
VDDCSS_CX_60_36_i_U1PW_U2	CX	0.5	0.6	0.1	36	60	0.300	17.70	-	40	-
VDDCSS_CX_60_36_i_U1PW_U3	CX	0.6	0.3	0.1	36	60	22.40	39.82	-	2	-
VDDCSS_CX_90_36_i_U1PW_U	CX	0.5	0.6	0.1	36	90	0.019	0.045	0.116	-	1.4
VDDCSS_CX_60_74_i_UP1W_U	CX	0.5	0.6	0.1	74	60	3	6.3	10.9	40	-
Multidirectional tests											
VDDCSS_CX_60_74_i_MD1_U (x)	CX	0.2	1	0.1	74	60	0.40	-	-	13	0.73
VDDCSS_CX_60_74_i_MD1_U (y)		0.2	-1								
VDDCSS_CX_60_74_i_MD2_U (x)	CX	0.4	1	0.1	74	60	0.16	0.54	9	124	-
VDDCSS_CX_60_74_i_MD2_U (y)		0.2	-1								
VDDCSS_CX_60_74_i_MD3_U (x)		0.2	1								

VDDCSS_CX_60_74_i_MD3 _U(y)	CX	0.4	0	0.1	74	60	0.12	0.13	0.15	-	-
VDDCSS_CX_60_74_i_MD4_U (x)	CX	0.4	1	0.1	74	60	0.19	0.34	46	349	-
VDDCSS_CX_60_74_i_MD4_U (y)		0.6	0.33								
VDDCSS_CX_100_74_i_MD1_U (x)	CX	0.2	1	0.1	74	100	0.21	0.27	0.37	-	0.70
VDDCSS_CX_100_74_i_MD1_U (y)		0.2	-1								
VDDCSS_CX_100_74_i_MD2_U (x)	CX	0.4	1	0.1	74	100	0.08	0.11	0.14	-	0.93
VDDCSS_CX_100_74_i_MD2_U (y)		0.2	-1								
VDDCSS_CX_100_74_i_MD3_U (x)	CX	0.2	1	0.1	74	100	0.04	0.06	0.07	-	0.80
VDDCSS_CX_100_74_i_MD3_U (y)		0.4	0								
VDDCSS_CX_100_74_i_MD4_U (x)	CX	0.4	1	0.1	74	100	0.19	0.27	34	559	-
VDDCSS_CX_100_74_i_MD4_U(y)		0.6	0.33								

Of the 23 tests,16 specimens failed within 3000 cycles. Selected tests are presented in Figure 4-21(a) to (f) throughout., displaying the cyclic stress-strain behaviour and stress-paths. The CSL is also shown in red on the stress path. The cycle of failure *Nf* criterion adopted in this study refers to when γ_{cyc} reaches 15% or Δu reaches 80%.

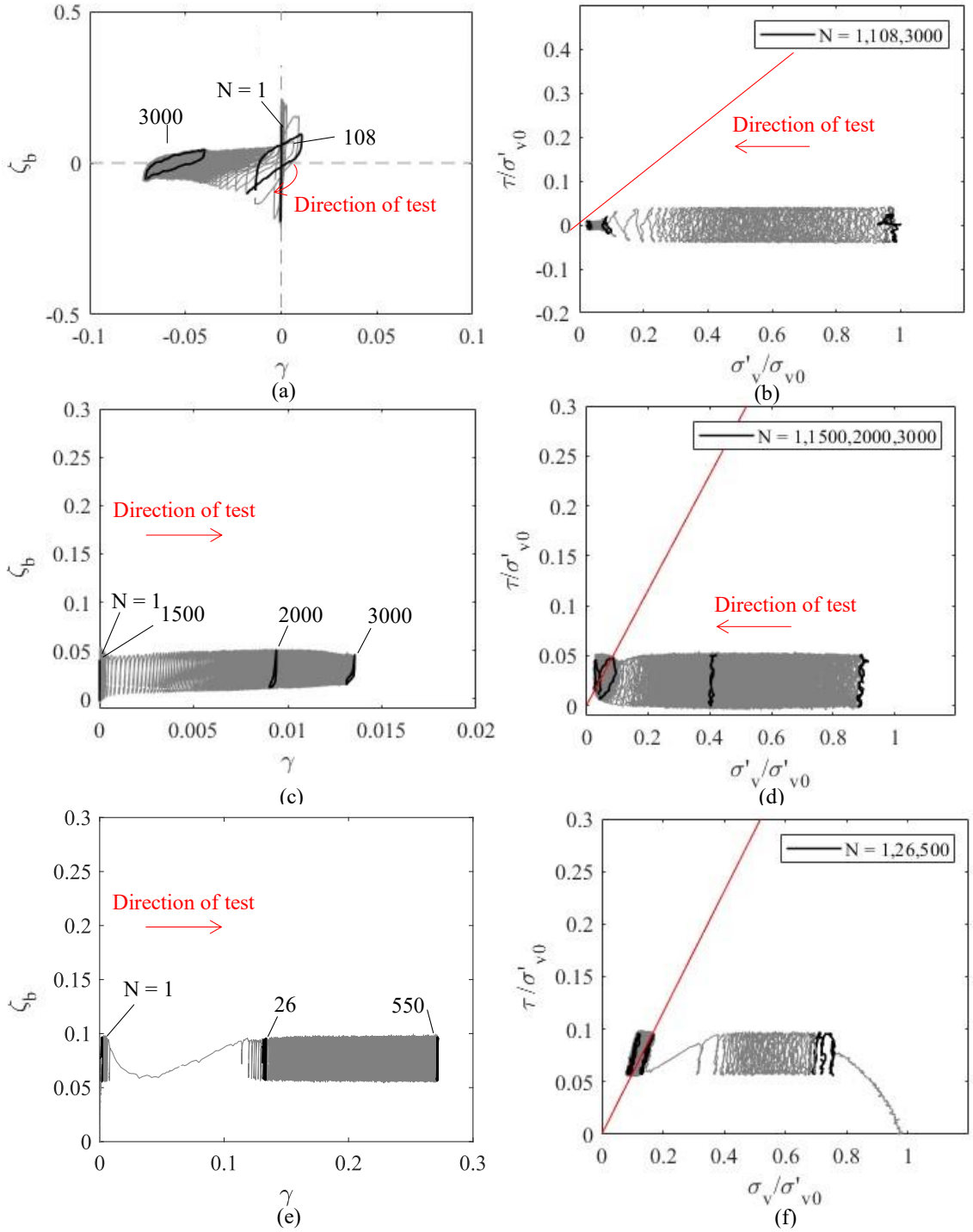


Figure 4-21 Undrained cyclic behaviour at D_r = 60%, σ'_v = 36kPa (a) Stress-strain ζ_b = 0.2, ζ_c =-1; (b) Stress-path ζ_b = 0.2, ζ_c = -1; (c) Stress-strain ζ_b = 0.4, ζ_c = 0; (d) Stress-path ζ_b = 0.4, ζ_c = 0; (e) Stress-strain ζ_b = 0.5, ζ_c = 0.6 (f) Stress-path ζ_b = 0.5, ζ_c = 0.6

4.4.2 Porewater pressure generation with cycles

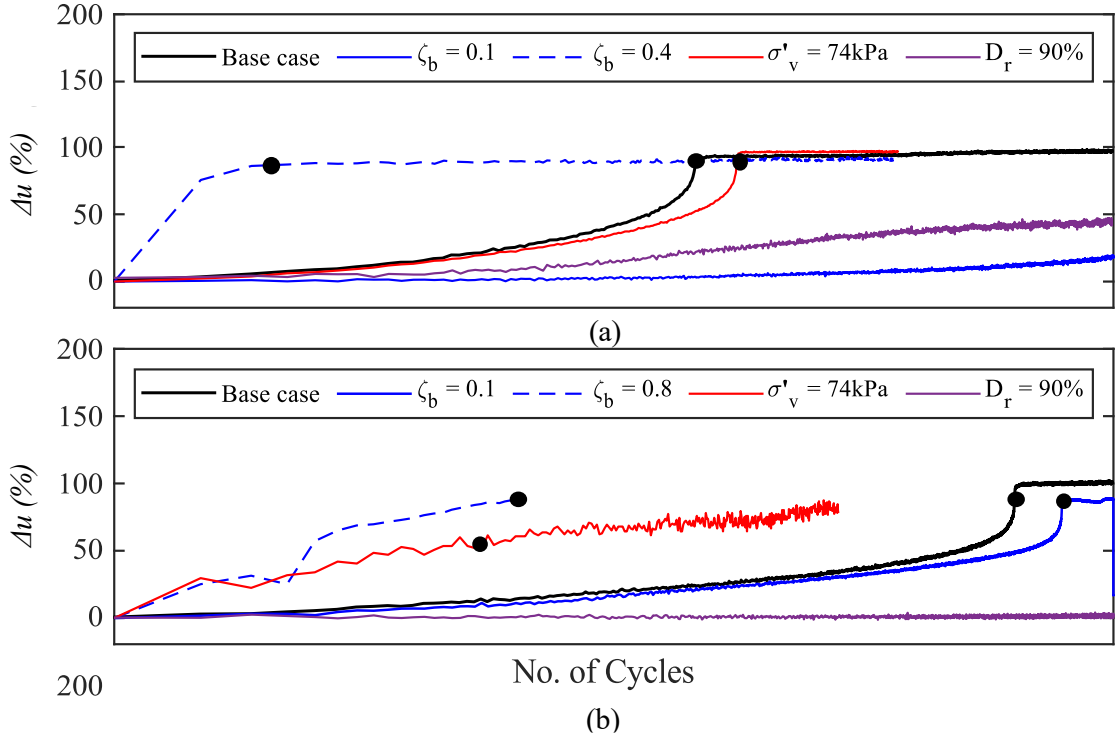
In undrained testing conditions, instead of densification, the development of porewater pressure, Δu occurs reducing σ'_v with cycles, see Figure 4-24(b),(d) and (e). An assumption in VDDCSS interpretation is that the $\Delta\sigma'_v$ is synonymous with pressure, Δu, (ref. Andersen (2015)).

This section presents and discusses the influence of ζ_b, ζ_c, σ'_v and D_r on the interpreted Δu from two-way, one-way, and partial one-way loading. These effects are considered against a base case condition, summarised in Table 4-5.

Table 4-5 Base case test conditions for constant volume tests

	Unidirectional two-way	Unidirectional one-way	Unidirectional partial two-way
ζ_b	0.2	0.4	0.5
ζ_c	-1	0	0.6
f (Hz)	0.1	0.1	0.1
D_r (%)	60	60	60
σ'_v (kPa)	36	36	36

Figure 4-22 presents the generation of Δu with number of cycles under two-way, one-way, and partial one-way loading, respectively. The cycle of failure N_f is represented by the solid black dot on the figures.



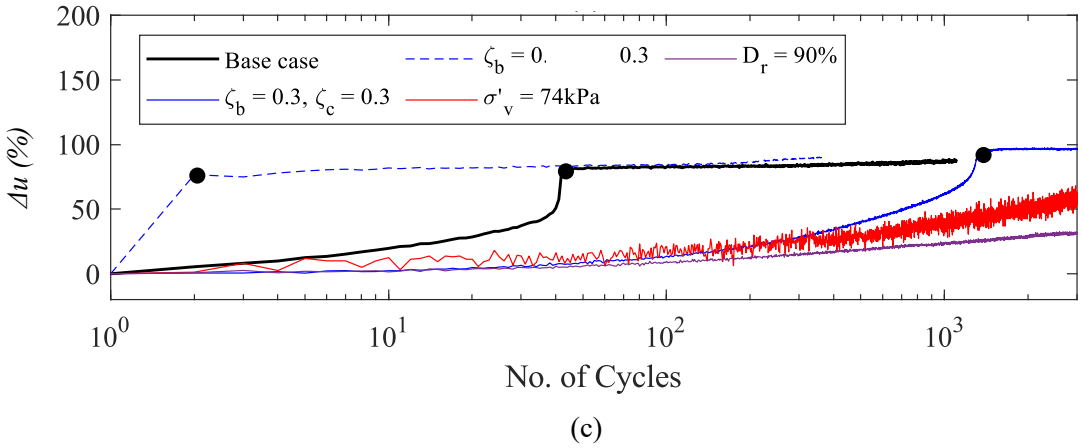


Figure 4-22 Δu with cycles under undrained loading, black dot denotes N_f (a) Two-way loading, base case: ζ_b = 0.2, ζ_c = -1, σ'_v = 36kPa, D_r = 60%; (b) One-way loading, base case: base case: ζ_b = 0.4, ζ_c = 0 σ'_v = 36kPa, D_r = 60%; and (c) Partial one-way loading base case: ζ_b = 0.5, ζ_c =0.6 σ'_v = 36kPa, D_r = 60%

For specimens that do fail, a rapid increasein Δu occurs at N_f which coincides with Δu = 90%, previous researchers have similarly observed rapid increases in Δu at N_f in undrained conditions on cohesionless soils by Nong et al. (2020), Do et al. (2023), Ma et al. (2023), Zhou et al. (2023) and Gao et al. (2024). Despite whether the specimen failed or not during cycling, all tests in this experiment generated some level of Δu with cycles. ζ_b is positively correlated with Δu, with higher ζ_b inducing a more rapid increase in porewater pressure with cycles than lower ζ_b. Therefore, ζ_b is negatively proportional to N_f in line with experimental observations by Andersen (2015). For low ζ_b, such as ζ_b = 0.2, ζ_c = -1, little Δu is generated and the specimen does not fail within 3000 cycles.

Under all loading regimes, the denser specimen consistently produces a significantly lower Δu and none of the 'dense' specimen fail within 3000 cycles. The marked influence of ζ_b and D_r on Δu observed in this study is consistent conclusions by Kokusho (2013), Andersen (2015) and Do et al. (2023).

Results from Section 4.2.3 demonstrate that the monotonic undrained response of CX material observes a peak shear stress, τ_{peak}. Once τ_{peak} is overcome, the soil exhibits either strain softening for 'loose' specimens or hardening for 'dense' specimens. For 'loose' specimens, the point at which τ_{peak} is overcome coincides with the point where Δu

rapidly increases (around 80 to 90%) and liquefaction occurs. It is theorised that under repeated cyclic loads cause 'loose' specimen to 'overcome' τ_{peak}, with higher ζ_b leading the specimen overcoming τ_{peak} more rapidly than lower ζ_b. This occurs when Δu increases to approximately 90%. Subsequently, the specimen exhibits strain-softening, and further cycles exhibit significantly reduced resistance. The case of 'dense' specimens is more complicated. In monotonic loading, if a τ_{peak} is observed, then strain softening is followed by strain hardening, which should continue to the steady state. If a τ_{peak} is not observed, then the specimen experiences only strain hardening. The point at which strain softening turns to strain hardening corresponds to the point where Δu changes from positive to negative (phase transformation). In this suite of cyclic tests, Δu is not seen to change from positive to negative, and thus phase transformation is not reached during cycling for dense specimens. Finally, the effect of σ'_v and loading asymmetry is marginal as the same trend in u is observed for the two σ'_v and across all regimes due to load normalisation.

4.4.3 Accumulated ratcheting with cycles

This section presents the accumulated ratcheting, γ_{acc} induced in soil specimens in undrained tests. The effects of ζ_b, ζ_c, σ'_v and D_r are investigated and considered against the base case condition described in Table 4-5. A maximum shear strain of 80% can be induced in the VDDCSS. Several one-way and partial one-way tests were terminated prior to 3000 cycles as the accumulated strain in the specimen reached the limit of the apparatus. Figure 4-23(a) and (b) presents the accumulated ratcheting response of the one-way and partial one-way undrained tests. N_f is represented by the solid black dot on the figures.

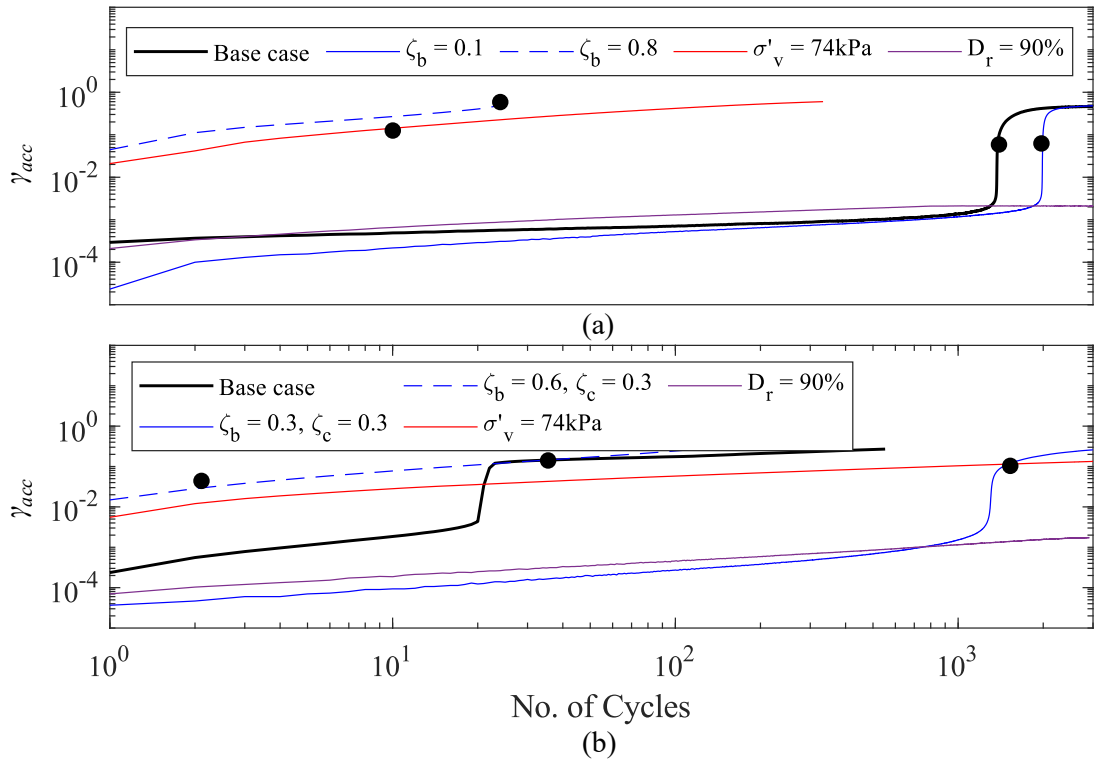


Figure 4-23 γ_{acc} with cycles under undrained loading, black dot denotes N_f (a) Two-way loading, base case: ζ_b = 0.2, ζ_c = -1, σ'_v = 36kPa, D_r = 60%; (b) One-way loading, base case: ζ_b = 0.4, ζ_c = 0 σ'_v = 36kPa, D_r = 60%; and (c) Partial one-way loading base case: ζ_b = 0.5, ζ_c = 0.6 σ'_v = 36kPa, D_r = 60%

From Figure 4-23, all tests show an increase in γ_{acc}, however, the rate at which ratcheting occurs is a function of ζ_b, D_r and σ'_v. A positive relationship between ζ_b and γ_{acc} is observed. Even after one cycle, γ_{acc} is substantial for sufficiently high ζ_b with subsequent cycles resulting in even more rapid γ_{acc} which quickly approaches the limit of the apparatus. The γ_{acc} is inversely proportional to D_r. A rapid change in γ_{acc} is not observed in any 'dense' specimen. Like the experimental work by Andersen (2015) it is seen here that it is impossible to bring the dense specimen to γ_{acc} = 15%, the criteria for failure. The influence of σ'_v is positively related with γ_{acc} across both loading regimes.

The cyclic contour diagram for the specimen prepare d to σ'_v = 36kPa, D_r = 60% at number of cycles, N = 10, 100, 1000 is presented in Figure 4-24(a) to (c) throughout.

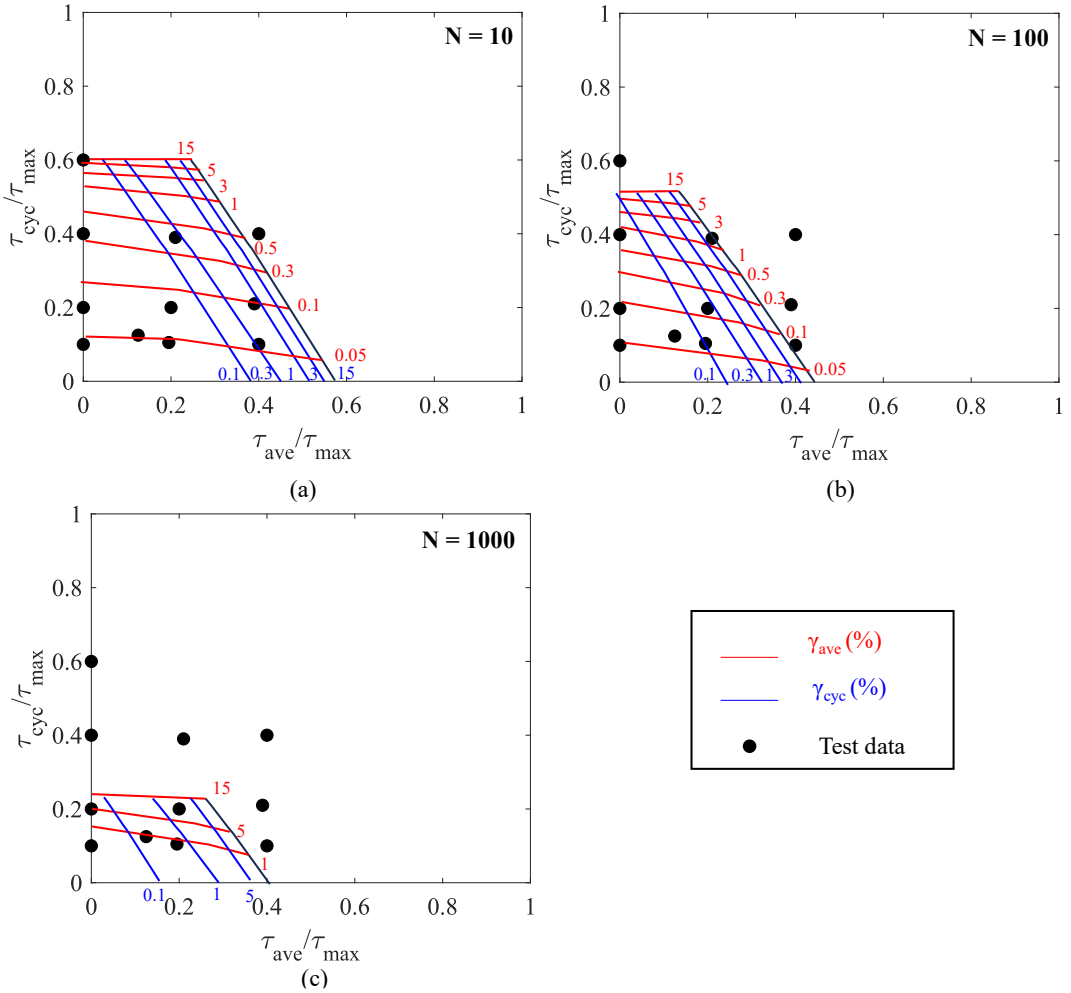


Figure 4-24 Cyclic contour diagrams for undrained tests D_r = 60%, σ'_v = 36kPa (a) N = 10; (b) N = 100; and (c) N = 1000

The contour diagrams reaffirm the conclusion that ζ_b increases γ_{acc}. The ζ_b (equal to τ_{cyc}/τ_{max}), increases the γ_{ave} developed in the specimen. For lower ζ_b there is little γ_{acc} until failure where a sudden increase in γ_{acc} occurs, and the strain quickly reaches the limit of the apparatus. Figure 4-25(c) demonstrates a significantly smaller failure envelope due to the sudden failure of many specimens. This rapid increase in γ_{acc} coincides with a rapid increase in Δu which both occurs at N_f. The average load applied to the specimen, τ_{ave} is positively correlated with γ_{cyc}. These contour diagrams display trends that are in line with studies by Andersen (2015), Qiu (2023) and Yang et al. (2023).

4.4.4 Stiffness and energy dissipation with cycles

This section discusses the effect of ζ_b, σ'_v. and D_r on changes to G_{sec} and η. These effects

are considered against the base case conditions listed in Table 4-5. The G_{sec} is normalised with the maximum shear stiffness, G_{max} obtained in Section 4.2.3. The variation of G_{sec}/G_{max} with cycles for two-way loading, one-way loading, and partial one-way loading are presented in Figure 4-25(a), (c) and (e) respectively. The evolution of η with cycles is presented in Figure 4-25(b), (d) and (f) for the same loading conditions.

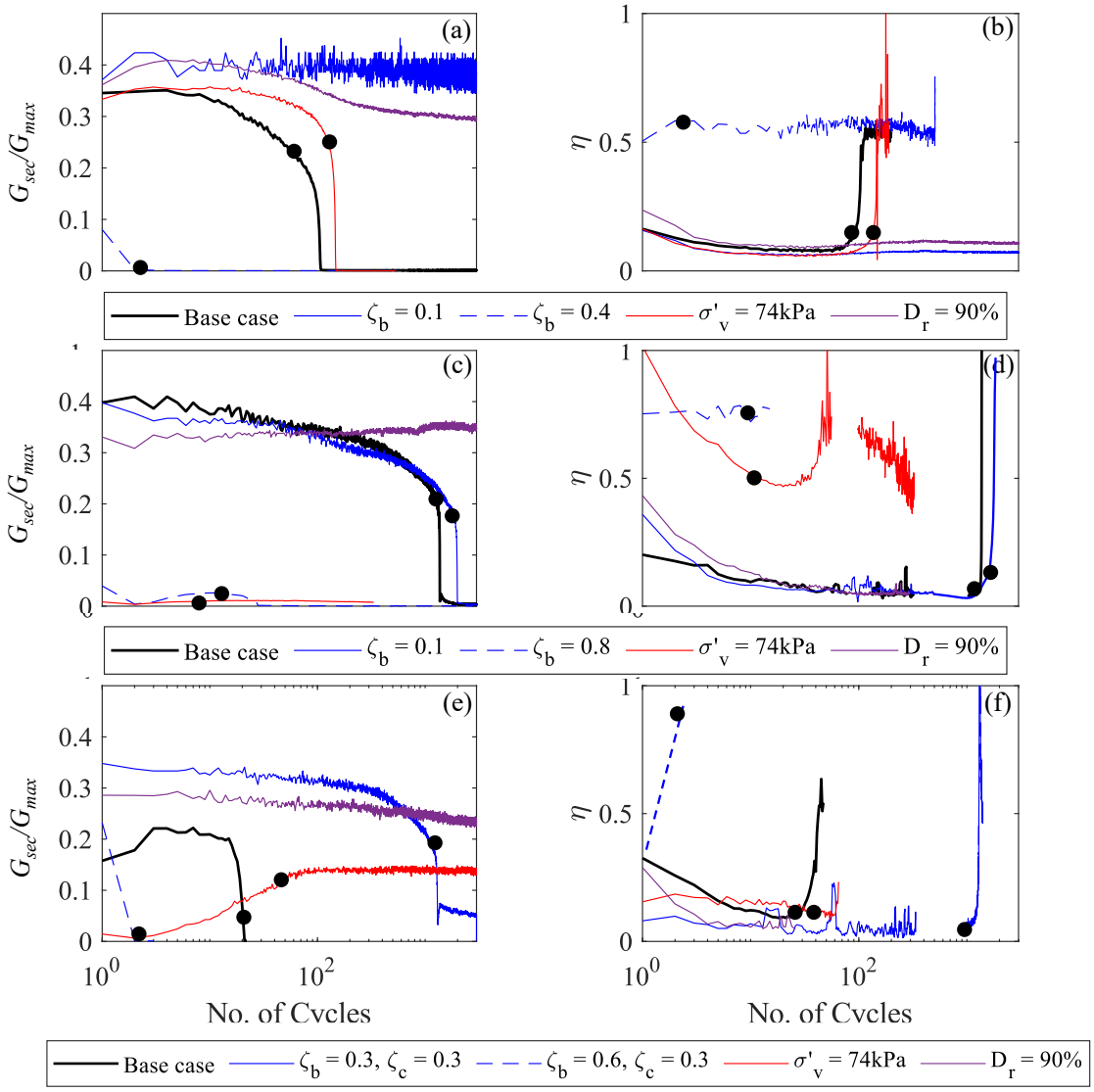


Figure 4-25 Stiffness (left column) and Energy dissipation (right column) with cycles under undrained loading, black dot denotes N_f (a)(b) Two-way loading, base case: ζ_b = 0.2, ζ_c = -1, σ'_v = 36kPa, D_r = 60%; (c)(d) One-way loading, base case: ζ_b = 0.4, ζ_c = 0 σ'_v = 36kPa, D_r = 60%; and; (e) and (f) Partial one-way loading base case: ζ_b = 0.5, ζ_c = 0.6 σ'_v = 36kPa, D_r = 60%

The evolution of G_{sec} and η with cycles is largely a function of ζ_b and D_r. Higher ζ_b reduces G_{sec} and increases η with fewer cycles. For very low ζ_b, such as the case of ζ_b = 0.2, ζ_c =

-1, the rapid change in G_{sec} and η does not occur. Notably, all 'dense' specimens did not fail in the 3000 cycles, exhibiting no rapid changes in G_{sec} nor η under any loading condition. σ'_v and loading asymmetry have negligible influence on the behaviour.

For specimens that endured the 3000 cycles of loading without failure, both G_{sec} and η decrease slightly but remain mostly constant. For tests that did fail, G_{sec} and η follow the same trend until N_f, where G_{sec} rapidly decreases and η rapidly increases. This effect is shown in Figure 4-26(a) and (b) below. Figure 4-26(a) depicts the cycles N = 1, 10, 50, and 100 that precede failure ($N < N_f$). Figure 4-26(b) presents cycles N = 110, 300, and 500 ($N > N_f$). The monotonic response of the specimen is also shown.

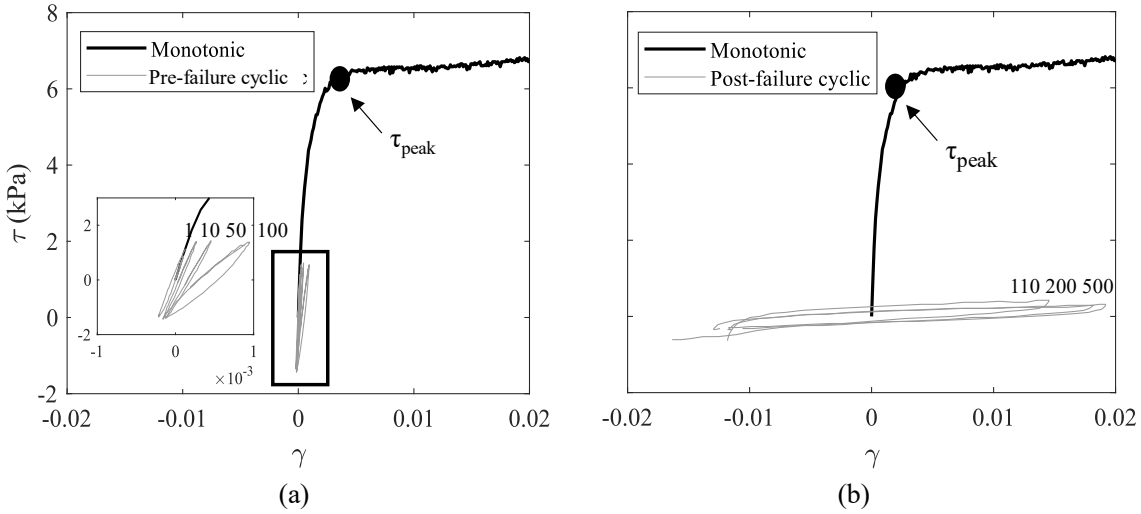


Figure 4-26 Example from VDDCSS_CX_60_36_UTW_U2, N_f = 108 (a) Pre-failure cycles, and (b) Post-failure cycles

The stiffness of the initial cycle in Figure 4-26(a) has the same value as the pre-peak stiffness from monotonic behaviour. Subsequent cycles show a slight decrease in secant stiffness; however, cycles prior to failure exhibit little deviation from one another. After failure, Figure 4-27(b) shows that the G_{sec} decreases significantly, and it is visually observed that the specimen has a reduced capacity as the specimen can no longer sustain the applied target load. This point corresponds with the onset of liquefaction, upon which the specimen instantly exhibits a loss in shear capacity as evidenced by the significantly reduced stiffness and increased energy dissipation at N_f. Any subsequent cycles are

applied to a specimen with a markedly lower stiffness which increases γ_{acc} with further cyclic loads since the soil has practically lost all resistance against cyclic loading.

4.4.5 Stress-path behaviour

In undrained tests, the stress-path of the specimen provides an indication of the position relative to liquefaction. It is of interest to examine the stress-paths of tests at the cycle of failure, N_f The stress-path for selected tests that failed within 3000 cycles are shown in Figure 4-27(a) to (d) throughout.

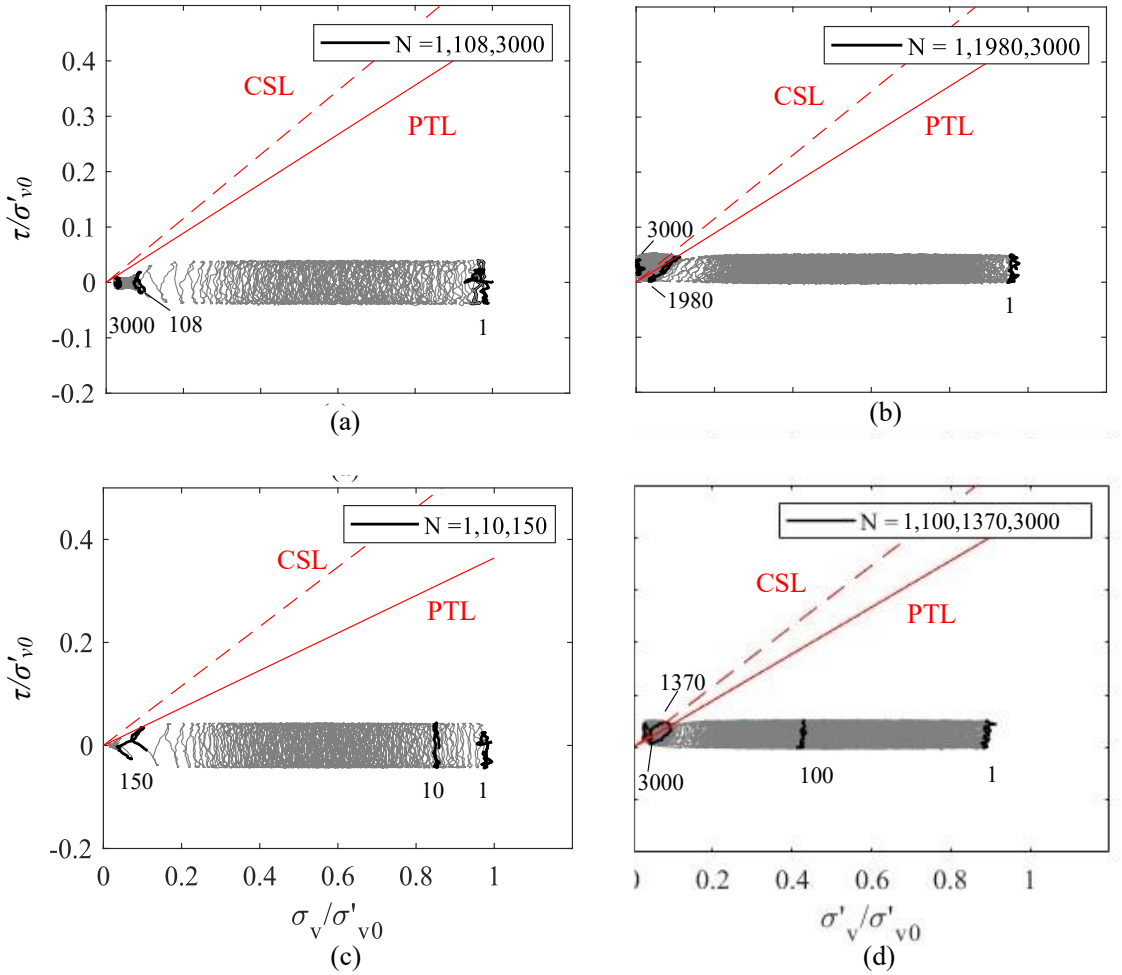


Figure 4-27 Stress-path from selected undrained tests (a) $\zeta_b = 0.2$, $\zeta_b = -1$, $\sigma'_v = 36$kPa, $D_r = 60\%$; (b) $\zeta_b = 0.2$, $\zeta_b = 0$, $\sigma'_v = 36$kPa, $D_r = 60\%$; (c) $\zeta_b = 0.2$, $\zeta_b = -1$, $\sigma'_v = 74$kPa, $D_r = 60\%$; and (d) $\zeta_b = 0.4$, $\zeta_b = 0$, $\sigma'_v = 36$kPa, $D_r = 60\%$

The location of the specimen's stress-path with respect to the PTL and CSL indicates the proximity of the specimen to failure. Undrained cyclic loading reduces σ'_v due to generation of u, moving the stress-path closer to the PTL and CS, also observed by other

researchers, ref. Mao and Fahey (2003), Porcino et al. (2008), Yang et al. (2023) and Zhou et al. (2023). Here, N_f coincides with where the stress-path intercepts with the PTL as opposed to the CSL, meaning the specimen fails as the soil is transitioning from contractive to dilative behaviour. The soil's inability to withstand the change in conditions at PTL can trigger instability and subsequently liquefaction.

The normalised stress-path for the two σ'_v are similar, see Figure 4-29(a) and (c) demonstrating negligible impact of σ'_v on the cyclic stress-path when identical ζ_b are applied, within the limited range of examined σ'_v in this study. Experiments undertaken by Park et al. (2020) indicate that σ'_v is negatively correlated to N_f for σ'_v = 100 to 200kPa in undrained conditions due to potential dilative behaviour appearing at high σ'_v values associated with changes to the state parameter, Ψ. This conclusion was not verified here due to the limited examined σ'_v values, furthermore, in this study normalised cyclic load amplitudes were kept constant as opposed to nominal cyclic load amplitudes.

A plot depicting N_f as a function of τ_{ave} and τ_{cyc} for tests undertaken at σ'_v = 36kPa, D_r = 60% is depicted in Figure 4-29(a). The influence of D_r on N_f for specimens undertaken at, σ'_v = 36kPa, D_r = 60% is shown in Figure 4-28(b). For specimens that did not fail within 3000 cycles N_f is presented as N = 3000.

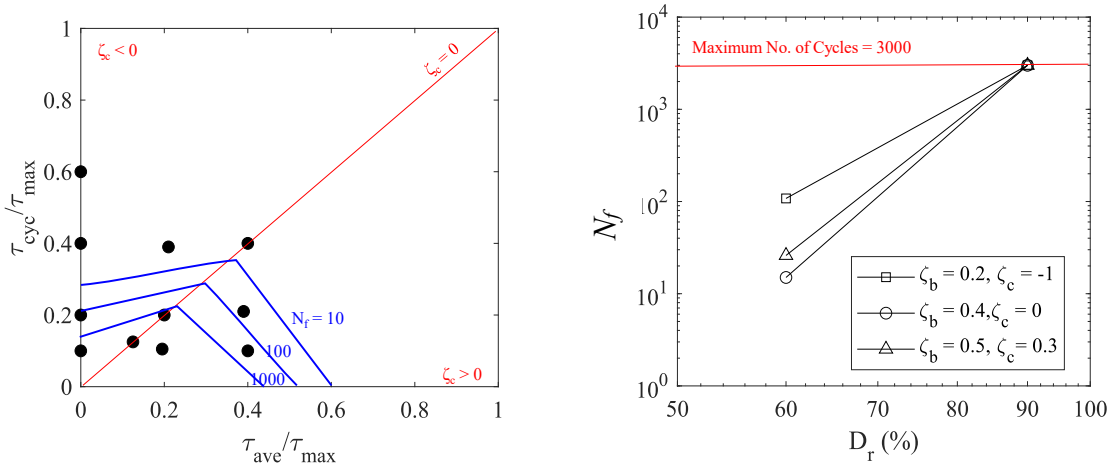


Figure 4-28 (a) Failure envelope from VDDCSS tests; and (b) N_f as a function of D_r for various loading regimes

Here it is clear that N_f is negatively proportional to τ_{cyc} (and hence ζ_b) as well as τ_{ave}. For sufficiently low τ_{cyc} and τ_{ave}, failure does not occur. The kink observed in the failure envelopes suggests that one-way loading increases N_f compared to two-way and partial loading for the same τ_{cyc}. All 'loose' specimen reach failure within 3000 cycles however their 'dense' counterparts do not, suggesting that N_f is positively related to D_r, a result described in Nong et al. (2020) and Andersen et al. (2023). The findings from this section suggest that N_f is negatively related with τ_{cyc} (and hence ζ_b) and τ_{ave}, and positively related with D_r. The N_f is seen to increase as ζ_c approaches 0 for both $\zeta_c < 0$ and $\zeta_c > 0$.

4.4.6 Post-cyclic behaviour

A post-cyclic stage was undertaken immediately after cyclic loading with no reconsolidation stage for undrained tests that did not fail within 3000 cycles. The post-cyclic stress-path of these tests are presented in Figure 4-29(a) to (d).

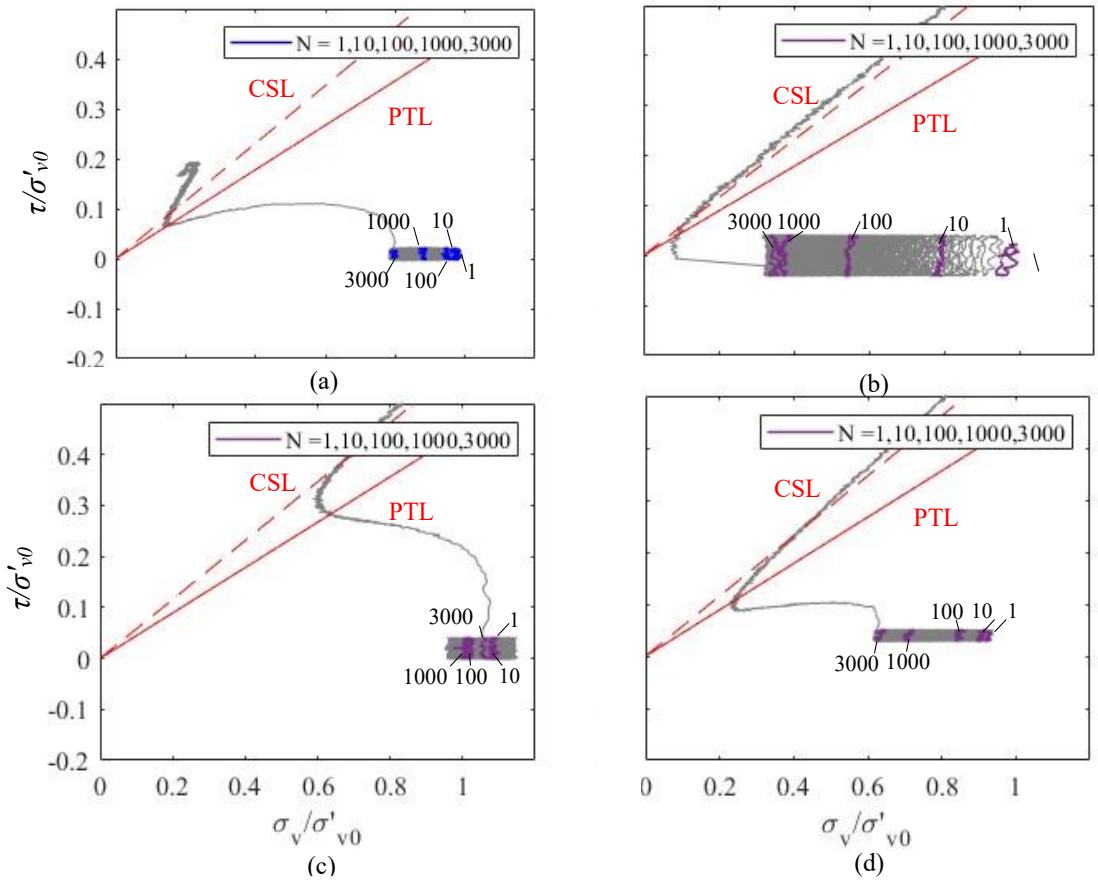
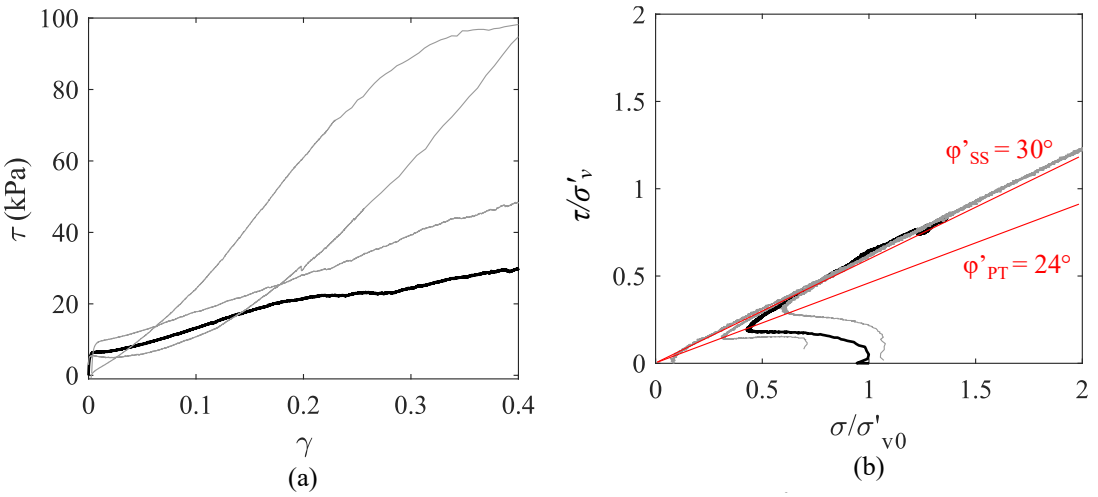


Figure 4-29 Post-cyclic stress-path of undrained specimen that did not fail within 3000 cycles (a) D_r=60% ζ_b = 0.1, ζ_c =-1; (b) D_r = 90% ζ_b = 0.4, ζ_c =-1; (c) D_r=90% ζ_b = 0.4, ζ_c = 0; and (d) D_r=90% ζ_b = 0.5, ζ_c = 0.6

Of the four specimen that did not fail under undrained cyclic loading, three tests were undertaken on 'dense' specimen and one test undertaken on 'loose' specimen at a low ζ_b. Typically, σ'_v reduces with cycles and moves the stress-path closer to the PTL and CSL. However, in the case of the test undertaken at $D_r = 90\%$ $\zeta_b = 0.4$, $\zeta_c = 0$, cyclic loading eventually increases σ'_v due to dilation, as shown in Figure 4-30(c). Given previous observations that certain anisotropic stress-states can induce dilative cyclic responses, referred to as a super-characteristic stress state, see Chang and Whitman (1988) and Park et al. (2020), it is likely that this specific specimen underwent a change from sub-characteristic to super-characteristic conditions from cyclic loading considering the PTL line position relative to the stress path in Figure 4-30(c). However, since exact stress-state cannot be directly measured in the VDDCSS, this transition cannot be verified. It is not clear whether further cycles of loading would eventually cause failure in the other three specimen or also induce dilatation and a subsequent an increase in σ'_v.

The PTL and CSL derived from the monotonic tests are still applicable to post-cyclic behaviour, suggesting that no changes to the soil's inherent properties has occured. The post-cyclic stress-strain and axial behaviour for 'dense' tests are shown on combined plots in Figure 4-31 (a) to (c).



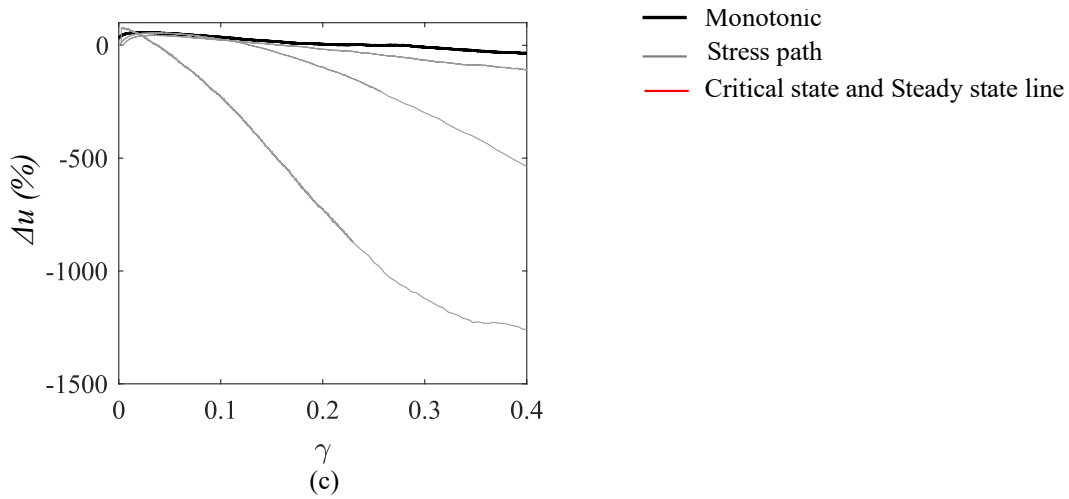


Figure 4-30 Post-cyclic undrained behaviour of 'dense' specimen (a) Stress-strain response; (b) Normalised stress-path; and (c) Porewater pressure generation

Figure 4-31(a) indicates that the original monotonic and post-cyclic response of 'dense' specimen exhibit a τ_{peak} and subsequent strain hardening. The post-cyclic two-way test produces a τ_{peak} significantly lower than the monotonic response. The post-cyclic one-way and partial two-way tests produce similar values of τ_{peak} to the monotonic response. Across all loading regimes, the post-peak hardening and dilation is more pronounced for post-cyclic tests compared to the original monotonic response. Figure 4-30(b) shows that same PTL and CSL derived from monotonic tests are applicable to describe the post-cyclic tests.

4.4.7 Multidirectional loading

This section explores the multidirectional cyclic response of soils in undrained conditions. The perpendicular multidirectional loading scheme was applied to undrained specimen. The same loading amplitudes and symmetries as multidirectional tests undertaken in drained conditions are applied here, see Section 4.3.6. Figure 4-31(a) and (b) present the multidirectional strain response from four loading conditions at two densities D_r = 60% and D_r = 90% respectively.

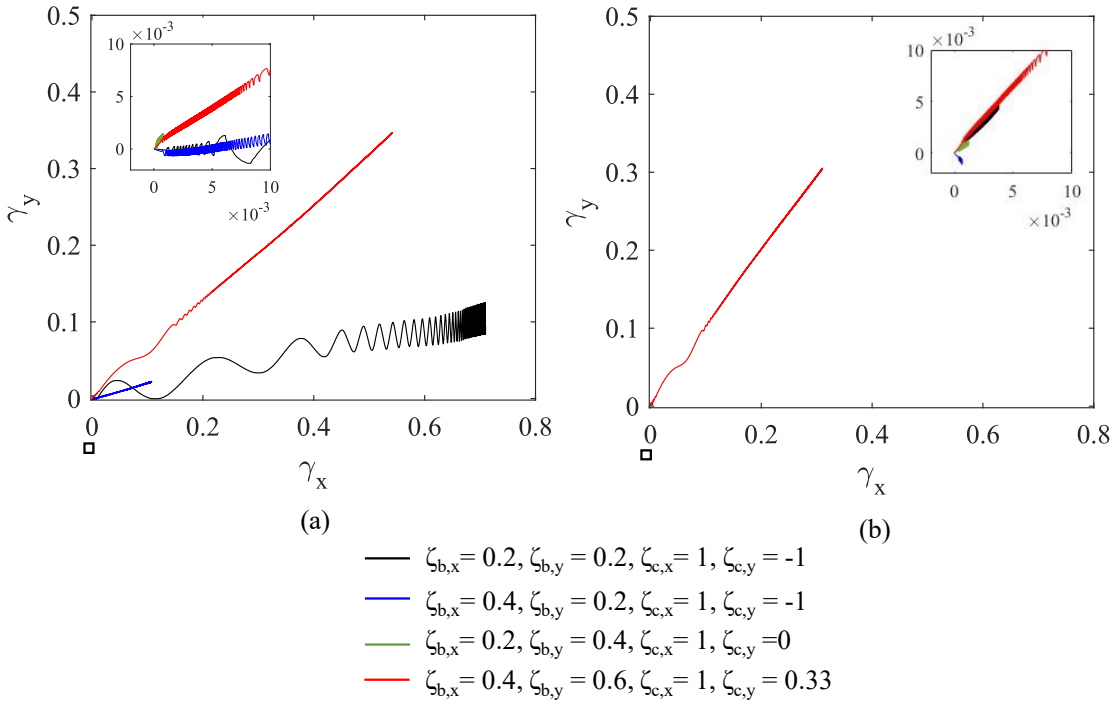


Figure 4-31 X and Y strain response of undrained multidirectional tests for σ'_v = 36kPa (a) D_r = 60%; and (b) D_r = 90%

Four of the eight multidirectional tests failed within 3000 cycles. For specimens that did not fail, little strain develops during cycling (< 0.7%) in either the direction of constant stress or the direction of cycling. For the tests that did undergo failure, the same trend is observed until N_f where significant strain develops. Prior to failure, the direction in which the strain accumulates acts at an angle, $\theta_{multi,}$ to the direction of constant loading for all tests. It is theorised that at small strains, the local particle configuration dominates the direction of accumulation. Upon failure, θ_{multi} is dependent on the loading regime, with partial-one way loading obtaining a higher θ_{multi} than the two-way loading. Additionally, like drained multidirectional loading, the amplitudes of constant stress and cycling also contribute to higher values of θ_{multi}.

Overall, 'dense' tests develop less strain than their 'loose' counterparts, with three of the four 'dense' tests accumulating less than 0.7% strain from the full 3000 cycles of loading. The same mechanisms of failure discussed in Sections 4.4.2 through 4.4.5 are observed for the multidirectional tests, including the rapid increase in Δu, γ_{acc} and η as

well as rapid decrease in G_{sec}. The evolution of Δu, γ_{acc}, G_{sec} and η with cycles for undrained multidirectional tests are presented in Figure 4-32(a) to (c) throughout. The conditions at two densities D_r = 60% and D_r = 90%, respectively. solid lines and dashed lines represent the 'loose' and 'dense' specimen, respectively.

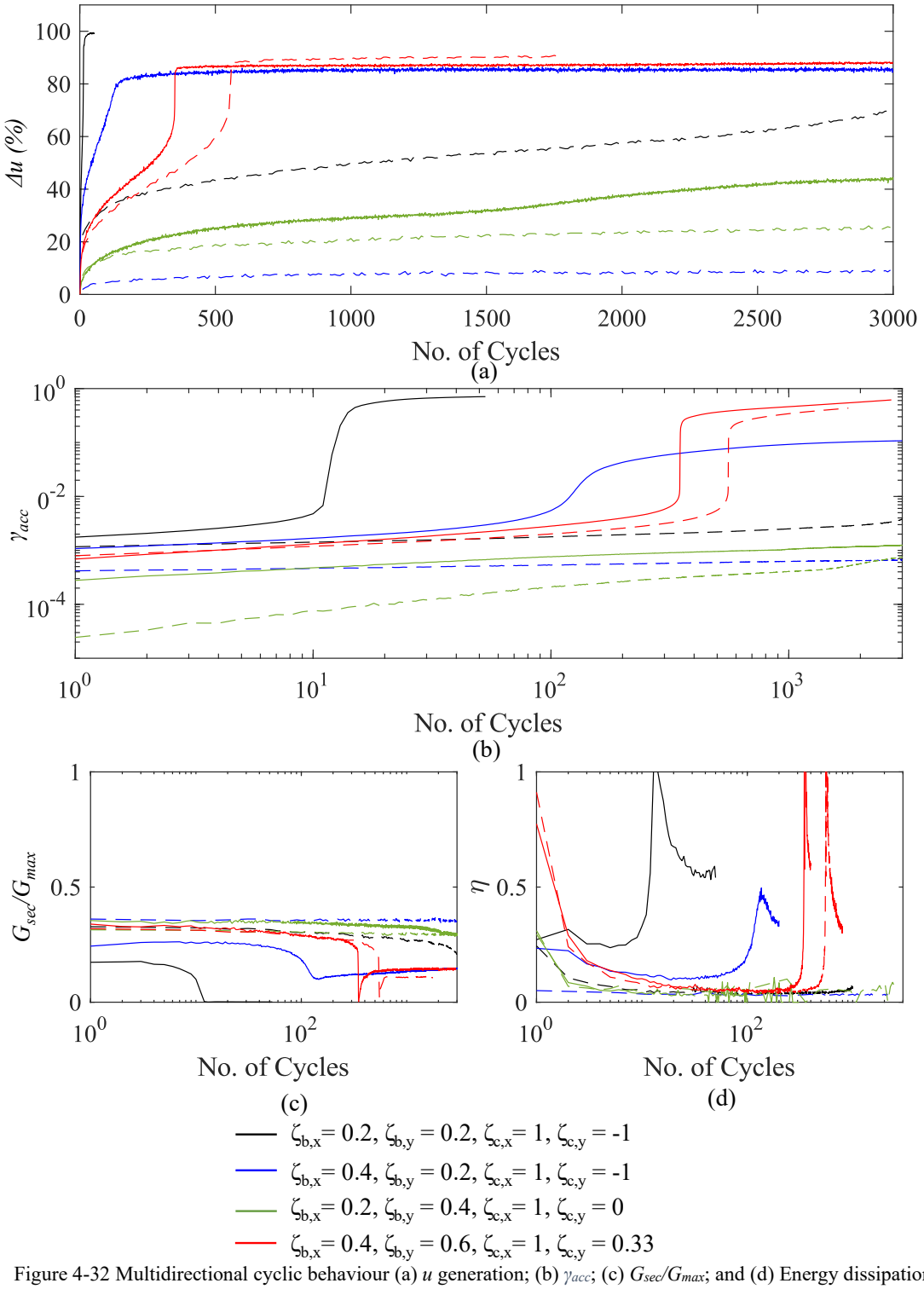
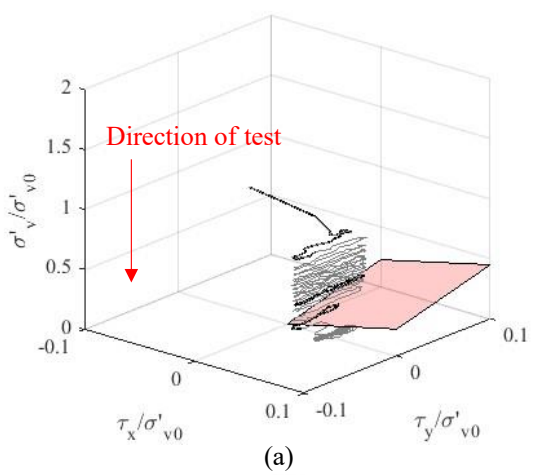


Figure 4-32 Multidirectional cyclic behaviour (a) *u* generation; (b) γ_{acc}; (c) G_{sec}/G_{max}; and (d) Energy dissipation

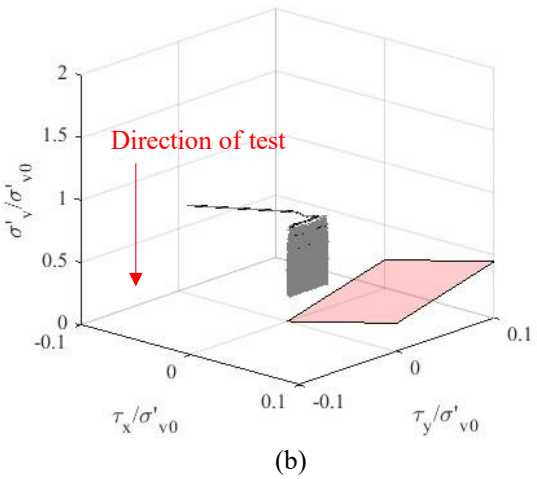
The results depicted in Figure 4-32 reiterate the same conclusions for unidirectional tests. However, an additional observation here is that the 'loose' test associated with $\zeta_{b,x}$ = 0.2, $\zeta_{b,y}$ = 1, $\zeta_{c,x}$= 0.2, $\zeta_{c,x}$ = -1 is the least resistant to cyclic loading (N_f =13) across all tests, despite having the lowest cyclic amplitude and constant stress. The equivalent 'dense' test is less resistant than expected producing more Δu and γ_{acc} and lower G_{sec} than two other 'dense' tests undertaken at a higher constant stress and/or cyclic amplitude, implying that higher constant stress is positively related to N_f.

As loading is applied in orthogonal planes in multidirectional tests, the stress-path of such specimens must be visualised in 3D space. Selected stress-paths of the multidirectional two-way tests are presented in Figure 4-33(a) to (d) throughout, and one-way and partial one-way tests are presented in Figure 4-34(a) to (d) throughout.

Since N_f coincides with the interception of the specimen's stress-path with the PTL in Section 4.4.5, a phase transformation plane is also shown on the figures. The plane is represented by the equation $673\tau_x$+$673\tau_y$-$300\ \sigma'_v$. This expression is derived assuming the PTL is inclined by the same angle (φ'_{PT} = 24°) to the x and y axis.



(a)



(b)

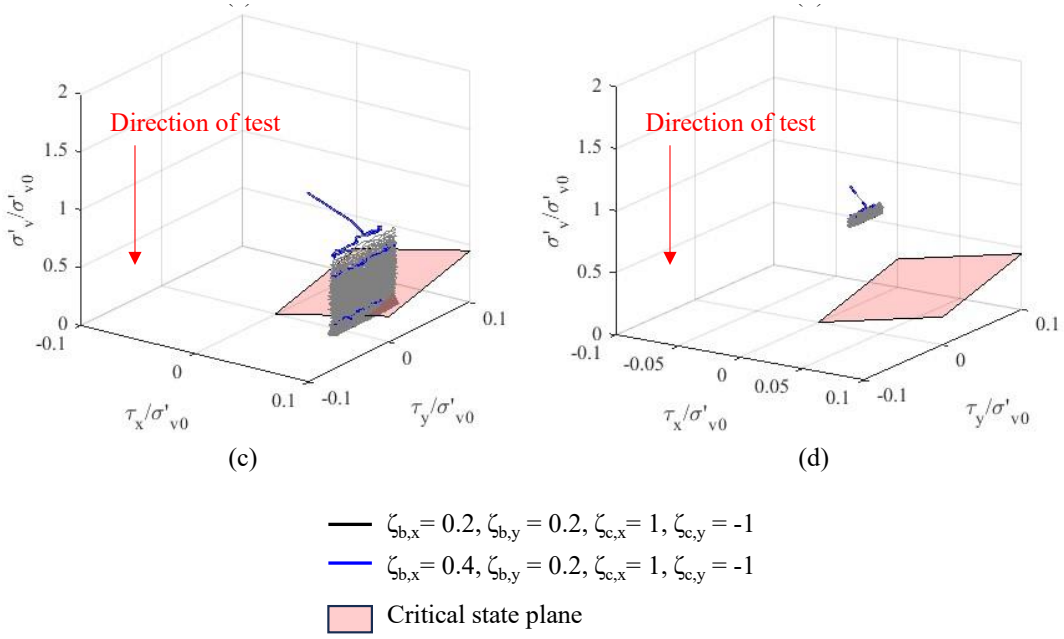


Figure 4-33 Multidirectional stress-path of two-way loading tests (a) Loose; (b) Dense; (c) Loose; and (d) Dense

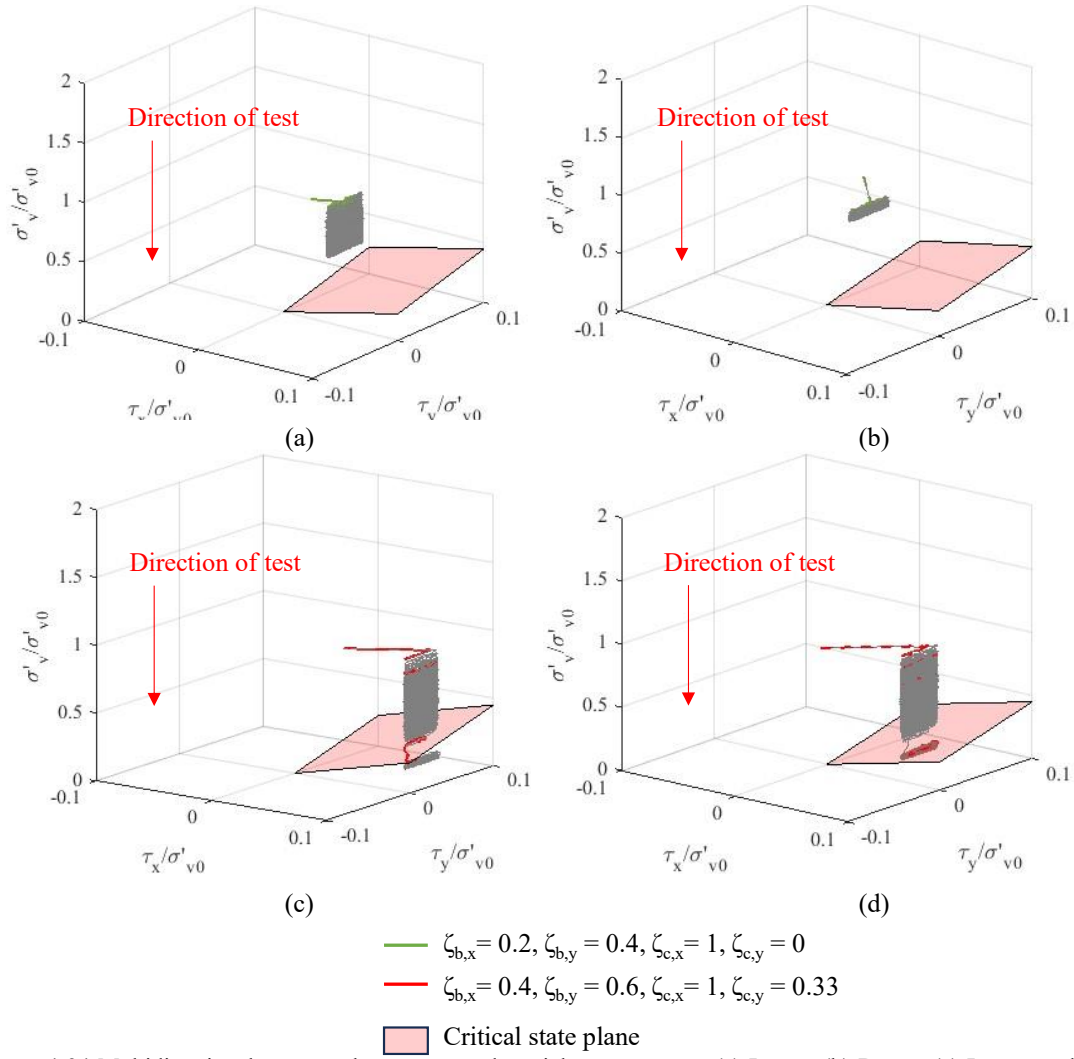


Figure 4-34 Multidirectional stress-path one-way and partial one-way tests (a) Loose; (b) Dense; (c) Loose; and (d) Dense

Like the unidirectional tests, cyclic loading acts to move the specimen's stress-path closer to the phase transformation plane. N_f occurs at the cycle where the stress-path of the specimen intersects with the phase transformation plane and is associated with a rapid increase in Δu, γ_{acc}, η and rapid decrease in G_{sec}.

The post-cyclic behaviour is examined for multidirectional tests that did not fail within 3000 cycles. The stress-strain, Δu and normalised stress-paths are presented in Figure 4-35(a) to (c) throughout. The solid and dashed lines refer to the 'loose' and 'dense' specimen respectively.

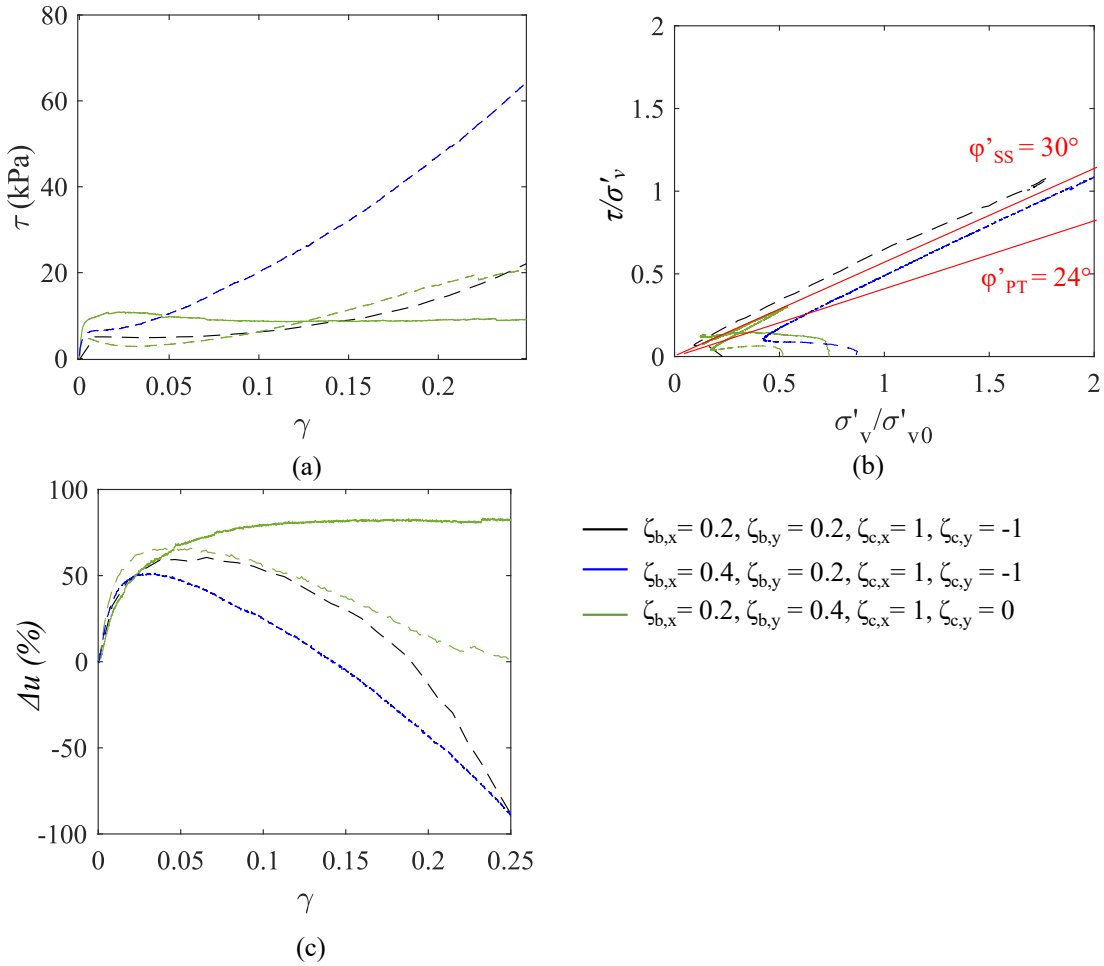


Figure 4-35 Post-cyclic behaviour (a) stress-strain response; (b) normalised stress-path; and (c) Δu

The τ_{peak} obtained from post-cyclic multidirectional tests ranges from 0.5 to 0.93 of the original monotonic value. The post-cyclic response of the 'dense' specimens exhibits strain-hardening and a dilative Δu response whilst the 'loose' specimen exhibits strain-

softening and a contractive Δu response. This confirms that undrained cyclic loading alters the stress of specimens. The stress-path of the post-cyclic tests indicate that the PTL and CSL remains the same as those derived from monotonic tests.

4.5 Reflections on cyclic behaviour

Sections 4.3 and 4.4 have presented a substantial collection of experimental results concerning the cyclic behaviour of cohesionless soils in drained and undrained conditions, respectively. In-depth discussions have outlined several key observations and conclusions drawn from these experiments. This section aims to contextualise the findings on cyclic behaviour within established soil mechanics frameworks for cohesionless soil, particularly those developed for monotonic behaviour such as the critical state framework. A comparison of material types is briefly investigated, and the implications of these findings for realistic offshore design scenarios are discussed, delineating design considerations in drained and undrained conditions.

4.5.1 Drained and undrained cyclic behaviour

In offshore environments, cohesionless soils are fully saturated, and neither drained nor undrained conditions fully encapsulate the true behaviour of the material subject to cyclic loading. It is likely that such soils exhibit a 'partially drained' response in the field which is dependent on the drainage length (a function of foundation geometry and soil layering), permeability of the material, and loading frequency. Lower frequencies of cycling, shorter drainage paths, and higher permeability of the material contribute to increased drainage of the system. Therefore, it is of interest to explore these limiting conditions which govern the cyclic behaviour of cohesionless soil. In this investigation, drainage condition emerges as a critical factor that influences cyclic behaviour, with the two conditions inducing markedly different responses. Figure 4-36(a) and (b) schematically show the idealised cyclic behaviour of specimens in σ'_v, e and σ'_v, τ space, respectively.

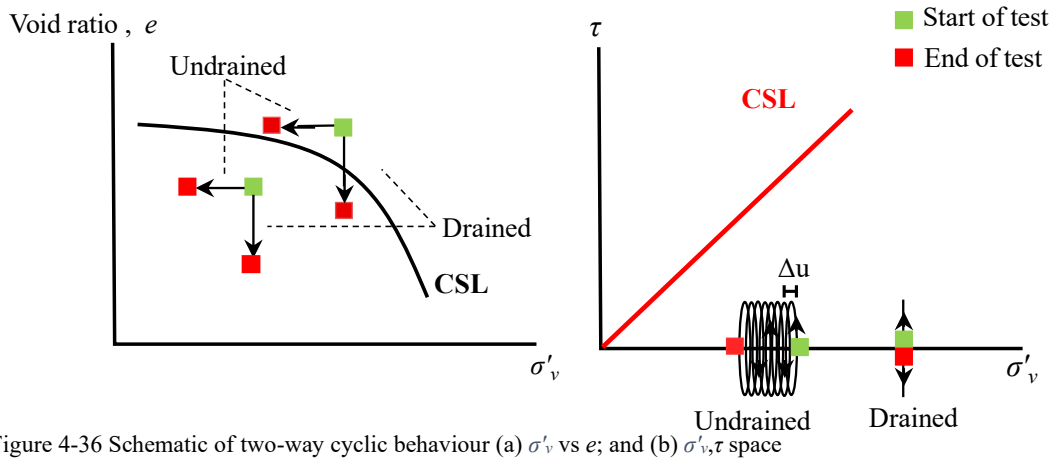


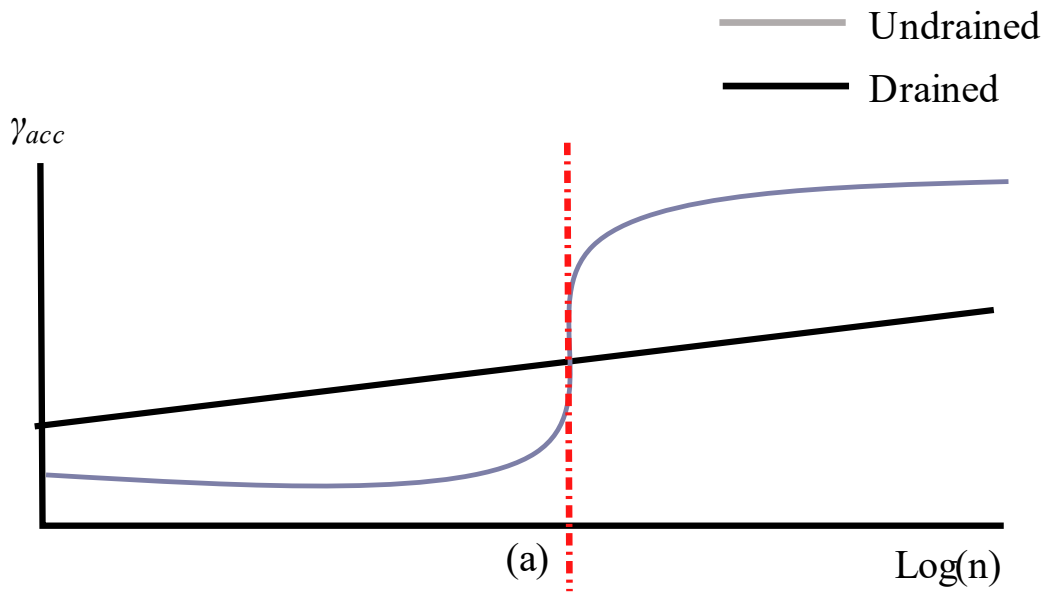
Figure 4-36 Schematic of two-way cyclic behaviour (a) σ'_v vs e; and (b) σ'_v,τ space

Across all drained tests in this investigation, cyclic loads cause densification of the specimen, irrespective of initial density. This effect is shown schematically in Figure 4-36(a) by the reduction in e, displayed for drained specimens. The post-cyclic response for all drained tests exhibits dilative behaviour, indicating that cyclic loading changes state for originally 'looser than critical' specimens to become 'denser than critical.' Figure 4-36(b) displays a schematic of the cyclic stress-path. In drained conditions, σ'_v remains constant, and cyclic loading acts to move the specimen's stress-path up and down the τ axis but fixed at $\sigma'_{v,0}$. This is because no u is generated under drained conditions suggesting that irrespective of the number of cycles, a drained cyclic test will never 'fail' for load amplitude $\tau < \tau_{max}$ as the specimen can never reach the PTL nor CSL in σ'_v, τ space. In the field, under fully drained conditions, accumulated ratcheting would likely be the limiting failure mechanisms for foundations subjected to cyclic loading as opposed to liquefaction.

In undrained conditions, the volume of the specimen is physically restricted, and no densification can occur. Instead, σ'_v reduces with cycles for both 'looser' and 'denser' than critical specimens. In this study no specimens experienced dilative behaviour within 3000 cycles and only positive u was generated. Therefore, in σ'_v/e space, both 'loose' and 'dense' specimens in this study were observed to move from left to right at a fixed e. This

differs from conventional critical state theory for monotonic loading where 'dense' specimens would observe dilation and subsequently develop negative u shifting the specimen right in σ'_v/e space. The post-cyclic response of undrained cyclic tests indicates that 'looser than critical' specimen remain loose and 'denser than critical' specimen remain dense after cycling in this study. Figure 4-36(b) depicts the cyclic stress-path of undrained specimens, which tends toward the CSL with cycling. This is caused by the development of u with cycles and reduction in σ'_v. The amount of generated u has been demonstrated to be a function of ζ_b, ζ_c and D_r. If substantial development of u occurs, a loss of strength in the specimen ensues, causing liquefaction, corresponding with the interception of the stress-path with the PTL. Therefore, in undrained conditions, the location of the specimen's stress-path is an indication of its proximity to failure.

The differences in cyclic behaviour introduced by drainage conditions are pertinent when examining other key cyclic features, namely, accumulated ratcheting, stiffness, and energy dissipation with cycles, n. Figure 4-37(a) to (c) throughout. schematically illustrate these idealised behaviours in drained and undrained conditions based on observations from experimental tests presented in Sections 4.3 and 4.4.



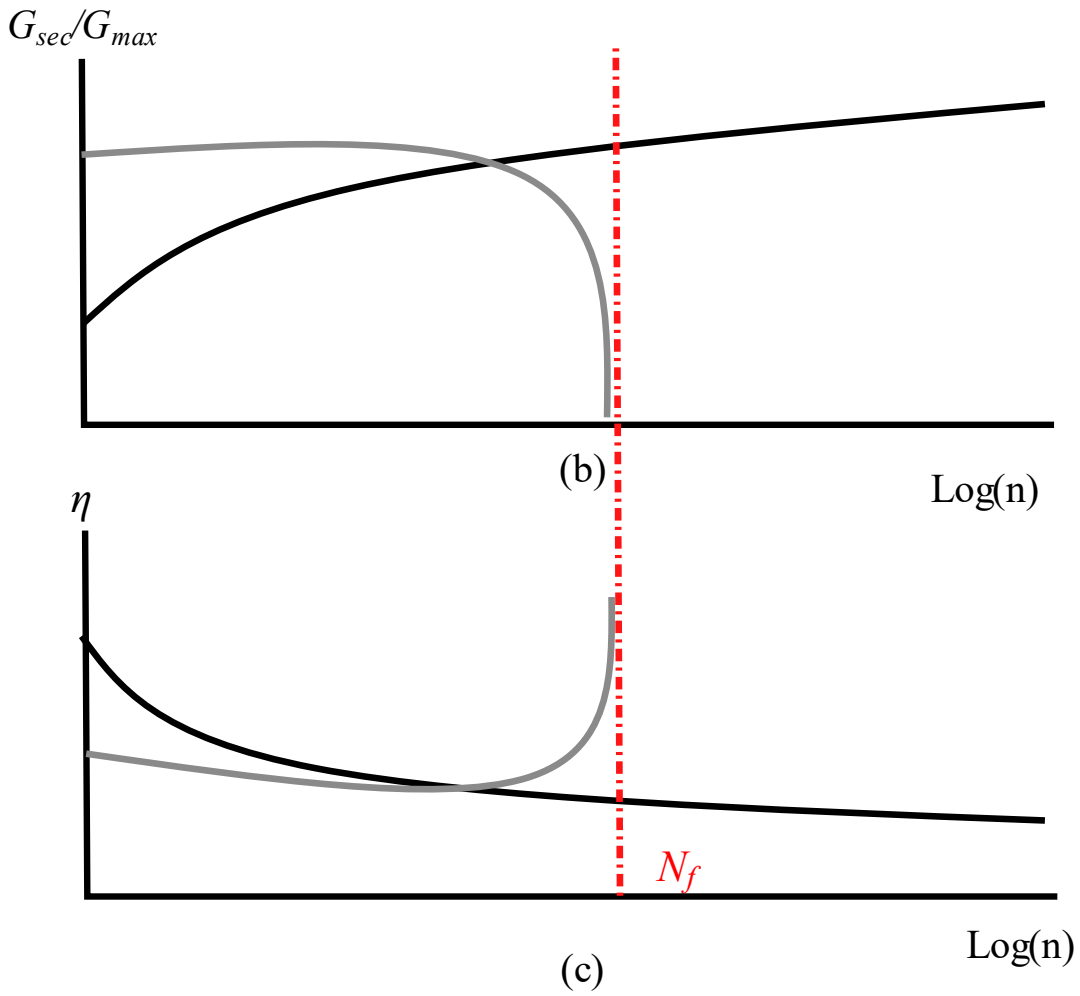


Figure 4-37 Idealisation of cyclic features with n (a) γ_{acc} (b)G_{sec}/G_{max} and (c) η

A pronounced difference exists in cyclic behaviour between tests undertaken in drained and undrained conditions. Tests undertaken in drained conditions exhibit a gradual increase in γ_{acc} and G_{sec} and gradual decrease in η with cycles and no generation of u. As mentioned previously, drained cyclic tests do not fail under cyclic loading if the amplitude τ remains < τ_{max} obtained from monotonic tests. In fact, cyclic loading acts to increase the cyclic resistance, herein referred to the soil's ability to withstand cyclic loading without liquefaction (undrained conditions) or excessive strain, γ >15% (drained conditions) of the specimen in drained conditions as evidenced by the increase in G_{sec} and post-cyclic capacity and reduction in η with cycles. The post-cyclic capacity of drained tests is up to 2.9 times the monotonic response in this experimental regime. As mentioned in Section

4.3, it is likely that densification and 'interlocking' account for this increased resistance. Like previous experimental studies, ζ_b emerges as key factor that governs drained cyclic behaviours. ζ_b is positively related with densification and accumulated ratcheting as higher ζ_b cause more movement in soil grains to fill in the voids of the specimen. Additionally, higher reversal load (lower ζ_c) induces more densification and simultaneously reduces accumulated ratcheting in the loading direction as they counter the effects of the extension load.

D_r influences certain cyclic behaviours and is negatively related to densification and accumulated ratcheting. In denser specimens, the reduced voids restrict soil grain movement, leading to decreased densification and accumulated ratcheting.

Cyclic behaviour is demonstrated to be insensitive to f in this study. Even though f is a contributing factor to drainage conditions, in the VDDCSS, the specimen height is roughly a third of the diameter resulting in a short drainage path. Therefore, undrained behaviour cannot be simulated by altering f, and the specimen consistently displays drained behaviour unless physically restricted.

Multidirectional testing indicates show consistent trends with unidirectional loading however additionally demonstrates the importance the constant load amplitude $\zeta_{b,x}$ on densification and accumulated ratcheting as well as the importance of cyclic amplitude $\zeta_{b,y}$ on the direction of ratcheting. Multidirectional tests also demonstrate that the post-cyclic increase of specimens sheared in the transverse direction are approximately half compared to in the direction of cyclic loading, again reiterating the influence of 'interlocking'.

Contrastingly, undrained tests generate a minimal Δu prior to failure. Additionally, undrained tests accumulate significantly γ_{acc} and produce higher nominal

values of G_{sec} and lower values of η compared to equivalent drained tests, suggesting a greater resistance to cyclic loading than their drained counterparts. Upon the cycle of failure, N_f, the resistance of undrained specimen experiences a pronounced reduction marked by rapid increases in Δu, γ_{acc}, and η and rapid decrease in G_{sec}. This is schematically shown in Figure 4-37, indicated by the dashed red line. Following N_f, the behaviour of γ_{acc}, shows an apparent equilibrium. However, this equilibrium is not reflective of the material's true behaviour but rather a result of the apparatus reaching its strain limit. These instantaneous changes are associated with the generation of u, which reduces σ'_v causing liquefaction. Whilst the post-cyclic capacity for drained tests, increased this effect is not seen for undrained tests. Instead, the post-cyclic response of undrained tests reflects the new stress level of the specimen as the post-cyclic shearing is undertaken on a specimen at a different σ'_v. The post-cyclic tests demonstrate an increase post-peak behaviour, and more dilation compared to the original monotonic response.

Undrained multidirectional tests reaffirm conclusions of the unidirectional tests. The stress-path of multidirectional tests can be expressed on a 3D axis, and the PTL can be appropriately represented as a plane. Cyclic loading moves the stress-path towards the phase transformation plane, and the point of intersection coincides with N_f.

Energy based methods for evaluating liquefaction potential rely on the strong correlation between Δu and η, with η as the sole indicator of liquefaction (Green 2000; Mele et al. 2019). In this study it is shown that rapid changes to γ_{acc}, G_{sec} are additional indicators of specimen failure, however γ_{acc}, G_{sec} and η do not contribute to the failure mechanisms of the specimen itself and are only indicators of liquefaction.

As mentioned previously, a partially drained response is likely to be induced by cyclic loading on OWTs. This behaviour falls between the fully drained and fully

undrained conditions examined in this study. Based on the behaviour observed in this investigation, it is theorised that under partially drained conditions, the soil will experience both the development of u and some densification with cycles. The exact amount of porewater pressure development and densification is likely to be a function of the frequency of cyclic loading, length of the drainage path, and permeability of the material. Lower frequencies of cycling, shorter drainage paths, and higher permeability of the material contribute to increased drainage of the system. In such scenarios, the generated porewater pressure can dissipate more readily between cycles, and greater densification can occur as particles rearrange. Conversely, higher frequencies of loading, longer drainage paths, and materials with low permeability exhibit the opposite effect. In these situations, the drainage of the system is reduced, and the u cannot as readily dissipate with cycles.

A limitation of the VDDCSS apparatus tests is that testing can only be conducted in fully drained or fully undrained conditions. Thus, partially drained monotonic and cyclic behaviour cannot be quantified experimentally using this device in its current state. A useful extension of this work is to investigate the partially drained response of cohesionless soils either using a modified VDDCSS or triaxial apparatus that physically alters the drainage (e.g., limiting the amount of water that can pass through the drainage line through modifying the surface area of the drainage pipe) or through 1g model tests in saturated soils under different loading frequencies.

4.5.2 Influence of material type

This section compares the cyclic response CX and LBS. Of particular interest is determining whether the same physical mechanisms that govern the cyclic behaviour for CX material, as observed in Section 4.3, also dominate the LBS material. A smaller suite of tests was undertaken on the LBS material as a point of comparison. All cyclic tests on

LBS were conducted in drained testing conditions. Selected CX tests are shown in Figure 4-39(a) and (c), and the corresponding LBS tests are presented in Figure 4-38(b), and (d).

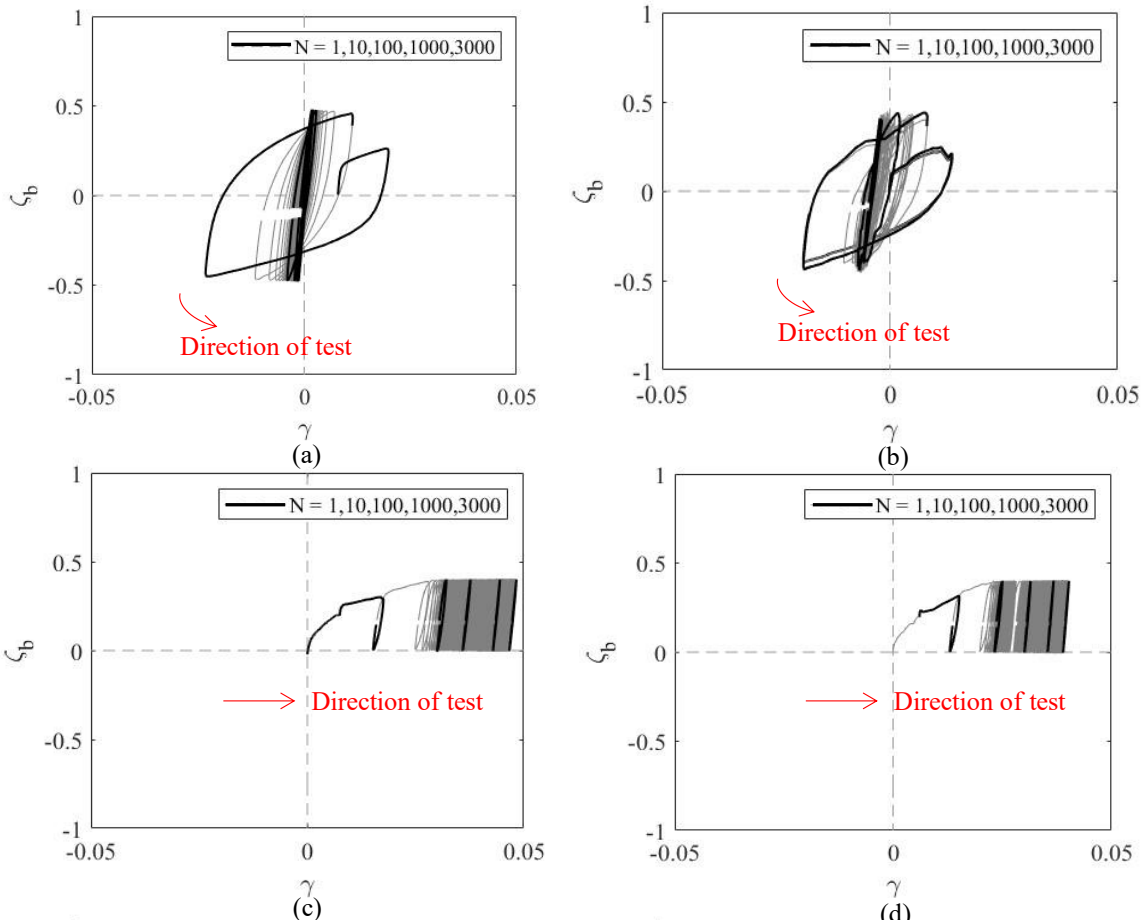
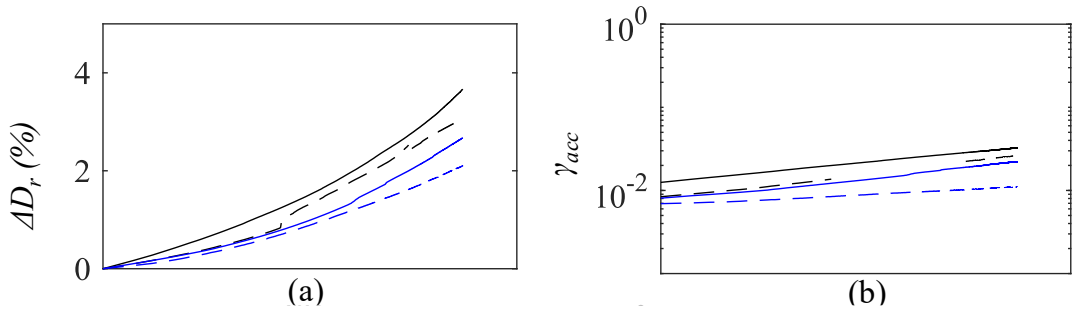


Figure 4-38 Selected cyclic tests from two materials (a) CX, ζ_b = 0.4, ζ_c =-1; (b) LBS, ζ_b =0.4, ζ_c =-1; (c) CX, ζ_b = 0.4, ζ_c = 0; and (d) LBS, ζ_b =0.4, ζ_c =0

Visually, it is observed that under the same test conditions (i.e., same cycling amplitude and loading regime), there is little deviation from both material types. The variation of densification and accumulated ratcheting, normalised stiffness and energy dissipation are for selected one-way tests presented in Figure 4-39(a) to (h) throughout.



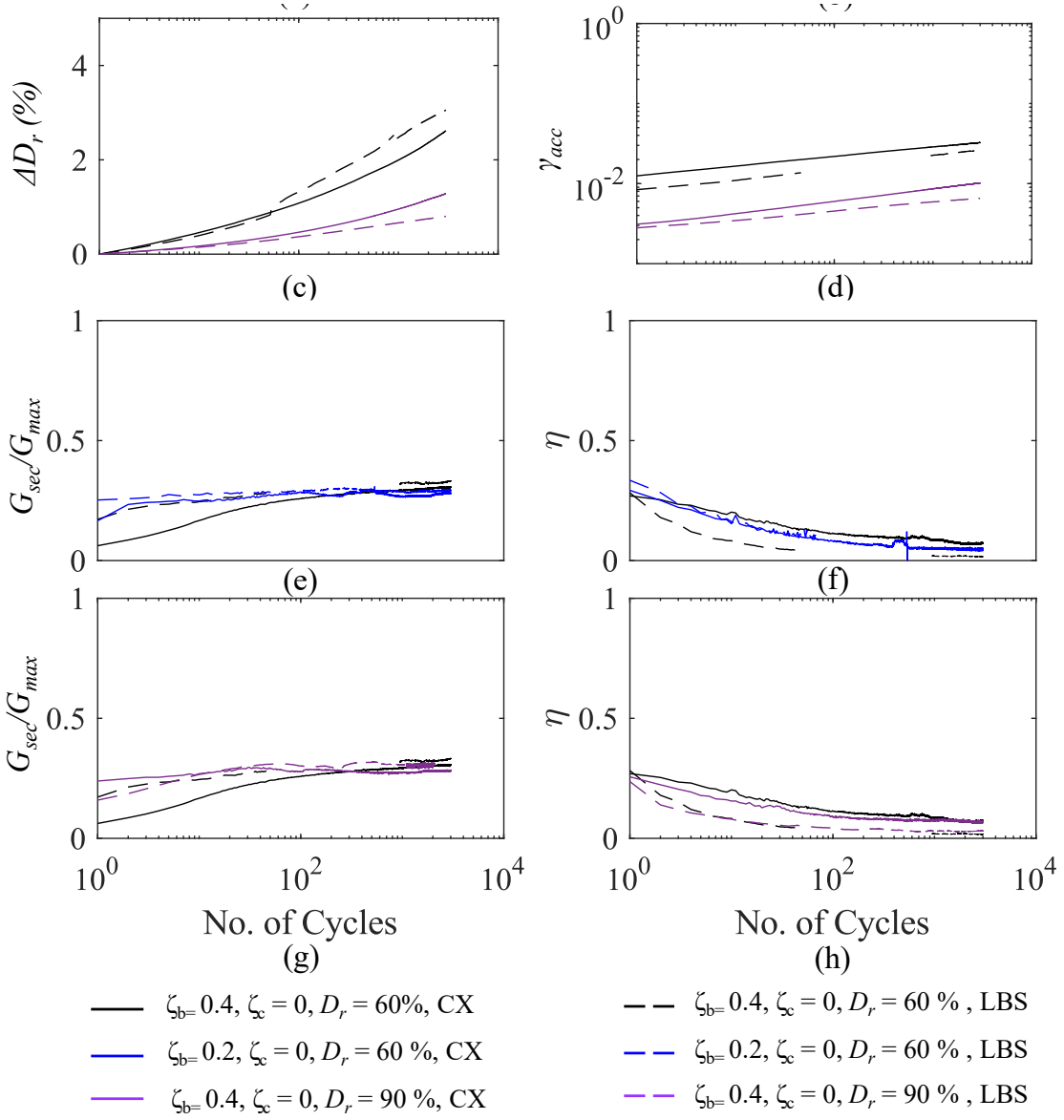


Figure 4-39 Cyclic behaviour of two materials, one-way loading (a) Densification, effect of ζ_b; (b) Ratcheting, effect of ζ_b; (c) Densification, effect of D_r; (d) Ratcheting, effect of D_r; (e) Normalised stiffness, effect of ζ_b; (f) Energy dissipation, effect of ζ_b; (g) Normalised stiffness, effect of D_r; and (h) Normalised stiffness, effect of D_r

The overall cyclic trends captured from the two materials are similar. The physical properties, ζ_b and D_r have the same effect on both materials and reiterate the findings from Section 4.3. LBS produces less densification, accumulates less ratcheting, and produces less stiffness increase than their CX counterparts. These differences can be attributed to the differing grain characteristics of the two materials, in particular, LBS has a lower C_u and higher d_{50} compared to CX sand, which is well-graded fined-grained sand (See Section 2.3 for details). As such, there is less room available for grains to move into

the voids of LBS specimens compared to the well-graded CX sand, where smaller grains readily fill the voids of the specimen.

Figure 4-40(a) to (d) throughout presents the post-cyclic behaviour and axial strain of the two materials.

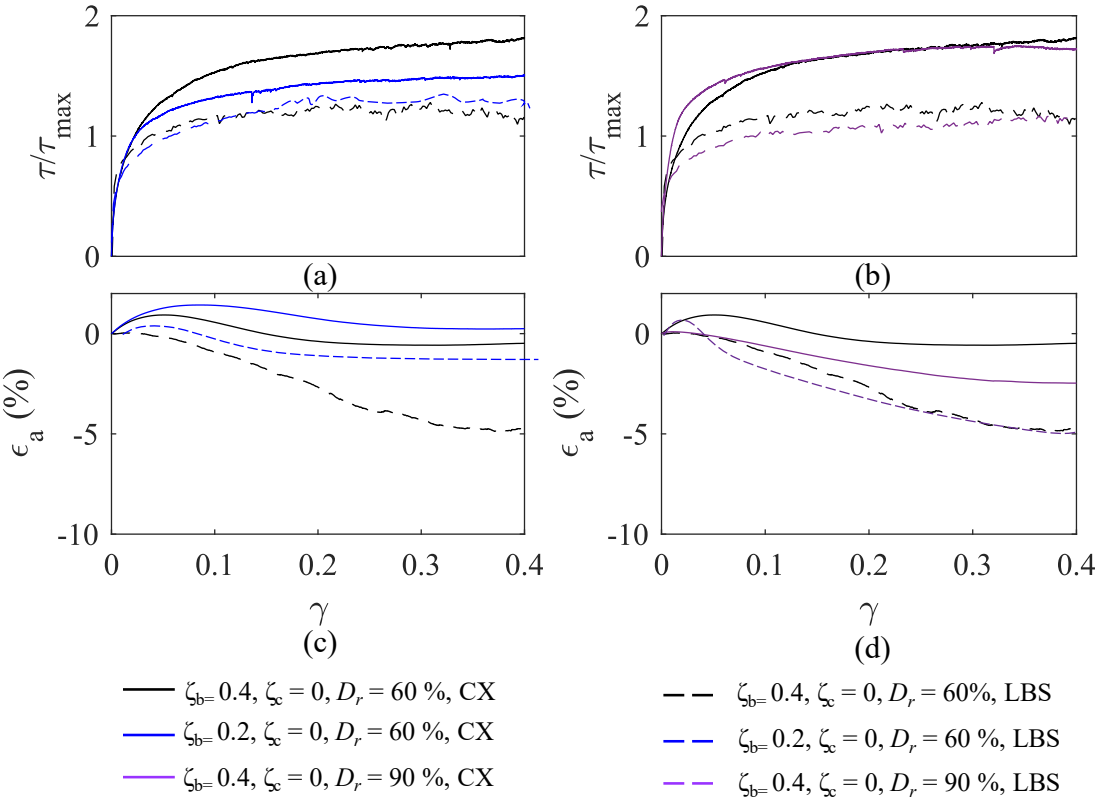


Figure 4-40 Post-cyclic behaviour across material types for one-way loading (a) Stress-strain, effect of ζ_b; (b) Stress strain, effect of D_r; (c) Axial strain, effect of ζ_b; and (d) Axial strain, effect *of* D_r

The post-cyclic capacity of both materials increases from the monotonic capacity as presented in Section 4.2, as seen in Figure 4-40(a) and (b). Furthermore, all specimens exhibit dilative post-cyclic behaviour displayed in Figure 4-40(c) and (d). A notable difference between the material types is seen as the CX material produces a significantly more pronounced increase in post-cyclic capacity compared to LBS. As previously discussed, the CX sand also produces more densification and stiffness increase than the LBS due to differences in the two materials' grain characteristics. Whilst some movement occurs in the grains of LBS, less densification and 'interlocking' of particles can be

induced compared to the well-graded soil matrix of CX, which therefore reduces the increase in cyclic resistance of the LBS. This suggests that the grain characteristics have an influence on the amount of increase in cyclic resistance of cohesionless soils under drained cyclic loading. It is likely that C_u is positively related to an increase in cyclic resistance. However, this should be further investigated across a larger range of PSD to confirm these conclusions.

It has been demonstrated that the global cyclic behaviour measured between the soils is similar and the examined properties, namely, ζ_b and D_r influence the two materials in the same manner, however, individual grain characteristics of cohesionless soils such as C_u or d_{50} contribute to the amount of densification and 'interlocking' in the specimen due to cyclic loading and therefore directly influence the increase in cyclic resistance of cohesionless soils.

4.5.3 Implication for design methods of OWT foundations

Current design methods for monopiles undergoing cyclic loading rely on the contour diagrams approach, which allow designers to approximate cyclic degradation factors to soil properties (Andersen et al. 2015). Such contour diagrams require data from several laboratory tests, including CDSS as well as cyclic TX compression and extension tests. Therefore, a large testing regime is required to develop these diagrams for every new site and new material type. Alternatively, designers can estimate cyclic properties from existing databases according to relationships derived from basic soil properties such as D_r, $F.C$, over consolidation ratio, plasticity index and undrained shear strength so long as the material is within the parameter space of these databases (Andersen et al. 2023).

Methods for evaluating liquefaction potential have been developed by Seed and Idriss (1971) in the context of assessing earthquake loading on saturated cohesionless soils which rely on the use of liquefaction charts, their effectiveness and consinued

relevance in engineering design are discussed in Dobry and Abdoun (2015). Energy based methods as those described in Green et al. (2000) rely on the close correlation observed in energy dissipation and pore pressure generation. These methods of assessing liquefaction are empirical in nature and relate the properties of soil and loading conditions to assess liquefaction potential. Current methods for assessing liquefaction provide information about the generation of u with cycles, useful for ULS design but do not provide progressive soil behaviour of other cyclic features γ_{acc} and G_{sec}/G_{max} which are necessary to demonstrate SLS and FLS requirements e.g., satisfaction of rotation limits and natural frequency assessment. Additionally, since liquefaction is unique to undrained loading conditions only, and since the loading on OWTs can produce a range of drainage conditions, liquefaction charts alone are not adequate for OWT design.

The theoretical developments established in this experimental testing regime can be leveraged in the design of OWT foundations undergoing cyclic loading by incorporating findings of this experimental regime into simple analytic models or more complex constitutive models. However, it should be noted that further experiments beyond the scope of this thesis would be required for robust calibration of such models. Section 4.3 and 4.4 have presented an extensive suite of cyclic simple shear tests in drained and undrained conditions and demonstrate a remarkably different response in the two limiting behaviours showcasing the necessity for separate design methodologies when considering these two drainage conditions in the context of OWT foundation design. A general discussion of the integration of experimental findings into analytical or constitutive models for cohesionless soils as well as their implications for general OWT foundation design procedures are herein presented.

4.5.3.1 Determination of load and loading conditions

In offshore environments, the complicated cyclic loading scenarios applied to foundations necessitate careful determination of loads and drainage conditions. The outcomes of this research have direct implications for understanding the effects of these loads on OWTs. The loads on an OWT, from lowest to highest frequencies, include wind and wave loads, operational loads from the blades passing the rotor, and extreme storm loads, with typical loading frequencies ranging between 0.01 to 1 Hz. These varying frequencies, coupled with factors such as drainage length (a function of foundation geometry) and material properties, suggest that a range of different drainage conditions exist in the field.

In instances where the response is closer to drained cyclic behaviour (e.g., low loading frequencies, short drainage lengths, and high permeability), it is expected that the trends shown in Section 4.3 would persist. The cyclic resistance increases with cycles due to densification and 'interlocking', and as such, the failure of the foundation would be governed by SLS criteria due to accumulated ratcheting in the direction of load bias. Conversely, if an undrained response is expected; the foundation is more likely to be governed by ULS criteria, associated with liquefaction. The large diameter of OWTs (D_p > 4m) suggests that a partially drainage is likely which means either of the failure mechanisms could govern the system.

The nominal value of loads is also of importance to designers when considering the findings of this research. Operational loads from rotor operation are several orders of magnitudes lower than the environmental loads and are associated with a relatively lower ζ_b, whilst wind and wave load approximately balance and correspond with a relatively higher ζ_b. The importance of ζ_b on cyclic behaviour of cohesionless soils in drained and undrained conditions has been demonstrated extensively in this study.

4.5.3.2 Design considerations in drained conditions

In drained loading conditions, the stress-path of a cohesionless soil specimen never intercepts with the CSL (refer, Figure 4-37(b)) for $\tau < \tau_{max}$ and subsequently the specimen never liquefies unlike their undrained counterparts. Furthermore, cyclic loading induces densification and 'interlocking' which increase the cyclic resistance as evidenced by the increase in stiffness and post-cyclic capacity. Whilst these conclusions appear to benefit the performance OWTs, the change in stiffness can impact the f_0 of the OWT system which potentially could impact FLS design, this is explored further in Chapter 5. Furthermore, accumulated ratcheting develops progressively in the direction of load bias with cycles, a concern for SLS design limits (see, Section 1.4 for details).

Section 4.3.3 demonstrates that accumulated ratcheting has a log-linear relationship with cycles, indicating that each cycle produces less ratcheting than the cycle before. This is likely because the stiffness of the soil also increases with cycles which reduces the ratcheting in subsequent cycles. Therefore, meaningful predictions of accumulated ratcheting stem from an understanding of stiffness evolution and increase in cyclic resistance. Densification and 'interlocking' contribute to increasing stiffness and subsequently the amount of accumulated ratcheting (Ref Section 4.3).

Section 4.3.6 additionally demonstrates the effects of multidirectional loading, where the accumulated ratcheting is related to constant stress amplitude, cyclic load amplitude and asymmetry. The constant stress amplitude is positively related to ratcheting and the cyclic load amplitude is positively related to the angle of ratcheting from the direction of constant stress for asymmetrical loading. Therefore, a model that adequately captures the accumulated ratcheting response would requires input of loading direction i.e., unidirectional, or multidirectional to predict the densification and 'interlocking'

which are functions of external loading ζ_b and ζ_c, soil conditions, D_r and soil properties C_u, d_{50} (See Section 4.3.7 and 4.5.2 for details).

4.5.3.3 Design considerations in undrained conditions

It is likely that certain loads on an OWT will produce an undrained or partially drained response. Under such conditions the accumulated ratcheting will not govern the failure of the specimen instead, soil typically fails due to u development and liquefaction. Liquefaction of the specimen subsequently induces a substantial reduction in G_{sec} and increase in γ_{acc} and η. Meaningful determination of the stress-path of soil specimen and its proximity to liquefaction depends on the generation of pore pressure and physical factors that contribute to such generation.

Section 4.4.2 suggest that generation of u is positively related to ζ_b and negatively related to the D_r. Additionally, the generation of u decreases as ζ_c approaches 0. However, in the field, the drainage conditions and subsequently, the generation of u is additionally a function of the drainage length, soil properties and loading frequency which has not been explored in this study (See Section 1.7.1). As such, to develop a wholistic model of u generation for OWT foundations in undrained or partially drained conditions, an investigation of the impact of 1) foundation geometry 2) soil permeabilities 3) grain characteristics and 4) loading frequency on the generation of u is required.

The scope of this work is limited to element testing which constrains the investigation to either drained or undrained conditions unless modifications to the test apparatuses are undertaken. Scaled physical testing and/or field testing would be required to understand combined effects of the four factors mentioned above on partially drained or undrained cyclic behaviour of OWTs founded in cohesionless soils.

4.6 Conclusions

The drainage condition emerges as the key mechanism to influence cyclic behaviour of cohesionless soils and therefore conclusions are presented separately. The key observations surrounding drained cyclic behaviour are summarised below:

1. In drained conditions, the shear stiffness and strength of specimens increases with cycles. This increase is attributed to densification (directly measured) and 'interlocking' of soil particles (inferred from experimental observations).
2. 'Interlocking' is supported by the following observations:
    - the post-cyclic capacity behaviour of the specimen is significantly greater than the densest specimen tested in the monotonic test regime, indicating densification cannot solely account for the increase in resistance.
    - Greater post-cyclic capacity in loading direction compared to transverse direction, suggesting predominant interlocking in the cycling direction.
    - Positive correlation of post-cyclic capacity in multidirectional tests with constant stress amplitudes, again indicating 'interlocking'.
    - LBS demonstrating a lower increase in stiffness and post-cyclic capacity. As LBS is coarser and more uniform, less interlocking can occur compared to CX which is a well graded material.
3. ζ_b, ζ_c, and D_r have considerable influence on the drained cyclic behaviour of cohesionless soils and their impacts are summarised below.
    - ζ_b positively correlates with densification, accumulated ratcheting, stiffness improvement, and increased post-cyclic capacity due to the increased movement and reshuffling of particles in the soil matrix.
    - D_r has the opposite effect due to less movement available in the soil matrix

- ζ_c is inversely proportional to densification, 'interlocking' and stiffness improvement as larger reversal loads induce greater soil movement. However, accumulated ratcheting increases as ζ_c approaches 0.

4. In the VDDCSS, liquefaction does not occur in drained conditions for $\tau < \tau_{max}$, as the specimen's stress path never intercepts the PTL or CSL in σ'_v, τ space never occurs in drained conditions from cycling in the VDDCSS.
5. Post-cyclic tests show spread of τ_{max} values despite constant σ'_v, demonstrating the limitations of critical state theory in accounting for cyclic behaviour.
6. Cyclic loading alters state of cohesionless soils in drained conditions, with all specimens exhibiting post-cyclic 'dilative' behaviour despite initially 'loose' conditions.

The key observations surrounding undrained cyclic behaviour are summarised below:

1. Undrained test exhibit greater cyclic resistance than their drained counterparts until N_f, where rapid increases in u cause liquefaction, leading to rapid reduction in $G_{sec.}$ and rapid increases to γ_{acc} and η simultaneously.
2. N_f is positively correlated to D_r and negatively correlated with ζ_b and τ_{ave}. N_f increases as ζ_c approaches zero for both $\zeta_c < 0$ and $\zeta_c > 0$.
3. The intersection of the specimen's stress-path with the PTL in undrained conditions coincides with N_f, suggesting that liquefaction is triggered by instability during transition between contractive and dilative behaviour.
4. Multidirectional cyclic loading shows positive relationship between N_f and $\zeta_{b,x}$.
5. Undrained post-cyclic tests exhibit lower τ_{peak} compared to monotonic tests, but the post-cyclic 'dense' specimens exhibit significantly more strain-hardening and dilative behaviour than monotonic tests.

The proper use of science is not to conquer nature but to live in it - Barry Commoner

CHAPTER 5

Application of experimental results to OWT foundation design

5.1 Introduction

The results of the experimental regimes presented in Chapter 3 and 4 are of significance to the design of OWT foundations. The way in which these experimental results inform practical design procedures of OWT forms the central focus of this Chapter. The results of Chapter 3 present a detailed investigation of small-strain stiffness, G_0 and the physical properties which influence this parameter. The investigation provides a range of appropriate values and variation of G_0 applicable to offshore marine sands. G_0 influences the design of OWT foundations in two primary areas. First, G_0 directly influences the soil-structure stiffness which dictates the displacement and rotation of the foundation which is constrained by SLS design requirements (DNVGL (2016). In addition, G_0 directly influences the value of the structure's natural frequency, f_0 which must be designed within key ranges to avoid resonance and subsequent damage to the structure, (DNVGL 2016).

A requirement of offshore foundation design is to satisfy the FLS criterion, requiring the structure to withstand cycles of loading and vibrations over its intended service life without experiencing fatigue failure. The significance of G_0 in relation to the fatigue performance of OWT is explored in this Chapter considering a case study on the 10MW DTU reference turbine (Bak et al. 2013). Several analysis tools to calculate f_0 are compared and evaluated. Subsequently, the influence of G_0 on the fatigue damage experienced by the OWT are assessed through a dynamic analysis using a 1D finite element model (FEM).

Chapter 4 presents a suite of monotonic and cyclic experiments that investigate salient features of cyclic behaviour and the physical properties that influence them. Similar cyclic behaviour is observed in the field and in model tests and therefore, a second aspect of this chapter is to compare and link the monotonic and cyclic response captured by element tests to realistic pile responses. A method of correlating soil and foundation responses is presented, and general design implications are discussed.

5.2 Elastic analysis of laterally loaded piles

As discussed in Section 1.4, the analysis of laterally loaded monopiles is commonly performed using the p-y method, which discretises the monopile into segments along the depth of the pile to which the response of the pile at each point is solved iteratively assuming non-linear behaviour for the soil-structure interaction.

Elastic analysis of laterally loaded piles is often used for design cases where the loading applied is considered sufficiently small such that it does not induce non-elastic soil-structure behaviour (Poulos and Davis 1980). This is the case for vibrational response of OWTs where applied loading to the monopile from the blades passing are relatively small. The elastic solution for laterally loaded piles usually simplifies the monopile analysis to examine only the behaviour of the monopile at the pile head. The substructure

and soil foundation are replaced with three-springs stiffness' that act at the ground level of the monopile (Arany et al. 2015). The foundation head movements and three-springs for the monopile is commonly expressed in the following 2 by 2 matrix form:

$$\begin{bmatrix} H \\ M \end{bmatrix} = \begin{bmatrix} K_L & K_{LR} \\ K_{LR} & K_R \end{bmatrix} \times \begin{bmatrix} v_G \\ \theta_G \end{bmatrix} \quad (5\text{-}1)$$

Where, H and M are the load and moment applied to the monopile, v_G and θ_G are the displacement and rotation of the monopile head. K_L, K_{LR} and K_R are the three-spring stiffness' often defined as the lateral, cross-coupling, and rotational stiffness terms of the soil-structure. There are several methods in which these three stiffness terms of the foundation can be approximated. These are broadly classified into analytical and numerical solutions; these are described in the following sections.

5.2.1 Analytical solutions for foundation stiffness

It is of interest in the geotechnical community to develop simplified expressions for the stiffness terms (K_L, K_{LR}, K_R) such that Equation (5-1) can be readily solved. Pile behaviour is classified as either slender or rigid and separate expressions have been developed for the two behaviour types. Rigid piles are short, stiff piles where the soil-structure interaction is dominated by the pile's flexural rigidity typically with L_p/D_p ratio <10. A rigid pile does not deform significantly along its length; instead, it tends to move as a single, solid body. Slender piles are long, flexible piles where the pile-soil interaction involves significant bending and deflection along the pile's length, these piles typically have a L_p/D_p ratio > 10. A slender pile experiences more complex deformation, with bending moments and deflections varying along its length.

It is also noteworthy that relationships derived for the stiffness parameters have been developed in three distinct soil stiffness profiles. 1) A homogenous stiffness profile is relevant for over consolidated cohesive materials 2) linear stiffness profile related to

normally consolidated cohesive materials and 3) a parabolic stiffness profile is associated with cohesionless soils.

Poulos and Davis (1980) developed nondimensional analytical solutions for rigid and slender piles in homogenous and linear soil stiffness profiles based on the subgrade reaction, k_h using elastic continuum solutions based on Mindlin solutions. Randolph (1981) developed expressions for slender piles in homogeneous and linear soil stiffness profiles where the stiffness parameters are a function of the stiffness of soil to pile ratio, E_s/E_p. Using this representation, Carter and Kulhawy (1992) developed expressions for rigid piles in rock. Higgins and Basu (2011) developed expressions for rigid piles in homogenous and linear soil stiffness profile using Fourier finite element method. Recent solutions by Shadlou and Bhattacharya (2016) have been derived based on the elasto-dynamic solution of the pile-structure system under dynamic loading for both rigid and slender piles in all three stiffness profiles.

The geometries of OWT monopiles classify them as rigid piles. As this research is concerned with the behaviour of OWT founded cohesionless soils, the solutions by Shadlou and Bhattacharya (2016) are the most appropriate as summarised in Table 5-1.

Table 5-1 Foundation stiffness relationships for rigid piles by Shadlou and Bhattacharya (2016)

K_L	K_{LR}	K_R
$3.2(E_{s0}D_p/f_{(vs)})(L_p/D_p)^{0.62}$	$-1.7(E_{s0}D_p^2/f_{(vs)})(L_p/D_p)^{1.56}$	$1.65(E_{s0}D_p^3/f_{(vs)})(L_p/D_p)^{2.5}$
$2.35(E_{s0}D_p/f_{(vs)})(L_p/D_p)^{1.53}$	$-1.775(E_{s0}D_p^2/f_{(vs)})(L_p/D_p)^{2.5}$	$1.58(E_{s0}D_p^3/f_{(vs)})(L_p/D_p)^{13.45}$
$2.66(E_{s0}D_p/f_{(vs)})(L_p/D_p)^{1.07}$	$-1.8(E_{s0}D_p^2/f_{(vs)})(L_p/D_p)^{2.0}$	$1.633(E_{s0}D_p^3/f_{(vs)})(L_p/D_p)^{3.0}$

Note: *D_p is pile diameter, L_p is pile length, k_h is soil subgrade modulus, E_{s0} is the soil's young modulus at $1D_p$ beneath mudline and $f(v_s) = 1 + |v_s - 0.25|$

5.2.2 Numerical solutions for foundation stiffness

Jalbi et al. (2017) proposes an alternative method from which the foundation stiffness parameters can be obtained by numerically, by first calculating v_G and θ_G and back

calculating the foundation stiffness terms. Numerical approaches include the semi-analytical iterative procedure proposed by Gupta and Basu (2016) which rely on the principle of virtual work integrated with a finite difference scheme, the 1D p-y method as described in Section 1.4 or a full 3D FEA of the monopile and soil.

In this method, the prediction of v_G and θ_G under two load scenarios needs to be evaluated 1) only horizontal loading applied at pile head and 2) only moment loading applied at pile head. Firstly, Equation (5-1) can be re-written as:

$$\begin{bmatrix} v_G \\ \theta_G \end{bmatrix} = [I] \times \begin{bmatrix} H \\ M \end{bmatrix} \tag{5-2}$$

$$\begin{bmatrix} v_G \\ \theta_G \end{bmatrix} = \begin{bmatrix} I_L & I_{LR} \\ I_{LR} & I_R \end{bmatrix} \times \begin{bmatrix} H \\ M \end{bmatrix} \tag{5-3}$$

Where I is the impedance matrix, the inverse of the stiffness matrix presented in Equation (5-1). Applying the loading scenario 1) where $H = H_1$ and $M = 0$, one derives:

$$\begin{bmatrix} u_1 \\ \theta_1 \end{bmatrix} = \begin{bmatrix} I_L & I_{LR} \\ I_{LR} & I_R \end{bmatrix} \times \begin{bmatrix} H_1 \\ 0 \end{bmatrix} \tag{5-4}$$

$$I_L = \frac{u_1}{H_1}, I_{LR} = \frac{\theta_1}{H_1} \tag{5-5}$$

Similarly, by applying load scenario 2) where $H = 0$ and $M = M_1$, the following expressions are obtained:

$$\begin{bmatrix} u_2 \\ \theta_2 \end{bmatrix} = \begin{bmatrix} I_L & I_{LR} \\ I_{LR} & I_R \end{bmatrix} \times \begin{bmatrix} 0 \\ M_1 \end{bmatrix} \tag{5-6}$$

$$I_{LR} = \frac{u_2}{M_1}, I_{LR} = \frac{\theta_2}{M_1} \tag{5-7}$$

The stiffness parameters can then be computed as:

$$K = \begin{bmatrix} K_L & K_{LR} \\ K_{LR} & I_R \end{bmatrix} = I^{-1} = \begin{bmatrix} I_L & I_{LR} \\ I_{LR} & I_R \end{bmatrix}^{-1} \tag{5-8}$$

$$K = \frac{1}{\left(\frac{u_1}{H_1} \times \frac{\theta_2}{M_1}\right) - \left(\frac{u_2}{M_1} \times \frac{\theta_1}{H_1}\right)} \times \begin{bmatrix} \frac{\theta_2}{M_1} & -\frac{u_2}{M_1} \\ -\frac{u_1}{H_1} & \frac{\theta_1}{H_1} \end{bmatrix} = \begin{bmatrix} K_L & K_{LR} \\ K_{LR} & K_R \end{bmatrix} \quad (5\text{-}9)$$

5.3 Fatigue analysis of OWT monopiles

This section introduces design calculations that have been proposed for fatigue analysis of OWT monopiles. The methods described in this section are implemented in Section 5.4, that presents the results of a fatigue analysis from a case study on a 10MW DTU OWT. The natural frequency, f_0, of the OWT and foundation is key for fatigue analysis as its position in relation to the wind, wave 1P and 3P rotational frequencies contribute to the extent of damage experienced by the foundation, see Figure 1-4. The determination of f_0 using two methods as described in Section 5.2.1 and 5.2.2 and damage calculations are described in Section 5.3.3 are applied.

5.3.1 Analytical predictions of f_0

This section describes the closed form analytical solution proposed by Aranay et al. (2017) to predict the natural frequency, f_0 of an OWT system. This solution assume f_0 is a function of the fixed based frequency, f_{FB} and the stiffness of the soil-structure interaction, represented by two coefficients. The general equation is expressed as:

$$\mathrm{f_0 = C_L C_R f_{FB}} \quad (5\text{-}10)$$

Where C_L and C_R are the lateral and rotational foundation coefficients described by:

$$\mathrm{C_L = 1 - \frac{1}{1+0.6\left(\eta_R - \frac{\eta_{LR}^2}{\eta_L}\right)}} \quad (5\text{-}11)$$

$$\mathrm{C_R = 1 - \frac{1}{1+0.5\left(\eta_R - \frac{\eta_{LR}^2}{\eta_L}\right)}} \quad (5\text{-}12)$$

$$\mathrm{\eta_L = \frac{K_L L_T^3}{EI_\eta}, \eta_{LR} = \frac{K_{LR} L_T^2}{EI_\eta}, \eta_R = \frac{K_L L_T}{EI_\eta}} \quad (5\text{-}13a,b,c)$$

Where K_L, K_{LR} and K_R are the spring stiffness parameters discussed in Section 5.2.1, L_T is the length of the tower, $EI\eta$ is the equivalent bending stiffness of the tower, calculated as:

$$\mathrm{EI_\eta} = \mathrm{E_T I_T f(q)} \tag{5-14}$$

$$\mathrm{f(q)} = \frac{1}{3} \cdot \frac{2\mathrm{q}^2(\mathrm{q}-1)^3}{2\mathrm{q}^2 \ln \mathrm{q} - 3\mathrm{q} + 4\mathrm{q} - 1} \tag{5-15}$$

$$\mathrm{q} = \frac{\mathrm{D_b}}{\mathrm{D_t}} \tag{5-16}$$

Where E_T is the young's modulus of the tower, I_T is the average area of moment of inertia of the tower, D_b is the diameter of the base of the tower and D_t is the diameter of the top of tower. The fixed base frequency, f_{FB}, can be approximated as:

$$\mathrm{f_{FB}} = \frac{1}{2\pi}\sqrt{\frac{\mathrm{k_0}}{\mathrm{m_0}}} = \frac{1}{2\pi}\sqrt{\frac{3\mathrm{E_T I_T}}{\mathrm{L_T^3}\left(\mathrm{m_{RNA}} + \frac{33}{140}\mathrm{m_T}\right)}} \tag{5-17}$$

Where m_T is the mass of the tower, m_{RNA} is the mass of the rotor-nacelle assembly and L_T is the length of the tower.

5.3.2 Eigenvalue analysis

Eigenvalue analysis is a mathematical operation that solves for the dynamic properties of a system using its characteristic equation composed of the system's mass and stiffness distribution. This is an alternative method from which f_0 for an OWT system can be obtained. The following derivations describe the solution for determining f_0 in a multi degree of freedom system (MDOF) under dynamic loading following Williams (2016). The equation of motion for a MDOF is commonly expressed via the following equation.

$$\mathrm{m\ddot{x} + c\dot{x} + kx = f} \tag{5-18}$$

Where m is the mass matrix, c is the damping matrix, k is the stiffness matrix, f is the applied load and x is the displacement vector. To solve the free vibration problem, the load is set to zero. The practical effect of damping caused by the 1P and 3P vibrational

loads on OWTs is minor due to their relatively low amplitudes. As stated previously, it is assumed soil-structure remains elastic under such loading and therefore, the damping term can be omitted to simplify Equation (5-18) to:

$$m\ddot{x} + kx = 0 \tag{5-19}$$

The displacement *x* varies as a function of position and time and can be expressed in terms of its velocity, *v*, and time, *t* only.

$$x = v \sin \omega t \tag{5-20}$$

Differentiating Equation (5-20) and substituting into Equation (5-19) gives

$$(\mathbf{K} - \omega^2\mathbf{M})v \sin \omega t = 0 \tag{5-21}$$

Equation (5-21) is often referred to as the characteristic equation of the system. An appropriate solution for Equation (5-21) requires the matrix ($\mathbf{K} - \omega^2\mathbf{M}$) to have no inverse. This in turn requires that its determinant is zero. One can therefore solve for ω via the following equation:

$$\det(\mathbf{K} - \omega^2\mathbf{M}) = 0 \tag{5-22}$$

f_0 of the system can be obtained by multiplying ω by 2π. Therefore, for a system with *n* DOFs, Equation (5-22) is an *n*th order polynomial that can be solved to give *n* values of ω and f_0 (not necessarily all different). Each natural frequency can be substituted into the following equation to find a corresponding vector *v*.

$$(\mathbf{K} - \omega^2\mathbf{M})v = 0 \tag{5-23}$$

An *n-DOF* system has *n* natural frequencies f_i, each associated with a corresponding deformation shape v_i referred to as the *mode shape*.

5.3.3 Damage calculation

The S-N curve method is a practical approach to predict the fatigue life of materials under cyclic loading and relies on the assumption of linear cumulative damage. S-N curves are

constructed from experimental data obtained through fatigue tests where the material is subjected to cyclic loading at different stress levels, the applied stress amplitude, S is plotted against number of cycles of failure N which forms the S-N curve. From the curves, the following equation can be used to calculate the amount of damage when the long-term stress range distribution is expressed by a stress histogram, consisting of a convenient number of constant stress range blocks $\Delta\sigma_i$ each with several stress repetitions n_i

$$D = \sum_{i=1}^{k} \frac{n_i}{N_i} = \frac{1}{\bar{a}} \sum_{i=1}^{k} n_i \cdot (\Delta\sigma_i)^m \leq \eta \tag{5-24}$$

Where D is the accumulated damage, $\bar{a}$ is the intercept of the S-N curve of the material, m is the negative inverse slope of the S-N curve, k is the number of stress blocks, n_i is the number of stress cycles in block i, N_i is the number of cycles to failure at constant stress range $\Delta\sigma_i$ and η is the usage factor. Further details related to fatigue analysis assumptions, fatigue failure modes, failure criterion and material specific S-N curves are outlined in detail in DNV (2008).

5.4 Case study of 10MW DTU

This section presents the results of case study investigating the response of the 10MW DTU reference turbine, Bak et al. (2013). This wind turbine was selected as the structural properties are well defined and has been used by other researchers whose results serve as validation for the work presented in this thesis, Alkhoury et al. (2021). This section seeks to quantify the influence of G_0 on the fatigue performance of OWT. This is conducted by first evaluating the influence of G_0 on f_0 and subsequently fatigue damage to the OWT from repeated cyclic loading. The determination of f_0 is undertaken using analytical solutions and eigenvalue analysis as described in Section 5.3.1 to 5.3.2. Discussion regarding the suitability of these methods for OWT design is presented. Fatigue and damage calculations additionally require dynamic analysis of the OWT which were

undertaken using OxDyn, a dynamic 1D FEM code, designed to simulate the static and dynamic response of simplified offshore wind turbine superstructures with advanced foundation soil-structure interaction. The method utilised forward time integration allowing for the time stress history of the OWT to be determined such that damage calculations can be performed. Full details of the modelling framework is provided in Ryan et al. (2023).

5.4.1 Load determination

To estimate the static wind load, it is assumed that the OWT is operating in region II (above cut-in and below rated wind speed) of the wind speed curve, representative of operating conditions, where the wind load varies quadratically with wind speed.

$$\mathrm{F_{wind}} = \frac{1}{2}\rho_{air} V_{wind}^2 A_T C_T \tag{5-25}$$

Where, ρ_{air} is the density of air, V_{wind} is the wind speed taken as 11.4m/s, the rated wind speed of the reference turbine, A_T rotor swept area taken as 140m and C_T is the thrust coefficient equal to 0.5 based on turbine characteristics as defined in Bak et al. (2013)

The dynamic analysis requires calculation of the turbulent wind kinematics that are added to the V_{wind} based on Kaimal spectrum following methodology presented in IEC (2019). The velocity spectrum is converted to a turbulent velocity time series using the spectral representation method outlined in Rose and Apt (2012).

Similarly, the determination of wave loads first required the wave kinematics before calculating the forces using Morison's equation with MacCamy–Fuchs corrections recommended by IEC (2019).

$$\mathrm{F_{wave}} = \frac{1}{2} C_d \rho_{water} D_{turbine} |V_{wave}| V_{wave} + C_m \rho_{water} \frac{\pi D_{turbine}^2}{4} \dot{V}_{wave} \tag{5-26}$$

Where C_d is the drag coefficient, C_m is the inertia coefficient, ρ_{water} is the density of water,

V_{wave} and $\dot{V}_{wave}$ are horizontal component of velocity and acceleration respectively and $D_{turbine}$ is the diameter of the turbine. V_{wave} and $\dot{V}_{wave}$ can be determined by following equations:

$$V_{wave} = \frac{H_s g k}{2\omega} \frac{\cosh\left(k(z + h_{sea})\right)}{\cosh\left(k h_{sea}\right)} \cos(kx - \omega t) \tag{5-27}$$

$$\dot{V}_{wave} = \frac{H_s g k}{2\omega} \frac{\cosh\left(k(z + h_{sea})\right)}{\cosh\left(k h_{sea}\right)} \sin(\omega t - kx) \tag{5-28}$$

Where, H_s is the significant wave height, g is gravity, k is the wavenumber, determined from $\omega^2 = gk\tanh(kh_{sea})$, z is the vertical distance, h_{sea} is the height of the maximum wave height above ground level, x is the horizontal distance, ω is the wave frequency is $\omega = 2\pi/T_p$, t is the time and T_p is the peak wave period. The values of H_s and T_p were obtained by linearly interpolating wave conditions in Wang et al. (2021) to the relevant V_{wind} and h_{sea} is taken as 25m based on metocean data presented in Arany et al. (2017). For the dynamic analysis, wave kinematics calculation based on IEC (2019) are undertaken. The Jonswap spectrum is used to estimate H_s and T_p based on V_{wind}.

The influence of f_{1P} and f_{3P} are included in the dynamic analysis and are based on operational values given for the 10MW DTU turbines and discussed in Xi et al. (2021). Based on the design tip speed ratio and minimum and maximum rotor speeds, the f_{1P} range is between 0.1 and 0.16Hz and the f_{3P} range is between 0.3 and 0.48Hz for the turbine. In the dynamic analysis, f_{1P} and f_{3P} are taken to be 0.16Hz and 0.3Hz respectively considering the 'worst case' scenario. The magnitude of the tangential forces associated 1P/3P loads is taken as 700kN, applied 154m above ground level.

5.4.1 Modelling the OWT structural components

This study was undertaken considering the 10MW DTU research wind turbine. The wind turbine characteristics are presented in Table 5-2.

Table 5-2 10MW DTU reference turbine characteristics

OWT component	Symbol (unit)	Value
Tower height	L_T (m)	119
Substructure height	L_S (m)	35
Structure height	L (m)	154
Diameter top	D_T (m)	8.3
Pile diameter	D_p (m)	8.3
Pile thickness	t_W (m)	0.09
Youngs Modulus (tower and	E_T (GPa)	210
Monopile depth	L_p (m)	45
Poisson ratio (steel)	ν (-)	0.3
Cut-in and rated rotor speed	ω (rpm)	6 and 9.6

The analytical solution for predicting f_0 as proposed by Arany et al. (2015) uses the structural parameters from Table 5-2 as direct inputs into Equation (5-17). For eigenvalue and fatigue analysis, the pile-tower structure is modelled as Timoshenko beam elements and the nacelle, rotor and blades are modelled by a lumped mass. The lumped mass properties of the 10MW DTU turbine are presented in Table 5-3.

Table 5-3 Lumped mass modelling properties

OWT component	Symbol (unit)	Value
Lumped mass	m (kg)	676723
Offset about x-axis	x_{off} (m)	0
Offset about y-axis	y_{off} (m)	0
Offset about z-axis	z_{off} (m)	-2.8
Moment of inertia about x-	I_x (kg.m2)	1.66E+08
Moment of inertia about y-	I_y (kg.m2)	1.27E+08
Moment of inertia about z-	I_x (kg.m2)	1.27E+08

5.4.2 Modelling the soil-foundation system

In the analytical for predicting f_0 as proposed by Arany et al. (2015), the foundation of the OWT is modelled by the three-spring model discussed in Section 5.2 and schematically shown in Figure 5-1(a). The foundation stiffness parameters were obtained using analytical relationships proposed by Shadlou and Bhattacharya (2016) for rigid piles founded in soils with parabolic varying stiffness profiles, (see Section 5.5.1) and

also using numerical methods proposed by Jalbi et al. (2017), (see Section 5.2.2), subsequently referred to as the 'simplified' and 'standard' method respectively.

Eigenvalue and fatigue analysis of the OWT required the use of the 1D FEM where the PISA design model is applied. In this model the soil-structure is represented by a series of interconnected 1D Timoshenko beam elements (see Figure 5-1(b)). A distributed lateral load and moment is assumed to act on the pile along its length, along with a skin friction shear force acting at the pile-soil interface, and a pile-base force and moment. The soil reaction curves are calibrated based on 3D finite-element analyses, and curve fits are based on four parameter conic functions and the resultant nonlinear finite-element equations are then solved for the displacement and rotation of each beam element. In this study, the Generalised Dunkirk Sand Model (GDSM) is implemented to represent the founding soil which is a general soil model calibrated based on the response of 11 medium-scale field tests and numerous 3D FEA across a range of monopile geometries founded Dunkirk sand as a part of the PISA project (McAdam et al. 2019; Taborda, Zdravkovic, et al. 2019; Burd et al. 2019) for details. The model requires 22 parameters as inputs and employs simple functions (linear or constant) to represent the dependency of each parameter on D_r. Based on whether the parameter in question exhibits a dependency on D_r from the calibration piles, it was assigned a linear or constant function to D_r. The appropriate calibration space of GDSM is for cohesionless soils of D_r = 45 to 90%, pile geometries of $2 \leq L_p/D_p \leq 6$, load eccentricities $5 \leq h/D_p \leq 15$ and diameters 5m $\leq D_p \leq$ 10m. These dimensions were selected to span a realistic design range for current and future monopiles.

The submerged unit weight of the Dunkirk sand site is $\gamma' = 10.09\text{kN/m}^3$ and the water depth is taken as 25m above ground level. The G_0 profile of the material is based

on calibrated parameters from *in-situ* and laboratory testing as detailed in Zdravković et al. (2020) and described below:

$$G_0 = \frac{B p'_{ref}}{0.3 + 0.7 e_0^2} \sqrt{\frac{p'}{P_a}} \tag{5-29}$$

Where, B is a stiffness fitting parameter taken as 940 for the base case, p' is the mean effective stress, P_a is the atmospheric pressure and e_0 is the void ratio of the soil (varies between 0.55 to 0.75 in this study equating to D_r = 45 to 90% which is within the calibration space of the GDSM.

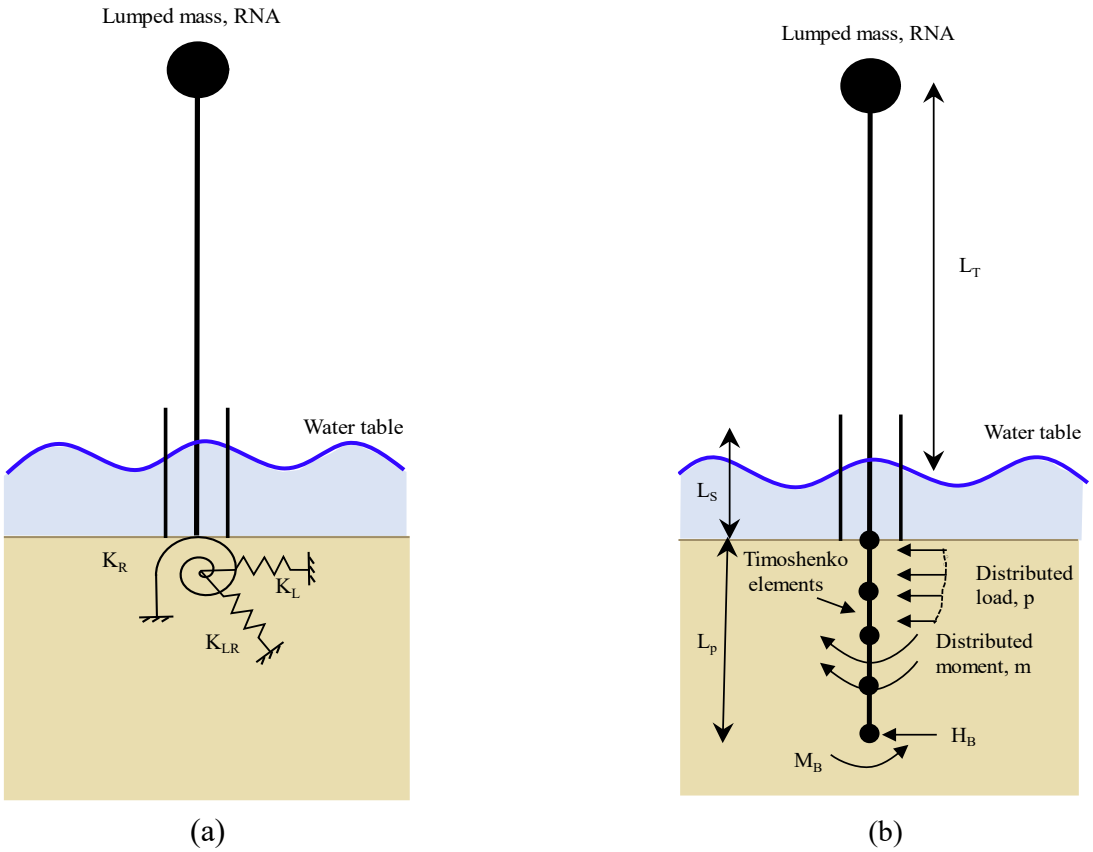


Figure 5-1 10MW DTU Turbine model (a) 3-spring model; and (b) 1D numerical model with idealisation of soil reaction as applied in OxDyn

5.4.3 Validation of 1D numerical method

There are currently no published f_0 measurements from experiments or 3D FEA for a OWT founded in Dunkirk sands or any of the three cohesionless soils studied in Chapter 3 and 4. Therefore the computed f_0 determined from the 'simplified', 'standard' and

eigenvalue analysis were initially validated against results from a 3D FEA of the 10MW DTU reference turbine founded in sandy soils by Alkhoury et al. (2021). As such, the G_0 profile used in their study was initially adopted and is described below:

$$\mathrm{G_0} = q_\mathrm{c}(0.0203 + 0.00125\eta - 1.216 \times 10^{-6}\eta^2)^{-1}$$
$$\eta = \mathrm{q_c}(\mathrm{P_a}\ \sigma'_\mathrm{v})^{-0.5} \quad \text{(5-30a,b,c)}$$
$$q_c = 60(\sigma'_\mathrm{v})^{0.5}\mathrm{e}^{2.91\mathrm{D_r}}$$

Where q_c is the cone tip resistance from CPT measurements, η is CPT factor P_a is the atmospheric pressure, σ'_v is the vertical effective stress, and D_r is the relative density. A summary of the computed f_0 measurements and those by Alkhoury et al. (2020) are presented Table 5-4 below.

Table 5-4 Validation results

		Loose (D_r=30%)	**Medium (D_r=50%)**	**Dense (D_r = 80%)**
	Average G_0	140	290	690
Alkhoury et al. (2020)	f_0 (Hz)	0.2009	0.2022	0.2034
Eigenvalue analysis		0.2004	0.2020	0.2040
	Error (%)	**-0.44**	**-0.0989**	**0.295**
'Simplified' method	f_0 (Hz)	0.2240	0.2240	0.2250
'Standard' method		0.2020	0.2050	0.2110

The 'simplified' produced values of f_0 that of approximately 10% higher than the results from the 3D FEA. An interesting observation is that the 'simplified' method yielded f_0 within 1% of the fixed based frequency, f_{FB} = 0.226. Upon further investigation, it was found that the 'simplified' method produced values of C_L and C_R of approximately unity across all ranges of soil stiffness. This implies that the method does not alter f_0 from f_{FB} essentially indicating that the effect of soil stiffness is not considered, highlighting an acute error in using such methods for f_0 predictions and the necessity to use alternative methods in solving for f_0. This observation aligns with the study by Bouzid et al. (2018) who similarly noted a f_0 very close to f_{FB} whilst using this method. The 'standard' method produced results closer to the 3D FEA values, with errors ranging between 1% to 3%.

Eigenvalue analysis implemented through the 1D FEM yielded f_0 very close to those of the 3D FEA with a computed error $\pm$0.5% demonstrating the accuracy and reliability of the method. Consequently, based on the validation study all subsequent analyses of f_0 were undertaken using the eigenvalue analysis implemented through the 1D FEM, employing the GDSM with parameters described by Burd et al. (2019), given its robust performance. The initial stiffness in the GDSM is primarily controlled by D_r with G_0 used only in the normalisation of the response.

5.4.4 Natural frequency

To examine the influence of G_0 on f_0, a soil sensitivity study was undertaken where the average G_0 of the soil profile was reduced by 0 to 20% of the base case G_0 profile described by Equation 5-5 by varying the void ratio, e across the calibrated regions of the GDSM model (e = 0.75-0.55, equating to D_r = 45 to 90%). Since the base case relative density was equal to 90%, it was not realistic to increase the soil stiffness profile. Thus, this study investigates the dynamic response of the OWT for a reduction in G_0 only.

First the influence G_0 variation on the various GDSM reaction curves used in the 1D FEM is explored. This is undertaken considering the 10MW DTU turbine founded in Dunkirk sand. The water depth was taken to be 25m above ground level.

The distributed lateral load, p with respect to displacement, v at the midpoint of the monopile (z = 22.5m), base horizontal force, H with respect to base displacement v_B, distributed moment, m with respect to rotation, θ at the midpoint of the monopile (z = 22.5m) and base moment, M with respect to base rotation, θ_B for several G_0 profiles are presented in Figure 5-2(a) to (d) throughout.

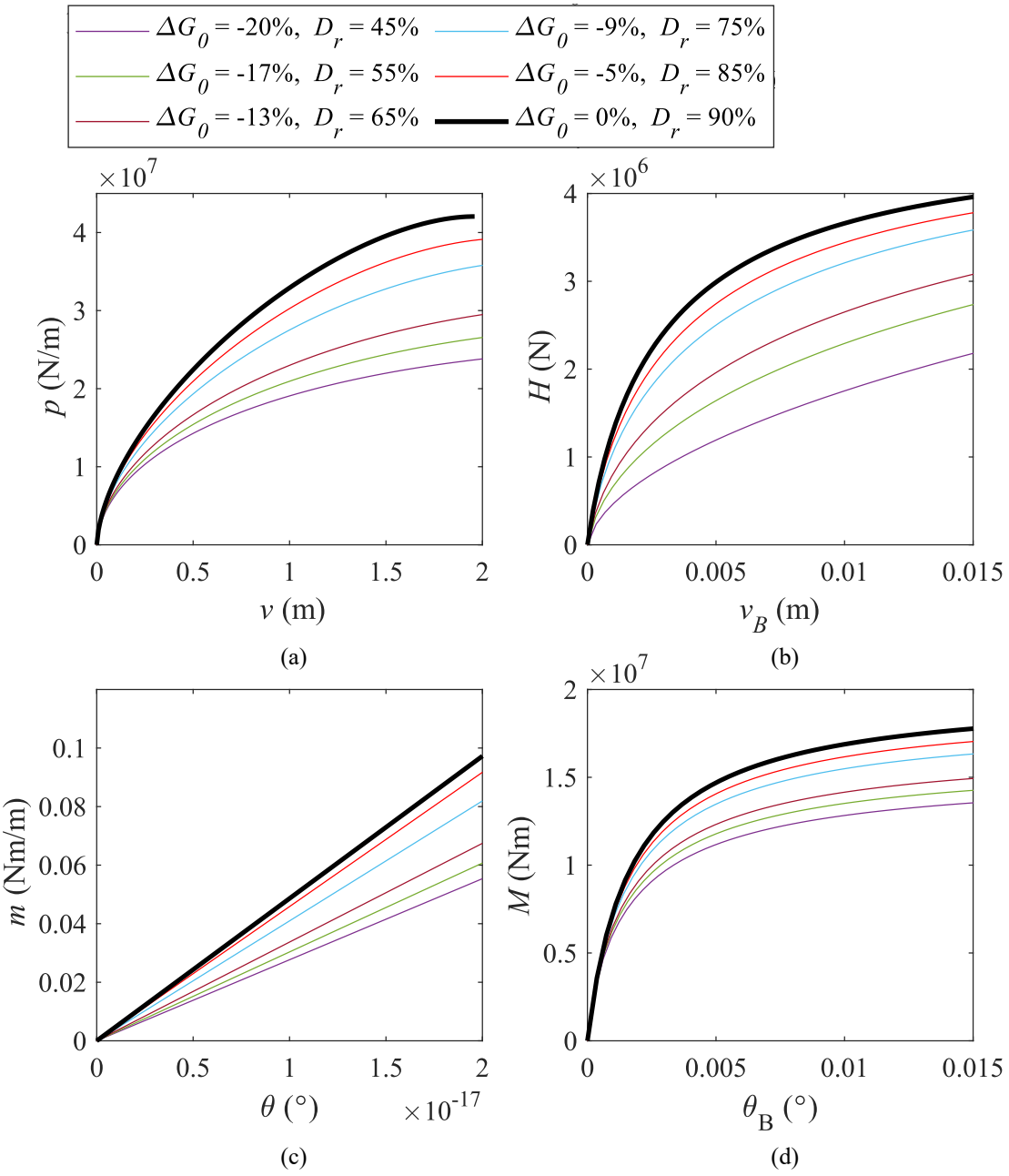


Figure 5-2 Effect of G_0 on GDSM soil reaction curves from Burd et al. (2019) (a) Distributed lateral load at z = 22.5m; (b) Base horizontal load; (c) Distributed moment at z = 22.5m; and (d) Base moment

It can be seen from Figure 5-2 that G_0 (and D_r) are positively correlated with the stiffness of each soil reaction curve. Subsequently, eigenvalue analysis was conducted to compute f_0 across the same range of G_0 and D_r for a range of pile diameters D_p = 7.5 to 18 m, spanning L_p/D_p ratios from 2 to 6, which are typical values for OWT monopiles. It is important to note that as pile diameters increase in size, it is likely that the structural

characteristics of the superstructure of the OWT would also change and the environmental conditions, such as water depth would not be the same for different sized diameters. However, in this study, these other conditions were not altered and the effects of changing D_p were investigated in isolation.

The computed f_0 are summarised in Table 5-5. The variation of change in f_0 as a function of change in G_0 and D_p is shown in Figure 5-3(a) and (b) respectively.

Table 5-5 Results of soil sensitivity study of f_0

ΔG_0 (%)/ΔD_r (%), D_p = 7.5m						
	-20 /-45	**-17/-35**	**-13/-25**	**-9/-15**	**-5/-5**	**0/0**
f_0 (Hz)	0.173	0.173	0.174	0.175	0.175	0.175
$f_0/f_{0,base}$	0.99	0.99	0.99	1.00	1.00	1.00
D_p = 8.3m*						
f_0 (Hz)	0.197	0.198	0.199	0.200	0.201	0.201
$f_0/f_{0,base}$	0.98	0.99	0.99	0.99	1.00	1.00
D_p = 10m						
f_0 (Hz)	0.250	0.252	0.253	0.254	0.254	0.255
$f_0/f_{0,base}$	0.98	0.99	0.99	0.99	0.99	1.00
D_p = 12m						
f_0 (Hz)	0.312	0.314	0.315	0.316	0.317	0.318
$f_0/f_{0,base}$	0.98	0.99	0.99	0.99	0.99	1.00
D_p = 14m						
f_0 (Hz)	0.371	0.375	0.376	0.377	0.378	0.379
$f_0/f_{0,base}$	0.98	0.99	0.99	0.99	0.99	1.04
D_p = 16m						
f_0 (Hz)	0.427	0.432	0.435	0.436	0.438	0.439
$f_0/f_{0,base}$	0.97	0.98	0.99	0.99	0.99	1.04
D_p = 18m						
f_0 (Hz)	0.478	0.487	0.488	0.493	0.493	0.500
$f_0/f_{0,base}$	0.86	0.98	0.99	1.01	1.02	1.05

Note: *10MW DTU reference turbine (base case)

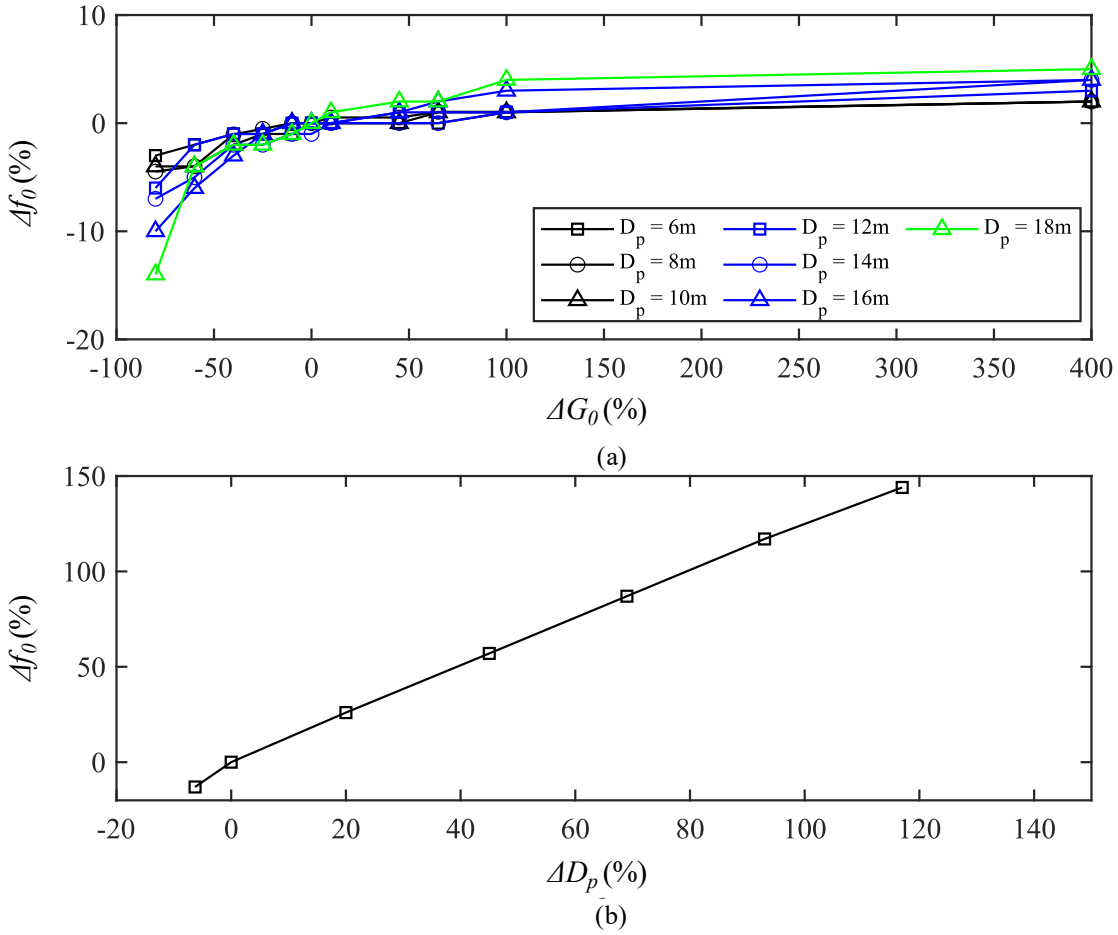


Figure 5-3 Variation of f_0 for different D_p (a) with respect to G_0; and (b) with respect to D_p, Base case ΔG_0 & $\Delta D_r = 0$

Figure 5-3(a) demonstrates a positive correlation between G_0 (and D_r) and f_0. Across the investigated G_0 and D_r, changes to f_0 remain under 5% across all investigated D_p. The f_0 becomes increasingly sensitivity to G_0 as D_p increases, with D_p = 18m exhibiting the greatest variation in f_0 from changes to G_0.

Figure 5-3(b) shows a linear relationship positive relationship between D_p and f_0 for the base case soil stiffness (D_r = 90%) where a near 1:1 relationship between the two parameters is seen. As D_p increases, the overall stiffness of the foundation increases which contributes to the increase in f_0. This is in line with results from Wan et al. (2023); Alkhoury et al. (2021) . For a reduction of G_0 of up to 20% (and reduction of D_r of 45%), very little changes to f_0 occur. These results suggest a coupled effect between D_p and G_0 (and D_r) on f_0 as it is observed that there is greater sensitivity to G_0 (and D_r) as D_p

increases. The range of G_0 (and D_r) examined is based on a realistic offshore profile (Dunkirk site) and it is shown here that realistic variations in G_0 (and D_r) do not considerably influence nominal values of f_0 within the GDSM framework where the initial stiffness is controlled by D_r and the influence of G_0 is difficult to decouple from D_r. Different outcomes are likely with other soil reaction curve models and in different materials. A more robust approach, that determines the change in f_0 for varying G_0 with a 3D FEA model is recommended for additional insights. 3DFEA was outside the scope of this research.

5.4.5 Fatigue and damage

Repeated vibration loads caused by the 1P and 3P excitation of the blades of the wind turbine causes damage to the OWT. The proximity of the f_0 of the OWT to the f_{1P} and f_{3P} indicates how much damage is induced with each load cycle. The f_0 is designed to sit between f_{1P} and f_{3P} to minimise damage. By undertaking a dynamic analysis across a range of excitation frequencies, f, one can visually observe the effect of excitation frequency on ground level displacement, v_G of the OWT, a proxy for damage. This is schematically shown in Figure 5-4. The ranges of f_{1P} and f_{3P} for the 10MW DTU OWT (ref. Section 5.4.1) are highlighted by the grey regions in the figure.

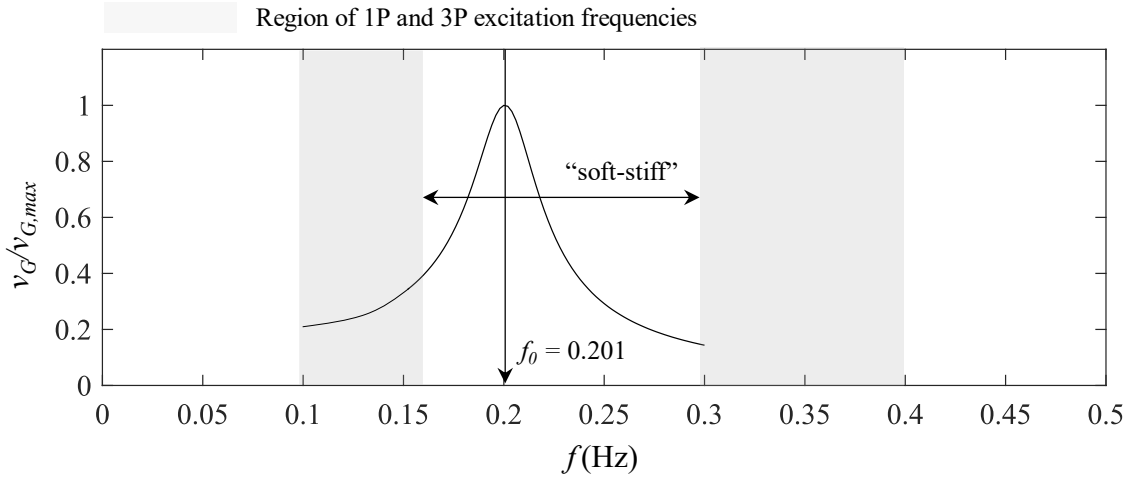
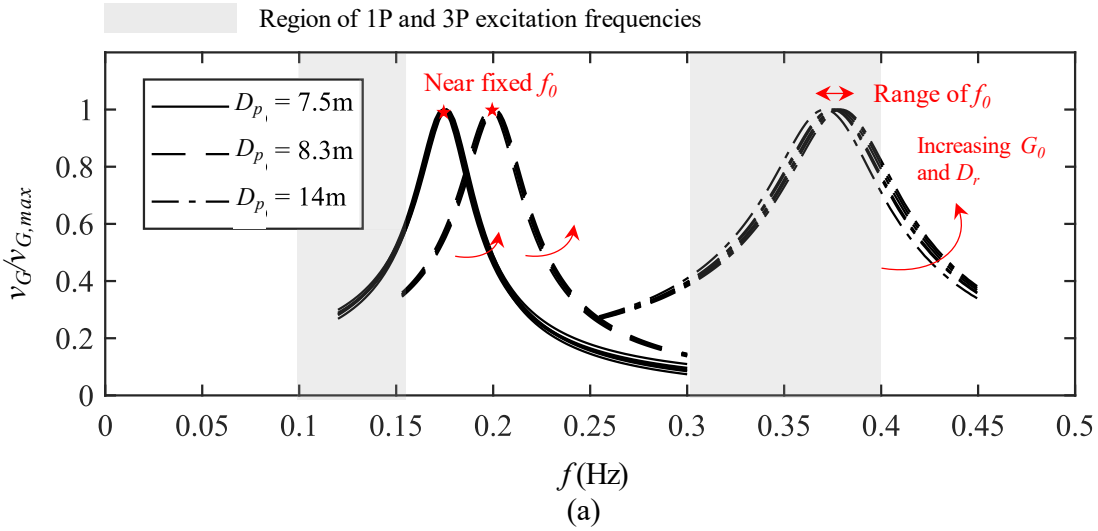
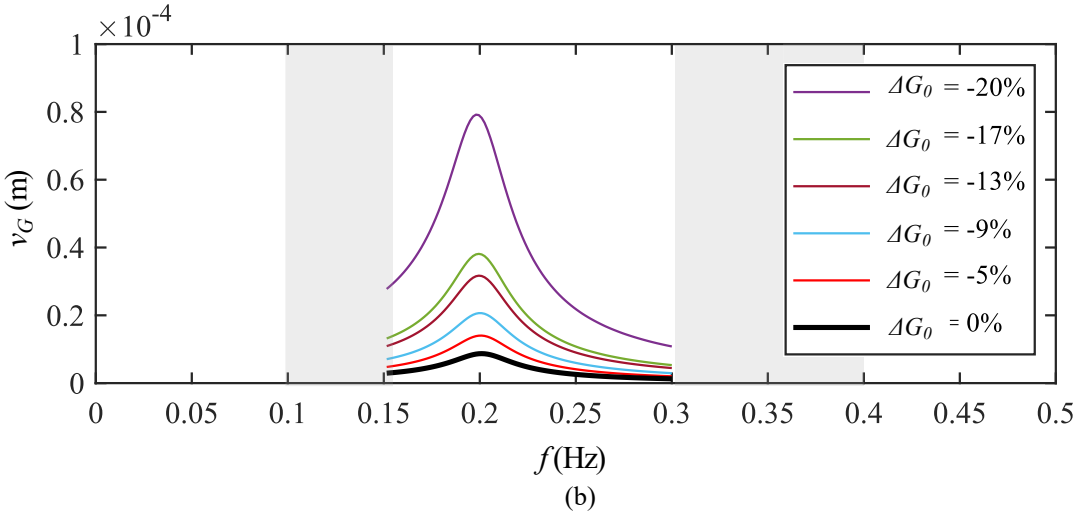


Figure 5-4 Excitation response of the 10MW DTU turbine for D_p = 8.3m, ΔG_0 = 0 base case

As expected, v_G significantly increases as the f approaches f_0, and maximum v_G (and hence damage) occurs at $f = f_0$, however the response is non-linear. Changes to v_G reduce as f moves further away from f_0. This implies that even if changes to f_0 are minor, the of damage to the structure (as represented by the area under the curve) can be significant. This effect is explored on the 10MW DTU turbine for three D_p values across the various G_0 profiles previously investigated. Again, it is important to remember that this investigation has investigated the impacts of varying D_p in isolation whilst for practical design purposes, changes in D_p would most likely be due changes in water depth and different D_p would also have different superstructure geometries and characteristics. The nominal values of the results from subsequent analysis are therefore not necessarily representative of an expected turbine with larger D_p but results demonstrate the overall trends associated with variation of D_p

Figure 5-5(a) presents the effect of G_0 variation on normalised v_G for D_p = 7.5, 8.3 and 14m which are represented by the solid, dashed and dashed-dot lines respectively. The influence of D_r and G_0 on the nominal values of v_G for D_p = 8.3m is displayed in Figure 5-5(b).





(b)

Figure 5-5 Variation of ground level displacement with excitation frequency (a) Normalised displacement for D_p = 7.5, 8.3 and 14 m; and (b) Nominal displacement for D_p = 8.3m

There are two notable observations here. First, the influence of D_p is significant. For the two smaller diameters (D_p = 7.5 and 8.3 m), f_0 remains mostly fixed as G_0 reduces. For D_p = 14m reduction in D_r and G_0 shifts f_0 into the f_{3P} region and the spread of f_0 becomes greater with changes to D_r and G_0, implying also that fatigue damage will become more sensitive to D_r and G_0. For the large diameter case, whilst the range of f_0 remains within 5%, the area under the curve changes substantially as D_r and G_0 reduces, and the fatigue damage increases non-linearly. Figure 5-5(b) indicates that D_r and G_0 are negatively related with the nominal value of v_G, and hence fatigue damage.

A further soil sensitivity study was undertaken to investigate the effects of D_r, G_0 and D_p on fatigue damage applying the method described in Section 5.3.3. For OWTs, it is appropriate to assume fatigue failure occurs at ground level along the sections of the monopile welded together. Therefore, the S-N curves for butt welds provided in DNV-RP-C203 was used. A summary of results is presented in Table 5-6. Figures 5-6(a) to (c) throughout present the calculated damage with respect to D_r and G_0 for D_p = 7.5, 8.3 and 14 m and a breakdown of contribution by wind and waves compared with 1P /3P loads. Figure 5-6(c) presents the variation of total damage with D_r and G_0 for the same D_p values.

Table 5-6 Soil stiffness sensitivity on fatigue damage

ΔG_0 (%)/ΔD_r(%), D_p = 7.5m						
	-20 /-45	**-17/-35**	**-13/-25**	**-9/-15**	**-5/-5**	**0/0**
Damage (1P/3P) × 10^{-}	6.72	6.65	7.27	7.33	7.38	7.27
Damage (Total) × 10^{-4}	6.57	6.56	6.53	6.50	6.49	6.45
Δ Damage (%)	+2.0	+1.7	+1.0	+<1	+<1	0
D_p = 8.3m*						
Damage (1P/3P) × 10^{-5}	2.51	2.50	2.49	2.48	2.48	2.47
Damage (Total) × 10^{-4}	2.37	2.37	2.36	2.36	2.36	2.35
Δ Damage (%)	+1.0	+1.0	+<1	+<1	+<1	0
D_p = 14m						
Damage (1P/3P) × 10^{-6}	2.05	1.75	1.36	1.34	1.32	1.29
Damage (Total) × 10^{-6}	6.80	6.57	6.01	5.97	5.93	5.85
Δ Damage (%)	+16	+12	+3.0	+2.0	+1.0	0

* Base case condition

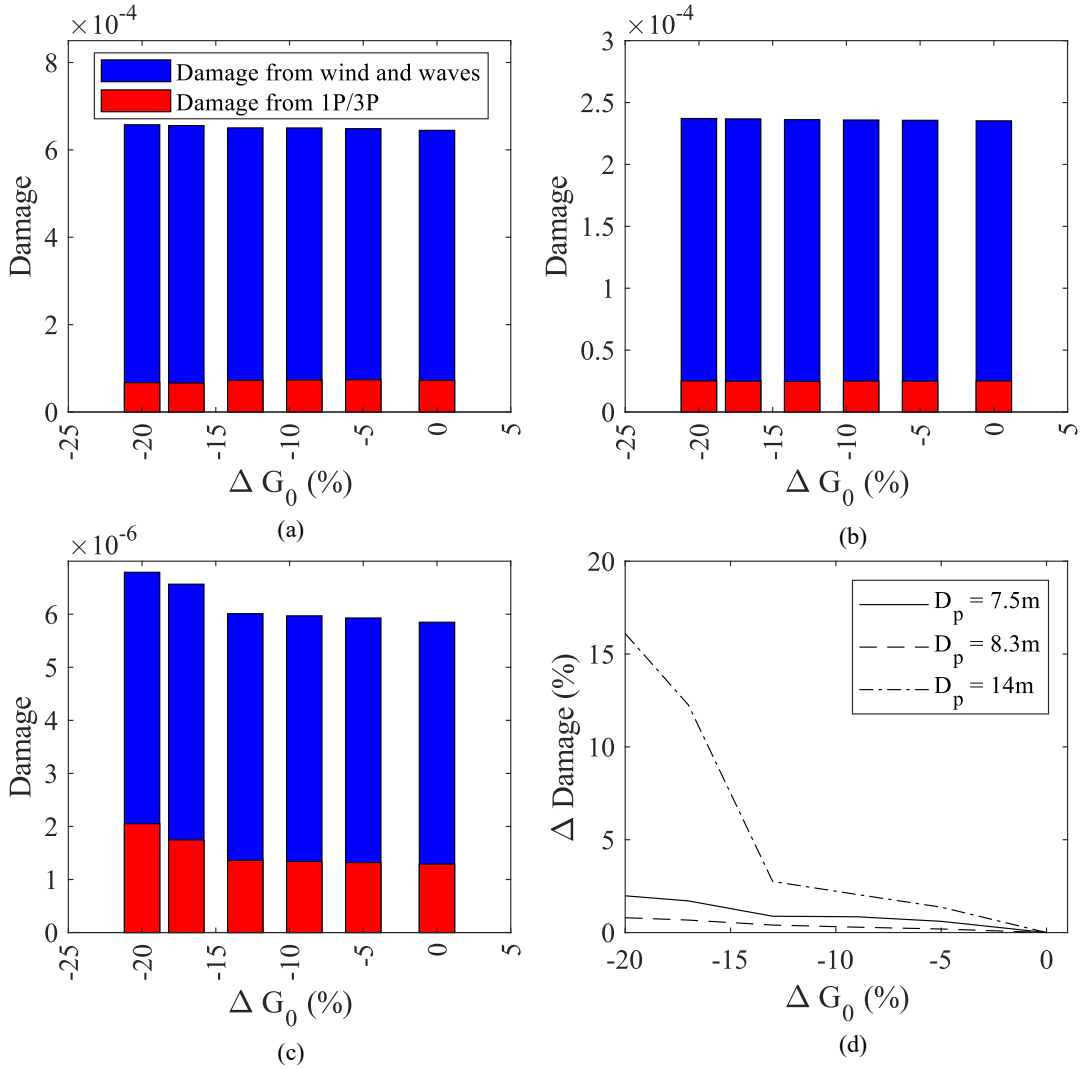


Figure 5-6 Fatigue damage as a function of G_0 (a) Contribution to damage by loads D_p = 7. 5m; (b) Contributions to damage by loads D_p = 8.3 m; (c) Contribution to damage by loads D_p = 14 m; and (d) Change in damage for three D_p

Results from Table 5-5 and Figure 5-6(a) and (b) indicate that 1P/3P loads account for 10 to 30% of total damage depending on D_p and D_r/G_0. The highest fatigue damage occurs for D_p = 7.5 m as f_0 is closest to the excitation frequencies of environmental and operational loads and the converse is true for the highest examined diameter, D_p = 14 m.

Irrespective of D_p, a reduction in D_r and G_0 shifts f_0 towards the excitation frequencies of environmental loads, increasing fatigue damage. For D_p = 7.5 and 8.3 m, f_0 shifts towards f_{1P} and for D_p = 14 m, f_0 shifts towards f_{3P}. For the two lower D_p examined, reduction to D_r and G_0 up to 20% has a marginal impact on damage, (See Figure 5-6(a) and (b)). This is likely because changes to D_r and G_0 do not have a profound influence on f_0 and hence fatigue damage for smaller diameters as discussed in Section 5.4.5. However, for D_p = 14m, a reduction in D_r and G_0 significantly increases the proportionality between damage induced by 1P/3P to total damage, see Figure 5-6(c) (c). Figure 5-6(d) shows that fatigue damage remains within 2% for a reduction in G_0 of up to 20% for D_p = 8.3m and 7.5 m. However, for D_p =14m changes to D_r and G_0 have a more pronounced effect on fatigue damage due to the nonlinear damage response as f_0 approaches the excitation frequency f_{3P} (see Figure 5-5(a)). This demonstrates that fatigue damage becomes increasingly sensitive to D_r and G_0 as D_p increases. For the largest diameter examined, D_p = 14m, the greatest increase in fatigue damage (+16%) is observed for a reduction in D_r and G_0 of 20%. Very sharp increases of fatigue damage occur for small changes to D_r and G_0 when G_0 is reduced by >13%.

5.4.6 Discussion

The results demonstrate that in sands, using GDSM soil reaction curves, variations of D_r and G_0 within the model calibration space do not largely influence the nominal value of f_0. Within the investigated region of D_r and G_0, f_0 remains within 5% of the original G_0 profile. However, the fatigue performance of OWTs is not solely governed by the nominal

values of f_0 but also the initial proximity of f_0 to excitation frequencies of environmental and operational loads and D_p. The assessment of D_r and G_0 on the fatigue performance of OWTs must also consider D_p and the initial proximity of f_0 to f_{1P} and f_{3P}, as these coupled factors govern the complicated fatigue damage response.

This study has shown that as D_p increases, f_0 and subsequently the fatigue damage becomes more sensitive to changes in D_r and G_0. The fatigue damage for f_0 initially closer to f_{1P} and f_{3P} is more sensitive to changes to D_r and G_0 compared to f_0 initially further away. This implies that a straightforward relationship between D_r and G_0 and the fatigue performance of OWTs cannot be generalised and depends on the initial D_r and G_0 profile, D_p and location of f_0 compared to f_{1P} and f_{3P}, necessitating case-by-case fatigue analysis.

Wen et al. (2024) demonstrates significant influence of aerodynamic interactions on the fatigue performance of OWTs due to the complexity in balancing aerodynamic efficiency with fatigue performance as wind farms grow. Their findings suggest that aerodynamic interactions will likely reduce the f_{1P} and f_{3P} regions, which additionally has the potential to increase the damage to OWTs. In these cases, the results of this study further suggest that G_0 variation might have an increasingly more pronounced impact on fatigue performance. Further investigation is required to determine how these effects might influence OWT monopile design.

The computed value of f_0 and fatigue damage are highly sensitive to changes in D_p and preliminary eigenvalue analysis also demonstrate that t_p has a similar marked effect whilst L_p has a marginal influence. As such, optimisation of design parameters D_p, and t_p is required to fulfil FLS design requirements and should be explored with consideration towards variation in G_0 and considering aerodynamic interactions.

5.5 Application to model and field tests

The monotonic and cyclic behaviour of an element of soil mimics the behaviour of full-sized foundations but are not identical. Like an element of soil, when subjected to monotonic loads, piles first exhibit a linear elastic response at small loads and non-linear and non-elastic behaviour at higher loads. The displacement, v_G, force, H response and rotation, θ_G, and moment, M, response of a pile, all follow a similar trend to the nonlinear stress-strain response of soil element tests. Furthermore, cyclic loading induces densification, generation of porewater pressure, accumulated ratcheting, stiffness improvement, and energy dissipation loss with the number of cycles and increase in post-cyclic capacity in cohesionless soils. These behaviours are observed model and field test behaviours well as in soil behaviour from element tests. Presumably the same physical factors that govern the cyclic response at an element level also influence the model and field scale pile behaviour, however the applicability of element tests in predicting realistic pile responses remains unclear for laterally loaded piles.

For the application of axially loaded piles, Jardine et al. (2012) proposes cyclic design flow charts including simple semi-empirical methods for assessing stability and predicting pile shaft degradation through calibration against field or model pile tests. The method also proposes to use laboratory element tests as a potential means of developing site-specific assessments. Buckley et al. (2024) presents the results of a field-testing investigation of axially loaded piles in medium-dense chalk. The method outlined in Aghakouchak (2015) to predict shaft degradation and assess stability of the pile based on laboratory element test behaviour is presented and validated with field tests of piles founded in chalk. These studies demonstrate the success of methods in which behaviour captured by element tests are applied to predict certain aspects of axial pile behaviour.

Utilising the results from Chapter 3 and 4, this section compares the soil response at an element level to 1g model tests and field test response and provides tentative relationships that link the monotonic and cyclic behaviours from an element of soil to a full-sized pile scale undergoing lateral cyclic loading. Such methods can be employed in concept design or early-stage assessment for OWT projects. For detailed designed, high quality site characterisation combined with FEA calibration of soil reaction curves is the preferred method. Additionally, it is important to note that these comparisons are drawn for drained conditions only as 1g model tests referenced in this work are undertaken in dry conditions.

5.5.1 Linking G_0 to foundation stiffness 'k_{max}'

The foundation stiffness associated with the pile's response within the elastic region has been described by the three-spring model in Section 5.4.2. Foundation stiffness is also commonly referred to as a single stiffness value, k_{max} expressed in terms of MN/m (k_{vG}) or MNn/ ° (k_θ) and represents the pile's initial resistance to displacement and rotation at ground level. This simplified representation refers to the response of a pile at a single point with no special dimensions is referred to as a 0D model. For an element of soil, the soil's initial resistance to shear loading is G_0, which suggests that there is likely that a relationship exists between the G_0 and the k_{max}. For example, Gazetas (1991) presents relationships between foundation stiffness depending on G_0 and foundation geometries for surface and embedded foundation types validated against experiments presented in Gazetas and Stokoe (1991).

For meaningful comparison of the k_{max} for a OWT monopile to values to G_0, the two parameters should be expressed in equivalent units. It is known that $G_0 = \tau/\gamma$, therefore, to link the two stiffness', it is necessary to convert the force applied on the pile to shear stress and to determine a value for shear strain.

If one treats the body of soil behind a monopile as an entire entity, the lateral movement of the whole soil body behind a monopile is akin to the movement of an element of soil in the VDDCSS. This is likely to be a reasonable assumption for small-scale 1g model tests but is a more tentative analogue for large-scale foundations. Therefore one may assume the ground level rotation of the pile is approximately equivalent to γ in VDDCSS tests. Wu (2023) carried out an extensive suite of 1g model tests with $L_p/D_p = 4$ in LBS and determined a relationship between ground level displacement, v_G, and rotation, θ_G, of 4:1 indicating that the point of rotation of the pile acts at approximately 2/3 of the pile length below surface level.

The horizontal load, H acting on the pile should be converted to a shear stress, τ by dividing H by an equivalent shear area, A_{eq}. This is the area of soil that is impacted behind the pile subjected to lateral loading, as shown schematically Figure 5-7(a) ($A_{eq} = D_p x$). The A_{eq} is unknown a priori as the distance of mobilised soil, x, behind the pile is unknown. As x is the only unknown in this solution, it can be solved by back calculating from G_0. It is theorised that A_{eq} is predominantly a function of h/L as a lower value of h/L acts to increase the resistance of the pile thus mobilising a larger shear area compared to a higher value of h/L.

1g model tests conducted by Richards (2020) and field tests undertaken by McAdam et al. (2019) provide monotonic pile responses in LBS and Dunkirk (DK) sands respectively. The k_{max} from both studies were determined considering the small-strain response of the tests via, $k_{vG} = H/v_G$ and $k_\theta = M/\theta_G$. 1g model tests were carried out in two soil densities, keeping the model pile geometry constant. Field tests were carried out on piles of different geometries and loading eccentricities in the same soil profile. G_0 of the founding soils from both studies are available from laboratory and field measurements.

These tests provide an avenue to connect G_0 to k_{max} using the method described above. By applying this method, the calculated values of x were determined and summarised in Table 5-7. The nominal value of x depends on the embedment depth, L_p of the pile which differs for each pile design case. It is therefore useful to consider an angle to represent the amount of impacted soil from lateral loading, α_s ($\alpha_s = \tan^{-1}(x/L_p)$) as shown in Figure 5-7(a) which is considered independent of L_p. The values of computed α_s are summarised in Table 5-7. A linear relationship between h/L and α_s is observed and shown in Figure 5-7.

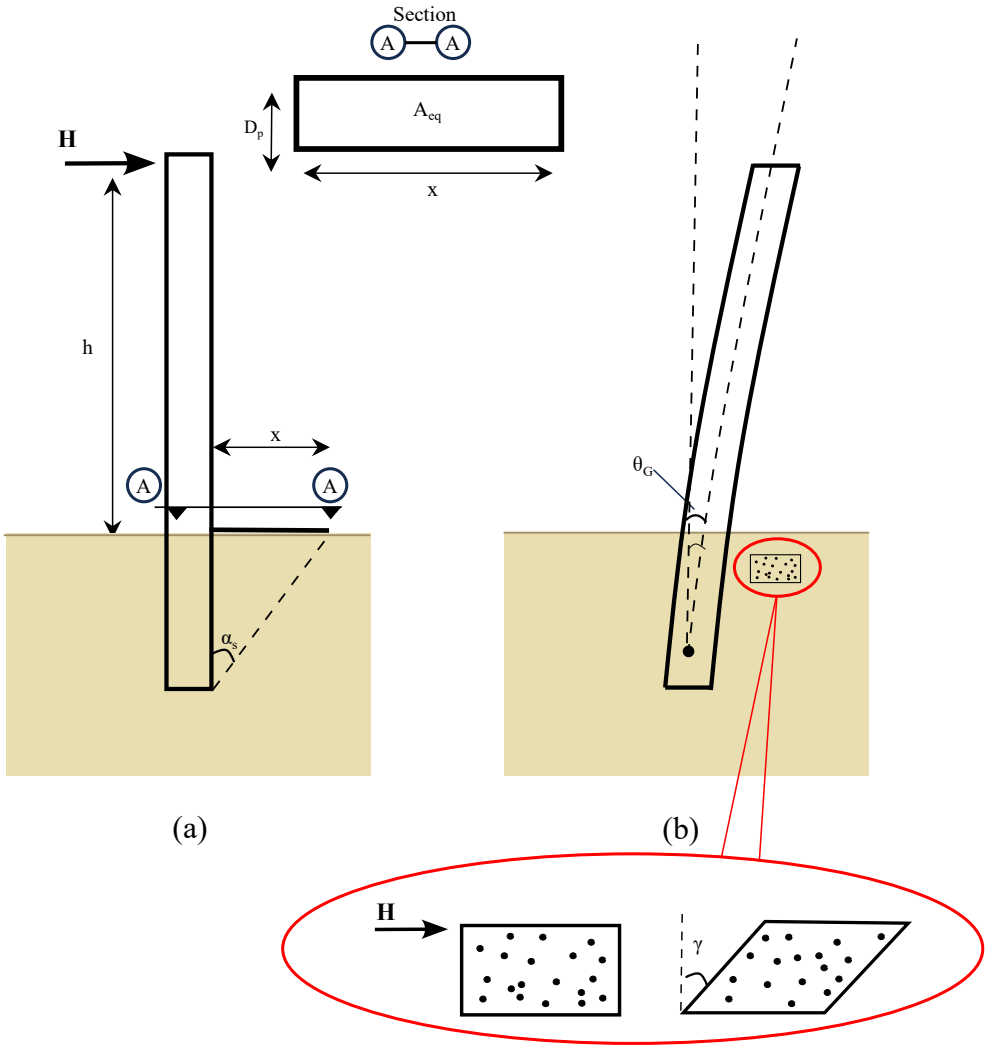


Figure 5-7 Schematic of shear loading of a monopile in the field and element of soil in the VDDCSS (a) Original pile configuration; and (b) Sheared pile configuration

Table 5-7 1g model and field test properties from Richards (2020) and McAdam et al. (2019) respectively

Test ID	Material	D_p (m)	t_w (mm)	L_p (m)	h (m)	k_{vG} (MN/m)	k_θ (MN/°)	G_0 (MPa)[1]	x (m)	α_s (°)
1g - loose[3]	LBS	0.08	8	0.32	0.8	-[2]	0.000933	44	1.34E-	0.0002
1g - dense[3]	LBS	0.08	8	0.32	0.8	-	0.000987	35	1.00E-	0.0001
DL1[4]	DK	2	38	10.5	10	106	41.27	121	0.0045	0.0248
DL2[4]	DK	2	38	10.5	10	108	57.9	121	0.0045	0.0248
DM3[4]	DK	0.76	2	6.1	10	22	5.29	100	0.00099	0.0092
DM4[4]	DK	0.76	14	4	10	14.34	3.44	90	0.00080	0.0115
DM5[4]	DK	0.76	10	2.29	10	5.14	1.23	80	0.00028	0.0069
DM6[4]	DK	0.76	16	4	10	14.5	4	90	0.00073	0.0104
DM7[4]	DK	0.76	10	2.29	10	5.29	1.32	80	0.00033	0.0082
DM9[4]	DK	0.76	14	4	10	12.1	2.93	90	0.00061	0.0087
DS1[4]	DK	0.27	7	1.43	5	2.51	0.14	66	0.00014	0.0056
DS2[4]	DK	0.27	7	1.43	5	2.68	0.11	66	0.00022	0.0089
DS3[4]	DK	0.27	7	2.18	5	3.52	0.16	68	0.00022	0.0057
DS4[4]	DK	0.27	7	2.73	5	3.94	0.18	60	0.00031	0.0064

1. Average G_0 in pile profile
2. No published value
3. 1g model tests as per Richards (2020)
4. Field tests as per McAdam et al. (2019)

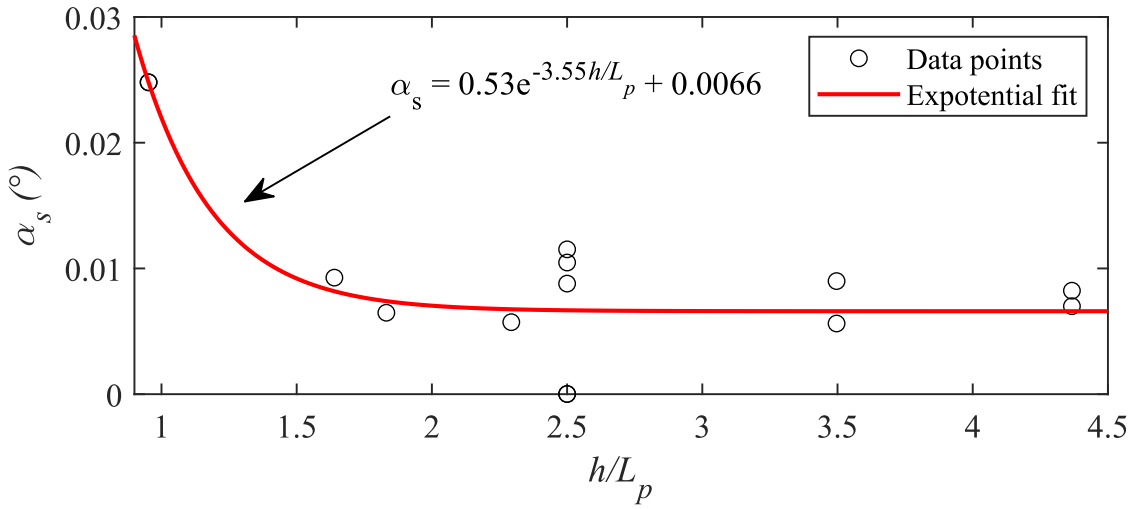


Figure 5-8 Relationship between loading eccentricity ratio, h/L_p and α_s from model and field tests

Figure 5-8 shows a negative exponential relationship between α_s and h/L_p based on model and field tests. A power-law regression was fitted to the data, yielding an $R^2 = 0.8$ with the corresponding model fitting parameters shown in the figure. This relationship can be leveraged to predict k_{max} of a given pile in the field based on its load eccentricity and founding G_0 profile. Beyond what has been discussed, it requires an additional parameter,

the elastic displacement, y_e or rotation θ_e which refers to the ground level displacement or rotation limit of elastic pile behaviour respectively. The determination of these parameters via RCA tests is discussed in Section 5.5.2.

5.5.2 Relationships for elastic behaviour

The elastic behaviour of soil is governed by the volumetric shear strain, γ_{tv}, a stiffness degradation parameter that can be measured by the RCA and was explored extensively in Chapter 3. In the field, the initial response of a pile undergoing lateral loading is also described as elastic at very small loads. Figure 5-7(b) schematically illustrates the practical assumption that equates the rotation of a foundation at ground level with the shear strain of a soil element. Therefore, like an element of soil, it can be said that the initial rotation, θ_e developed in a pile governs the elastic behaviour of the pile. Richards (2020) conducted several monotonic and cyclic 1g model tests in LBS, with a specific emphasis on capturing the initial pile response. Characteristics of 1g model tests are presented in Table 5-7. This section serves to compare the initial responses observed in these 1g model tests with the elastic responses obtained from LBS using the RCA, as outlined in Chapter 3. Table 5-8 summarises the testing conditions and measurements of γ_{tv} and θ_e.

Table 5-8 Comparison of γ_{tv} and θ_e between RCA tests in this study and 1g model tests by Richards (2020)

Test ID	Material	D_r (%)	p' or σ'_v (kPa)[1]	θ_e (rad)	γ_{tv} (rad)	Test condition
1g - loose[2]	LBS	1	5	0.000018	-	dry
1g - dense[2]	LBS	90	5	0.000025	-	dry
RCA_LBS_28_5	LBS	28	5	-	0.000010	dry
RCA_LBS_70_5	LBS	70	5	-	0.000027	dry
DL1[3]	DK	75	133.99	0.0047	-	*in-situ*
DL2[3]	DK	75	133.99	0.0033	-	*in-situ*
DM3[3]	DK	75	89.59	0.0025	-	*in-situ*
DM4[3]	DK	75	68.40	0.0028	-	*in-situ*
DM5[3]	DK	75	51.15	0.00241	-	*in-situ*
DM6[3]	DK	75	68.40	0.0022	-	*in-situ*

DM7[3]	DK	75	51.15	0.0026	-	*in-situ*
DM9[3]	DK	75	68.40	0.0025	-	*in-situ*
DS1[3]	DK	75	42.47	0.0016	-	*in-situ*
DS2[3]	DK	75	42.47	0.0032	-	*in-situ*
DS3[3]	DK	75	50.04	0.0022	-	*in-situ*
DS4[3]	DK	75	55.59	0.0024	-	*in-situ*
	DK	75			0.00103[4]	-

Note: 1. In 1g model and field tests, this is taken to be the vertical effective stress at the pile tip, in RCA this is the mean confining stress 2. 1g model tests by Richards (2020) 3. Field tests as per McAdam et al. (2019)Non-linear elasticity – shear stiffness degradation reported from Taborda, Zdravković, et al. (2019)

As presented in Table 5-8, the observed γ_{tv} and θ_e for LBS are all in close proximity, measured at roughly 10^{-5}. For both the 1g model tests and element tests γ_{tv} and θ_e are higher for the denser specimen in line with results from Section 3.6.3. For the DK, only a single constant value of γ_{tv} was used to characterise the material as per Taborda et al. (2019), suggesting the parameter is independent of σ'_v. Results in Section 3.6.2 demonstrate the relative independence of γ_{tv} and p' supporting this assumption. The values of γ_{tv} and θ_e are slightly higher for the DK at 10^{-3} than the LBS material which is consistent with experimental observations from Section 5.3 where the fine grained well-graded NE and CX sand (more similar to DK sand) obtained higher γ_{tv} than the coarse uniform LBS. These observed trends suggests that the measured values of γ_{tv} from RCA tests serve as a robust estimator for θ_e in the elastic region where no significant load has been applied to the soil or structure.

5.5.2.1 Proposed framework for predicting k_{max} from the RCA

Section 5.5.1 and 5.5.2 establish a framework to predict k_{max}, from RCA tests. Here, k_{max} represents a "global" stiffness that characterises the elastic response of a pile undergoing lateral loading and encompasses all three spring stiffness terms K_L, K_{LR} and K_R (defined in Equation 5-1) within it. The framework is presented below:

1) Determine the angle of affect soil, α_s
    a) Refer to Figure 5-8 to select the appropriate α_s based onloading eccentricity

2) Calculate length of mobilised soil length, x

   a) Compute x based on the geometry of a triangle and L_p

3) Calculate equivalent shear area, A_{eq}

   a) $A_{eq} = x \cdot D_p$ (refer to Figure 5-7 for guidance).

4) Calculate the "elastic force", H or "elastic moment", M (limiting value load applied prior to the onset of plastic pile behaviour) using Hooke's law:

   a) $H = G_0 \cdot A_{eq}$, where G_0 is the initial shear modulus measured from RCA tests or other techniques of the founding soil

   b) $M = H \cdot h$

5) Use RCA measurements to determine γ_{tv}

   a) Approximate $\theta_e = \gamma_{tv}$

   b) Obtain y_e from relationships developed from model tests e.g., Wu et al (2023)

6) Determine k_{max}

   a) $k_{max} = M/\theta_e$ (Step 4b and 5a)

   b) $k_{max} = H/y_e$ (Step 4a and 5b)

While this framework provides a preliminary method to connect element behaviour to field applications, additional validation through field tests, experimental data, and/or numerical analysis is necessary to ensure its reliability. The framework accounts for pile geometry parameters, such as loading eccentricity, L_p and D_p are encompassed in this framework (see Steps 1, 2a and 3a), but other factors that could influence the determination of k_{max} have not been investigated. Notably, the following limitations of this framework should be considered:

1) Pile material and stiffness properties

a) The empirical relationship proposed in Figure 5-8 is based on thin-walled steel piles only.
b) Piles made of different materials or with varying stiffness properties (affecting the pile-soil stiffness ratio) may exhibit different responses and trends for connecting α_s and h/L_p.
c) The consideration of fully closed pile may yield different relationships

2) Pile weight
   a) The impact of pile weight has not been explicitly investigated, albeit its effects may be implicitly captured through L_p and D_p and differences in pile material as noted in point 1b.

3) Pile aspect ratio
   a) This study has been calibrated to piles with L_p/D_p ratios between 4 and 8. It is unclear whether this framework is applicable for different L_p/D_p ratios
   b) The mechanics of slender piles versus stocky piles may differ and have not been explored here

4) Soil strength to stiffness ratio
   a) Impact of soil strength to stiffness ratio has not been considered, it could be possible that this ratio could alter the trend for connecting α_s and h/L_p.

5.5.2.2 Validation of proposed framework

The validity of the proposed framework as outlined in Section 5.5.2.1 was tested by predicting the k_θ values of the 1g model and field test piles summarised in Table 5-9. Analytical predictions of elastic foundation stiffness by Shadlou and Bhattacharya (2016) and Gupta and Basu (2018) as discussed in Section 5.2.1 are also summarised in the table as a point of comparison.

Table 5-9 Validation of framework for obtaining k_θ from RCA tests

Test ID	Measured k_θ (MN/°)	This framework k_θ (MN/°)	Shadlou and Bhattacharya (2016) k_θ (MN/°)	Gupta and Basu (2018) k_θ (MN/°)
1g - dense	0.000936	0.146	0.021	
1g - loose	0.000979	0.092	0.026	
DL1	41.27	184.9	2031	3038
DL2	57.9	184.9	2031	3038
DM3	5.29	11.20	419.0	2245
DM4	3.44	5.395	109.9	2243
DM5	1.23	2.715	18.33	2240
DM5	4	5.395	109.9	2243
DM7	1.32	2.715	18.33	2240
DM9	2.93	5.395	109.9	2243
DS1	0.14	0.248	3.901	1090
DS2	0.11	0.2485	3.901	1090
DS3	0.16	0.3994	14.07	1091
DS4	0.18	0.4832	23.94	1092

Predictions of k_θ from analytical equations by Shadlou and Bhattacharya (2016) and Gupta and Basu (2018), show that the predicted values overestimate the measured values by several orders of magnitude. In contrast, the framework adopted here tends to overpredict the values, but to a significantly lower degree.

5.5.3 Relationships for full monotonic behaviour

This section compares the full monotonic response of the element tests captured by the Variable Dynamic Direct Simple shear (VDDCSS) on LBS to that of the 1g model tests in the same material. A summary of the test conditions is presented in Table 5-9.

Table 5-10 Comparison of full monotonic behaviour between 1g model tests and VDDCSS tests

Test ID	Material	D_r (%)	p' or σ'_v (kPa)*	Test condition
1g - loose	LBS	1	5	dry
1g - dense	LBS	90	5	dry
VDDCSS_LBS_60_5_M_D	LBS	60	5	dry
VDDCSS_LBS_90_5_M_D	LBS	90	5	dry

Note: *In 1g model test, this is taken to be the vertical effective stress at the pile tip, in VDDCSS this is the applied vertical stress

The stress-strain response captured in the VDDCSS is difficult to directly compare to the model test response as the M-θ and F-v_G response of a model pile cannot be directly converted to the units of the stress-strain response of the VDDCSS. Section 5.5.2 presents

a method in which the small-strain response of an element of soil can be linked to the initial response of a foundation. Building upon these relationships, it is therefore convenient to compare the medium to large strain response between the VDDCSS and model tests by normalising the response with the small-strain response i.e., G_0 and k_{max}.

Figure 5-9(a) and (b) below presents the soil's normalised soil stiffness (G/G_0) foundation stiffness (k/k_{max}) degradation in loose soil and dense soil respectively.

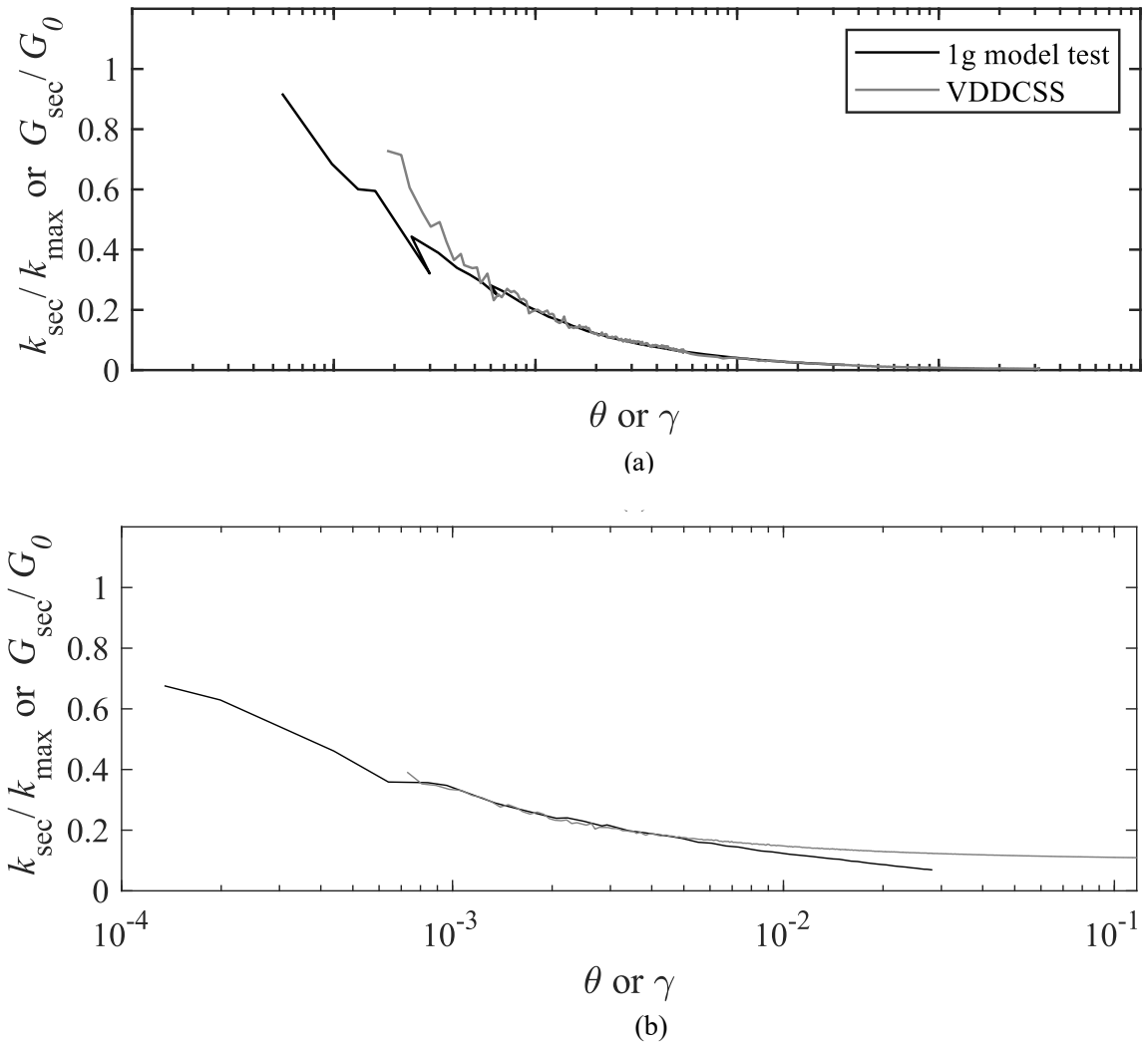


Figure 5-9 Normalised stiffness degradation of soil and foundation (a) Loose soil; and (b) Dense soil

As shown in Figure 5-9(a) and (b), the normalised soil stiffness degradation and foundation stiffness degradation are practically identical for both loose and dense

specimens. It is important to note that the comparison of 1g model test and element tests have been undertaken considering tests conducted in an unsaturated condition (dry sand). Chapter 4 has shown that the drainage conditions significantly alter the monotonic and cyclic of cohesionless soils. It is well established that in offshore environments, monopiles likely experience a partially drained or undrained response. Partially drained conditions can be induced in 1g model tests and field tests; however, it is difficult to simulate these conditions in the VDDCSS. For example, results of Section 4.4 indicate that loading frequency in the VDDCSS has a marginal influence on soil behaviour as the drainage path of the specimen in the device is fixed. It may be possible to induce a partially drained condition in the VDDCSS by altering the drainage system such that the rate at which water drain is altered (e.g., by reducing cross-sectional area of the drainage pipe), however this has not been explored here. Whilst the normalised stiffness degradation of an element of soil and foundation are almost identical in fully drained conditions, this has not been verified for partially drained or undrained conditions.

Despite these limitations, the similarity between the stiffness degradation of an element of soil and foundation can be leveraged for design purposes in drained conditions. A framework for scaling lateral p-y curves from DSS stress-strain has been presented for clay and relies on scaling factors that convert the stress-strain response from DSS to p-y curves for a particular stress level based on the similarity the shape of the stress-strain response and p-y curves, see Jeanjean et al. (2017) and Zhang and Andersen (2017) for details. In this investigation, similarity between certain responses from a combination of element tests and 1g model tests suggest that it is possible to utilise small-strain stiffness response from the RCA combined with the VDDCSS stress-strain response to obtain the full monotonic response of a monopile. Measurements from the RCA provide G_0, and γ_{tv}

which can be linked to k_{max} and θ_e via the methods discussed in Section 5.5.1 and Section 5.5.2 respectively. The medium-large strain stiffness degradation measured by the VDDCSS follows a very similar trend to foundation stiffness degradation. One may therefore obtain k_{sec} at any strain level from VDDCSS tests and then multiply G_{sec}/G_0 by k_{max} to which the M-θ response can be produced. Wu (2023) presented several relationships between v_G and θ_G based on 1g model tests in LBS which can then be used to then obtain the corresponding F-v_G response. This procedure, herein referred to as the 'simplistic matching approach' is schematically shown in Figure 5-10(a). Examples applying this method to replicate the 1g model response for a loose and dense case using element tests in Chapter 4 are shown in Figure 5-10(b) and (c) respectively.

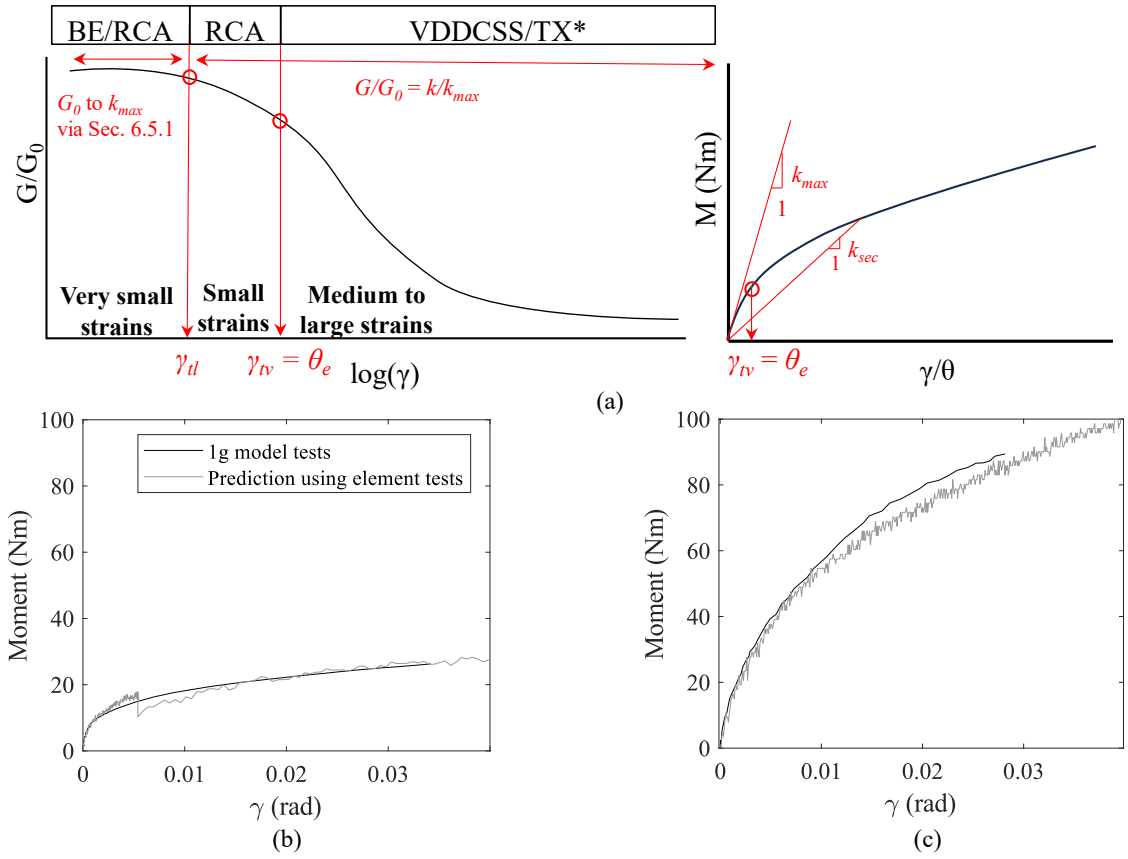


Figure 5-10 Simplistic matching approach from an element of soil to foundation behaviour (a) schematic of derivation process*TX refers to Triaxial device; (b) Prediction of loose LBS response; and (c) prediction of dense LBS response

With current available data, the simplistic matching approach can only be validated against 1g model tests of a single pile geometry and in two densities, therefore it is not guaranteed whether this approach would be effective in predicting a full sized monopile response. Additionally, this approach has only been verified for drained loading conditions only. Therefore, an important extension of this work would be to validate these findings with realistic sized pile tests in the field, examining different foundation geometries, L_p/D_p ratios, potentially under different drainage conditions to provide further confidence in this approach.

As discussed in Section 5.5.2.1, several factors, including pile weight, the pile-to-soil stiffness ratio, and the soil stiffness-to-strength ratio, remain unexplored n the context of pile stiffness behaviour. Quantifying the effects of these properties on k_{max} and the degradation of k_{max} is critical to further generalise and improve the reliability of this method. The medium-scale field tests currently underway at Cuxhaven and provide a point of verification with RCA and VDDCSS test in the same material as presented in Chapter 3 and 4 of this study. However, it is important to note that even with further verification, this simplistic matching approach cannot be applied to a layered soil profile and is limited to homogenous soil profiles only.

5.5.4 Relationships for cyclic behaviour

A suite of 1g model tests were performed by Richards (2020) on loose and dense LBS in drained conditions. An equivalent set of VDDCSS tests were undertaken at matching densities and across identical loading regimes to provide a direct comparison between the cyclic response captured by the testing method. All VDDCSS tests in this section were undertaken at σ'_v = 5kPa A summary of the test conditions is presented in Table 5-11.

Table 5-11 Test schedule of model and element tests

Test ID	Test	No. Cycles	$\zeta_{b,x}$	$\zeta_{c,x}$	$\zeta_{b,y}$	$\zeta_{c,y}$	f (Hz)	D_r (%)
L.TW.04*	1g model	2000	0.4	-1	0	0	0.1	1
L.OW.04	1g model	10000	0.4	0	0	0	0.1	1
L.PT.260	1g model	1000	0.2	-	0	0	0.1	1
L.PO.633	1g model	1000	0.6	0.3	0	0	0.1	1
L.T.02	1g model	1000	0.2	1	0.2	-1	0.1	1
L.L.04	1g model	1000	0.2	1	0.4	0	0.1	1
L.TH.04	1g model	1000	0.4	1	0.2	-1	0.1	1
D.TW.008	1g model	1000	0.08	-1	0	0	0.1	90
D.TW.016	1g model	1000	0.16	-1	0	0	0.1	90
D.TW.32	1g model	1000	0.32	-1	0	0	0.1	90
D.OW.03	1g model	10000	0.3	0	0	0	0.1	90
D.PT.260	1g model	1000	0.2	-	0	0	0.1	90
D.PO.333	1g model	1000	0.3	0.3	0	0	0.1	90
D.T.01	1g model	1000	0.1	1	0.1	1	0.1	90
D.L.02	1g model	1000	0.1	1	0.2	0	0.1	90
D.TH.02	1g model	1000	0.2	1	0.1	-1	0.1	90
VDDCSS_LBS_60_5_UTW1_D	VDDCSS	2000	0.4	-1	0	0	0.1	60
VDDCSS_ LBS_60_5_UOW1_D	VDDCSS	10000	0.4	0	0	0	0.1	60
VDDCSS_ LBS_60_5_UP2W1_D	VDDCSS	1000	0.2	-	0	0	0.1	60
VDDCSS_ LBS_60_5_UP1W1_D	VDDCSS	1000	0.6	0.3	0	0	0.1	60
VDDCSS_ LBS_60_5_MD1_D	VDDCSS	1000	0.2	1	0.2	-1	0.1	60
VDDCSS_ LBS_60_5_MD2_D	VDDCSS	1000	0.2	1	0.4	0	0.1	60
VDDCSS_ LBS_60_5_MD3_D	VDDCSS	1000	0.4	1	0.2	-1	0.1	60
VDDCSS_LBS_90_5_UTW1_D	VDDCSS	1000	0.08	-1	0	0	0.1	90
VDDCSS_LBS_90_5_UTW2_D	VDDCSS	1000	0.16	-1	0	0	0.1	90
VDDCSS_LBS_90_5_UTW3_D	VDDCSS	1000	0.32	-1	0	0	0.1	90
VDDCSS_ LBS_90_5_UOW1_D	VDDCSS	10000	0.3	0	0	0	0.1	90
VDDCSS_ LBS_90_5_UP2W1_D	VDDCSS	1000	0.2	-	0	0	0.1	90
VDDCSS_ LBS_90_5_UP1W1_D	VDDCSS	1000	0.3	0.3	0	0	0.1	90
VDDCSS_ LBS_90_5_MD1_D	VDDCSS	1000	0.1	1	0.1	1	0.1	90
VDDCSS_ LBS_90_5_MD2_D	VDDCSS	1000	0.1	1	0.2	0	0.1	90
VDDCSS_ LBS_90_5_MD3_D	VDDCSS	1000	0.2	1	0.1	-1	0.1	90

Note: *1g model test naming convention – A.B.C where A refers to density L = loose, D = dense, B refers to loading type TW = two way, OW = one-way, PO = partial-one way, PT = partial two-way, L = multidirectional L shape, T = multidirectional T shape TH = multidirectional T shape high mean and C refers to loading amplitude

As discussed, in Chapter 4, there are several pertinent features that define the cyclic behaviour of both an element of soil and full-sized foundations in drained conditions

including, densification, accumulated ratcheting, stiffness, and energy dissipation changes with cycles. Fully drained loading conditions can exist for low frequency cyclic loading of offshore foundations situated in high permeability materials with short drainage lengths. However, the combination of different loading types on OWTs will also likely produce partially drained and undrained conditions. In these cases, the generation of porewater pressure also ensues. All 1g model tests in LBS were undertaken in dry conditions and therefore comparisons in cyclic features only considers the drained cyclic response only.

An important distinction between element and foundation behaviour is that in the laboratory, it is possible the monitor changes to the specimen volume whereas this is less straightforward to measure in model tests and in the field. As such, it is only possible to compare the accumulated ratcheting, (defined as γ_{acc} or θ_{acc} for element and model tests respectively), changes to stiffness, (defined as G_{sec} or k_{sec} for element and model tests respectively) and energy dissipation, η across the two testing methods.

Figure 5-11(a) to (d) throughout present a comparison of the changes to G_{sec}/k_{sec} and η with cycles for two-way loading conditions in the VDDCSS and 1g model tests at two densities. Figure 5-12(a) to (f) throughout present a comparison of the $\gamma_{acc}/\theta_{\mathrm{acc}}$, changes to G_{sec}/k_{sec} and η with cycles for one-way, partial one-way and partial two-way loading conditions in the VDDCSS and 1g model tests at two densities.

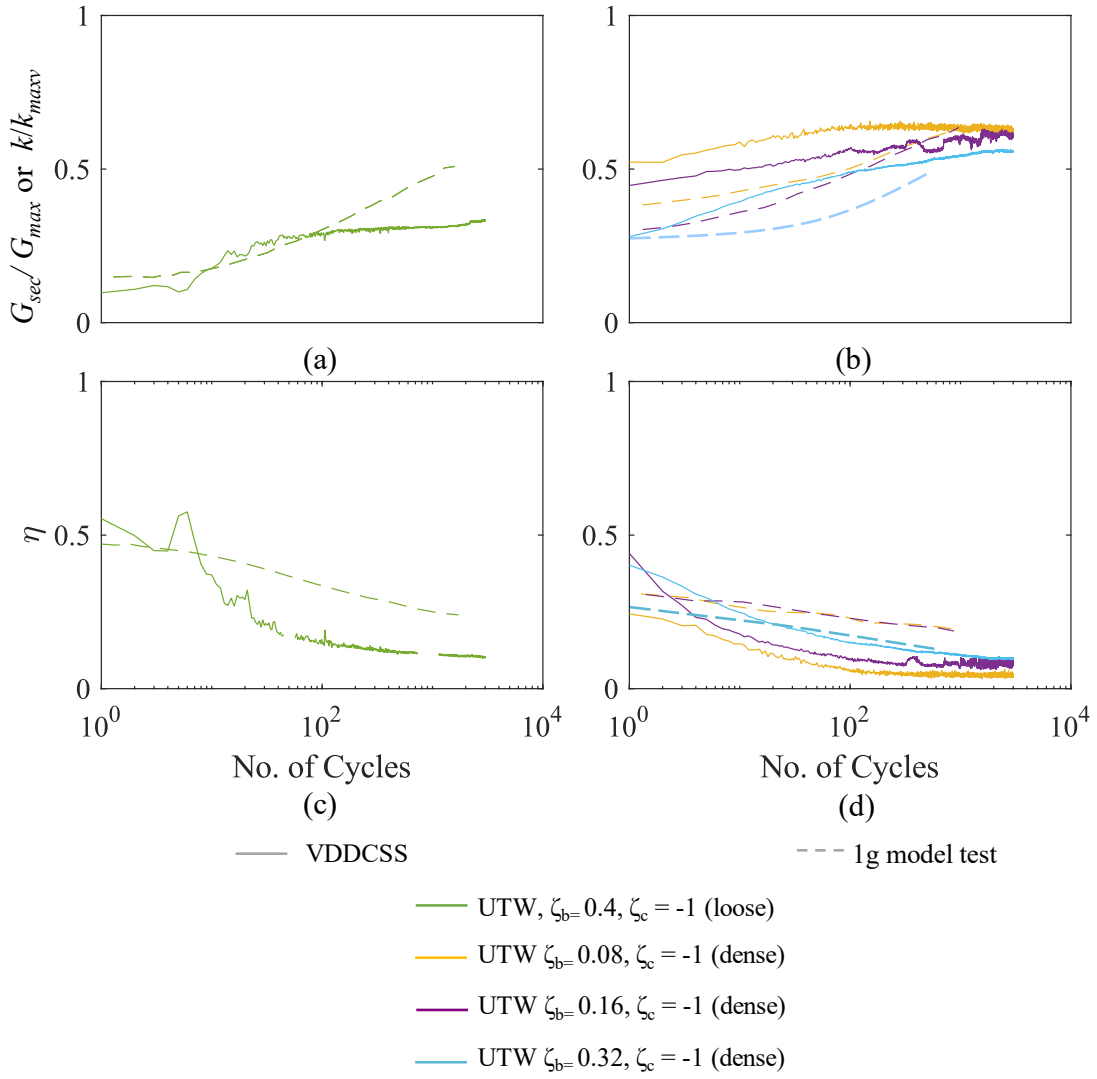


Figure 5-11 Cyclic behaviour of two-way tests from VDDCSS and 1g model tests (a) Normalised stiffness (loose); (b) Normalised stiffness (dense); (c) η (loose); and (d) η (dense)

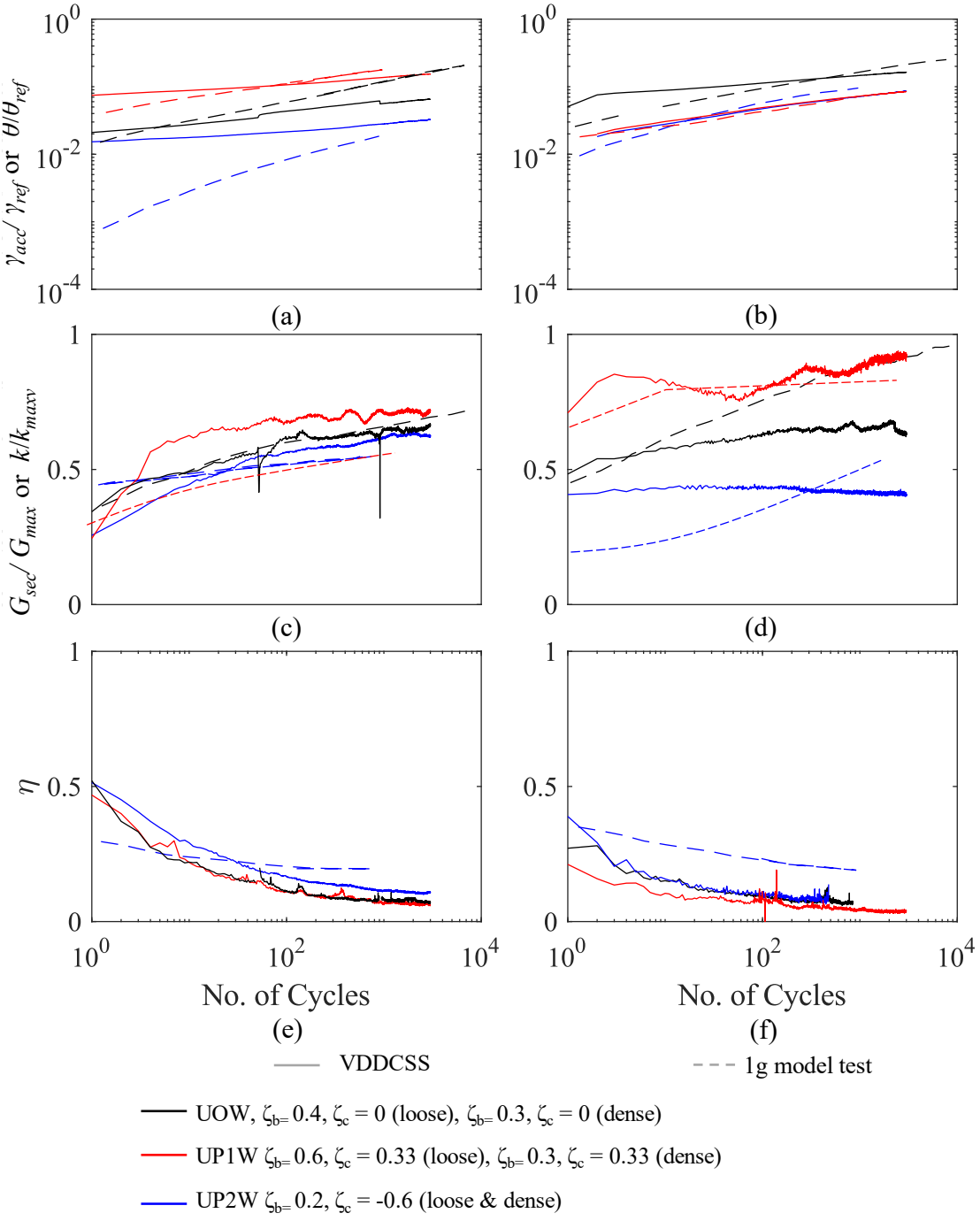


Figure 5-12 Cyclic behaviour of one-way, partial one-way and partial two-way tests from VDDCSS and 1g model tests (a) Normalised accumulated ratcheting (loose); (b) Normalised accumulated ratcheting (dense); (c) Normalised stiffness (loose); (d) Normalised stiffness (dense); (e) η (loose); and (f) η (dense)

Although the rate at which $\gamma_{acc}/\theta_{acc}$, G_{sec}/k_{sec} and η evolve with cycles vary between the VDDCSS and 1g model tests, the impact of ζ_b and ζ_c have a similar effect on the cyclic behaviours across both test methods.

Figure 5-11(a) and (b) and Figure 5-12(c) and (d) indicate all specimens see an increase in G_{sec}/k_{sec} with cycles, with ζ_b positively correlated increase in stiffness across both test methods, see Figure 5-12(c) and (d), an observation in line with Section 4.3.4. In general, changes to G_{sec} in the VDDCSS reach an equilibrium after 50 to 100 cycles to which subsequently changes to G_{sec} plateau. This is not the case for 1g model tests which continue to see an increase in k_{sec} even after 1000 cycles. This discrepancy is likely attributed to the volume of soil in the VDDCSS being substantially smaller that of the 1g model tests. A smaller specimen size allows the reshuffling of soil particles to reach an equilibrium more rapidly. Once the soil grains reach an equilibrium, no further densification or 'interlocking' can take place and likewise changes to G_{sec} cease. The larger body of material in 1g model tests suggests that a significantly larger number of cycles would be required for the reshuffling of soil particles to reach an equilibrium.

The η reduces with cycles in both VDDCSSS and 1g model tests, indicating an increase in cyclic resistance with cycles as seen Figure 5-10(c) and (d) and Figure 5-11(e) and (f). ζ_b, is positively related with energy dissipation for both test methods as shown in Figure 5-11(e) and (f), again in-line with experimental findings from Section 4.3.4. In parallel with the trends observed in stiffness changes, the η in VDDCSS tests reaches a state of equilibrium after 50 to 100 cycles. In contrast, the 1g model tests demonstrate a continual decrease in energy dissipation with each cycle. This divergence in behaviour is once again attributed to the relatively smaller specimen size in the VDDCSS.

The $\gamma_{acc}/\theta_{\text{acc}}$ for both VDDCSS and 1g model tests presented in Figure 5-12(a) and (b) are consistent with experimental conclusions discussed in Section 4.3.3. One-way and partial-one-way tests consistently accumulate more ratcheting than partial two-way tests across both test methods and densities as it is likely that the larger load reversal of partial

two-way tests reverse the impact of the extension load on ratcheting.

A comparison of post-cyclic tests from element and 1g model tests under various are presented in Figure 5-13(a) and (b) for loose and dense specimen respectively.

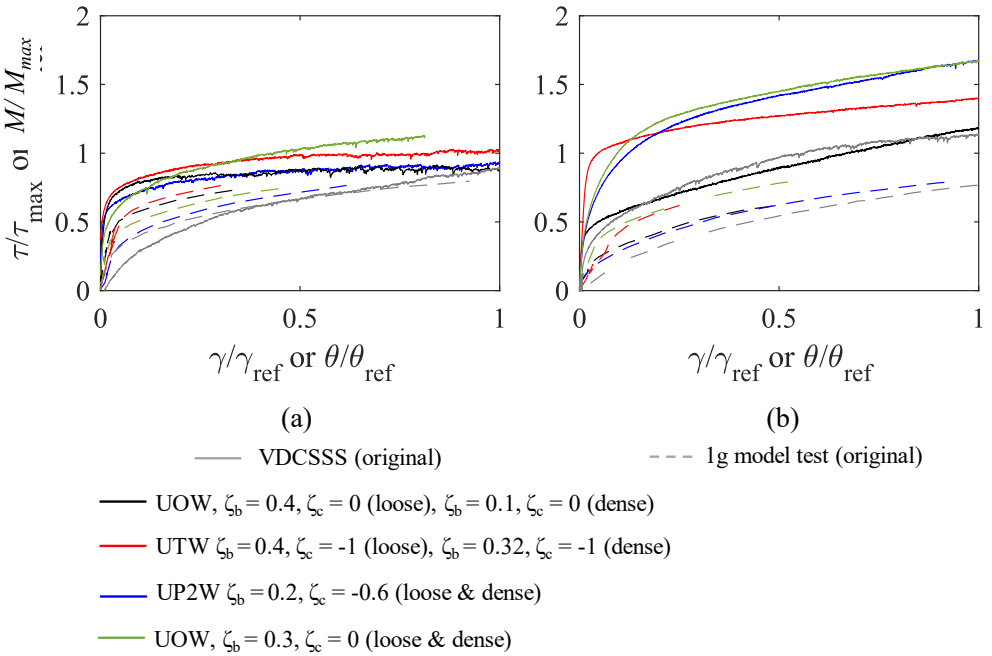


Figure 5-13 Post-cyclic behaviour of VDDCSS and 1g model tests (a) loose specimens; and ten (b) dense specimens

Both test methods see an increase in original monotonic capacity, however, the increase is much greater for VDDCSS tests. As discussed previously, changes to G_{sec} and η tend towards an equilibrium with cyclic loading for VDDCSS tests but not in 1g model tests. Model tests typically do not reach equilibrium even after 3000 cycles and have the capacity to increase in resistance with further cycles, thus leading to a reduced post-cyclic response compared to VDDCSS tests which have reached their maximum resistance. ζ_b and D_r positively influence the post-cyclic capacity of in both test methods. This is likely due to the greater densification and 'interlocking' that occur with these mechanisms.

Figure 5-14(a) and (b), display the multidirectional strain response of the VDDCSS and 1g model tests. Multidirectional tests are loaded in the direction of constant stress (x-axis) and cycled in the orthogonal axis (y-axis).

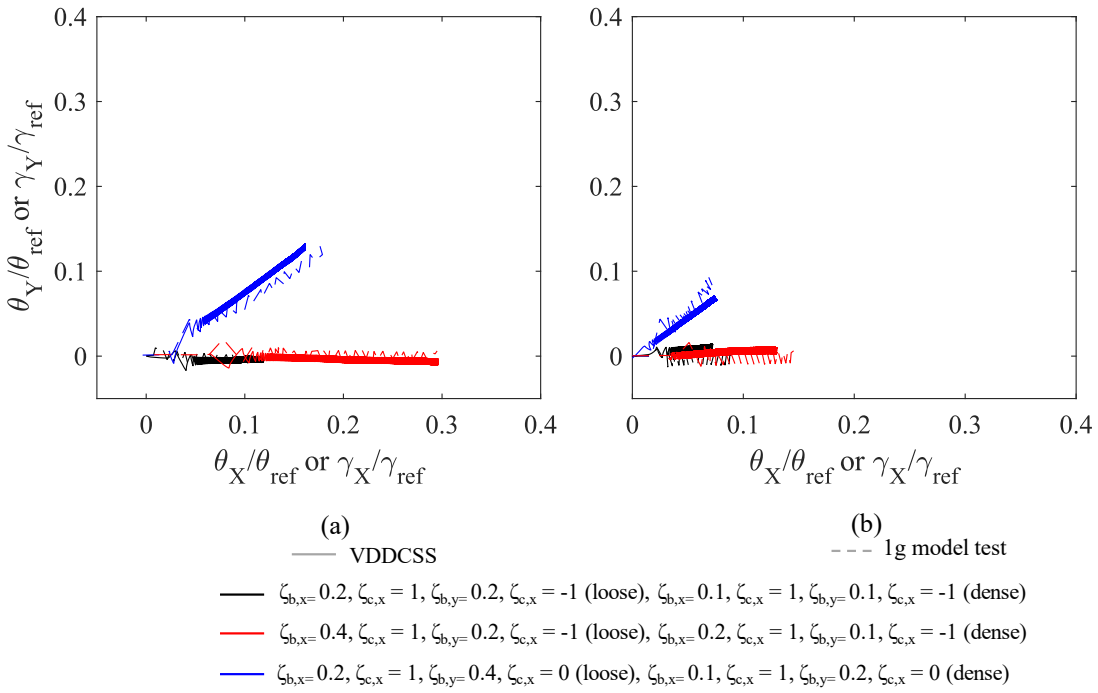
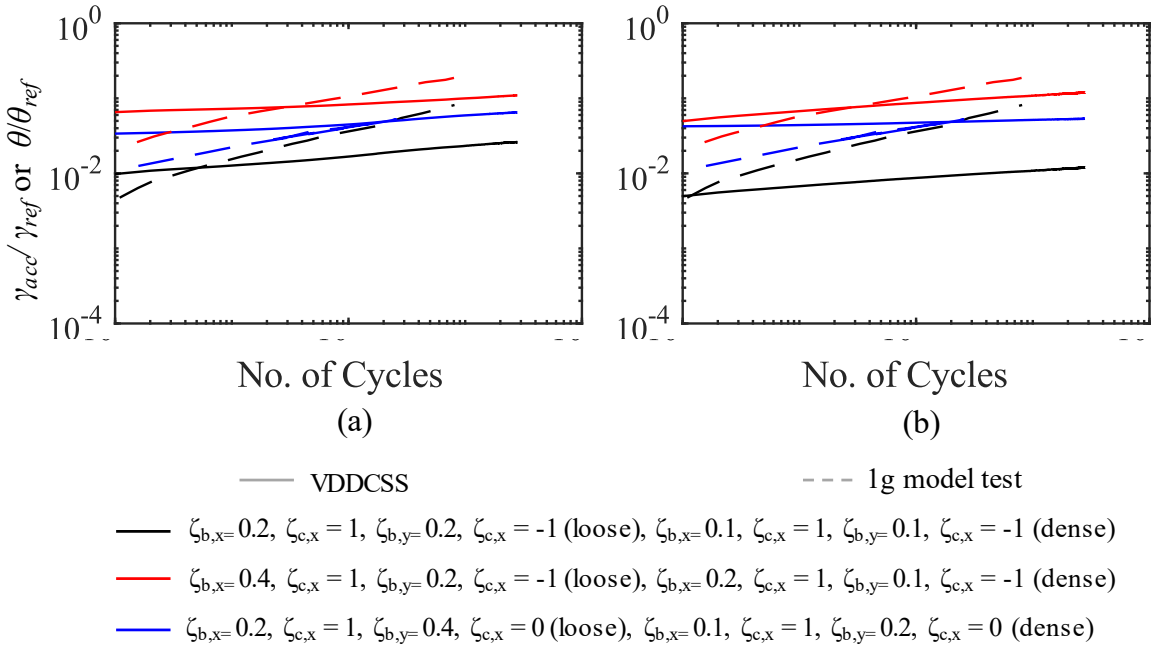


Figure 5-14 Multidirectional strain from VDDCSS and 1g model tests (a) loose specimens (b) dense specimens

When normalised by $\gamma_{ref}/\theta_{ref}$, the direction and amount of γ/θ developed for both test methods are similar. Like Section 4.3.6, two-way loading induces ratcheting in the direction of constant stress. For one-way cyclic loading, $\gamma_{acc}/\theta_{acc}$ accumulates at an angle to x-axis in the direction of cycling. Figure 5-15(a) to (f) display the $\gamma_{acc}/\theta_{acc}$, changes to G_{sec}/k_{sec} and η behaviour from VDDCSS and model tests.



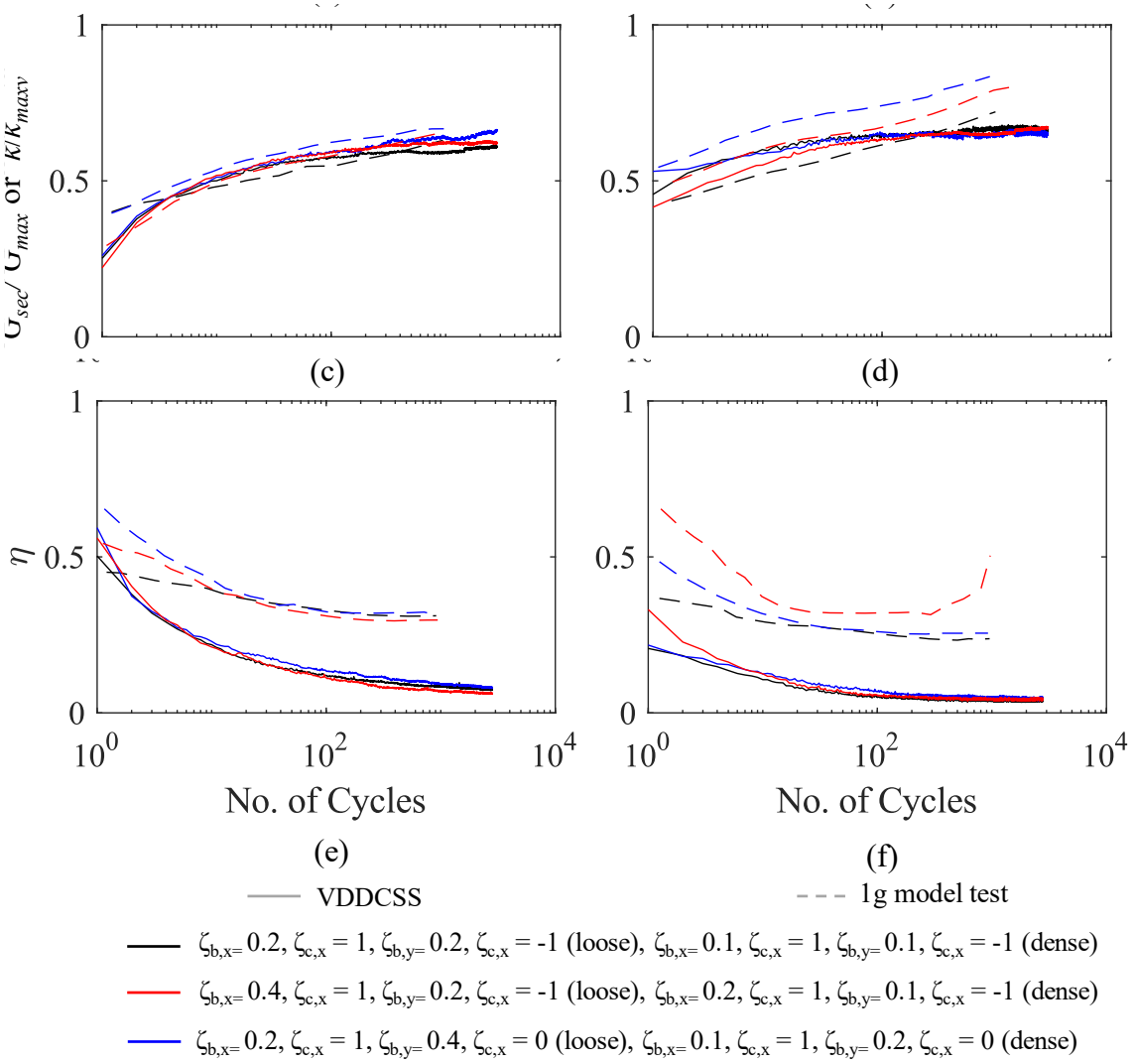


Figure 5-15 Cyclic behaviour multidirectional tests (a) Accumulated ratcheting (loose) (b) Accumulated ratcheting (dense) (c) Normalised stiffness (loose) (d) Normalised stiffness (dense) (e) Energy dissipation (loose) (f) Energy dissipation (dense)

Once again, the influence of ζ_b and ζ_c are the same for both test types. The constant stress amplitude $\zeta_{b,x}$ is positively associated with accumulated ratcheting for both test types. Figure 5-15(a) and (b) demonstrate that the rate of $\gamma_{acc}/\theta_{acc}$ is higher for model tests compared to the VDDCSS tests. Figure 5-15(c) and (d) show that changes in G_{sec} reach an equilibrium in element tests but k_{sec} continue to increase in model tests corroborating observations for unidirectional tests. The η values are lower for element tests than model tests another observation identical to unidirectional tests.

The global cyclic behaviours are similar between element and model tests and the examined physical properties appear to influence the cyclic behaviours of both methods similarly. This suggests that the conclusions discussed in Section 4.5 are certainly applicable to model and field behaviour confirming that the same mechanisms that influence the drained cyclic behaviour of an element of soil also exist in the field.

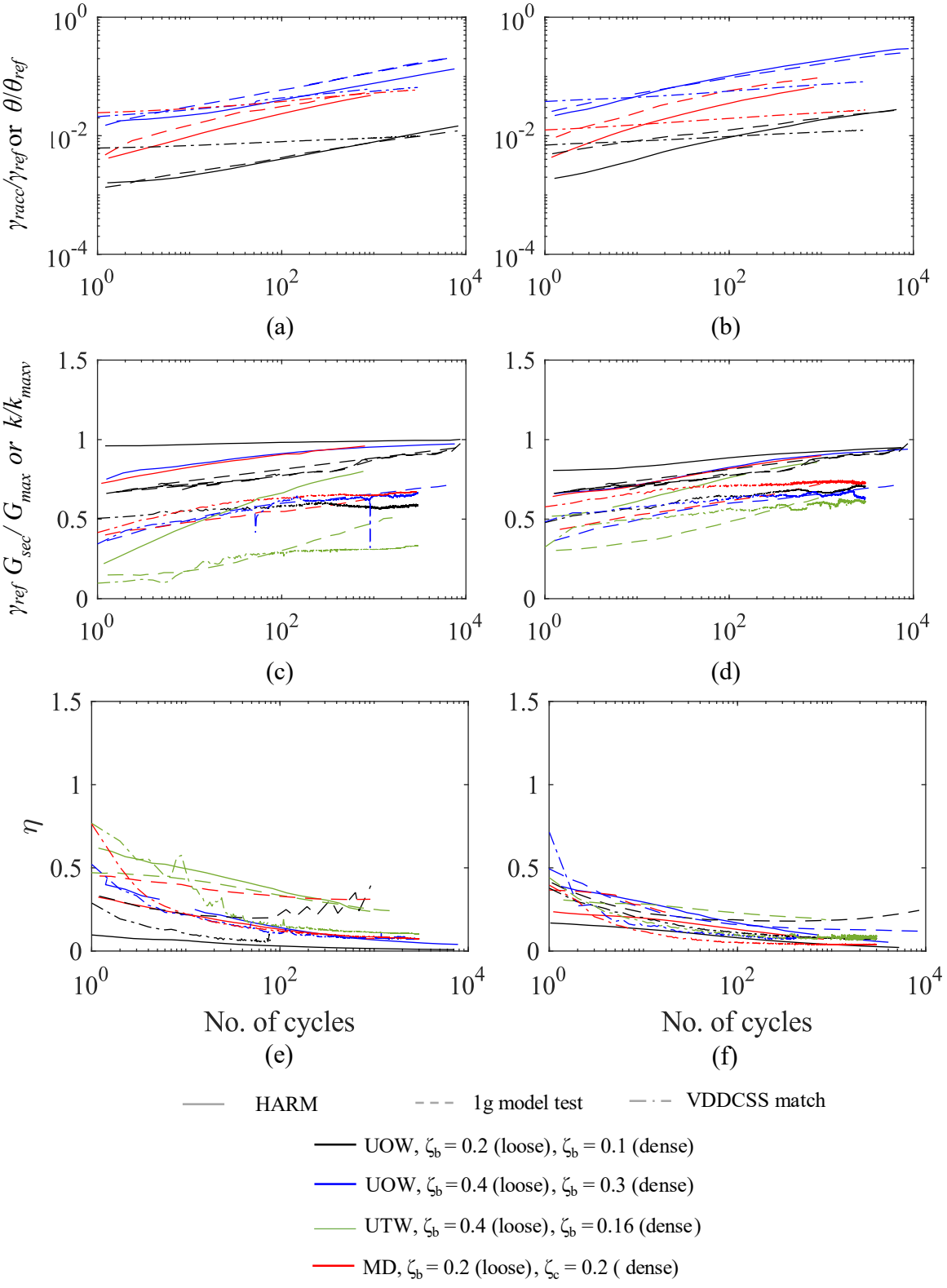
However, the evolution of the cyclic features is not identical between the methods. It is theorised the amount of densification and 'interlocking' that occurs with cycles is different between test methods due to the difference in volume of material that are affected. The significance of densification and 'interlocking' on $\gamma_{acc}/\theta_{acc}$, G_{sec}/k_{sec} and η is demonstrated in Section 4.3 and thus provides a plausible explanation to these diverging behaviours. The similarity observed between VDDCSS and 1g model tests for a single monotonic load is not present for cyclic behaviour, suggesting the simplistic matching approach cannot produce precise cyclic predictions of full sized OWTs.

5.5.5 Comparison with high cycle accumulation models

Richards (2020) additionally presents a set of comparisons between the 1g model tests in LBS and predictions using the Hyperplastic Accelerated Ratcheting Model (HARM) framework with details described in Houlsby et al. (2017). This model addresses the non-linear response on loading, hysteretic behaviour on unloading and reloading, and the phenomenon of ratcheting under very many cycles as observed in this study. The methodology enables the entire load-deflection response to be predicted incrementally whilst adhering to the Laws of Thermodynamics by using the hyperplasticity approach described in Houlsby and Puzrin (2007).

The evolution of $\gamma_{acc}/\theta_{acc}$, G_{sec}/k_{sec} and η with cycles and post-cyclic response of the 1g model tests were predicted applying the simplistic matching approach and predictions following the using HARM framework, refer to Richards (2020) for

calibration details. These predictions alongside actual test data are shown Figure 5-15(a) to (h) throughout.



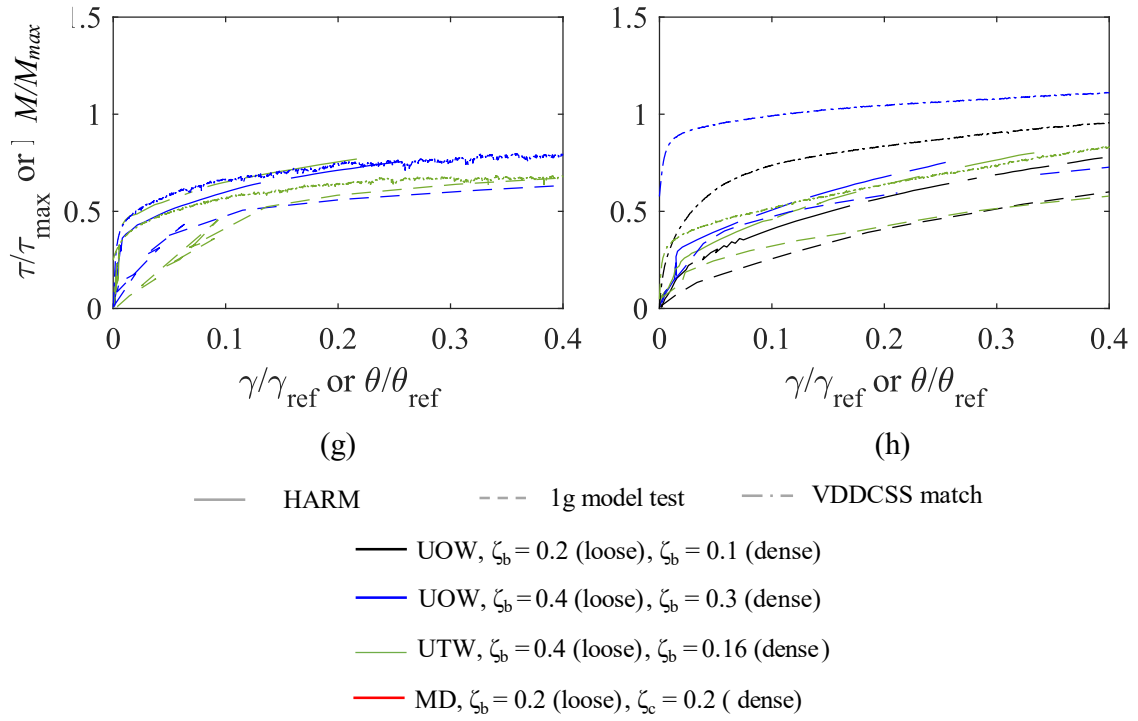


Figure 5-16 Cyclic response of 1g model tests in LBS with predictions using HARM and simplistic matching approach (a) θ_{acc} (loose) (b) θ_{acc} (dense) (c) k_{sec}/k_{max} (loose)(d) k_{sec}/k_{max} (dense) (e) η (loose) (f) η (loose) (g) Post-cyclic response (loose) (h) Post-cyclic response (dense)

Figure 5-16(a) and (b) shows that the evolution of θ_{acc} predicted by the HARM model follows the 1g model tests relatively accurately whilst the simplistic matching approach underpredicts the rate of θ_{acc} evolution. Figure 5-16(c) through (f) indicate that both the HARM and simplistic matching approach do not capture the evolution of k_{sec}/k_{max} nor η very precisely for most instances. HARM tends to over predict k_{sec} and under predict η while the simplistic matching approach is closer to experimental results in nominal value but does not capture the rate of change of these features well. Both HARM and simplistic matching approach over predicts the post-cyclic capacity of the 1g model test, the difference is higher for the simplistic matching approach. Since SLS design criterion requires the accurate prediction of long-term θ_{acc}, the accuracy demonstrated by the HARM model confirms its suitability for evaluating such design conditions.

The simplistic matching approach requires further development to accurately predict the cyclic behaviour of monopiles. One method to improve this approach involves

utilising the mathematical models proposed by researchers such as, Leblanc et al. (2010a), Truong et al. (2018) and Richards (2020) to describe the evolution of θ_{acc}, k_{sec} and η for 1g model piles undergoing cyclic loading in drained conditions.

$$\frac{\theta_{acc,N}}{\theta_R} = AN^{\beta} \tag{5-7}$$

$$\frac{k_{sec,N}}{k_{max}} = \frac{k_{sec,1}}{k_{max}} + B_L \ln(\mathrm{N}) \tag{5-8}$$

$$\eta_N = 1/k_{sec,N} \tag{5-9}$$

Where N is the number of cycles and A and β are fitting parameters that control the magnitude and rate of evolution of θ_{acc} respectively, $k_{sec,1}$ is the secant stiffness of the pile after 1 cycle and B_L is a fitting parameter that controls the rate of k_{sec} change. The curve fitting parameters above A, β and B_L depend on loading conditions, (ζ_b, ζ_c) soil properties (D_r, C_u, $F.C$, $G.C$) and pile geometries, (h,L_p,D_p) and are calibrated for each new model test.

The cyclic data gathered from the VDDCSS can also be fit to these expressions and A_{lab}, β_{lab} and $B_{L,lab}$ can be derived. Further 1g model tests or field tests with different pile geometries could enable the development of a scaling factor to convert these parameters to field conditions (A_{field}, β_{field}, $B_{L,field}$) based on a material constant, h, L_p and D_p. The ongoing medium-scale field at Cuxhaven provide an opportunity to achieve this.

Additionally, the cyclic response from VDDCSS tests can be compared to soil-structure reactions at specific depths along a monopile. Based on the similarity of these responses, a scaling approach could be developed to calibrate cyclic soil reaction curves with stress-strain curves from VDDCSS tests, like the framework proposed by Zhang and Andersen (2017) for monotonic soil-reaction curves. These calibrated soil reaction curves can then be implemented into a 1D FEM for OWT monopile design.

Developing the above approaches allows for a less computationally expensive determination of cyclic behaviour based on routine laboratory results (VDDCSS tests). These approaches provide a straightforward and practical method for OWT design.

5.5.6 Discussion

This Section has compared the cohesionless soil behaviour from element tests (RCA and VDDCSS) with 1g model and field tests. A method in which G_0 can be converted k_{max} is proposed in Section 5.5.1, which relies on an angle of impacted soil, α, which the lateral loading acts over in monopile systems and loading eccentricity ratio h/L. The method uses a 0D representation of the lateral loaded pile system and currently has been validated against on 12 field and 4 1g model tests. The performance of this method can be enhanced and verified through 3D FEA predictions.

Key features of the monotonic behaviour of foundation systems and soil are compared between an element of soil and full-scale foundation in Section 5.5.1 through 5.5.3. It is seen that γ_{tv} measured by the RCA and θ_e from the 1g model test are approximately equal. The normalised stiffness degradation in the VDDCSS, and 1g model tests are almost identical. A simplistic matching approach in which the full monotonic response of a monopile from a combination of element tests is presented and validated with 1g model tests at two densities. Additional verification of the procedure across different drainage conditions, materials and monopile geometries is required to ensure the method is suitable to predict the response of a full-sized monopile.

Section 5.5.4 and 5.5.5 compares the cyclic behaviour of VDDCSS and 1g model tests. Global trends related to cyclic features, θ_{acc}, k_{sec} and η with cycles are consistent across methods and the physical properties examined influence cyclic behaviour in the same manner across both methods. However, the rate at which these cyclic features evolve is different suggesting that a simplistic matching approach at this stage is not

representative for cyclic loading. This is further confirmed with comparisons with predictions using the HARM model. Presently, this suggests that a high strain accumulation model such as HARM is a robust design tool for evaluating SLS design. However, constitutive model that incorporates key cyclic behaviours of cohesionless soils implemented through FEA is required to accurately predict all cyclic behaviours of a full sized monopile under cyclic loading, required for ULS and FLS design.

There are several limitations to the comparisons undertaken in this research. Comparisons between the element and 1g model behaviour are limited to drained conditions without considering undrained and partially drained conditions. Similarly, comparisons have been limited to one pile geometry in a homogenous soil profile. It is important to verify the conclusion of this research across a range of realistic design scenarios. The extensive field-testing campaign is planned at Cuxhaven and can be used to validate and develop the comparative methods discussed in this section.

5.6 Conclusion

This chapter has demonstrated two means in which experimental results in this thesis inform design processes for OWTs. Section 5.3 explored the influence G_0 on f_0 and subsequently fatigue performance of OWTs. Key conclusions are herein discussed.

1. Several methods of obtaining f_0 were compared including the 'simplified', 'standard' and eigenvalue analysis implemented through a 1D FEM. It is demonstrated that the 'simplified' method does not alter the f_0 from the fixed based frequency of the system, highlighting a serious error in applying such methods to predict f_0.
2. A 1D numerical case study of the 10MW DTU reference wind turbine was conducted and validated against 3D FEA. The 1D FEM achieved high accuracy

predicting f_0 values within ±0.5% of the 3D FEA, demonstrating robust performance.

3. Accurate predictions of f_0 of OWTs are demonstrated to be essential for FLS design as 1P and 3P loads are account for 10-30% of overall damage depending on D_r and G_0, D_p and initial proximity of f_0 to f_{1P} and f_{3P}.
4. The D_p is a key design parameter that influences f_0 and direct proportionality between the two parameters is identified.
5. The relationship between D_r and G_0 and the fatigue performance of OWTs are complex and cannot be de-coupled using the adopted GDSM formulations; it depends on multiple factors including the initial D_r and G_0 profile, D_p, and the initial proximity of f_0 to f_{1P} and f_{3P}. The results indicate that precise fatigue analysis is crucial for FLS design because the impact of D_r and G_0 on fatigue performance varies significantly with different design scenarios.
6. For example, in scenarios with highly stiff/dense soil profiles, low D_p, and an initial f_0 far away from f_{1P} and f_{3P}, the fatigue performance is likely to be largely independent of D_r and G_0. Conversely, in scenarios with less stiff soil profiles, higher D_p, and an initial f_0 close to f_{1P} and f_{3P}, the fatigue performance becomes highly sensitive to D_r and G_0.

Secondly, Section 5.4 has compared the elastic, monotonic and cyclic behaviour of soils measured by element tests RCA and VDDCSS with 1g model tests and field tests. The key conclusions discussed below.

1. A simplistic matching approach to obtain the monotonic behaviour of a monopile in a homogenous soil from a combination of element tests is proposed, based on parallels of soil behaviour captured by the RCA/VDDCSS to field and 1g model

tests. Its application to large scale field tests in uncertain. It is necessary to validate this procedure against different monopile geometries, stress levels and drainage conditions to ensure it can be appropriately applied to a full sized monopile case.

2. Consistent features of cyclic behaviour between VDDCSS and 1g model tests suggest similar underlying mechanisms governing both scales. This implies that the same mechanisms controlling cyclic behaviour in the VDDCSS (ref. Chapter 5) also govern at the 1g model test scale and likely at the field scale.
3. The evolution of cyclic features in VDDCSS differ from 1g model tests and predictive responses using HARM, suggesting that the simplistic matching is not feasible in its current state to predict complex cyclic behaviour.
4. There are several potential areas to enhance cyclic pile design procedures based on laboratory behaviour pending the completion of the medium-scale field tests. The methods are summarised below.
    - **Improving simplistic matching approach:** This can be achieved with a scaling factor that converts the ratcheting, stiffness, and energy dissipation captured by the VDDCSS to field scale based on pile geometry and loading eccentricity.
    - **Scaling approach based on soil-structure reaction:** Like Zhang and Andersen (2017), a scaling approach that allows for calibration of cyclic soil-structure reaction curve based on the cyclic stress-strain curves from VDDCSS can be developed and implemented into a 1D numerical model for OWT monopile design.

CHAPTER 6

Conclusion and recommendations

6.1 Introduction

This thesis has experimentally explored the mechanical behaviour of cohesionless soils through advanced element soil testing. The primary focus of the experimental aspect of this thesis is an investigation into the physical mechanisms that influence the small-strain stiffness and cyclic behaviours of such soils. The results of the experimental programme are subsequently used to inform the design procedures for OWT monopiles. The mechanical behaviour of cohesionless soils provides key theoretical insights that contribute to the wider understanding of soil-structure interaction. Parallels between soil element behaviour and the behaviour observed in 1g model and field tests are evident, and efforts have been made to link these behaviours. This concluding chapter seeks to summarise the key findings and implications of this research within the context of OWT monopile design. Recommendations for future research directions are also discussed.

6.2 Key contributions

Site characterisation of PICASO Cuxhaven site

This research has contributed to the site characterisation of the Cuxhaven test site, where medium-scale field tests for the PICASO project are scheduled to take place. Chapter 2 summarises the contributions to the initial site investigation activities, including the interpretation of in-situ Cone Penetration Tests (CPTs) to derive relative density (Dr) and soil classification tests such as particle size gradings, minimum and maximum densities, and particle density. Chapter 3 summarises the advanced laboratory testing conducted using the Resonant Column Apparatus (RCA) to characterise the soil stiffness profile of the site.

Evaluation of the RCA for obtaining stiffness degradation parameters

The RCA was extensively used in this research to measure the stiffness and stiffness degradation of soils at small strains. This research demonstrates the procedure and associated challenges in obtaining representative stiffness parameters using the RCA, acknowledging its limitation in characterising elastic soil behaviour only (see Section 4.5). The results demonstrate the necessity of small strain checks in routine RCA testing and suggest that a combination of soil testing methods is necessary to accurately characterise the full stiffness degradation profile.

Parametric study on small-strain stiffness of cohesionless soil

Chapter 3 also explores the physical mechanisms that influence soil stiffness in the small-strain region. A thorough literature review in this area suggests that certain soil properties and testing conditions largely dictate stiffness, including initial effective stress, p'_0, D_r, d_{50} and C_u. An extensive parametric study was undertaken on three cohesionless soils, investigating these properties as well as saturation. The results of this study demonstrate

that nominal values of stiffness are altered by these parameters; however, the variation in stiffness degradation (i.e., characterised by the rate of degradation) within the elastic region is narrow. Changes in p'_0, D_r, soil type and saturation had a negligible influence on the measured stiffness degradation response by the RCA. The elastic region of soil is narrow; therefore, it is likely that the stiffness degradation in this range exhibits limited sensitivity to variations in soil properties and testing conditions.

Investigation of cyclic behaviour of cohesionless soil

Chapter 5 explores the cyclic behaviour of cohesionless soils captured by the Variable Dynamic Direct Cyclic Simple Shear (VDDCSS) device. Cyclic loading is known to induce several phenomena, including densification, generation of porewater pressure, accumulated ratcheting, changes to stiffness and energy dissipation, and changes to post-cyclic strength. The effects of several physical mechanisms on the cyclic behaviour of cohesionless soils have been explored in detail in this investigation. Drainage conditions have emerged as perhaps the most notable mechanism influencing these cyclic behaviours. Undrained tests exhibit a rapid increase in porewater pressure, accumulated ratcheting, and energy dissipation, as well as a rapid decrease in stiffness at the cycle of failure. Conversely, drained tests exhibited continuous stiffness increases with cycles and decreased energy dissipation, indicating a greater resistance to loading with cycles. Several other conclusions relating to the influence of ζ_b, ζ_c, f, σ'_v and D_r on cyclic and multi-directional loading are discussed in this chapter. Discussions regarding the implications and possible integration of experimental findings with OWT foundation design and constitutive modelling are presented. The conclusions drawn in this chapter can assist in informing design methods for offshore foundations, which are likely to be influenced by the same physical mechanisms in the field.

Soil sensitivity study on the fatigue response of OWT

To quantify the effects of initial soil stiffness on the fatigue response of OWTs, a case study considering the 10MW DTU reference wind turbine was undertaken (see Section 5.4). Using a 1D numerical method, the influence of initial soil stiffness, G_0 on natural frequency, f_0 and subsequently fatigue damage is examined. While nominal values of f_0 remain relatively unaffected by variation in G_0 across all examined D_p, the potential for G_0 to influence the fatigue performance OWTs is evident. Specifically, the sensitivity of the OWT fatigue response increased significantly to variations in G_0 as D_p and the proximity of f_0 to f_{1P} and f_{3P} increased.

The relationship between G_0 fatigue performance proved complex, with no direct correlation between the two observed, given the coupling of the problem with D_p and the initial f_0 location. These findings demonstrate the necessity of precise fatigue analysis as large fluctuations in fatigue performance can occur depending on the design scenario.

Extracting key element behaviours to field scale

A comparison between the monotonic and cyclic behaviour from element tests with 1g model tests and field tests was undertaken to explore other practical implications of the experimental programme and is discussed in Section 5.5. A method to obtain initial foundation stiffness and the full monotonic response of monopiles from G_0 is proposed using a combination of field tests from the PISA project and 1g model tests undertaken by Richards (2020) and laboratory tests undertaken in this thesis.

A comparison of the cyclic behaviours from 1g model tests and VDDCSS tests is also presented. Global trends measured from the VDDCSS such as the influence of ζ_b, ζ_c, and D_r are consistent with results from model tests implying that the conclusions relating to the physical mechanisms that influence cyclic behaviour at an element test scale (as

discussed in Chapter 3 and 4) are applicable to field-scale behaviour. However, a major difference observed between the VDDCSS and 1g model tests is that most cyclic features reached an equilibrium in the former but did not in the latter. Thus, a simple scaling approach from element behaviour to full size monopile behaviour cannot be undertaken for cyclic loading.

6.3 Future research

Beyond small-strain stiffness

This research has extensively explored the stiffness response of cohesionless soils within the elastic region. It is demonstrated that within this region, the nominal value of stiffness of the material depends on factors such as D_r, p'_0 grain characteristics, and saturation. However, the rate of stiffness degradation, G/G_0 is essentially independent of these factors within the elastic region. From a practical perspective, this suggests that geotechnical designers can approximate the stiffness degradation of soil within the elastic region rather crudely. The results of this research demonstrate that the stress-strain behaviour of cohesionless soils is largely dependent on the 'state' (characterised by Ψ) and drainage conditions. As G at any shear strain is simply τ/γ, it is theorised that the G/G_0 at medium to large strains is also governed by these factors. Since this research demonstrates that the RCA cannot solely determine all relevant stiffness degradation parameters, a natural extension of this work is to investigate the influence of Ψ and drainage on G/G_0 across a wide strain range using alternative test methods such as triaxial tests with local gauges or a combination of test methods such as RCA and triaxial at the same stress states.

Fatigue performance of OWTs

The findings from the 1D numerical case study demonstrate that the influence of G_0 on f_0 and the fatigue performance of OWTs is largely coupled with other factors such as D_p and the proximity of initial f_0 to f_{1P} and f_{3P}. For the base case condition, where f_0 *is* located far away from both f_{1P} and f_{3P}, variations in G_0 have a negligible impact on f_0 and fatigue performance. However, Wen et al. (2024) has demonstrated that aerodynamic interactions, such as turbine-wake effects and farm-atmospheric effects, can cause large reductions to f_{1P} and f_{3P}, especially as wind turbines and farms increase in size. This would effectively change the proximity of initial f_0 to f_{1P} and f_{3P} which has been demonstrated in this study to increase sensitivity of fatigue performance to G_0 changes. From a practical perspective, OWT designers will need to investigate how foundation designs must be adapted to mitigate the adverse effects of aerodynamic interactions on fatigue performance (i.e., through optimisation of design parameters) whilst maintaining optimal aerodynamic efficiency. The effectiveness of the 1D numerical tool used in this study for OWT analysis suggests its potential utility in such future research endeavours.

Design of OWT monopiles under cyclic loading

This research has identified key physical mechanisms that influence the cyclic behaviour of cohesionless soils in the VDDCSS. These mechanisms are demonstrated to hold true at a 1g model scale under drained conditions. Noteworthy empirical models that predict accumulated ratcheting and stiffness with cycles for monopiles primarily consider ζ_b, ζ_c, and D_r, as detailed in Richards (2019). Results from this study additionally suggest that cyclic loading increases the cyclic resistance of cohesionless soils due to densification and 'interlocking'. Integrating these findings into these models can enhance their predictive accuracy. Furthermore, these features can also be implemented into constitutive models that describe the ratcheting response of cohesionless soil behaviour

under cyclic loading, which can ultimately be implemented into an FEA to predict the cyclic response of a full-sized monopile.

Given the growing significance of drainage in cohesionless soil behaviour, there is a need to investigate whether insights derived from undrained behaviour in element tests can be applied to undrained 1g models, centrifuge, and/or field tests—an aspect not covered in the current research. While this study is confined to exploring the fully drained and fully undrained bounds of cyclic behaviour, which proves relevant for specific design scenarios like low-frequency wind loading or sudden events such as earthquakes or storms, it's crucial to acknowledge the likelihood of OWTs exhibiting a partially drained response. Future research should extend to include element tests and physical scale tests conducted in partially drained and/or undrained conditions. Meaningful comparisons examining the evolution of porewater pressure, stiffness, energy dissipation, and stress-path in these conditions can then be undertaken.

Currently, medium-scale field tests at the Cuxhaven test site are underway as part of the PICASO project. These tests are anticipated to provide valuable insights into the cyclic behaviour of monopiles across a range of drainage conditions, monopile geometries, and loading regimes. By combining the results of these field tests with the laboratory tests in this thesis, several activities can be undertaken to improve the design methods of OWTs following the work presented in this thesis:

1. These field tests can be used to validate the method of linking element tests to full-sized monopiles as discussed in Section 5.5.3 over a wider range of design scenarios than currently presented.
2. The cyclic stress-strain curves derived from the VDDCSS at several σ'_v can be compared with the soil-structure response at locations along an

instrumented monopile. Should the cyclic stress-strain and soil-structure responses resemble each other, a scaling approach like that of Zhang and Andersen (2017) could be developed for cyclic loading. This would require comparisons regarding stiffness improvement and increased post-cyclic capacity of monopiles.

REFERENCES

Adamidis, O., Vasic, N., and Kassas, K. (2017). "Small strain shear modulus of Hostun sand." Zurich.

Agaiby, S. W., and Ahmed, S. M. (2019). "Determination of Sand Void Ratio Using CPT and SPT. " *Geo-Congress.* https://doi.org/10.1061/9780784482131.005.

Aghakouchak, A. (2015). "Advanced laboratory studies to explore the axial cyclic behaviour of driven piles." PhD Thesis, Imperial College.

Ahmed, S., Agaiby, S., and Mayne, P. (2014). "Sand compressibility aspects related to CPT." *3rd International Symposium on Cone Penetration Testing (CPT'14).* Las Vegas, Nevada, USA.

Ahmed, S. M. (2017). "Enhancing the CPT correlation with the small strain shear stiffness of sands." *Ain Shams Engineering Journal,* 8: 539–548.

Al Tarhouni, M. A., and Hawlader, B. (2021). "Monotonic and cyclic behaviour of sand in direct simple shear test conditions considering low stresses." *Soil Dynamics and Earthquake Engineering,* 150: 106931. https://doi.org/10.1016/j.soildyn.2021.106931.

Alarcon-Guzman, A., Chameau, J. L., Leonards, G. A., and Frost, J. D. (1989). "Shear Modulus and Cyclic Undrained Behavior of Sands." *Soils and Foundations,* 29: 105–119. https://doi.org/10.3208/sandf1972.29.4_105.

Alkhoury, P., Soubra, A.-H., Rey, V., and Aït-Ahmed, M. (2021). "A full three-dimensional model for the estimation of the natural frequencies of an offshore wind turbine in sand." *Wind Energy,* 24: 699–719. https://doi.org/10.1002/we.2598.

Altun, S., and Goktepe, A. B. (2006). "Dependence of dynamic shear modulus of uniform sands on stress level and density." *Civil Engineering and Environmental Systems,* 23: 101–116. https://doi.org/10.1080/10286600600743372.

Amer, M., Kovacs, W., and Aggour, M. (1987). "Cyclic simple shear size effects." *Journal of Geotechnical Engineering,* 113: 693–707.

Amoroso, S. (2014). "Prediction of the shear wave velocity VS from CPT and DMT at research sites." *Frontiers of Structural and Civil Engineering,* 8: 83–92.

Andersen, K. (2015). "Cyclic soil parameters for offshore foundation design. " *Frontiers in Offshore Geotechnics III.* https://doi.org/10.1201/b18442-4.

Andersen, K. H., Engin, H. K., D'Ignazio, M., and Yang, S. (2023). "Determination of cyclic soil parameters for offshore foundation design from an existing data base." *Ocean Engineering,* 267: 113180. https://doi.org/10.1016/j.oceaneng.2022.113180.

Andrus, R. D., Mohanan, N. P., Piratheepan, P., Ellis, B. S., and Holzer, T. L. (2007). "Predicting shear-wave velocity from cone penetration resistance." Proceedings of the *4th International Conference on Earthquake Geotechnical Engineering,* Thessaloniki, Greece.

API. (2010). "Recommended Practice for Planning, Designing, and Constructing Fixed Offshore Platforms." *Working Stress Design.*

Arangelovsk, G., and Towhata, I. (2004). "Accumulated Deformation of Sand with Initial Shear Stress and Effective Stress State Lying Near Failure Conditions." *Soils and Foundations,* 44: 1–16. https://doi.org/10.3208/sandf.44.6_1.

Arany, L., Bhattacharya, S., Adhikari, S., Hogan, S. J., and Macdonald, J. H. G. (2015). "An analytical model to predict the natural frequency of offshore wind turbines

on three-spring flexible foundations using two different beam models." *Soil Dynamics and Earthquake Engineering,* 74: 40–45. https://doi.org/10.1016/j.soildyn.2015.03.007.

Arany, L., Bhattacharya, S., Macdonald, J., and Hogan, S. J. (2017). "Design of monopiles for offshore wind turbines in 10 steps." *Soil Dynamics and Earthquake Engineering,* 92: 126–152. https://doi.org/10.1016/j.soildyn.2016.09.024.

Arroyo, M., Muir Wood, D., Greening, P. D., Medina, L., and Rio, J. (2006). "Effects of sample size on bender-based axial G0 measurements." *Géotechnique,* 56: 39–52. https://doi.org/10.1680/geot.2006.56.1.39.

Arulnathan, R., Boulanger, R. W., and Riemer, M. F. (1998). "Analysis of Bender Element Tests." *Geotechnical Testing Journal,* 21: 120–131. https://doi.org/10.1520/GTJ10750J.

ASTM. (2006). "Standard test methods for maximum index density and unit weight of soils using a vibratory table." *ASTM International,* West Conshohocken.

ASTM. (2015). "ASTM D4015-15e1, Standard Test Methods for Modulus and Damping of Soils by Fixed-Base Resonant Column Devices." *ASTM International,* West Conshohocken. https://doi.org/10.1520/D4015-15E01.

Bai, L. (2010). "Preloading Effects on Dynamic Sand Behavior by Resonant Column Tests." PhD Thesis, Technical University of Berlin.

Bak, C., Zahle, F., Bitsche, R., Kim, T., Yde, A., Henriksen, L. C., Hansen, M. H., Blasques, J. P. A. A., Gaunaa, M., and Natarajan, A. (2013). "The DTU 10-MW Reference Wind Turbine." *Danish Wind Power Research.*

Baldi, G., Bellotti, R., Ghionna, V., Jamiolkowski, M., and Pasqualini, E. (1986)."Interpretation of CPTs and CPTUs; 2nd part: drained penetration of sands." Proceedings of *Fourth International Geotechnical Seminar,* 143–156. Singapore.

Bartake, P., and Singh, D. (2007). "Studies on the determination of shear wave velocity in sands." *Geomechanics and Geoengineering,* 2: 41–49.

Bayton, S. (2020). "Centrifuge Modelling of Monopiles in Sand Subject to Lateral Loading." PhD Thesis, University of Sheffield.

Been, K., Jefferies, M., Crooks, J., and Becker, D. (1986). "The cone penetration test in sands: Part I, state parameter interpretation." *Géotechnique,* 36: 239–249. https://doi.org/10.1680/geot.1986.36.2.239.

Benz, T. (2007). "Small-Strain Stiffness of Soils and its Numerical Consequences." PhD Thesis, Universität Stuttgart.

Berrill, J. B., and Davis, R. O. (1985). "Energy Dissipation and Seismic Liquefaction of Sands: Revised Model." *Soils and Foundations,* 25: 106–118. https://doi.org/10.3208/sandf1972.25.2_106.

BGS. (2022a). "Geology of the country around Chester and Winsford. Memoir for 1:50 000 geological sheet 109 (England and Wales)."Accessed August 2022.

BGS. (2022b). "Geology of the country around Leighton Buzzard. Memoir for 1:50 000 geological sheet 220 (England and Wales)." Accessed August 2022.

Bhaumik, L., Rutherford, C. J., Cerna-Diaz, A., Olson, S. M., Numanoglu, O. A., Hashash, Y. M. A., and Weaver, T. J. (2017). "Volumetric Strain in Non-Plastic Silty Sand Subject to Multidirectional Cyclic Loading." *Geotechnical Special Publication,* 150–159.

Bhaumik, L., Rutherford, C. J., Olson, S. M., Hashash, Y. M. A., Numanoglu, O. A., Cerna-Diaz, A., and Weaver, T. J. (2023). "A Multidirectional Cyclic Direct

Simple Shear Device for Characterizing Dynamic Soil Behavior." *Geotechnical Testing Journal.*

Bjerrum, L.and Landva, A. (1966). "Direct Simple-Shear Tests on a Norwegian Quick Clay." *Géotechnique*, 16: 1-20. 10.1680/geot.1966.16.1.1

Boulanger, R. W., and Seed, R. B. (1995). "Liquefaction of sand under bidirectional monotonic and cyclic loading." *Journal of Geotechnical Engineering,* 121(12), 870–878. https://doi.org/10.1061/(ASCE)0733-9410(1995)121:12(870)

Bouzid, D. A., Bhattacharya, S., and Otsmane, L. (2018). "Assessment of natural frequency of installed offshore wind turbines using nonlinear finite element model considering soil-monopile interaction." *Journal of Rock Mechanics and Geotechnical Engineering,* 10(2), 333–346. https://doi.org/10.1016/j.jrmge.2017.11.010

BS (1990). "Methods of test for soils for civil engineering purposes, Part 4: Compaction-related tests. " British Standard BS1377:4:1990, Clauses 4.2 and 4.4. London: British Standards Institution.

Buckley, R. M., Jardine, R. J., Kontoe, S., Liu, T., Byrne, B. W., McAdam, R. A., Schranz, F., and Vinck, K. (2024). "Axial cyclic loading of piles in low-to-medium-density chalk." *Géotechnique,* 74(6), 570–583. https://doi.org/10.1680/jgeot.22.00044

Budhu, M. (2011). "Failure state of a sand in simple shear. " *Canadian Geotechnical Journal,* 25(3), 395–400. https://doi.org/10.1139/t88-041

Burd, H. J., Taborda, D. M. G., Zdravković, L., Abadie, C. N., Byrne, B. W., Houlsby, G. T., Gavin, K. G., Igoe, D. J. P., Jardine, R. J., Martin, C. M., McAdam, R. A., Pedro, A. M. G., and Potts, D. M. (2019). "PISA design model for monopiles for offshore wind turbines: Application to a marine sand." *Géotechnique,* 0(0), 1–19. https://doi.org/10.1680/jgeot.18.P.277

Byrne, B., McAdam, R., Burd, H., Houlsby, G., Martin, C., Beuckelaers, W. J. A. P., Zdravković, L., Taborda, D. M. G., Potts, D., Jardine, R., Ushev, E., Liu, T., Abadias, D., Gavin, K., Igoe, D., Doherty, P., Gretlund, J., Pacheco Andrade, M., Wood, A., and Plummer, M. (2017). "PISA: New design methods for offshore wind turbine monopiles. " *Géotechnique.*

Byrne, B. W., Houlsby, G. T., Burd, H. J., Gavin, K., Igoe, D., Jardine, R. J., Martin, C., McAdam, R. A., Potts, D. M., Taborda, D. M. G., and Zdravković, L. (2020). "PISA design model for monopiles for offshore wind turbines: Application to a stiff glacial clay till. " *Géotechnique,* 70(11), 1030–1047. https://doi.org/10.1680/jgeot.18.P.275

Carroll, M. D. (1979). "Sample size effects using the NGI direct simple shear apparatus. " PhD Thesis, Rensselaer Polytechnic Institute.

Carter, J., and Kulhawy, F. (1992). "Analysis of laterally loaded shafts in rock. " *Journal of Geotechnical Engineering,* 118(6), 839–856. https://doi.org/10.1061/(ASCE)0733-9410(1992)118:6(839)

Cary, C. (2011). "Pore water pressure response of a soil subjected to traffic loading under saturated and unsaturated conditions. " PhD Thesis, Arizona State University.

Casagrande, A. (1936). "Characteristic of cohesionless soils affecting the stability of slopes and earth fills. " *Journal of Boston Society of Civil Engineers,* 23(1), 13–32.

Castro, G., Enos, J., France, J., and Poulos, S. (1982). "Liquefaction induced by cyclic loading. " *NASA STI/Recon Technical Report N,* 83(1), 13308.

Cataño-Arango, J. (2006). “Stress-strain behavior and dynamic properties of Cabo Rojo calcareous sands. ” PhD Thesis, University of Puerto Rico

Cavallaro, A., Maugeri, M., and Mazzarella, R. (2001). “Static and dynamic properties of Leighton Buzzard sand from laboratory tests. ” *Proceedings of the 4th International Conference on Recent Advances in Geotechnical Earthquake Engineering and Soil Dynamic,* San Diego, USA

Chang, C. S., and Whitman, R. V. (1988). “Drained permanent deformation of sand due to cyclic loading. ” *Journal of Geotechnical Engineering,* 114(10), 1164–1180. https://doi.org/10.1061/(ASCE)0733-9410(1988)114:10(1164)

Chen, A. T., and Stokoe, K. H. (1979). “Interpretation of strain-dependent modulus and damping from torsional soil tests.” U.S. Geological Survey.

Chen, G., Zhou, Z., Sun, T., Wu, Q., Xu, L., Khoshnevisan, S., and Ling, D. (2019). “Shear modulus and damping ratio of sand–gravel mixtures over a wide strain range.” *Journal of Earthquake Engineering, 23*(10): 1407-1420. https://doi.org/10.1080/13632469.2017.1387200

Chung, R. M., Yokel, F. Y., and Drnevich, V. P. (1984). “Evaluation of dynamic properties of sands by resonant column testing.” *Geotechnical Testing Journal, 7*(1): 60-69. https://doi.org/10.1520/GTJ10594J

Clayton, C. R. I. (2011). “Stiffness at small strain: Research and practice.” *Géotechnique, 61*(1): 5-37. https://doi.org/10.1680/geot.2011.61.1.5

Clayton, C. R. I., Priest, J. A., and Best, A. I. (2005). “The effects of disseminated methane hydrate on the dynamic stiffness and damping of a sand.” *Géotechnique, 55*(6): 423-434. https://doi.org/10.1680/geot.2005.55.6.423

Cubrinovski, M., and Rees, S. (2008). “Effects of fines on undrained behaviour of sands.” *Geotechnical Engineering Journal of the SEAGS & AGSSEA, 39*(2): 1-12.

Cui, L., Bhattacharya, S., Nikitas, G., and Bhat, A. (2019). “Macro- and micro-mechanics of granular soil in asymmetric cyclic loadings encountered by offshore wind turbine foundations.” *Granular Matter, 21*(1): 73. https://doi.org/10.1007/s10035-019-0924-4

Dammala, P. K., Krishna, A. M., Bhattacharya, S., Nikitas, G., and Rouholamin, M. (2017). “Dynamic soil properties for seismic ground response studies in Northeastern India.” *Soil Dynamics and Earthquake Engineering, 100*: 357-370. https://doi.org/10.1016/j.soildyn.2017.06.003

Darendeli, M. B. (2001). “Development of a new family of normalized modulus reduction and material damping curves.” PhD.Thesis, University of Texas at Austin.

De Josselin de Jong, G. (1971). “Discussion Session 2. Stress-strain behavior of soils.” In *Roscoe Memorial Symposium*, edited by G. T. Foulis, R. H. G. Parry, and Co., 258-261. Henley on Thames, United Kingdom.

DeAlba, P., Chan, C. K., and Seed, H. B. (1975). “Determination of soil liquefaction characteristics by large-scale laboratory tests.” *Earthquake Engineering Research Center, University of California, Berkeley*.

Delfosse-Ribay, E., Djeran-Maigre, I., Cabrillac, R., and Gouvenot, D. (2004). “Shear modulus and damping ratio of grouted sand.” *Soil Dynamics and Earthquake Engineering, 24*(6): 461-471. https://doi.org/10.1016/j.soildyn.2004.02.004

DIN. (1996). “Bestimmung der Dichte nichtbindiger Böden bei lockerster und dichtester Lagerung.” Deutsches Institut für Normung, Berlin, Germany.

DNV. (2008). “Fatigue design of offshore steel structures: DNV-RP-C203.” *Fatigue analysis based on S-N data*. Norway.

DNVGL. (2016). “Support structures for wind turbines: Laterally loaded piles.” *DNVGL-ST-0120*.

Do, T. M., Laue, J., Mattsson, H., and Jia, Q. (2023). “Excess pore water pressure generation in fine granular materials under undrained cyclic triaxial loading.” *International Journal of Geo-Engineering, 14*: 8. https://doi.org/10.1186/s40703-023-00185-y

Dobry, R. (1989). “Some basic aspects of soil liquefaction during earthquakes.” *Annals of the New York Academy of Sciences, 558*: 172-182. https://doi.org/10.1111/j.1749-6632.1989.tb22567.x

Dobry, R., and Abdoun, T. (2015). “3rd Ishihara Lecture: An investigation into why liquefaction charts work: A necessary step toward integrating the states of art and practice.” *Soil Dynamics and Earthquake Engineering, 68*: 40-56. https://doi.org/10.1016/j.soildyn.2014.09.011

Doherty, J., and Fahey, M. (2011). “Three-dimensional finite element analysis of the direct simple shear test.” *Computers and Geotechnics, 38*(7): 917-924. https://doi.org/10.1016/j.compgeo.2011.05.005

Doygun, O., Brandes, H. G., and Polito, C. P. (2021). “Large-strain damping of sands: Parameter effects.” *Journal of Geotechnical and Geoenvironmental Engineering, 147*(6). https://doi.org/10.1061/(ASCE)GT.1943-5606.0002572

Dyvik, R., Berre, T., Lacasse, S., and Raadim, B. (1987). “Comparison of truly undrained and constant volume direct simple shear tests.” *Géotechnique, 37*(1): 3-10. https://doi.org/10.1680/geot.1987.37.1.3

EGDI. (2024). “Pan-European 1:100000 geological map.” Accessed September 2024. https://maps.europe-geology.eu/#baslay=baseMapGEUS&extent=-246581.81946403347,1153040.9167842031,8751561.819464033,5312339.083215797

El Mohtar, C. S., Drnevich, V. P., Santagata, M., and Bobet, A. (2013). “Combined resonant column and cyclic triaxial tests for measuring undrained shear modulus reduction of sand with plastic fines.” *Geotechnical Testing Journal, 36*(4): 484-492. https://doi.org/10.1520/GTJ20120129

Ellis, E. A., Soga, K., Bransby, F., and Sato, M. (2000). “Resonant column testing of sands with different viscosity pore fluids.” *Journal of Geotechnical and Geoenvironmental Engineering, 126*(1): 10-20. https://doi.org/10.1061/(ASCE)1090-0241(2000)126:1(10)

EuropeanCommission. (2023). “European Wind Power Action Plan.” *Brussels: European Union*.

Figueroa, J. L., Saada Adel, S., Liang, L., and Dahisaria Nitin, M. (1994). “Evaluation of soil liquefaction by energy principles.” *Journal of Geotechnical Engineering, 120*(9): 1554-1569. https://doi.org/10.1061/(ASCE)0733-9410(1994)120:9(1554)

Fioravante, V., Jamiolkowski, M., and Lo Presti, D. (1994). “Stiffness of carbonatic Quiou sand.” *Proceedings of the International Conference on Soil Mechanics and Foundation Engineering*, 163-167.

Fleischer, M., Abegunrin, A., Hepp, D. A., Kreiter, S., Coughlan, M., and Mörz, T. (2023). “Stratigraphic and geotechnical characterization of regionally extensive and highly competent shallow sand units in the southern North Sea.” *Boreas, 52*: 78-98. https://doi.org/10.1111/bor.12595]

Foundation Offshore Wind Energy. (n.d) “Foundations.”Retrieved from

https://www.offshore-stiftung.de/en/foundations.php
Franke, E., Kiekbusch, M., and Schuppener, B. (1979). “A new direct simple shear device.” *Geotechnical Testing Journal, 2*(3): 190-199.
Gabryś, K., Soból, E., Sas, W., Šadzevičius, R., and Skominas, R. (2021). “Warsaw Glacial Quartz Sand with Different Grain-Size Characteristics and Its Shear Wave Velocity from Various Interpretation Methods of BET.” *Materials, 14*(3): 544.
Gazetas, G. (1991). “Formulas and Charts for Impedances of Surface and Embedded Foundations”, *Journal of Geotechnical Engineering*, 117: 1363-81.
Gazetas, G.and Stokoe, K. H. (1991). “Free vibration of embedded foundations: theory versus experiment.” *Journal of Geotechnical Engineering*, 117: 1382-401
Geo-Engineering (2023) “Summary report for site investigation in Nordholz”. Bremen: Geo-Engineering GmbH.
Gielan, D., Boshell, F., Saygin, D., Bazilian, M. D., Wagner, N., and Gorini, R. (2019) “The role of renewable energy in the global energy transformation. ” *Energy Strategy Reviews, 24*, 38–50.
Goto, S., Suzuki, Y., Nishio, S. Y., and Oh-oka, H. (1992) “Mechanical properties of undisturbed Tone-River gravel obtained by in-situ freezing method. *Soils and Foundations, 32*(3), 15–25. https://doi.org/10.3208/sandf1972.32.3_15
Green, R., Mitchell, J., and Polito, C. (2000) “An energy-based excess pore pressure generation model for cohesionless soils.” *Proceedings of the John Booker Memorial Symposium,*383-390, Sydney, Australia.
Gu, Q.-Y., Sarkar, D., Goudarzy, M., and Wichtmann, T. (2021) “Combined effect of grain shape and grading on the small-strain stiffness of granular soils at different densities and stress states.” *Conference: 3. Bodenmechanik Tagun*.
Gu, X., Yang, J., Huang, M., and Gao, G. (2015) “Bender element tests in dry and saturated sand: Signal interpretation and result comparison.” *Soils and Foundations, 55*, 951–962. https://doi.org/10.1016/j.sandf.2015.09.002
Gupta, B. K., and Basu, D. (2016) “Analysis of laterally loaded rigid monopiles and poles in multilayered linearly varying soil.” *Computers and Geotechnics, 72*, 114–125. https://doi.org/10.1016/j.compgeo.2015.11.008
Hardin, B., and Black, W. (1968) “Vibration modulus of normally consolidated clay.” *Journal of Soil Mechanics and Foundations Division, ASCE, 94*.
Hardin, B., and Drnevich, V. (1972a) “Shear modulus and damping in soil: Measurement and parameter effects.” *Journal of Soil Mechanics and Foundations Engineering, ASCE, 98*(6), 603–624. https://doi.org/10.1061/JSFEAQ.0001756
Hardin, B., and Black, W. L. (1966) “Sand stiffness under various triaxial stresses.” *Journal of Soil Mechanics and Foundations Division, 92*(2), 27–42. https://doi.org/10.1061/JSFEAQ.0000865
Hardin, B., and Drnevich, V. P. (1972b) “Shear modulus and damping in soils: Design equations and curves.” *Journal of Soil Mechanics and Foundations Division, 98*(7), 667–692. https://doi.org/10.1061/JSFEAQ.0001760
Hardin, B., and Kalinski, M. E. (2005) “Estimating the shear modulus of gravelly soils.” *Journal of Geotechnical and Geoenvironmental Engineering, 131*(7), 867–875. https://doi.org/10.1061/(ASCE)1090-0241(2005)131:7(867)
Hardin, B., and Richart, J. F. (1963) “Elastic wave velocities in granular soils.”*Journal of Soil Mechanics and Foundations Division, 89*.

Hegazy, Y., and Mayne, P. (2006) "A global statistical correlation between shear wave velocity and cone penetration data." *Site and Geomaterial Characterization* , 243-248https://doi.org/10.1061/40861(193)31

Higgins, W., and Basu, D. (2011) "Fourier finite element analysis of laterally loaded piles in elastic media." *Internal Geotechnical Report*.

Hight, D. W., Gens, A., and Symes, M. J. (1983) "The development of a new hollow cylinder apparatus for investigating the effects of principal stress rotation in soils." *Géotechnique, 33*(4), 355–383. https://doi.org/10.1680/geot.1983.33.4.355

Houlsby, G., and Puzrin, A. (2007) "Principles of hyperplasticity: An approach to plasticity theory based on thermodynamic principles." *Springer Science and Business Media.*

Houlsby, G. T., Abadie, C. N., Beuckelaers, W. J. A. P., and Byrne, B. W. (2017) "A model for nonlinear hysteretic and ratcheting behavior. " *International Journal of Solids and Structures, 120*, 67–80. https://doi.org/10.1016/j.ijsolstr.2017.04.031

Hwang, S. K. (1997) "Investigation of the dynamic properties of natural soils." PhD Thesis, University of Texas at Austin.

IEC (2019) "Wind energy generation systems - Part 3-1: Design requirements for fixed offshore wind turbines." *International Electrotechnical Commission.*

Ishihara, K. (1996) "Soil behaviour in earthquake geotechnics. " *Oxford Engineering Science Series.*

Ishihara, K., and Yamazaki, F. (1980). "Cyclic simple shear tests on saturated sand in multi-directional loading." *Soils and Foundations*, 20: 45-59.

Iwasaki, T., Tatsuoka, F., and Takagi, Y. (1978). "Shear Moduli of Sands under Cyclic Torsional Shear Loading." *Soils and Foundations*, 18: 39-56. https://doi.org/10.3208/sandf1972.18.39

Jalbi, S., Shadlou, M., and Bhattacharya, S. (2017). "Chapter 16 - Practical Method to Estimate Foundation Stiffness for Design of Offshore Wind Turbines." Trevor M. Letcher (ed.), *Wind Energy Engineering*. https://doi.org/10.1016/B978-0-12-809451-8.00016-3

Jamiolkowski, M., Lo Presti, D., and Manassero, M. (2001). "Evaluation of Relative Density and Shear Strength of Sands from CPT and DMT." *ASCE Geotechnical Special Publication* No. 119: 201–238. *10.1061/40659(2003)7*

Jardine, R., Puech, A., and Andersen, K. H. (2012). "Keynote Address: Cyclic Loading of Offshore Piles: Potential Effects And Practical Design." *SUT Offshore Site Investigation and Geotechnics*: SUT-OSIG-12-06

Jardine, R. J. (1992). "Some Observations on the Kinematic Nature of Soil Stiffness." *Soils and Foundations*, 32: 111-24. https://doi.org/10.3208/sandf1972.32.2_111

Jeanjean, P., Zhang, Y., Zakeri, A., Andersen, K. H., Gilbert, R., and Senanayake, A. (2017). "A Framework for Monotonic P-Y Curves in Clays." *Offshore Site Investigation Geotechnics 8th International Conference Proceeding*: 108-41. 10.3723/OSIG17.108

Jefferies, M., and Been, K. (2015). "Soil Liquefaction: A Critical State Approach, Second Edition." CRC Press.

Jeffries, M., and Been, K. (2006). "Soil Liquefaction: A Critical State Approach, Second Edition." (Taylor and Francis: 2 Park Square, Milton Park, Abingdon, Oxon OX14 4RN, 270 Madison Ave, New York, NY 10016, USA)

Jonkman, J. M. (2007). "Dynamics Modeling and Loads Analysis of an Offshore Floating Wind Turbine." (Report No. NREL/TP-500-41958). National Renewable Energy

Laboratory. 10.2172/921803
Jostad, H. P., Dahl, B. M., Page, A., Sivasithamparam, N., and Sturm, H. (2020). "Evaluation of soil models for improved design of offshore wind turbine foundations in dense sand." *Géotechnique*, 70: 682-99. 10.1680/jgeot.19.TI.034
Kallehave, D., Byrne, B. W., LeBlanc Thilsted, C., and Mikkelsen, K. K. (2015). "Optimization of monopiles for offshore wind turbines." *Philosophical Transactions of the Royal Society A: Mathematical, Physical and Engineering Sciences*, 373: 20140100. doi:10.1098/rsta.2014.0100
Kammerer, A. M. (2002). "Undrained response of Monterey 0/30 sand under multidirectional cyclic simple shear loading conditions." PhD Thesis, University of California, Berkeley
Kang, X., Ge, L., Chang, K.-T., and Kwok, A. O.-L. (2016). "Strain-Controlled Cyclic Simple Shear Tests on Sand with Radial Strain Measurements." *Journal of Materials in Civil Engineering*, 28: 04015169
Kang, X., Xia, Z., Chen, R., Ge, L., and Liu, X. (2019). "The critical state and steady state of sand: A literature review." *Marine Georesources & Geotechnology*, 37: 1105-18. 10.1080/1064119X.2018.1534294
Kim, D.-S. (1991). "Deformational characteristics of soils at small to intermediate strains from cyclic test." PhD Thesis, The University of Texas at Austin
Kim, J., Won, J., and Park, J. (2021). "Effects of water saturation and distribution on small-strain stiffness." *Journal of Applied Geophysics*, 186: 104278. https://doi.org/10.1016/j.jappgeo.2021.104278
Kokusho, T. (1980). "Cyclic triaxial test of dynamic soil properties for wide strain range." *Soils and Foundations*, 20: 45-60
Kokusho, T. (2013). "Liquefaction potential evaluations: energy-based method versus stress-based method." *Canadian Geotechnical Journal*, 50: 1088-99. 10.1139/cgj-2012-0456
Kokusho, T., and Esashi, Y. (1981). "Cyclic triaxial test on sands and coarse materials." *Proceedings of the 10th international conference on soil mechanics and foundation engineering*, 673-79
Kovacs, W. D., and Leo, E. (1981). "Cyclic simple shear of large scale sand samples: effects of diameter to height ratio." *International Conferences on Recent Advances in Geotechnical Earthquake Engineering and Soil Dynamics,* 19.
Kramer, S. L., and Stewart, J. P. (2024). "Geotechnical earthquake engineering." CRC Press.
Kulhawy, F. H., and Mayne, P. H. (1990). "Manual on estimating soil properties for foundation design." (Report No. EPRI-EL-6800). Electric Power Research Institute (EPRI).
Ladd, R. S. (1978). "Preparing Test Specimens Using Undercompaction." *Geotechnical Testing Journal*, 1: 16-23. 10.1520/GTJ10364J
Lade, P. V., and Duncan, J. M. (1973). "Cubical triaxial tests on cohesionless soil." *Journal of the Soil Mechanics and Foundations Division*, 99: 793-812
Lade, P. V., and Ibsen, L. B. (1997). "A study of the phase transformation and the characteristic lines of sand behaviour." *Proc. Int. Symp. on Deformation and Progressive Failure in Geomechanics*, 353-59, Nagoya.
Lanzo, G., Vucetic, M., and Doroudian, M. (1997). "Reduction of shear modulus at small strains in simple shear." *Journal of Geotechnical and Geoenvironmental Engineering*, 123: 1035-42

Le, V. H., Glasenapp, R., and Rackwitz, F. (2024). "Cyclic Hysteretic Behavior and Development of the Secant Shear Modulus of Sand under Drained and Undrained Conditions." *International Journal of Geomechanics*, 24: 04024126. doi:10.1061/IJGNAI.GMENG-9380

Le, V. H., and Rackwitz, F. (2020). "A New Cyclic Simple Shear Test Procedure with Multidirectional Loading." *Geotechnical Testing Journal*, 43: 275-86

Leblanc, C., Byrne, B. W., and Houlsby, G. T. (2010a). "Response of stiff piles to long term cyclic loading." *Géotechnique*, 60: 79-90. 10.1680/geot.7.00196

Leblanc, C., Byrne, B. W., and Houlsby, G. T. (2010b). "Response of stiff piles to random two-way lateral loading." *Géotechnique*, 60: 715-21. 10.1680/geot.09.T.011

Lee, K. L., and Albaisa, A. (1974). "Earthquake induced settlements in saturated sands." *Journal of the Geotechnical Engineering Division*, 100: 387-406.

Leong, E., Yeo, S., and Rahardjo, H. (2005). "Measuring Shear Wave Velocity Using Bender Elements." *ASTM Geotechnical Testing Journal*, 28: 11-11. 10.1520/GTJ12196

Li, Q., Ling, X., Hu, J., and Zhou, Z. (2019). "Residual deformation and stiffness changes of frozen soils subjected to high- and low-amplitude cyclic loading." *Canadian Geotechnical Journal*, 56: 263-74. 10.1139/cgj-2017-0720

Li, S., Zhang, Y., and Jostad, H. P. (2019). "Drainage conditions around monopiles in sand." *Applied Ocean Research.*

Li, X.-S., Dafalias, Y. F., and Wang, Z.-L. (1999). "State-dependant dilatancy in critical-state constitutive modelling of sand." *Canadian Geotechnical Journal*, 36: 599-611.

Li, X. S. and Cai, Z. Y. (1999). "Effects of Low-Number Previbration Cycles on Dynamic Properties of Dry Sand." *Journal of Geotechnical and Geoenvironmental Engineering*, 125: 979-87. doi:10.1061/(ASCE)1090-0241(1999)125:11(979)

Li, Y., Yang, Y., Yu, H.-S., and Roberts, G. (2017). "Monotonic Direct Simple Shear Tests on Sand under Multidirectional Loading." *International Journal of Geomechanics*, 17: 04016038. doi:10.1061/(ASCE)GM.1943-5622.0000673

Liang, F., Zhang, Z., Wang, C., Gu, X., Lin, Y., and Yang, W. (2021). "Experimental Study on Stiffness Degradation and Liquefaction Characteristics of Marine Sand in the East Nan-Ao Area in Guangdong Province, China." *Journal of Marine Science and Engineering*, 9: 638. 10.3390/jmse9060638

Liu, T., Aghakouchak, A., Taborda, D. M., and Jardine, R. J. (2017). "Advanced laboratory characterization of a fine marine sand from Dunkirk, France." Proceedings of the 19th *International Conference on Soil Mechanics and Geotechnical Engineering*, Seoul, Korea.

Liu, X., Li, S., and Sun, L. (2020). "The study of dynamic properties of carbonate sand through a laboratory database." *Bulletin of Engineering Geology and the Environment*, 79: 3843-55. 10.1007/s10064-020-01785-z

Lo Presti, D. C. F. (1991). "Discussion on 'Threshold strain in soils'." *Proceedings of 10th ECSMFE*, 4: 1282-83

Lo Presti, D. C. F., Jamiolkowski, M., Pallara, O., Cavallaro, A., and Pedroni, S. (1997). "Shear modulus and damping of soils." *Géotechnique*, 47: 603-17. 10.1680/geot.1997.47.3.603

Lunne, T., Knudsen, S., Blaker, Ø., Vestgården, T., Powell, J. J. M., Wallace, C. F., Krogh, L., Thomsen, N. V., Yetginer, G., and Ghanekar, R. K. (2019). "Methods used to determine maximum and minimum dry unit weights of sand: Is there a

need for a new standard?", *Canadian Geotechnical Journal*, 56: 536-53. 10.1139/cgj-2017-0738

Lunne, T., Powell, J. J. M., and Robertson, P. K. (1987). "Cone Penetration Testing in Geotechnical Practice (1st ed.)." CRC Press, https://doi.org/10.1201/9781482295047

Luong, M. and Sidaner, J. (1981). "Undrained behaviour of cohesionless soils under cyclic and transient loading." *International Conferences on Recent Advances in Geotechnical Earthquake Engineering and Soil Dynamics.* 13.

Madhusudhan, B. R. (2022). "A review of cyclic simple shear test on soils: challenges and new solutions." *International Journal of Advances in Engineering Sciences and Applied Mathematics.*

Maher, M. H., Ro, K. S., and Welsh, J. P. (1994). "High strain dynamic modulus and damping of chemically grouted sand." *Soil Dynamics and Earthquake Engineering*, 13: 131-38. https://doi.org/10.1016/0267-7261(94)90005-1

Mahmoudi, Y., Cherif Taiba, A., Belkhatir, M., Arab, A., and Schanz, T. (2018). "Laboratory study on undrained shear behaviour of overconsolidated sand–silt mixtures: effect of the fines content and stress state." *International Journal of Geotechnical Engineering*, 12: 118-32. 10.1080/19386362.2016.1252140

Mao, X. and Fahey, M. (2003). "Behaviour of calcareous soils in undrained cyclic simple shear." *Géotechnique*, 53: 715-27. 10.1680/geot.2003.53.8.715

Matlock, H. (1970). "Correlation for Design of Laterally Loaded Piles in Soft Clay." *Offshore Technology Conference*, 18. Houston, Texas. 10.4043/1204-MS

Matsuda, H., Shinozaki, H., Okada, N., Takamiya, K., and Shinyama, K. (2004). "Effects of multi-directional cyclic shear on the post-earthquake settlement of ground." *13th World Conference on Earthquake Engineering*, 13. Vancouver, Canada

Mayne, P. W. (2006). "The Second James K. Mitchell Lecture: Undisturbed sand strength from seismic cone tests." *Geomechanics and Geoengineering*, 1: 239-57. 10.1080/17486020601035657

McAdam, R. A., Byrne, B. W., Houlsby, G. T., Beuckelaers, W. J. A. P., Burd, H. J., Gavin, K. G., Igoe, D. J. P., Jardine, R. J., Martin, C. M., Wood, A. M., Potts, D. M., Gretlund, J. S., Taborda, D. M. G., and Zdravković, L. (2019). "Monotonic laterally loaded pile testing in a dense marine sand at Dunkirk." *Géotechnique*, 0: 1-13. 10.1680/jgeot.18.PISA.004

McGann, C. R., Bradley, B., Cubrinovski, M., Taylor, M. L., and Wotherspoon, L. M. (2015). "Development and evaluation of CPT-Vs correlation for Canterbury, New Zealand soils of the shallow Christchurch and Springston formations." *Bulletin of the New Zealand Society for Earthquake Engineering,* 48(2): 819. 10.5459/bnzsee.48.2.81-91

Mele, L., Lirer, S., and Flora, A. (2019). "The specific deviatoric energy to liquefaction in saturated cyclic triaxial tests." *Earthquake Geotechnical Engineering for Protection and Development of Environment and Constructions – Silvestri & Moraci (Eds)*, 3861–68. Rome. 10.1201/9780429031274

Menq, F.-Y. (2003). "Dynamic properties of sandy and gravelly soils." PhD Thesis, University of Texas at Austin.

Mola-Abasi, H., Dikmen, U., and Shooshpasha, I. (2015). "Prediction of shear-wave velocity from CPT data at Eskisehir (Turkey), using a polynomial model." *Near Surface Geophysics*, 13: 155-68. https://doi.org/10.3997/1873-0604.2015010

Molina-Gómez, F., Viana da Fonseca, A., Ferreira, C., and Camacho-Tauta, J. (2020). "Dynamic properties of two historically liquefiable sands in the Lisbon area." *Soil Dynamics and Earthquake Engineering*, 132: 10610.1 https://doi.org/10.1016/j.soildyn.2020.106101

Nong, Z., Park, S.-S., Jeong, S.-W., and Lee, D.-E. (2020). "Effect of Cyclic Loading Frequency on Liquefaction Prediction of Sand." *Applied Sciences*, 10: 4502.

Nong, Z. and Park, S. (2021). "Effect of Loading Frequency on Volumetric Strain Accumulation and Stiffness Improvement in Sand under Drained Cyclic Direct Simple Shear Tests." *Journal of Geotechnical and Geoenvironmental Engineering.*

Norden, B., Bauer, K., and Krawczyk, C. M. (2023). "From pilot knowledge via integrated reservoir characterization to utilization perspectives of deep geothermal reservoirs: the 3D model of Groß Schönebeck (North German Basin)." *Geothermal Energy*, 11: 1. 10.1186/s40517-022-00242-2

Ogino, T., Kawaguchi, T., Yamashita, S., and Kawajiri, S. (2015). "Measurement deviations for shear wave velocity of bender element test using time domain, cross-correlation, and frequency domain approaches." *Soils and Foundations*, 55: 329-42. 10.1016/j.sandf.2015.02.009

Okur, D. V. and Ansal, A. (2007). "Stiffness degradation of natural fine grained soils during cyclic loading." *Soil Dynamics and Earthquake Engineering*, 27: 843-54. https://doi.org/10.1016/j.soildyn.2007.01.005

OU. (2022). "Scope for site investigation at proposed sand testing area – Chester, UK.", University of Oxford.

Oztoprak, S. and Bolton, M. D. (2013). "Stiffness of sands through a laboratory test database." *Géotechnique*, 63: 54-70. 10.1680/geot.10.P.078

Pan, K., Xu, T. T., Liao, D., and Yang, Z. X. (2022). "Failure mechanisms of sand under asymmetrical cyclic loading conditions: experimental observation and constitutive modelling." *Géotechnique*, 72: 162-75. 10.1680/jgeot.20.P.004

Papadimitriou, A. G., and Bouckovalas, G. D. (2002). "Plasticity model for sand under small and large cyclic strains: A multiaxial formulation." *Soil Dynamics and Earthquake Engineering*, 22, 191-204 https://doi.org/10.1016/S0267-7261(02)00009-X

Patiño, H., Martínez, E., and Galindo, R. (2020). "Dynamic behavior of a granular medium subjected to resonant column tests: Application to Ottawa sand." *Geotechnical Testing Journal*, 43, 132-150 https://doi.org/10.1520/GTJ20170322

Payan, M., Khoshghalb, A., Senetakis, K., and Khalili, N. (2016). "Effect of particle shape and validity of Gmax models for sand: A critical review and a new expression." *Computers and Geotechnics*, 72, 28-41. https://doi.org/10.1016/j.compgeo.2015.11.003

Payan, M., Senetakis, K., Khoshghalb, A., and Khalili, N. (2016). "Effect of gradation and particle shape on small-strain Young's modulus and Poisson's ratio of sands." *International Journal of Geomechanics*, 17, 04016120. https://doi.org/10.1061/(ASCE)GM.1943-5622.0000811

Porcino, D., Diano, V., Triantafyllidis, T., and Wichtmann, T. (2020). "Predicting undrained static response of sand with non-plastic fines in terms of equivalent granular state parameter." *Acta Geotechnica*, 15: 867-882.

Poulos, H. G., and Davis, E. H. (1980). *Pile foundation analysis and design*. Wiley, New York.

Qadimi, A., and Coop, M. R. (2007). "The undrained cyclic behaviour of a carbonate sand." *Géotechnique*, 57, 739-750. https://doi.org/10.1680/geot.2007.57.9.739

Qi, W., Qifei, L., Haiyang, Z., Chengshun, X., and Guoxing, C. (2022). "Experimental investigation of dynamic shear modulus of saturated marine coral sand." *Ocean Engineering*, 264, 112412. https://doi.org/10.1016/j.oceaneng.2022.112412

Qiu, Z. (2023). "Cyclic simple shear testing of Cowden till." DPhil Thesis, University of Oxford.

Quinteros, S., Lunne, T., Krogh, L., Bøgelund-Pedersen, R., and Clausen, J. B. (2018). "Shallow depth characterisation and stress history assessment of an over-consolidated sand in Cuxhaven, Germany." *Cone Penetration Testing*, 525-531

Randolph, M. F. (1981). "The response of flexible piles to lateral loading." *Géotechnique*, 31, 247-259.

Reese, L. C., Cox, W. R., and Koop, F. D. (1974). "Analysis of laterally loaded piles in sand." *Offshore Technology Conference*, 11, Houston, Texas: Offshore Technology Conference. https://doi.org/10.4043/2080-MS

Richards, I. (2019). "Monopile foundations under complex cyclic lateral loading." DPhil Thesis, University of Oxford.

Richards, I. A., Byrne, B. W., and Houlsby, G. T. (2020). "Monopile rotation under complex cyclic lateral loading in sand." *Géotechnique*, 70, 916-930. https://doi.org/10.1680/jgeot.18.P.302

Richart, F. (1970). *Vibrations of soils and foundations*. Prentice Hall, Englewood Cliffs, New Jersey.

Rieman, L. P., Buckley, R. M., Shinde, N. S., and Wheeler, S. J. (2024). "A modified linear-elastic model for calibration of resonant column devices accommodating drive system compliance." *Géotechnique*, 0, 1-41. https://doi.org/10.1680/jgeot.23.00272

Robertson, P. K. (2009). "Interpretation of cone penetration tests: A unified approach." *Canadian Geotechnical Journal*, 46, 1337-1355. https://doi.org/10.1139/T09-065

Rollins, K. M., Evans, M. D., Diehl, N. B., and D. D. III, W. (1998). "Shear modulus and damping relationships for gravels." *Journal of Geotechnical and Geoenvironmental Engineering*, 124, 396-405.

Roscoe, K. H. (1953). "An apparatus for the application to simple shear to soil samples." *Proc., 2nd ICSMFE*, Zurich, 1953, 1, 186-191.

Rose, S., and Apt, J. (2012). "Generating wind time series as a hybrid of measured and simulated data." *Wind Energy*, 15, 699-715. https://doi.org/10.1002/we.499

Ryan, G., Adcock, T., and McAdam, R. (2023). "Influence of soil plasticity models on offshore wind turbine response." *Wind Energy*, https://doi.org/10.1002/we.2876

Sadrekarimi, A. (2016). "Estimating relative density of sand with cone penetration test." *Proceedings of the Institution of Civil Engineers - Ground Improvement*, 169, 253-263. https://doi.org/10.1680/jgrim.15.00017

Sagaseta, C., Cuellar, V., and Pastor, M. (1991). "Cyclic loading." *Proc. 10th European Conference on Soil Mechanics and Foundation Engineering*, 981-999. Balkema, Rotterdam.

Santos, J., and Correia, A. (2001). "Reference threshold shear strain of soil. Its application to obtain a unique strain-dependent shear modulus curve for soil." *15th*

International Conference on Soil Mechanics and Geotechnical Engineering, 267-270, Istanbul, Turkey.

Saxena, S. K., Avramidis, A. S., and Reddy, K. R. (1988). "Dynamic moduli and damping ratios for cemented sands at low strains." *Canadian Geotechnical Journal*, 25: 353-368.

Schmertmann, J. H. (1976). "An updated correlation between relative density DR and Fugro-type electric cone bearing, qc." (Report No. DACW 39-76 M6646). Waterway Experimental Atation. Vicksburg, Mississippi.

Seed, H. B., and Idriss, I. M. (1970). "Soil moduli and damping factors for dynamic response analyses." *Earthquake Engineering Research Center*, University of California, Berkeley.

Seed, H. B., and Idriss, I. M. (1971). "Simplified procedure for evaluating soil liquefaction potential." *Journal of the Soil Mechanics and Foundations Division*, 97, 1249-1273. https://doi.org/10.1061/JSFEAQ.0001662

Seed, H. B., Wong, R. T., Idriss, I. M., and Tokimatsu, K. (1986). "Moduli and damping factors for dynamic analyses of cohesionless soils." *Journal of Geotechnical Engineering*, 112, 1016-1032. https://doi.org/10.1061/(ASCE)0733-9410(1986)112:11(1016)

Senetakis, K., Anastasiadis, A., and Pitilakis, K. (2013). "Normalized shear modulus reduction and damping ratio curves of quartz sand and rhyolitic crushed rock." *Soils and Foundations*, 53, 879-893.

Shadlou, M., and Bhattacharya, S. (2016). "Dynamic stiffness of monopiles supporting offshore wind turbine generators." *Soil Dynamics and Earthquake Engineering*, 88, 15-32. https://doi.org/10.1016/j.soildyn.2016.04.002

Shen, C., Sadigh, K., and Herrmann, L. (1978). "An analysis of NGI simple shear apparatus for cyclic soil testing." *Dynamic Geotechnical Testing* (ASTM International).

Shibuya, S., Tatsuoka, F., Teachavorasinskun, S., Xian Jing, K., Abe, F., You-Seong, K., and Choon-Sik, P. (1992). "Elastic deformation properties of geomaterials." *Soils and Foundations*, 32, 26-46. https://doi.org/10.3208/sandf1972.32.3_26

Stokoe, K. H., Isenhower, W. M., and Hsu, J. (1980). "Dynamic properties of offshore silty samples." *Offshore Technology Conference*, OTC-3771-MS. OTC.

Taborda, D. M. G., Zdravković, L., Potts, D. M., Burd, H. J., Byrne, B. W., Gavin, K. G., Houlsby, G. T., Jardine, R. J., Liu, T., Martin, C. M., and McAdam, R. A. (2019). "Finite-element modelling of laterally loaded piles in a dense marine sand at Dunkirk." *Géotechnique*, 70: 1-16. https://doi.org/10.1680/jgeot.18.PISA.006

Tatsuoka, F., Iwasaki, T., and Takagi, Y. (1978). "Hysteretic damping of sands under cyclic loading and its relation to shear modulus." *Soils and Foundations*, 18: 25-40. https://doi.org/10.3208/sandf1972.18.2_25

Tika, T., Kallioglou, P., Papadopoulou, A., and Pitilakis, K. (2003). "Shear modulus and damping of natural sands." *Deformation characteristics of geomaterials*, 401-407.

Truong, P., Lehane, B. M., Zania, V., and Klinkvort, R. T. (2018). "Empirical approach based on centrifuge testing for cyclic deformations of laterally loaded piles in sand." *Géotechnique*, 69: 133-145. https://doi.org/10.1680/jgeot.17.P.203

Upreti, K., and Leong, E. (2019). "Effect of mean grain size on shear modulus degradation and damping ratio curves of sands." *Géotechnique*: 1-33. https://doi.org/10.1680/jgeot.18.p.169

Vardanega, P. J., and Bolton, M. D. (2013). “Stiffness of clays and silts: Normalizing shear modulus and shear strain.” *Journal of Geotechnical and Geoenvironmental Engineering*, 139: 1575-1589.

Verdugo, R., and Ishihara, K. (1996). “The steady state of sandy soils.” *Soils and Foundations*, 36: 81-91.

Viggiani, G., and Atkinson, J. H. (1995). “Interpretation of bender element tests.” *Géotechnique*, 45: 149-154. https://doi.org/10.1680/geot.1995.45.1.149

Vinale, F., d’Onofrio, A., Mancuso, C., Santucci de Magistris, F., and Tatsuoka, F. (1999). “The pre-failure behaviour of soils as construction materials.” *Proceedings of the Second International Conference on Pre-failure Behaviour of Geomaterials*, 27-29. Torino, Italy.

Vucetic, M. (1994). “Cyclic threshold shear strains in soils.” *Journal of Geotechnical Engineering*, 120: 2208-2228. https://doi.org/10.1061/(ASCE)0733-9410(1994)120:12(2208)

Vucetic, M., and Dobry, R. (1988). “Degradation of marine clays under cyclic loading.” *Journal of Geotechnical Engineering*, 114: 133-149. https://doi.org/10.1061/(ASCE)0733-9410(1988)114:2(133)

Wan, J.-H., Bai, R., Li, X.-Y., and Liu, S.-W. (2023). “Natural frequency analysis of monopile supported offshore wind turbines using unified beam-column element model.” *Journal of Marine Science and Engineering*, 11: 628.

Wang, S., Larsen, T. J., and Bredmose, H. (2021). “Ultimate load analysis of a 10 MW offshore monopile wind turbine incorporating fully nonlinear irregular wave kinematics.” *Marine Structures*, 76: 102922. https://doi.org/10.1016/j.marstruc.2020.102922

Wang, Y.-H., and Tsui, K.-Y. (2009). “Experimental characterization of dynamic property changes in aged sands.” *Journal of Geotechnical and Geoenvironmental Engineering*, 135: 259-270. https://doi.org/10.1061/(ASCE)1090-0241(2009)135:2(259)

Wen, K. Z., Dehtyriov, D., and Byrne, B. W. (2024). “Assessing aerodynamic influences on monopile design for large wind farms.” *WindEurope Annual Event 2024*. *Journal of Physics*. Bilbao, Spain.

White, J. (2020). “A laboratory investigation into the behaviour of sand at low confining stresses.” DPhil thesis, University of Oxford.

Wichtmann, T., Navarrete Hernández, M. A., and Triantafyllidis, T. (2015). “On the influence of a non-cohesive fines content on small strain stiffness, modulus degradation and damping of quartz sand.” *Soil Dynamics and Earthquake Engineering*, 69: 103-114. https://doi.org/10.1016/j.soildyn.2014.10.017

Wichtmann, T., Niemunis, A., and Triantafyllidis, T. (2005). “Strain accumulation in sand due to cyclic loading: Drained triaxial tests.” *Soil Dynamics and Earthquake Engineering*, 967-979. https://doi.org/10.1016/j.soildyn.2005.02.022

Wichtmann, T., Rojas, B., Niemunis, A., and Triantafyllidis, T. (2011). “Prediction of drained and undrained cyclic behaviour of a fine sand using a high-cycle accumulation model.” 5*th International Conference on Earthquake Geotechnical Engineering*, 10-13. Santiago, Chile.

Wichtmann, T., and Triantafyllidis, T. (2009). “Influence of the grain-size distribution curve of quartz sand on the small strain shear modulus G_max.” *Journal of Geotechnical and Geoenvironmental Engineering*, 135: 1404-1418.

Wichtmann, T., and Triantafyllidis, T. (2013). "Effect of uniformity coefficient on G/G_max and damping ratio of uniform to well-graded quartz sands." *Journal of Geotechnical and Geoenvironmental Engineering*, 139: 59-72. https://doi.org/10.1061/(ASCE)GT.1943-5606.0000735

Williams, M. (2016). *Structural dynamics*, CRC Press.

Wu, K.-W. (2023). "Rate effects for monopile foundations." DPhil thesis, University of Oxford.

Xi, R., Du, X., Wang, P., Xu, C., Zhai, E., and Wang, S. (2021). "Dynamic analysis of 10 MW monopile supported offshore wind turbine based on fully coupled model." *Ocean Engineering*, 234: 109346. https://doi.org/10.1016/j.oceaneng.2021.109346

Xu, D.-S., Tang, J.-Y., Zou, Y., Rui, R., and Liu, H.-B. (2019). "Macro and micro investigation of gravel content on simple shear behavior of sand-gravel mixture." *Construction and Building Materials*, 221: 730-744. https://doi.org/10.1016/j.conbuildmat.2019.06.091

Yamashita, S., Shibuya, S., and Tanaka, H. (1997). "A case study for characterizing undrained cyclic deformation properties in young sand deposit from in-situ and laboratory tests." *Soils and Foundations*, 37: 117-126. https://doi.org/10.3208/sandf.37.2_117

Yang, J., and Gu, X. (2013). "Shear stiffness of granular material at small strains: Does it depend on grain size?" *Géotechnique*, 63: 165-179. https://doi.org/10.1680/geot.11.P.083

Yang, J., and Liu, X. (2016). "Shear wave velocity and stiffness of sand: The role of non-plastic fines." *Géotechnique*, 66: 500-514. https://doi.org/10.1680/jgeot.15.P.205

Yang, S., He, B., Andersen, K. H., and Firouzianbandpey, S. (2023). "Monotonic and cyclic properties of silty sand and sandy silt for foundation design of offshore windfarms." *Canadian Geotechnical Journal*, 60: 366-379. https://doi.org/10.1139/cgj-2022-0009

Yasuda, N., and Matsumoto, N. (1993). "Dynamic deformation characteristics of sands and rockfill materials." *Canadian Geotechnical Journal*, 30: 747-757. https://doi.org/10.1139/t93-067

Yasuda, N., and Matsumoto, N. (1994). "Comparisons of deformation characteristics of rockfill materials using monotonic and cyclic loading laboratory tests and in situ tests." *Canadian Geotechnical Journal*, 31: 162-174. https://doi.org/10.1139/t94-022

Yasuda, N., Ohta, N., and Nakamura, A. (1996). "Dynamic deformation characteristics of undisturbed riverbed gravels." *Canadian Geotechnical Journal*, 33: 237-249.

Zdravković, L., Jardine, R. J., Taborda, D. M. G., Abadias, D., Burd, H. J., Byrne, B. W., Gavin, K. G., Houlsby, G. T., Igoe, D. J. P., Liu, T., Martin, C. M., McAdam, R. A., Wood, A. M., Potts, D. M., Gretlund, J. S., and Ushev, E. (2020). "Ground characterisation for PISA pile testing and analysis." *Géotechnique*, 70: 945-960. https://doi.org/10.1680/jgeot.18.PISA.001

Zhang, J., Andrus, R. D., and Juang, C. H. (2005). "Normalized shear modulus and material damping ratio relationships." *Journal of Geotechnical and Geoenvironmental Engineering*, 131: 453-464.

Zhang, Y., and Andersen, K. H. (2017). "Scaling of lateral pile p-y response in clay from laboratory stress-strain curves." *Marine Structures*, 53: 124-135. https://doi.org/10.1016/j.marstruc.2017.02.002